UNIVERSIDADE DE LISBOA

INSTITUTO SUPERIOR TÉCNICO

Development and application of uniaxial and multiaxial ultrasonic fatigue testing methods

Pedro Ferreira Rodrigues da Costa

Supervisor: Doctor Luís Filipe Galrão dos Reis

Co-Supervisor: Doctor Diogo Coelho de Carvalho Montalvão e Silva

Thesis approved in public session to obtain the PhD Degree in Mechanical Engineering

Jury final classification: Pass with Distinction and Honour

2022

UNIVERSIDADE DE LISBOA

INSTITUTO SUPERIOR TÉCNICO

Development and application of uniaxial and multiaxial ultrasonic fatigue testing methods

Pedro Ferreira Rodrigues da Costa

Supervisor: Doctor Luís Filipe Galrão dos Reis

Co-Supervisor: Doctor Diogo Coelho de Carvalho Montalvão e Silva

Thesis approved in public session to obtain the PhD Degree in

Mechanical Engineering

Jury final classification: Pass with Distinction and Honour

Jury

Chairperson: Doctor José Arnaldo Pereira Leite Miranda Guedes, Instituto Superior Técnico, Universidade de Lisboa

Members of the Committee:

Doctor Manuel José Moreira de Freitas, Instituto Superior Técnico, Universidade de Lisboa

Doctor Abílio Manuel Pinho de Jesus, Faculdade de Engenharia, Universidade do Porto

Doctor Luís Filipe Garlão dos Reis, Instituto Superior Técnico, Universidade de Lisboa

Doctor Ricardo António Lamberto Duarte Cláudio, Escola Superior de Tecnologia de Setúbal, Instituto Politécnico de Setúbal

Funding Institutions

Fundação para a Ciência e Tecnologia

2022

To my love **Carolina** ‘In you I’m lost’

Thom York

Acknowledgements

Across all the thesis conducted work, there are many to whom I am thankful for their personal or professional support and contribution. In these first pages I would like to express my sincere gratitude to all I had the privileged to be accompanied by.

First and foremost, I would like to express my gratitude to my supervisor, professor Luís Reis. Since my master's degree, he took me in and fully trusted in my capabilities towards such an interesting and complex project. The researcher I am today was built by his guidance, his trust and devotion. From professor Luís Reis I came to meet my co-supervisor Diogo Montalvão. From him, amazing new ideas and debates came to fruition. I thank all the help and all I have come to learn.

One of the most insightful professors I have come to meet must be acknowledged, Professor Manuel Freitas. I feel really lucky to have worked with someone I truly admire and respect. I am grateful for the given opportunity to work by his side and for all the knowledge and guidance I have received.

The present document is entirely dedicated to the person who believed in me the most. Without her I am sure I would never have reached this pinnacle of my career. She appeared in my life in one of my lowest moments. She gave me the strength and motivation to raise myself and to continue pushing onwards. To all you have given me I dedicate this thesis with all my heart to you Carolina Nogueira.

I would like to express my love to my family, especially to my mother and father. They have built the basis of the person I am genuinely proud to be today. I will always carry with me their unconditionally devotion and love.

I would like to give a special thanks to my fellow working companions. Across all these years I found myself surrounded by one the most intelligent, hardworking, and amazing people. To all fellow student companions I came across, thank you for the countless coffee breaks where some of the most amazing thoughts and problem-solving ideas were discussed. They are without any doubt imbed on this present document. From all students I have met, I would like to leave a special acknowledgement to: João Marques, Andreia Sofia Oliveira, Manuel

Sardinha, Diogo Rechena, Frederico Alves and Henrique Soares. May we find ourselves working side by side again.

In the hosting institution of the present thesis, I came to meet many professors and non-professors that received me as their co-worker and as their student. I would like to dedicate a caring acknowledgement to four professors who had their door always open to me: Professor Fátima Vaz , Relógio Ribeiro, Virgina Infante and Augusto Moita de Deus.

Likewise, I could never forget three non-professor workers of the Instituto Superior Técnico: Pedro Teixeira, João Vicente, Carina Tavares. These three people embrace me as their peer with an extraordinary friendship I will not ever fail to recall. They have become and always will be my true friends. I will always cherish this incredible friendship we have built.

In the course of these years, one colleague and a friend departed too soon. The weight laid upon me only two days from holding your baby belly with my own hands has scarred this chapter of my life. These words will be my last tribute to Patrizia Paradiso.

I would like to leave my last words to my companions in life, my dearest friends. ‘Happiness is only real when shared’ (Christopher McCandless). To André Carrilho, Daniel Rocha, António Amorim, Pedro Neves, Duarte Crawford, João Gameiro, Ricardo Ramalho, and Ana Simões, a special gratitude.

To those I did not mention my sincere apologies, your name might not appear written, but it won’t ever be forgotten.

I would also like to acknowledge the institution, Fundação para a Ciência e a Tecnologia, for the given financial support in the project GCYCLEFAT - PTDC/EME-EME/7678/2020.

Abstract

The focus of this dissertation is the development of ultrasonic fatigue testing (UFT) experimental methods across four different loading conditions, including in-plane biaxial and combined tension-torsion. Structural components from bridges to aeroplanes can be subjected from 10^6 (one million) to 10^9 (one billion) cycles across their service life. UFT methods have thus appeared to respond to the industry demand for failure predictability of materials beyond one million cycles, the Very High Cycle Fatigue regime (VHCF). The primary objective of ultrasonic fatigue methods is to induce high cycle frequency (from 20 kHz), thus enabling the VHCF study in a timely and energy reliable manner.

The design of an UFT machine and specimens that enable getting a determined and bespoke stress state of interest requires specialised study and experimental analyses to fully guarantee valid and consistent fatigue test results. The complexity of ultrasonic machines and the respective experimental procedure together with new influential variables (i.e., that were not relevant in conventional testing) demand high-end research. Such complexity increases with complex multiaxial stress states.

Two uniaxial (tension and torsion) and two novel multiaxial (in-plane biaxial and combined tension-torsion) methods were studied and continuously improved in the present work. The two innovative biaxial ultrasonic machines are axial-axial cruciform testing and tension/torsion cylindrical specimens. Thorough numerical, analytical and experimental analyses and UFT were first conducted in the two uniaxial ultrasonic methods followed by the two novel biaxial. The base numerical and experimental methodologies were built and transferred to the two biaxial methods from the first uniaxial ultrasonic tests. All results were compared and analysed, proving the reliability of the proposed methodologies. Base analytical guidelines for the novel methods were also proposed, and together with the more accessible methodology, the base for future standardisation of ultrasonic multiaxial methods was outlined.

Keywords

Ultrasonic Fatigue; Multiaxial fatigue; Tension/Torsion; Cruciform specimen; Standardisation; Ultrasonic methodologies

Resumo

A presente dissertação tem como foco o estudo e o desenvolvimento de ensaios de fadiga ultrassónica, nomeadamente quatro diferentes tipos de ensaios e respetivas metodologias experimentais. Desde aviões até pontes, diversas máquinas e estruturas da Era moderna quotidiana estão sujeitas entre 10^6 (um milhão) e 10^9 (mil milhões) ciclos de fadiga na sua vida operacional. Devido a uma maior exigência de possível previsibilidade de falha após um milhão de ciclos, regime de fadiga de muito elevado número de ciclos, as máquinas de fadiga ultrassónica foram assim projetadas para uma viável realização de estudos de fadiga em tempo e energia consumida.

A projeção e o desenvolvimento de uma máquina de fadiga ultrassónica, para um determinado regime de tensão, requer estudo e desenvolvimento experimental especializado para garantir uma testagem à fadiga válida e consistente. Devido à complexidade associada a máquinas ultrassónicas, respetivas metodologias experimentais e novas influentes variáveis (i. e. não relevantes em testes de fadiga convencional), é necessária a realização prévia de estudos de elevada exigência. No momento em que se consideram regimes multiaxiais existe ainda uma acrescida complexidade.

Dois métodos ultrassónicos uniaxiais – tensão-compressão e torção - e dois novos métodos multiaxiais são alvo de estudo intensivo e continuo melhoramento. Os respetivos métodos de fadiga multiaxial são axial-axial através de provetes cruciformes, e fadiga multiaxial tensão/torção através de provetes cilíndricos. Um extensivo estudo numérico, analítico e experimental é realizado, primeiramente, aos ensaios uniaxiais, criando assim toda a metodologia para os inovadores e mais complexos ensaios multiaxiais. Todos os resultados são comparados e analisados demonstrando a viabilidade da metodologia numérica e experimental aplicada. Em conjunção com as estabelecidas metodologias numérica e experimental, são posteriormente propostas diretivas analíticas inerentes aos dois novos ensaios multiaxiais com o principal objetivo de criar a base para uma normalização dos ensaios estudados e de outros futuros.

Palavras-Chave

Fadiga ultrassónica; Multiaxial; Cruciforme; Tensão/Torção; Normalização; Metodologias ultrassónicas

Table of Contents

List of Figures

List of Tables

Acronyms

AM	Additive Manufacturing
ASTM	American Society for Testing and Materials
CFRP	Carbon Fiber Reinforced Polymer
CNC	Computer Numerical Control
C-T x	Compression-Tension Out-of-phase cruciform *x*
DAQ	Data Acquisition
Dn	Displacement node
EDS	Energy Dispersive Spectroscopy
FALSTAFF	Fighter Aircraft Loading Standard for Fatigue
FE	Finite Element
FEA	Finite Element Analysis
FGA	Fine Granular Area
FRF	Frequency Response Function
F*x* T-T	First Tension-Tension in-phase cruciform geometry *x*
GBF	Granular Bright Facet
HCF	High Cycle Fatigue
IDMEC	Instituto de Engenharia Mecânica
ISO	International Organization for Standardization
LCF	Low Cycle Fatigue
LH	Longitudinal Horn
LEM^2	Laboratório de Ensaios Mecânicos e de Materiais
Mach *x*	Machine sequence of the torsional horn
MI	Mode of Interest
Nx T-T	Second and New Tension-Tension in-phase cruciform geometry
ODA	Optically Dark Area
PM	Parasite Mode
PSD	Power Spectrum Density

SEM	Scanning Electron Microscope
SLM	Selective Laser Melting
SLS	Structured-Light Scanning
Sn	Stress node
SnB	Booster-Horn Stress node connection region
SnH	Horn-Specimen Stress node connection region
S-N	Fatigue Stress -Life
SVD	Singular Value Decomposition
S*x*	Cruciform representative ultrasonic tensile specimen Slice *x*
TH	Torsional Horn
Ts	Torsional Section -Tension-Torsion specimen
UFT	Ultrasonic Fatigue Testing
VHCF	Very High Cycle Fatigue
2B+2H	Two boosters two horns ultrasonic setup

Nomenclature

A_0	Measured axial displacement amplitude
A_{0r}	Measured rotational displacement amplitude
c	Wave propagation velocity
dR	Strain gauge electric resistance variation
E	Young's Modulus
f	Frequency
G	Shear Modulus
HV	Vickers Hardness
k	Stiffness
K	Gauge factor
K_I	Stress intensity factor mode I
ΔK_{th}	Threshold stress intensity factor
m	Mass
N	Number of cycles
R	Stress Ratio
R_a	Roughness average arithmetic mean deviation
R_i	Strain gauge resistance
Rz	Roughness maximum height
Rz1max	Roughness maximum sample peak to valley height
U	Displacement
U_B	Input Voltage
U_y	Axial displacement
U_s	Strain energy
U_r	Rotational displacement
U_{mag}	Displacement magnitude
V_o	Output Voltage
w_n	Natural frequency

w_d	Natural damped frequency
α	Thermal expansion coefficient
γ	‘Flapping motion’ factor
δ	Area difference factor
ε	Strain
$\varepsilon_x, \varepsilon_y$	Normal Strain
ε_{xy}	Shear strain
ε_{max}	Fracture strain
ζ	Viscous damping
η	Hysteretic damping
ν	Poisson’s ratio
ρ	Density
σ	Stress
σ_1, σ_2	Principal stress
$\sigma_{0.2\%}$	Yield Stress
σ_{max}	Normal stress maximum amplitude
σ_{min}	Normal stress minimum amplitude
σ_r	Ultimate Stress
σ_w	Fatigue limit stress
σ_x, σ_y	Normal Stress
τ_{xy}	Shear stress

1

Introduction

After more than a century from its acknowledgement, material fatigue damage and failure is still a significant research field with an imperative impact on machinery, maintenance, structural design and construction. The fatigue failure phenomenon's complexity and intricacies bring many challenges for any researcher to fully characterise its behaviour in a continuously growing multitude of materials. Material samples are applied in a wide range of machines imposing cyclic deformation to reproduce fatigue behaviour and characterise a material fatigue strength. From mechanical to hydraulic, fatigue machines vary in size, imposing force magnitude and direction, with many available fixtures for more complex fatigue studies as imposing high and low temperatures.

In the last decades, a new type of fatigue testing machine with its respective method has seen a surge of interest, the ultrasonic fatigue machines. Ultrasonic Fatigue Testing (UFT) has grown to be a subfield within fatigue research topics with its respective conferences. It gave a reliable manner for researchers to study fatigue up to a billion cycles, the Very High Cycle Fatigue (VHCF) regime, with the ability to induce more than twenty thousand cycles per second. Many researchers have dedicated their work from developing and improving ultrasonic fatigue machines and methods to the associated fatigue behaviour and fracture mechanics in the VHCF regime.

1.1 Objectives

The present work focused on ultrasonic fatigue experimental methods and machines. It utilizes the known knowledge and experience around ultrasonic machines to design and develop new ultrasonic induced fatigue damage and respective methodologies.

Ultrasonic methods are still under research and development compared to conventional fatigue machinery. By utilizing resonance as a mean to achieve high-frequency fatigue testing, new complexities and variables are brought that may affect the fatigue result outcome. Core research questions surrounding today the ultrasonic fatigue researchers are:

- Does high frequency (high strain rate) affect the material stress-life? If so, how could it be quantified?
- How does the ultrasonic specimen size and shape influence the resonance stress-induced response, the obtained fatigue fracture, and the resulting stress-life?
- What are the requirements for the ultrasonic machine methods and respective methodologies to be standardised?
- How could the ultrasonic methods be adapted towards more complex fatigue stress fields?

The presented issues and many others are still under debate. The present study focused primarily on the final two questions. Therefore, the present thesis main objective was to achieve analytical, numerical and experimental methodologies towards developing, improving and standardise ultrasonic fatigue methods and machines.

To achieve the pretended objectives and contribute to ultrasonic fatigue enlightenment, considerable advances and changes were made to an already built tension-compression ultrasonic machine in Instituto de Engenharia Mecânica (IDMEC) mechanical and material testing laboratory (LEM^2). A pure torsional ultrasonic machine is built following Claude Bathias design, and two multiaxial methods are developed, tension/torsion and cruciform ultrasonic fatigue testing.

Across all four conducted ultrasonic fatigue tests, a deep study of the machine's modal response and surrounding experimental methodologies was carried out. Three different materials were studied in the context of this thesis ultrasonic machines: the already built and

improved tension-compression; newly built pure torsion; biaxial tension-compression torsion; and tension-tension cruciform.

Every ultrasonic fatigue test was first analysed through finite element analysis (FEA). All experimental methodologies around the four ultrasonic methods were built around the published research knowledge and numerical results. A comparison between numerical results, experimental results, and the ultrasonic scientific community consolidates all findings and conclusions.

In summary, the present work's main objective is to build base experimental methodologies from uniaxial to multiaxial ultrasonic fatigue machines, driving this growing fatigue research branch towards a fatigue study method that could be standardised. All results presented here were conducted to elevate the ultrasonic methods towards a known applicable and trusted mechanical testing method.

1.2 Document Structure

The presented thesis is composed of six main chapters: Introduction and objectives; State of the art; Finite element analysis; Materials, equipment, and experimental methodology; Results and respective analysis; and finally the Conclusions.

After the introduction and the thesis objectives, chapter 2 focuses on state of the art, from conventional to ultrasonic fatigue. Chapter 2 begins by establishing a fatigue base framework with a short introduction to fatigue main concepts, characterisation, and conventional testing methods and machinery. UFT objectives and base concepts are then described in more detail after a brief historical background. The tension-compression ultrasonic fatigue method is first thoroughly explained with all associated base concepts that allowed to achieve such high-frequency fatigue. Being the first built and most straightforward ultrasonic fatigue machine, the applied mechanical concepts were a starting point and were consistently applied in subsequent UFT methods. Followed by the tensile ultrasonic machine, an extensive literature with a detailed description of current UFT research and latest developments is made focusing on: all applied different UFT methods and methodologies, influential variables when conducting UFT, as the frequency effect, and finally the related VHCF fracture analysis.

The main emphasis of chapter 3 is the executed numerical methodology and the associated results. The chapter is divided across the four studied and executed ultrasonic fatigue methods in order: tension-compression; pure torsion; tension-torsion; cruciform axial-axial. The exact order will be followed in the succeeding chapters. An introduction of how the machine works and present components is first made between each ultrasonic method subchapter. The explained ultrasonic mechanical concepts in chapter 2 are associated with all studied methods using the numerical software results. All ultrasonic methods final subchapters describe in detail all complex obtained results and conducted modal analysis and their objective towards solving the perceived problems and achieving the intended objectives. For the two novel multiaxial methods of the thesis project, an analytical solution is also presented and explained.

The fourth chapter introduces the ultrasonic fatigue-tested materials with the respective static properties, the ultrasonic structure rig and all utilised equipment, and conducted experiments with associated methodologies and calculations. Two core measurement methods were used, a vibrometer laser for modal analysis and strain gauges for measuring the strains. A first introduction to the theory and analytical calculations to modal analysis and strain gauges is first made, followed by the associated experimental methodology. The chapter ends with a detailed description of the ultrasonic fatigue methodologies for the VHCF regime study.

The fifth chapter is dedicated entirely to the obtained experimental results. Just as in chapter 3, the same UFT method order is followed. For each ultrasonic method, the results are separated into three categories: modal analysis, strain and displacement measurements, and UFT stress-life results with fatigue fracture surface analysis.

The thesis closes in the sixth chapter, where all main reached conclusions and future work proposals are presented. All drawn conclusions from the four conducted ultrasonic methods are sequentially presented in the same order as chapters 3 and 5. From all the major withdrawn conclusions surrounding the thesis project, description of recommended future works to continue and improve all executed methods is also made.

2

State of the art

2.1 Introduction to Fatigue

Every component made by any material subjected to dynamic loads is subordinated to most frequent and the most complex type of failure, and therefore more difficult to predict, fatigue. Fatigue arises in a given material when cyclic loads are applied. Such loads will induce discontinuities leading to crack initiation, propagation and inevitable failure.

Almost two centuries after Wohler's pioneer investigation of railway axles failure [1], the fatigue field of research shows a continuous search for new, more intrinsic knowledge and improved experimental methods.

The complexity of fatigue damage in materials, its extreme difficulty of detection, and being one of the most common machine failures makes the fatigue research field essential for failure prevention and machine design. The fatigue study importance can easily be understood through specific machine and structures failure analysis research. M. Freitas et al. [2; 3] investigated a crankshaft and a gear wheel failure of marine engines that reached a premature fatigue failure on service.

One of the main defining material fatigue strength parameters is the number of loading cycles to failure for a given deformation. The cycle range is commonly divided into three regimes: Low Cycle Fatigue (LCF) up to 10^4 cycles; High Cycle Fatigue (HCF) 10^4 – 10^6 cycles; Very High Cycle Fatigue (VHCF) $>10^6$ cycles.

All three mentioned cyclic regimes can be reached with any load type and combination. All materials have a respective fatigue stress-life response for a given deformation type cyclic

damage: tension-compression, bending, torsion loading, or any combination of the three load types. Beyond the type of applied load, several other variables affect the fatigue strength of a given material as: stress range and stress ratio; structural detail of the component's geometry; material characteristics; environmental conditions; and the manufacturing process.

With three different cycle regimes, a wide range of loading conditions, and a considerable number of influential variables, many different machines and methodologies were created to fulfil all fatigue testing analysis requirements. This work distinguishes two different machine and fatigue testing categories with respective methodology: conventional fatigue testing and ultrasonic fatigue testing (UFT). Both the conventional and ultrasonic fatigue test methods are presently described with many of the currently in use machine testing rigs.

Fatigue tests were first predominantly focused on inducing uniaxial loads, meaning one single directional cycle load was applied. However, multiaxial stresses were later recognised as the leading dynamic stress state in machines and structures [4]. Since most components and machines are subjected to multiaxial cyclic loads, many researchers have dedicated their studies to multiaxial technological developments and fatigue properties.

Technological advances in transportation, general machinery, and other industries demand higher working speeds and life spans. Therefore, a need for a higher life span fatigue resistance characterisation method in the VHCF regime was required. VHCF has been associated with automotive, aerospace and train components [5; 6]. Even concrete bridges [7], mass transit and offshore structures [8], and wind turbines and their foundation [9] can surpass the HCF range, reaching cycle damage above 10^8 in their service life.

To reach the VHCF range, no ordinary machinery would execute the fatigue analysis in a time-reliable manner. The ultrasonic fatigue machines were then created to enable the very high cycle testing requirement.

Just as 'conventional' fatigue transposed from uniaxial to multiaxial testing mechanisms, UFT testing developments are also following the same trend.

The presented PhD study focuses on UFT methodologies to study the VHCF regime in uniaxial loading conditions and the development of two novel UFT in multiaxial stress states. All conducted fatigue tests were made through the use of ultrasonic fatigue machines built at the hosting institution Instituto Superior Técnico within the IDMEC research department.

For uniaxial loading conditions, UFT tension-compression and pure torsion were conducted. The pure torsion machine was fully designed, built, and tested in the course of the present study.

Two different multiaxial methodologies were studied, tested, and analyzed: In-phase tension-torsion with different stress ratios and axial-axial cruciform biaxial fatigue.

An introduction to fatigue testing fundamentals is first made through conventional fatigue methodologies such as fatigue range; stress type and ratio, applied specimens and manufacturing processes influence. Multiaxial fatigue conventional methods and base concepts are also discussed. Following the established basic uniaxial and multiaxial fatigue notions, the UFT machines, different methodologies, and all basic surrounding concepts are extensively described and explained.

2.1.1 Conventional fatigue testing

In fatigue testing, a material sample will be subjected to dynamic cyclic loads in a controlled machine and environment. The applied methodologies will depend on used machinery, testing material, the fatigue range of study, and specific parameters of interest, such as temperature or resistance to corrosion.

Due to the proven concept and considerable proven published research, the most basic conventional fatigue testing methods are standardised, each with the respective standard reference. Some of such fatigue testing standards are here presented by the American Society for Testing and Materials (ASTM) and International Organization for Standardization (ISO):

- ASTM E606 / E606M - 19: Standard Test Method for Strain-Controlled Fatigue Testing
- ASTM E2207 - 15: Standard Practice for Strain-Controlled Axial-Torsional Fatigue Testing with Thin-Walled Tubular Specimens
- ASTM E2789 - 10(2015): Standard Guide for Fretting Fatigue Testing
- ASTM E2368 - 10(2017): Standard Practice for Strain Controlled Thermomechanical Fatigue Testing

- ASTM E2948 - 16a: Standard Test Method for Conducting Rotating Bending Fatigue Tests of Solid Round Fine Wire
- ISO 12106:2017: Metallic materials - Fatigue testing - Axial-strain controlled method
- ISO 22407:2021: Metallic materials - Fatigue testing - Axial plane bending method
- ISO 12108:2018: Metallic materials - Fatigue testing - Fatigue crack growth method

The above-mentioned experimental standards specify specimen geometries and experimental methodology for the LCF and HCF.

Looking at the most straightforward test, the tensile (tension-compression) test, servo-hydraulic machines or electromechanical are generally utilised for applying a sinusoidal load to a specimen.

2.1.1.1 Fatigue basic damage parameters

When testing the fatigue resistance of a given material, the applied damage through stress has different influential parameters to be considered, type of induced load, the associated stress amplitude, and stress ratio.

Three different uniaxial loading conditions can be considered: Tensile tension-compression, bending, torsion. Multiaxial loading conditions can be any combination of the three mentioned uniaxial loadings (e.g. tension-torsion) and/or a multidirectional uniaxial loading (e.g. cruciform two orthogonal cyclic tension-compression cyclic loads). Since one primary focus of the present study is associated with multiaxial fatigue, it has a dedicated state of the art description in chapter 2.2.

The fatigue life testing can be generally described as the application of sinusoidal loading repetitions, number cycles (N), until a final catastrophic failure. When applying any given cyclic stress (S), its amplitude is directly associated with the resulting life. Fatigue strength is then associated with the applied stress amplitude to the resulting number of cycles until sample failure, the fatigue stress-life (S-N). As aforementioned, the fatigue study can be divided into three different regimes: LCF, HCF and VHCF.

LCF occurs within the range of the plastic deformation region for the testing material. LCF is far from the present study's focus. A strain gauge is applied to standardised specimen geometries, and the test is strain-controlled. The loading control, response, type of associated failure, number of cycles, and overall experimental results are far different. Therefore, no attention is given to this type of fatigue study in this thesis.

For the HCF test, the control is made through the applied force. For both the LCF and HCF testing regimes, servo-hydraulic and electromechanical machines are most commonly employed. An example of a hydraulic machine used for multiaxial HCF testing in LEM^2 Técnico's Experimental Mechanics laboratory is presented in Figure 2-1.

Figure 2-1. Servo-hydraulic tension-torsion fatigue testing machine Instron 8874

In the published research by Luis Reis et al. [8], HCF multiaxial fatigue testing was conducted for two different multiaxial loading paths using Figure 2-1 machine. This machine can conduct tension-compression, pure torsion, and multiaxial tension-torsion fatigue testing with any given stress ratio and phase between load types. With specific modifications, it can also conduct fatigue testing in corrosive environments, as shown in the published research by F. A. Canut et al. [10].

There are several possible cycling loading fatigue testing manners to study or even replicate the deformation of understudy components, each with a resultant life-cycle relation [11]. The fatigue stress amplitude is the difference between the highest/lowest stress to the mean stress value. Figure 2-2 represents the stress amplitude for zero mean stress followed by the stress ratio (R) calculation method, equation (2.1).

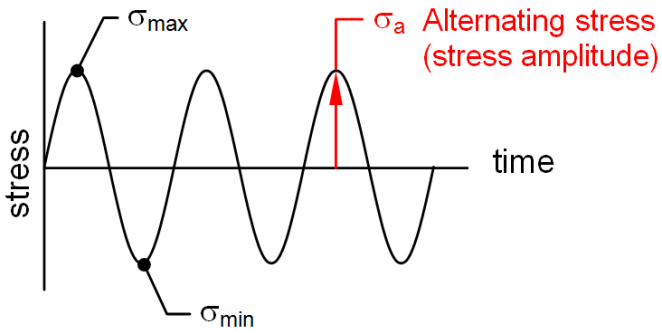

Figure 2-2. Fatigue cyclic stress amplitude and stress ratio representation

$$R = \frac{\sigma_{min}}{\sigma_{max}} \tag{2.1}$$

In Figure 2-2, the mean stress is zero resulting in an R= -1 stress ratio. In this work, all conducted uniaxial fatigue tests followed an R=-1 stress ratio similar to the stress cycle shown in Figure 2-2. To research non-zero mean stress fatigue, R≠-1, a static force must be applied across the fatigue cyclic test execution [12; 13].

Different sample geometries and machines are applied for different loading conditions. The specimen geometry can also be dependent on the fatigue range and other fatigue variables of the study, such as crack propagation. Tension specimens can follow a cylindrical shape format, as H. Soares et al. [14] used to study railway wheel fatigue strength in the HCF regime, or sheet plate shaped as Jiunn-Yuan et al. [12] use for the stainless steel 316L HCF in-depth study. Jiunn-Yuan sheet-shaped specimen allowed to fatigue test V groove Gas Tungsten Arc Welding (GTAW). Pure torsion fatigue testing follows similar cylindrical shaped specimens. Zhao et al. [15] conducted extensive fatigue strength experiments on aluminium 7075-T651 with plate and cylindrical tension specimens and cylindrical torsional specimens. Figure 2-3 shows the uniaxial specimens used by the Zhao research team with the respective tension and torsion load represented.

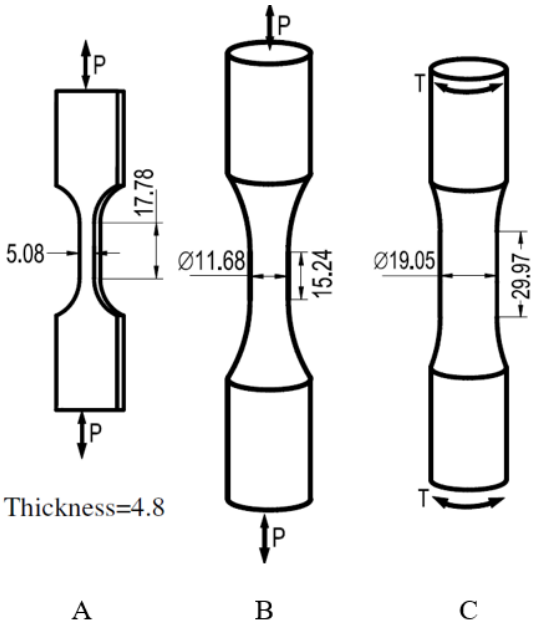

Figure 2-3. Conventional fatigue specimen geometries: (A) plane tensile; (B) cylindrical tensile; (C) cylindrical pure torsion [15].

Uniaxial bending fatigue tests can have different setups as three or four bending points, with or without fixing the specimen to each point. Fatigue bending tests are widely used for composite materials. Baere et al. [16] applied both three and four point bending fatigue with and without clamping to a carbon fibre laminate composite. Sheet sandwich composites are also commonly fatigue studied through bending fatigue. Harte et al. [17] studied the fatigue strength of aluminium face sheets with an aluminium alloy foam core in a four-point bending unclamped rig. Sandwich composite honeycomb structures are widely used due to their high stiffness to weight ratio. The cellular structures as honeycomb are also commonly bending fatigue tested, as conducted by Giulia et al. [18].

The environment to which any component or structure is subjected is an undeniably vital aspect to be considered, both in static and dynamic loading conditions. The main influential environmental parameters are temperature, corrosive environments and exposure to electric voltage or current. The temperature has a significant influence on the material response and behaviour. In conventional fatigue, a temperature controlling rig is unnecessary unless the effect on fatigue strength of a high or low temperature is under research. As later explained, ultrasonic methods generate unwanted heat that must be controlled not to affect the fatigue results.

2.1.1.2 Material characteristics and Manufacturing Process

Most metals have isotropic behaviour, but for an anisotropic material the imposed load direction will have a different response. Magnesium is an example of an anisotropic metal. The direction for which the Magnesium specimens are machined needs to be considered when conducting any mechanical property analysis as fatigue strength [19; 20].

Considering isotropic metals, there are essential factors that influence the overall fatigue strength. Some of the most critical factors in fatigue resistance are heat treatment, microstructure, fabrication method; surface roughness, defects, and inclusions.

The overall fatigue strength of a given material depends not only on its basic properties, but it is also influenced by the manufacturing process.

The present PhD project conducted ultrasonic fatigue test to Ti6Al4V titanium alloy manufactured by Selective Laser Melting (SLM), a powder bed Additive Manufacturing (AM) method. AM processes naturally have influential variables to the final material fatigue strength, such as the type of AM process employed, manufacturing parameters and post-manufacturing treatments. The study focused on the impact of the SLM process surface roughness and post-treatment polishing fatigue strength on the VHCF fatigue strength.

AM has propelled mechanical design and prototyping in an unprecedented way. Offering an almost infinite geometric freedom, it enables the production of complex geometries, which are very difficult to obtain by conventional manufacturing means, with possible gains such as lower weight, multifunctionality and enhanced behaviour of parts, and even waste and costs savings. A 2019 market report [21] states that the metal AM components market would generate approximately $228 billion in the following decade. It also anticipates its shift from a prototype focused technology to the production industry. Even so, at the present time, when compared with conventional manufacturing, AM has significant limitations to consider, such as low achievable geometric tolerances; mechanical behaviour predictability; availability of materials; print defects; increased surface roughness with higher defect densities; lack of fusions; and porosities [22–24]. All such adversities lead to different and lower fatigue strengths of components. Sterling et al. [25] compared wrought machined and AM laser Engineering Net Shaping Ti6Al4V titanium alloy, describing a distinct difference in fundamental mechanical properties and fatigue strength.

A vast amount of AM research focuses on fatigue characterisation linking its massive interest and advantages to real-world applications. In contrast to the high geometrical benefits,

AM has higher affecting fatigue variables when compared with conventional methods that need to be understood and characterised. Thus, associated AM fatigue studies developed a research subfield of their own. The additive manufactured materials fatigue behaviour has been associated with printing part orientation [26] and other printing parameters such as laser scan speed; hatch spacing and layer thickness [27]. For metal powder AM methods, the powder particle size and shape have shown to be a non-negligible parameter [28]. The significant and growing number of printing methods and materials together with a vast number of affecting parameters display the scale and complexity of the AM fatigue field of research.

Fatigue failure within the elastic deformation region (HCF and VHCF) is usually related to sections where stress concentration is formed, leading to local plastic deformation, crack formation, and, lastly, total failure. Such sections, termed crack initiation sites, are mainly associated with surface roughness and internal defects (inclusions, voids, inner gas pores, smooth facets, and lack of fusion). Thus, surface quality and roughness play an essential role in the fatigue strength of a given component. Joy Gockel et al. [29] showed how manufacturing process parameters associated with lower surface roughness could lead to higher fatigue life. Since surface quality could be an AM limitation, examining its impact on fatigue strength and ways to diminish is imperative. The surface roughness influence can be characterised by comparing the fatigue strength of specimens with and without surface treatment. Kasperovich and Hausmann [30] showed that some specimens had increased fatigue strength when they were polished. Formanoir et al. [31] investigated the polish treatment impact, the microstructure and building direction of Ti6Al4V additive manufactured samples produced by Electron Beam Melting method. L. Denti et al. [32] assessed AM Power Bed Fusion Ti6Al4V fatigue strength in HCF. They compared as-built samples with different surface finish treatments. Every related research observes a distinct increase in fatigue strength in treated surfaces. The overall taken conclusions prove the negative impact a rough surface has on fatigue strength. For as-built specimens, crack initiation occurs mainly at the surface in the HCF regime. All shown surface treatments have proven to improve the fatigue stress-life results. Depending on the surface treatment, the crack initiation can arise in the sub-surface and/or internal region of the tested samples.

2.2 Multiaxial Fatigue

To date, all studied and developed fatigue mathematical models and experimental methods were built to suit current needs within the available knowledge and technologies. The first constructed conventional fatigue machines focused on pure uniaxial cyclical load testing, meaning one single cyclical directional load. Multiaxial stresses were later recognised as the leading dynamic stress state in machines and structures [4], meaning two directional loads (biaxial state) or three directional loads (triaxial state). Different examples of multiaxial dynamic loads can be seen in many industries, including railway, aerospace, industrial manufacturing machines, energy, space, and others [33–35]. However, the study and testing of multiaxial fatigue is far more complex and brings new challenges.

In 1935 Gough and Pollard were pioneers with their published fatigue test in combined alternating stress test [36]. Gough and Pollard applied plane bending torsion stresses through a complex built machine capable of achieving 1500 cycles per minute to round specimens.

For a biaxial stress state, a high number of devised and tested methods are already put to use, being the most common: rotating bending, plane fatigue testing through cruciform specimens, and tension-torsion [37; 38]. Machines that induce such multi-stress states are inevitably more complex and more expensive. Plane cruciform fatigue and tension-torsion conventional methods are the main focus of the present study. These two conventional multiaxial methods were adapted towards ultrasonic fatigue. Since they are a central focus in this thesis, their base knowledge and surrounding research are discussed in separate subchapters.

Triaxial stress state fatigue tests are rare and uncommon due to their added complexity. Two possible triaxial stress methods have been published: tension-torsion stress with variable inner pressure applied to a hollow cylinder specimen [39; 40] and a tension-compression-compression cyclic load [41].

Lefebvre et al. [39] developed a biaxial fatigue test method using thin-walled tube under cyclical axial load and variable pressure to achieve the first mentioned triaxial method. Morishita et al. applied the same method to hollow cylinder Ti6Al4V specimens [40]. Figure 2-4 shows Lefebvre hollow thin-walled specimen design. The specimen is under tension torsion by a servo-hydraulic machine while a variable inner pressure is induced for an orthogonal tension induced stress. All three applied deformations are computer-controlled for correct deformation amplitude and phase.

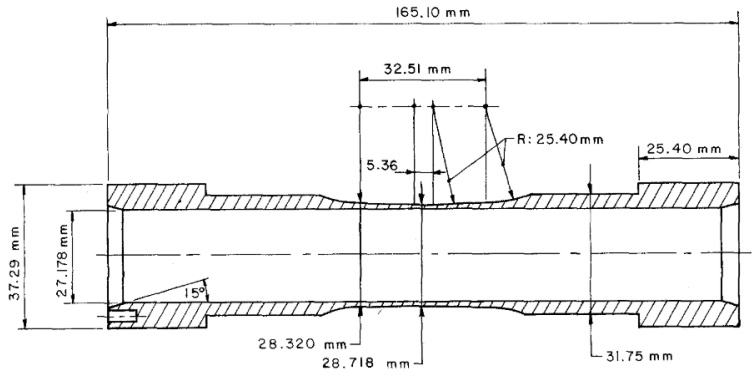

Figure 2-4. Lefebvre et al. [39] hollow thin-walled specimen design for triaxial tension-tension-torsion fatigue test.

Zhao et al. [41] applied the second mentioned tension-compression-compression triaxial cyclic load to prim shaped plain concrete specimens. A complex servo-hydraulic system applied tension-compression in all three directional axes. This type of machinery is very rare, with little published research.

As previously introduced for uniaxial fatigue, the applied cyclic load differs in amplitude and mean value. Each applied load has its own amplitude and mean value when regarding multiaxial fatigue. The applied load's phase and principal orientation axis between each one must also be taken into account.

The fatigue applied multiaxial loads can be defined as proportional and non-proportional. For a specific cyclic applied load to be proportional in all load instances, the principal stress axis must be fixed in relation to the tested component axis. All uniaxial fatigue cyclic loads are proportional. Only specific multiaxial cyclic loads are proportional. Considering biaxial fatigue loading, the two principal stresses σ_1 and σ_2 can be cyclic represented in their phase, amplitude and mean value. A schematic representation of some biaxial σ_1 and σ_2 proportional cases at a constant cyclic amplitude are shown in Figure 2-5.

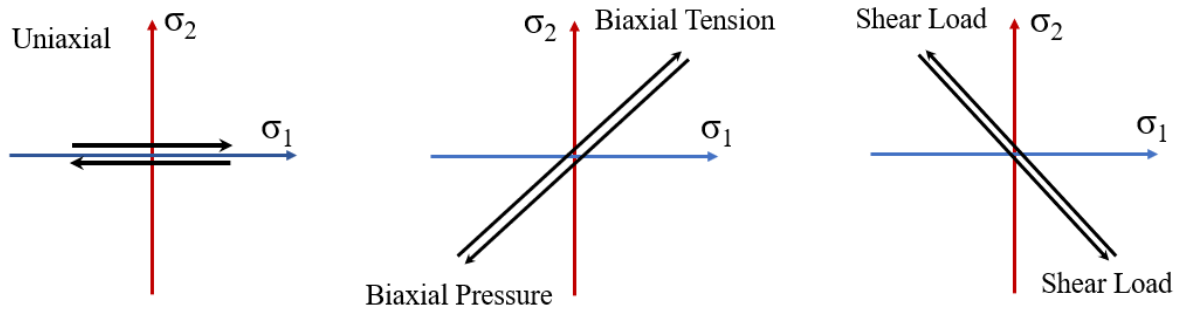

Figure 2-5. Biaxial proportional loading examples.

If all applied loads are in phase, being biaxial or triaxial, the applied load is always proportional. When the applied load combination is not in phase, it can be proportional or not. For non-proportional cyclic loading, the principal stresses axes rotate in time. The non-proportional load possibilities are limitless. Figure 2-6 presents some examples of biaxial non-proportional load cycles in the principal stress axis plane σ_1 and σ_2.

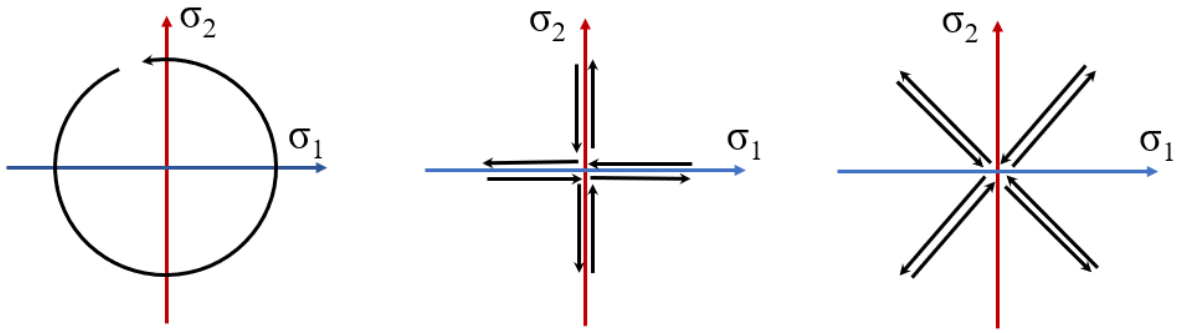

Figure 2-6. Biaxial non-proportional loading cycles examples.

Since the present study focused on multiaxial tension-torsion and cruciform fatigue, a brief introduction to their base concepts, objectives and respective conventional methodologies is made.

The present work focused on bringing tension-torsion and cruciform testing biaxial methods towards ultrasonic fatigue. After more than twenty years since the first VHCF dedicated conference, no other project or research team has ever presented ultrasonic fatigue machines, experimental methodologies, and fractured results in the two most common multiaxial fatigue testing methods. The already complexity of multiaxial testing by conventional means together with the ultrasonic fatigue challenges, make multiaxial stress state high-frequency transformation a high complexity task only reached by our team's dedicated work and creativity in overcoming all obstacles.

2.2.1 Tension-Torsion Loading

One of the most imposed multiaxial dynamic fatigue damage combinations to components is the tensile and torsional stresses [4]. Cylindrical and tubular-shaped specimens are utilised to carry tension/bending with torsion fatigue tests. Solid cylindrical specimens can be used to simulate driving shafts [42]. Tubular specimens can be thin or thick-walled. Tubular specimens are used to replicate real-life structures such as bridge girders, high-pressure containers, and deep submersibles in power plants or even as protective oil casing conduits in oil and natural gas extraction [43].

One standard fatigue method to study tension-torsion is by rotating bending. This is the actual stress combination method applied by Gough and Pollard in 1935 [33]. The method applies a bending force and a alternate cyclic torsion to a cylindrical specimen. The rotation provides cyclic shear and the cyclic axial stresses through an imposed bending applied force.

More complex servo-hydraulic machines, as presented in Figure 2-1, allow different tension-torsion combinations in proportional or non-proportional loading cycles and both mean shear and axial stress. Henrique et al. [44] researched a railway wheel under multiaxial fatigue in proportional and non-proportional load cycles through Figure 2-1 servo-hydraulic machine. However, most components are subjected to complex alternating stress amplitudes.

Standardised complex loading sequences were created to study the fatigue resistance of complex loaded components [45]. Such complex loading spectrums are denoted as superposed loading cycles. Luis et al. [46] applied several different tension-torsion loading sequences: a full reversal loading path; random loading sequence based on the first non-random, and a loading spectrum obtained by the Fighter Aircraft Loading Standard for Fatigue (FALSTAFF) that represents the loading spectrum of a lower wing root panel from a combat aircraft. Figure 2-7 compares Luis et al. [46] applied non-random non-proportional and the FALSTAFF tension-torsion loading sequences.

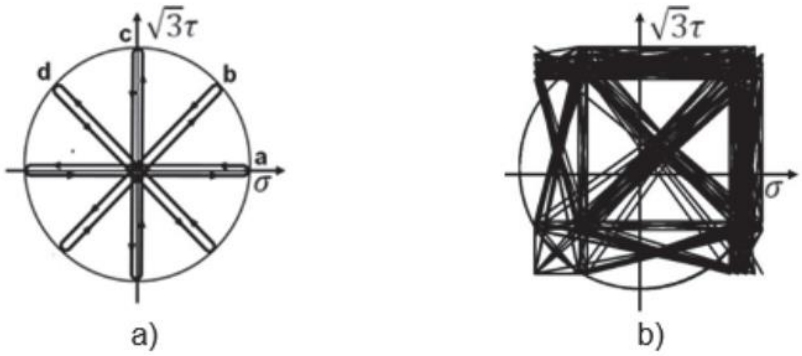

Figure 2-7. Luis et al. [46] tension-torsion loading sequences: (a) non-random non-proportional; (b) FALSTAFF combat aircraft

Due to the required cylindrical shape specimens, tension-torsion methods suffer one major drawback: because of the thickness and the fact that the surface of the specimen is curved, the induced stress state distribution is not constant. The cylindrical shape also makes it difficult to manufacture fibre laminate specimens and anisotropic rolled and flat sheet metal tension-torsion fatigue samples.

2.2.2 Biaxial Plane fatigue

A cyclical biaxial plane stress state is required when testing multiaxial fatigue strength regarding sheet materials. One example of biaxial plane stresses can be found in aeroplane fuselage cabin pressure. Sunder et al. [47] studied the crack propagation of plane biaxial cruciform specimens under biaxial cyclic constant load and superposed load spectrum simulating the variable cabin pressure of an aircraft.

In 1981 Young et al. [48] devised a hydraulic pressure bulge tester, inducing a biaxial bending stress state to a clamped sheet metal specimen. The sample sheet metal was under cyclic bulged deformation from the imposed variable pressure, inducing a fatigue biaxial bending stress state. Palin Luc et al. [49] followed the cyclic deformation concept and adapted it towards ultrasonic fatigue. The ultrasonic biaxial bending machine induces a similar deformation shape to a disk specimen. The later described ultrasonic concepts are used to explain the conceptualisation made by Palin Luc research team towards the transformation of the conventional biaxial bending to ultrasonic.

Another possible method to reach in-plane biaxial fatigue is through tubular specimens under axial loading and inner variable pressure. In 1973 Andrews and Ellison [50] developed a biaxial machine for tubular specimens where a servo-hydraulic actuator imposed the axial mechanical load, and a high-pressure piston induced an inner variable pressure. Lefebvre et al. [39] triaxial tension-tension-torsion fatigue method followed the same concept adding a torsion load.

All such machines have disadvantages and limitations. Bulge biaxial bending test method has the inability to create different non-unitary loading ratios ($R \neq 0$) and zero mean $R=-1$ cyclic stress. Servo-hydraulic together with variable pressure cannot fully represent the biaxial stress state at laminate sheet-shaped materials due to the circular thin tubed specimen shape.

The cruciform testing methodology has been shown the most advantageous and realistic biaxial testing method created. Of all biaxial testing procedures, cruciforms provide the most realistic stress state because of the application of in-plane stresses and strains on the perpendicular arms of a cross-shaped specimen. On the downside, it brings many challenges to the required testing machine rigs and specimen shape. Researchers have developed different machine testing rigs [51–53], and especially many cruciform specimen shapes [54–57].

Biaxial in-plane 'conventional' fatigue tests usually require at least four simultaneously controlled actuators that must maintain the centre of the specimen with and without load during the test to ensure symmetry and correct induced deformation. The servo-hydraulic actuator type is the most common option available in the market for biaxial in-plane fatigue tests. The costs of a four servo-hydraulic system, complex control and data acquisition, maintenance, and energy consumption are considerably higher than any uniaxial method.

Some researchers have built different cruciform fatigue machines with linear actuators for a less expensive and lower maintenance machine rig. Freitas et al. [51] developed a cruciform testing rig through four iron-core motors. The iron core motors allow for independent control for each four-axis and a considerable high maximum load, considering non-servo-hydraulic machines. This allows for a stable 20 Hz fatigue test, guarantying a close to zero displacement specimen centre, a requirement for every cruciform conventional testing machine.

Cruciform geometries vary significantly between published research. They are designed with one primary objective: the cruciforms must induce one single highest stress combination region with load axis oriented plane stress field. Testing materials, from isotropic metals to

laminate composites, is a complex task to guarantee a plane uniform stress field. In the published literature, the main problem areas are the transition between the perpendicular arms of cruciform specimens. Because of the proximity of these areas to the gauge area, they have a noticeable influence on the recorded stresses uniformity at the centre [58]. Demmerle et al. [59] discuss the main cruciform criteria for a working and optimal design: a homogenous stress and strain distribution in the fatigue specimen analysis region; the highest stress combination in the midpoint, and lower stress concentration outside the central region.

Cruciform geometries have been made with cut slits or notched corners to tackle these issues. Made slits to the arms of cruciforms are reported to reduce the influence of the specimen arms on the size of the stress field as well as smoothing the stress field in the central gauge area fatigue region [60]. Notched corners were introduced to increase strain levels in the central area of the specimen while reducing stress concentrations at the corners formed by the arm-to-arm transitions [61]. A thickness reduction in the central region can be applied in both notched and slit cruciforms.

From all different published cruciform shapes the followed geometry by this thesis was designed by Baptista et al. [62] for conventional fatigue methods. The shape was optimised to be applied in the referenced smaller, more efficient and affordable iron core cruciform machine rig. Therefore, the reached geometry was optimised for conducting fatigue experiments in thin sheet samples, ensuring a maximum deformation location at the cruciform midpoint fatigue testing region.

An example of a slit cut, a notched corner, and a combination of the two cruciforms together with the Baptista followed geometry are shown in Figure 2-8.

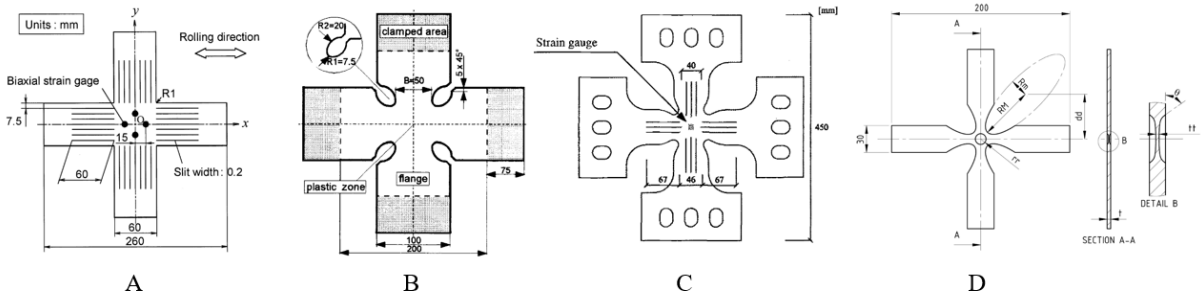

Figure 2-8. Cruciform shape specimens: (A) with cut slips [63];(B) notched corners [64];(C) cut slips and notched corners combination [65]; (D) thesis followed optimised geometry by Baptista et al. [62].

Two different cruciform stress states were created and tested in the present thesis: an in-phase tension-tension compression-compression denoted T-T (equibiaxial), and an out-of-phase tension-compression compression-tension C-T (pure shear). The first experiments were done to unitary stress ratio axial-axial cruciform. Ultrasonic T-T and C-T biaxial principal stresses are in-phase, and the loading cycle is proportional. Figure 2-9 shows and associates the T-T and C-T principal stress paths.

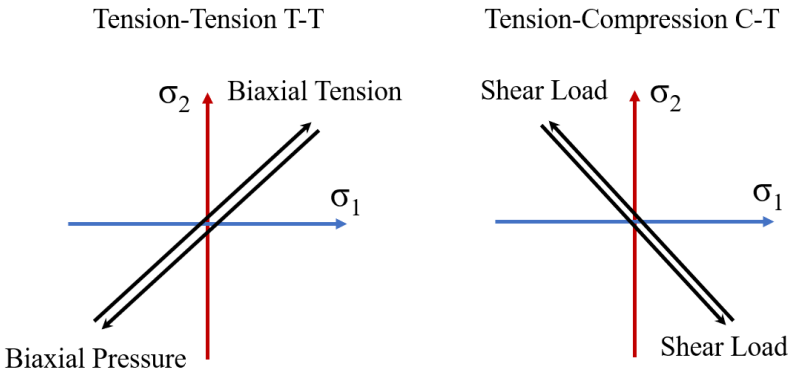

Figure 2-9. Ultrasonic cruciform T-T and C-T proportional loading paths representation

2.3 Introduction to Ultrasonic Fatigue

When conducting any fatigue test experiment, a cycle limit should be established. The test is interrupted if the specimen does not fail when it reaches the established limit. A new specimen is then introduced with a higher load or higher strain value. This happens because the specimen is leaving the studied regime, and it could take too long to reach the necessary cycles for it to possibly fail. If the specimen does not break afterwards, it could take an unreasonable amount of time than the already spent to reach a not guaranteed failure, thus being unpractical in time and energy consumption to continue. A 10^6 to 10^7 limit of cycles are commonly established in an HCF test. If a 5 Hz cycle frequency is used, to reach a 10^6 cycle limit, 56 hours of service are required. For some metals, HCF fatigue results showed a cycle region where the stress-life function seems to reach an asymptote curve at a given stress, and no failure was ever reached in lower stresses. This behaviour is in line with what was defined as the fatigue limit concept. However, what is the fatigue limit, and why did researchers and engineers consider it?

From experimental data, fatigue limit was determined as the threshold stress for crack propagation and not the critical stress for crack initiation [66; 67]. This limit defines a stress amplitude for which no full fatigue failure is expected to occur if a lower stress amplitude is induced to a given component during its life in service. Therefore, no fatigue failure up to 10^7 cycles is predicted for lower stresses than the considered fatigue limit. Crack initiation can still occur but no full propagation resulting in fatigue failure.

Due to the difficulty of achieving such a high number of cycles through the mentioned conventional machines for one single specimen, and because the material did not present significant evidence of having accumulated damage, no failure beyond HCF was assumed to exist. Such fatigue limit concept showed not to be entirely correct, and failure showed to be present in the regime of VHCF where it was considered not to occur [68; 69]. Ultrasonic fatigue machines introduced a reliable fatigue analysis method for the VHCF regime, and thus a growing and high-value fatigue research topic arose.

UFT has become a highly pursued fatigue researched testing method in the last decades. It was created with the primary purpose of studying material fatigue life in the Very High Cycle Fatigue (VHCF) regime between 10^7 and 10^9 cycles in a reliable time and energy manner. The necessity to characterise and study material fatigue strength within a new realm of the very high number of cycles created the need for a new, faster, more reliable fatigue testing method. Conventional machinery can easily take more than a month to achieve such a high number of cycles in one specimen alone, also adding a considerable energy consumption. In the published research on loading frequency effects by Zhang et al. [70], an Inconel 718 specimen in rotary-bending at 52.5 Hz took 45 days to reach $2.04*10^8$ cycles, while in ultrasonic fatigue testing at 20 kHz, a specimen took only about four days to achieve failure at $5.37*10^9$ cycles.

After a brief historical framework, the first and simplest ultrasonic fatigue machine (uniaxial tension-compression) is thoroughly described to fully explain all main concepts. These described concepts are always followed in any created designed ultrasonic fatigue testing machines and respective experimental methodology. They are vital to comprehend and achieve a working and reliable fatigue testing method at such high frequencies.

2.3.1 Historical Framework

The standard scientist tends to formulate hypothesis based on tendencies and limited acquired knowledge. Metal fatigue strength was initially believed to have a limit to which no failure would arise, the 'fatigue limit'. Due to the metal fatigue stress-cycle tendency and the considerable number of cycles higher than 10^7 cycles, failure was assumed not to occur beyond this range [69]. It was only later proven that a new fatigue stage does exist between 10^7 to 10^9 cycles [6], the VHCF regime. The bold infinite life assumption was assumed for two main reasons: fatigue response tendency presented a curve with an asymptote appearance, and the available testing methods would take months to reach failure in the VHCF range. Figure 2-10 shows a fatigue stress-cycle diagram representation of the fatigue tendencies between the HCF (I/II) and VHCF (II/III) regimes made by Pyttel et al. [69].

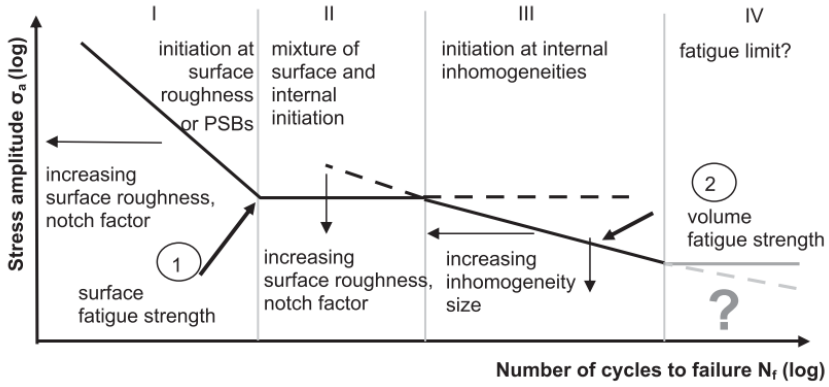

Figure 2-10. S-N curve from HCF (I/II) to VHCF (II/III) with influencing factors and crack initiation site [69].

Conventional fatigue testing machines have operational frequencies that typically span between 20 Hz and 150 Hz. To reach 10^9 cycles, a 150 Hz machine would take more than one month for a single specimen. A new method was needed to study, understand, and characterise fatigue behaviour in the VHCF regime, a faster and more energy-efficient method. The first uniaxial ultrasonic fatigue machine with the intention to study VHCF was built in 1950 by Mason [71]. Mason's test showed to be an outstanding achievement since he established the base methodology and frequency standard of 20 kHz for most ultrasonic fatigue research published to date. Before Mason's published machine, Hopkinson created in 1911 a resonance fatigue machine through magnets and coils [72]. The machine was built to study the materials fatigue limit faster and try to perceive if damage imposed frequency affected the materials stress-life response. The machine was able to induce 7000 cycles per second (7000Hz). Mason's machine followed the same concept but through piezoelectric excitation.

Several other ultrasonic machines with higher frequencies were later built, as one made by Girard in 1959 with 92kHz and one with 199 kHz by Kikukawa in 1965 [71]. Higher testing frequencies bring a size problem to the specimen and setup to ensure resonance. It also requires a more complex controlling and measuring system. For these reasons the general scientific community made the frequency established by Mason the work standard for such tests up to date.

Since Mason, many researchers have dedicated their research to VHCF testing through his ultrasonic fatigue machine concept. Claude Bathias was one of the most renowned researchers in the area, having published a vast number of papers in the ultrasonic fatigue research field. His work not only focuses on ultrasonic fatigue testing methods, machines and the analysis of the associated fracture mechanics in the VHCF regime, he was also one of the main drivers of VHCF and ultrasonic testing conferences [73].

Today several ultrasonic test machines with different applied stresses and conditions were developed as well as measuring technics [74; 75]. Many built ultrasonic machines and methods are later described in this document.

As aforementioned, ultrasonic fatigue testing was created to achieve a very high number of cycles within a reliable and affordable time and energy. Using such high frequencies solves the time issue but brings new problems and difficulties. The most significant and discussed effects on fatigue performance within ultrasonic fatigue machines are explained in the following subchapters, focusing on material properties, specimen shape, size, and testing frequency.

2.3.2 Ultrasonic Fatigue Base Concepts and Methodologies

A working, normalised, and comprehensive methodology is vital for every standardised and employed mechanical testing method. Every mechanical and material testing method research aims to ensure the correct acquisition and evaluation of the material behaviour, making it comparable and normalised between other future research results. After considerable proven research, standardisation will be proceeded, just as conventional fatigue. Due to the ultrasonic machine's fast frequency pace and associated difficulties, it took several years to be accessible to most researchers. One major issue was the development of a trusted measuring, controlled and deterministic methodology. Claude Bathias, the ultrasonic fatigue pioneer [73], brought

ultrasonic fatigue testing (UFT) to the fatigue research world. His book extensively details UFT methodology for all uniaxial loading conditions [71].

All ultrasonic fatigue tests rely on resonance concepts to achieve high enough stresses at such high frequencies. Resonance can be defined as the highest displacement response of a component or structure for a given force. To vibrate a particular structure at its resonance frequency means to dynamically excite the structure with the highest displacement for the lowest applied force. An undamped system in resonance would mean a never reached steady-state of vibration with infinitely increased amplitude [76].

A particular setup with a material sample is excited in resonance in ultrasonic fatigue machines. To achieve resonance a piezoelectric transducer is most utilised. The present work and most commonly used piezoelectric transducers have an operating frequency range of 19,5 kHz to 20,5 kHz. Marines et al. [77] applied both a 20 kHz and a 30 kHz piezoelectric transducer to study the VHCF of AISI-SAE 521000 bearing steel.

Other researchers have followed the same concepts through high-frequency shakers and different shaped specimens. G. J. Yun [78] and T. J. George [79] excited specimens in bending resonance, while Milosevic et al. [80] developed a high-frequency shaker testing rig capable of inducing tension-compression. These researchers have proposed a different vibrational fatigue method with frequencies ranging from 1 kHz to 7 kHz.

To reach a functional vibrational fatigue machine all components must be carefully designed and modally analysed to have a specific resonant mode within the transducer working frequency range. The final frequency of work is the frequency of the combined resonance modes of all attached components. In other words, the transducer will excite the resonance mode of the structure setup (a setup of sequenced components) composed by combining resonance modes of all components. Every component is designed to have resonance with displacement compliance with all the other components, always having the induced stress type of interest in mind [81].

Most ultrasonic machine setups are composed of a booster, a horn and the research material specimen. The booster and the horn have the same purpose of displacement amplification. They can amplify the transducer displacement due to their area reduction towards the specimen. The displacement amplification will help achieve higher displacements in the specimen and thus higher strain. The specimens usually have a cross-section area reduction to

provide a last induced stress increase and guarantee one single higher stress region for the fatigue study.

The resultant setup vibration profile has stress and displacement nodes. **Stress nodes (Sn)** are the regions where the stress is null and where the displacement is the highest. **Displacement nodes (Dn)** are, as expected, the null displacement regions with the highest stress amplitudes. **Stress nodes** are made to be at the extremities of every component so that all connections points have the lowest applied stresses. The major **Displacement node** should be at the centre of the specimen, where the displacement is the lowest and, most importantly, the stress the highest.

When testing at such high frequencies, a high-rate strain deformation is induced to a material sample, resulting in high-temperature generation [82]. This heat generation is associated with the material damping effect. In ultrasonic fatigue machines, high temperature is generated at the centre of specimen, the highest strain region. Since temperature is directly correlated with fatigue strength and static material properties, there is a need to restrict the testing temperature at the specimen's centre. Every ultrasonic fatigue machine requires a cooling system focused on the specimen displacement node. Most ultrasonic fatigue researchers employ simple air-cooling systems to maintain the specimen within a controlled temperature range [83]. Some studies have also placed low temperature surrounding environments to ensure a constant testing temperature due to the self-heating of the specimen [84].

Bathias and Paris [71] begin their book with the first and simplest uniaxial tension-compression R=-1 ultrasonic machine to explain all base concepts surrounding ultrasonic fatigue machines. The present study does also begin with the tension-compression ultrasonic machine base concept and an extensive description of the proposed standard experimental methodology sequence: booster horn setup design; dimensional specimen determination; measuring and control methods; induced stress determination analytical solution.

2.3.3 Tension-Compression Ultrasonic Fatigue Machine and Testing Standard

The first designed ultrasonic machine, the uniaxial tension-compression ultrasonic fatigue test, is first explained in detail to clarify all ultrasonic followed concepts. The ultrasonic tension-compression machine has a compliant longitudinal resonant mode between every component. The compliant longitudinal displacement between components leads to a set vibration profile with high enough tension-compression cyclic stress in the specimen's centre region.

Figure 2-11 shows the uniaxial tension-compression ultrasonic test machine's stress and displacement distribution representation from Bathias book. From careful observation, Figure 2-11 presented distributions have all mentioned stress and displacement nodes, as well as the displacement amplification from the booster and horn, and the stress increase by the specimen hourglass shape. As mentioned, the stress nodes are at the component's connection regions, and the specimen displacement node is at its centre, where the stress is the highest.

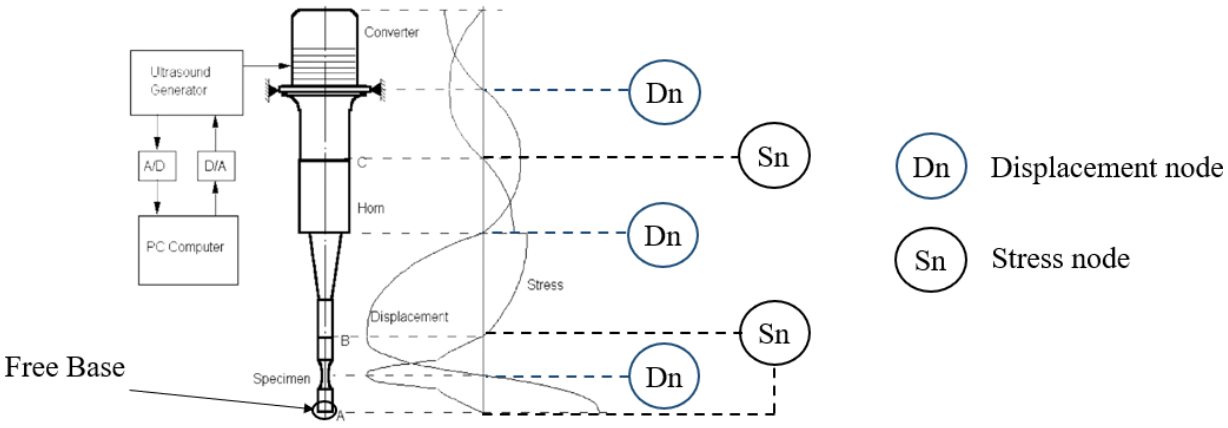

Figure 2-11: Representation of the displacement and stress distribution throughout the tension-compression ultrasonic fatigue test machine [71].

This study conducted two different tension-compression ultrasonic fatigue tests using a built machine in Instituto Superior Técnico. The built machine illustration is shown in Figure 2-12 with components designations and the support ring.

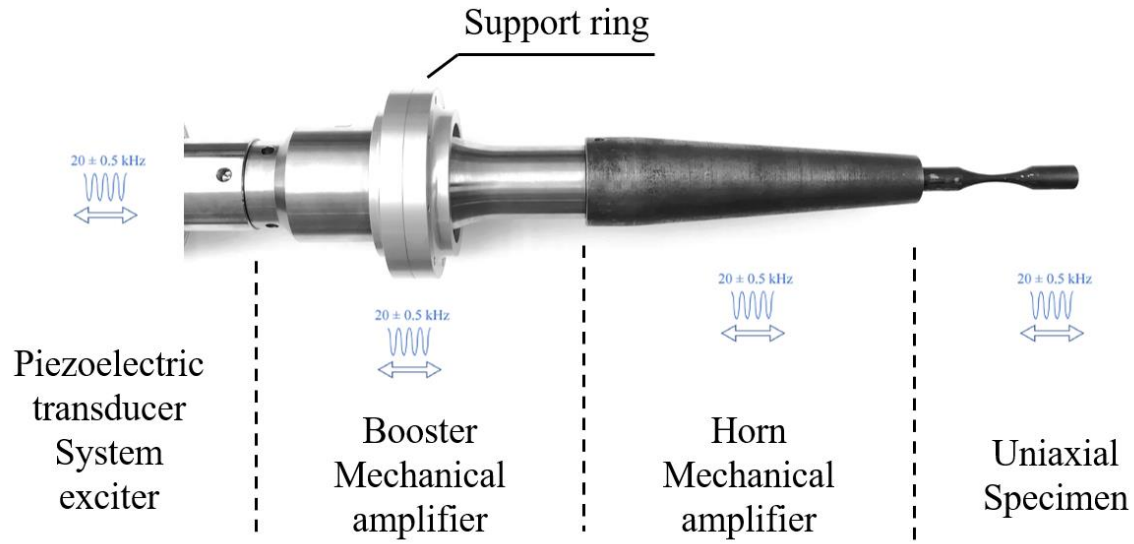

Figure 2-12. Instituto Superior Técnico uniaxial tension-compression ultrasonic fatigue machine setup with component designations.

The Instituto Superior Técnico ultrasonic fatigue machine from Figure 2-12 only shows one of the tested tapered horn geometry. A second hyperbolic horn with higher displacement amplification was also applied for tension-compression ultrasonic fatigue testing.

To determine the stress amplitude being induced, a measurement method must be conducted to the specimen's modal shape behaviour. The free base of the specimen on the setup end is a stress node, having the highest displacement and null stress (Figure 2-11). The high displacement and free flat region provide a reliable displacement measuring region. Many different apparatuses have been used to measure displacement: Laser vibrometer [85–87]; optical fibre sensor [88; 89]; and inductive or capacitive displacement gauge [75; 90]. Strain gauges can also be applied to the specimen's centre for strain measurement and, therefore, stress determination [75; 91–93].

Bathias and Paris [71] present a methodology and analytical solution for tension-compression UFT. The analytical method can be conducted for two different variable cross-section ultrasonic samples, hyperbolic and exponential. For each proposed curvature, a respective analytical solution is presented. The material sample final dimensions for a specific resonance frequency can be determined following the analytical solution. It then determines the deformation and stress gradient across the specimen's length through the measured displacement at the free base.

Following Bathias calculation methodology, the wave propagation velocity c is first calculated.

$$c = \sqrt{\frac{E}{\rho}} \tag{2.2}$$

Where E is the material dynamic Young's modulus and ρ is the material density. The resonance of any given component and/or structure is directly dependent on its stiffness and mass. Since all VHCF fatigue tests should be performed in the elastic behaviour of the material, the main material properties required for component's set and specimen design are the Young's modulus, Poisson's ratio and density. Before the wave velocity determination, both the Young's Modulus and density must be empirically determined. As an example, copper purity has a big influence not only on fatigue properties as well and the overall static stiffness. A non-predicted rigidity may result in a specimen's resonance frequency outside the transducer's range. More than for most common metals, the Young's modulus of the copper is highly sensitive to its purity. Therefore, tensile tests and strain rate influence on E are required to ensure the correct specimen modelling [94].

The study transducer working frequency is *f*=20 kHz. With the wave velocity *c* (equation (2.2)) and the frequency of excitation *f* a factor k is calculated

$$k = \frac{\omega}{c} = \frac{2\pi f}{c} \tag{2.3}$$

Figure 2-13 presents two different geometries with respective dimensional variables. The two curves follow a circular profile in machining and FEA analysis. Bathias proves the negligible difference between circular and hyperbolic/exponential shapes, considering the respective ultrasonic specimen final dimensions. Such consideration is made to simplify the numerical calculation.

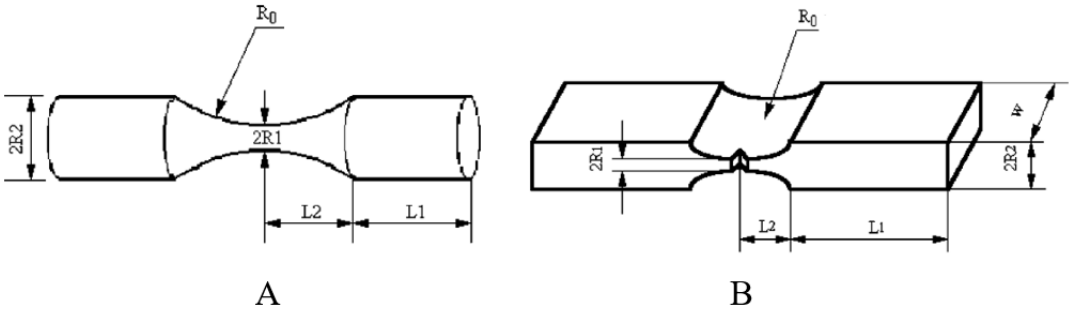

Figure 2-13. Uniaxial tensile ultrasonic fatigue curved specimens and respective dimensional variables: (A) hyperbolic curvature; (B) exponential curvature [71].

The respective geometrical solution equations to both hyperbolic and exponential curve specimen are presented sequentially in Table 2-1.

Table 2-1. Sequential geometrical analytical solution equations for hyperbolic and exponential ultrasonic tension-compression specimen.

Hyperbolic curve	**Exponential curve**	#
$\alpha = \frac{1}{L_2} arccosh(\frac{R_2}{R_1})$	$\alpha = \frac{1}{2L_2} \ln(\frac{R_2}{R_1})$	(2.4)
$\beta = \sqrt{\alpha^2 - k^2}$		(2.5)
$\varphi(L_1, L_2) = \frac{\cos(kL_1)\cosh(\alpha L_2)}{\sinh(\beta L_2)}$	$\varphi(L_1, L_2) = \frac{\cos(kL_1)\exp(\alpha L_2)}{\sinh(\beta L_2)}$	(2.6)
$L_1 = \frac{1}{k}\arctan\left\{\frac{1}{k}[\beta\coth(\beta L_2) - \alpha\tanh(\alpha L_2)]\right\}$	$L_1 = \frac{1}{k}\arctan\left\{\frac{1}{k}[\beta\coth(\beta L_2) - \alpha]\right\}$	(2.7)

For Table 2-1, *k* is the working frequency to wave velocity factor (equation (2.3)), R_1, R_2 and L_2 are the pre-established specimen dimensions (Figure 2-13), and L_1 is the final determined specimen dimension of the constant cross-section area length.

With the specimen geometry dimensions established, UFT can be initiated. The displacement, deformation, and stress gradient can be calculated with the measured amplitude at the specimen's free base and equations (2.4) to (2.7).

Considering first the hyperbolic curved specimen, the displacement (U) distribution along the length of the specimen is as follows,

$$\begin{cases} U(x) = A_0 \cdot \varphi(L_1, L_2)\frac{\sinh(\beta x)}{cosh(\alpha x)}, for\ x < L_2 \\ U(x) = A_0 \sin\big(k(L - x)\big), for\ L_2 < x < L \end{cases} \tag{2.8}$$

Where A_0 is the measured displacement at the specimen extremity and *x* is the distance from the specimens' centre to the free base. With the displacement distribution, the resulted strain and stress distributions are as follows.

$$\begin{cases} \varepsilon(x) = A_0 \cdot \varphi(L_1, L_2)\left[\frac{\beta\cosh(\beta x)\cdot\cosh(\alpha x) - \alpha\sinh(\beta x)\cdot\sinh(\alpha x)}{cosh^2(x\alpha)}\right], for\ x < L_2 \\ \varepsilon(x) = k \cdot A_0 \sin\big(k(L - x)\big), \qquad for\ L_2 < x < L \end{cases} \tag{2.9}$$

$$\sigma(x) = E\ \varepsilon(x) \tag{2.10}$$

$$\begin{cases} \sigma(x) = E \cdot A_0 \cdot \varphi(L_1, L_2) \left[\frac{\beta \cosh(\beta x) \cdot \cosh(\alpha x) - \alpha \sinh(\beta x) \cdot \sinh(\alpha x)}{cosh^2(\alpha x)} \right] & for\ x \leq L_2 \\ \sigma(x) = E \cdot k \cdot A_0 \sin\big(k(L-x)\big), & for\ L_2 < x \leq L \end{cases} \quad (2.11)$$

For the exponential curve with the respective equations (2.4) to (2.7), the resulting displacement and stress distribution solution is

$$\begin{cases} \mathrm{U(x)} = \mathrm{A_0} \cdot \varphi(\mathrm{L_1}, \mathrm{L_2}) \cdot sinh(\beta x) \cdot exp\ (-\alpha x), \text{for } \mathrm{x} < \mathrm{L_2} \\ \mathrm{U(x)} = \mathrm{A_0} \cdot \cos\big(\mathrm{k(L-x)}\big) \quad , \text{for } \mathrm{L_2} < \mathrm{x} < \mathrm{L} \end{cases} \quad (2.12)$$

$$\begin{cases} \sigma(x) = E \cdot A_0 \cdot \varphi(L_1, L_2)[\beta \cosh(\beta x) - \alpha \sinh(\beta x)] \exp(-\alpha x), & for\ x \leq L_2 \\ \sigma(x) = E \cdot k \cdot A_0 \sin\big(k(L-x)\big), & for\ L_2 < x \leq L \end{cases} \quad (2.13)$$

From equations (2.11) and (2.13), the induced cyclic stress at the specimen's centre (x=0) can be determined by the displacement measure in the specimen's free base (A_0).

In sum, Bathias presented analytical solution [71] provides a specimen design method and a measuring location with the respective calculation for the associated induced stress determination. By following the standardised methodology for isotropic material, uniaxial UFT can be thoroughly conducted. The present study intends to achieve the same objective by proposing an experimental, numerical and analytical procedure for two novel biaxial ultrasonic testing methods.

The specimen dimensional determination and machining process become more complex when considering an anisotropic material. Few research has been done in such conditions. Some examples of such anisotropic materials tested in UFT are composites as carbon fibre laminates [95] and magnesium [96–98]. Such studies won't be discussed in depth because they fall outside the remit of this thesis. Isotropic metals have been the main focus of most UFT studies, like steel [99], aluminium [100–102], titanium [87] and copper [103–105]. Unique research by Michael et al. [106] conducted an unordinary ultrasonic fatigue test on a cylindrical shape concrete specimen.

Since Mason's first ultrasonic machine, there has been a wide range of different machines and adaptations to study different fatigue stresses and influential fatigue parameters, such as temperature and environment.

2.3.4 Different Uniaxial Ultrasonic Fatigue Machines and Methods

With all the ultrasonic base concepts introduced, other uniaxial ultrasonic fatigue machines, such as pure torsion and bending machines, can now be more easily explained on how they work and employ the same ultrasonic concepts. Bathias et al. [74] have shown piezoelectric fatigue testing machines in high and low temperatures, with R≠ -1 stress ratios and fretting. Considerable worldwide research has followed Bathias well-created and methodically presented methodology [81; 91; 107; 108]. Many of the different built UFT machines and methods are described, and their concepts explained.

2.3.4.1 Ultrasonic bending fatigue machines

A bending 20 kHz resonant fatigue testing concept was first described in 1980 by Hoffelner [109]. The testing rig consisted of a three-point bending test where a dynamic actuator applied resonant vibrations to a bar-shaped specimen. The complete setup is placed in a rig with a static actuator to apply static load between the specimen and the testing rig.

Bathias and Paris [71] and H. Q. Xue et al. [107] later studied and applied the same technique. Xue et al. [107] fully describe the ultrasonic method, the analytical equations for isotropic bending specimen dimension and induced stress determination before conducting a three-point bending fatigue test to TiAl alloy specimens. An optical sensor was used to measure the specimen displacement.

Ultrasonic bending can be achieved by inducing a bending resonant mode to a specific specimen using a similar ultrasonic set to the tension-compression. The bending specimen is not attached and screwed to the ultrasonic machine. Instead, the horn has a tip base establishing a surface-to-surface connection to the specimen. The specimen is placed between two supports made with a specific distance in accordance with the displacement nodes of the specimen's bending resonant mode. The specimen must be correctly aligned to ensure no displacement regions on the rigid supports. The tip of the horn is then set on top of the specimen's length centre. Contrarily to the tension-compression specimen, the horn specimen connection is not a stress node. The specimen region where the horn touches the specimen is the highest stress amplitude.

A static load is applied between the horn and the specimen. An electromechanical machine can be used to apply the required static load between the specimen and the horn. Xue et al. [107] ultrasonic bending rig was installed in the electromechanical INSTRON 1122 testing machine. The ultrasonic transducer booster horn setup is attached to the rig through the booster support ring (Figure 2-12). The support ring is located at the booster displacement node, allowing static load application without compromising the setup resonance and vibration transmission to the structure.

Figure 2-14 shows an ultrasonic bending test machine representation in an INSTRON electromechanical testing machine.

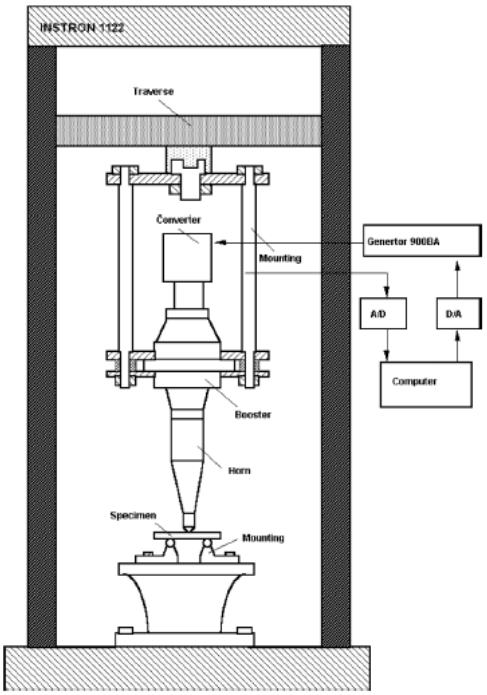

Figure 2-14. Three-point bending ultrasonic fatigue test representation [71].

Ultrasonic bending methods unlock this high-frequency fatigue testing method to composite materials such as laminates and sandwiches. Since the specimen no longer needs to be cylindrical, the plate geometry allows for easier manufacturing of composite specimens and to induce the desirable stress state fatigue damage. Wolfgang et al. [110] used a 37 kHz piezoelectric ultrasonic machine setup similar to Figure 2-14 to excite a commercial double cantilever beam substrate consisting of an Al2O3 ceramic layer and Cu.

Carbon and glass fibre laminates can more easily be tested in the ultrasonic bending format, but an important factor must be considered, high-temperature generation. Due to high polymer damping, laminated fibre composites have a high heat generation in high-frequency testing [111]. Backe et al. [95] applied a 20 kHz ultrasonic three-point bending fatigue test to carbon fibre reinforced polymer (CFRP). Pulse-pause fatigue sequence was followed together with continuous dry compressed air cooling to ensure no temperature damage. Wenbin et al. [89] also conducted ultrasonic fatigue testing on CFRP specimens using a developed liquid nitrogen cooling system to ensure no high-temperature regions were achieved, which could invalidate the fatigue life estimates.

To achieve a working composite specimen, meaning a specimen with the desirable resonance at the transducer working frequency, FEA simulations are required. The anisotropic material complexity together with the required resonance working frequency and displacement node locations for the support rig, make the FEA the best method to fully achieve a working specimen. Wenbin et al. [89] CFRP FEA obtained specimen can be observed in Figure 2-15.

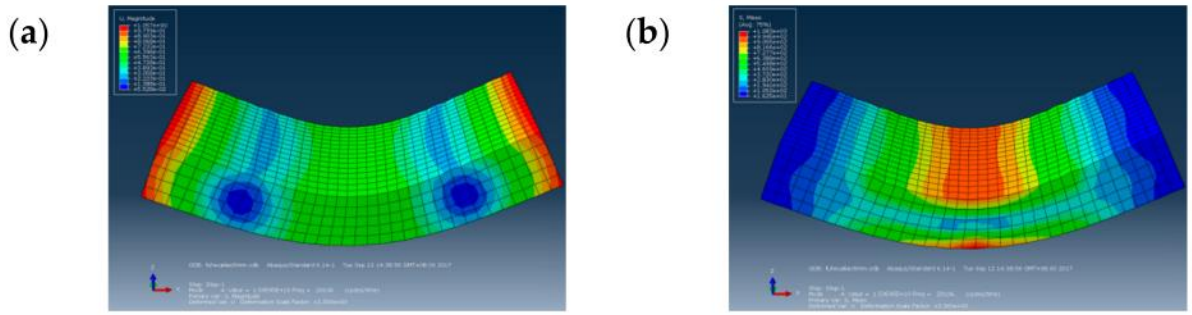

Figure 2-15. Wenbin et al. [89] CFRP three-point bending specimen FEA (a) displacement magnitude distribution (b) Mises stress distribution.

One research led by Palin Luc has achieved an ultrasonic fatigue machine able to induce a multiaxial bending stress state through the excitation of a disk-shaped specimen [49]. Figure 2-16 shows the Palin Luc et al. [48] multiaxial bending machine. The machine rig is similar to the one presented in Figure 2-14. Only the specimen geometry and the supporting rig are adjusted to achieve a different resonant mode shape and, therefore, a different cycle stress state. Palin biaxial method took the biaxial hydraulic pressure bulge tester developed in 1981 by Young et al. [48] and transformed it towards ultrasonic fatigue machines.

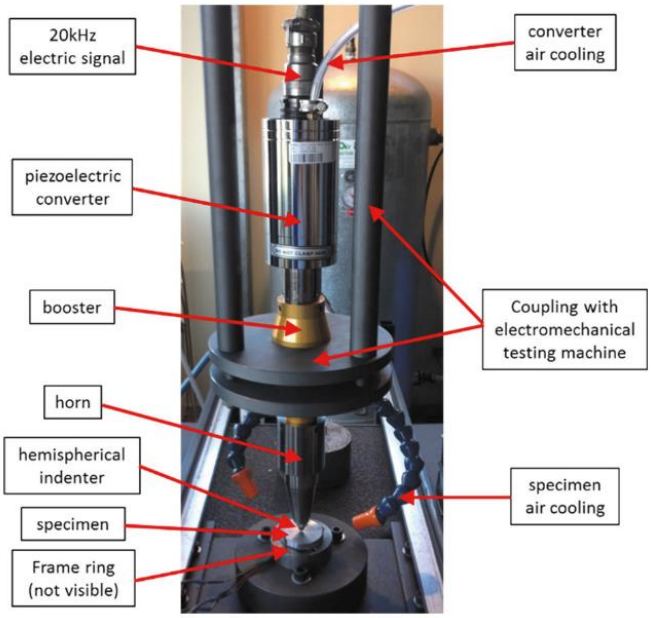

Figure 2-16. Palin Luc et al. biaxial bending ultrasonic fatigue machine [49].

2.3.4.2 Pure torsional fatigue test machines

Ultrasonic fatigue testing in a pure torsion stress state has also been achieved. The first built machine design was made again by Bathias et al. [112], and it is composed sequentially by axial piezoelectric transducer; longitudinal horn; connecting pin; torsional horn, and torsional specimen. A scheme of the machine is presented in Figure 2-17.

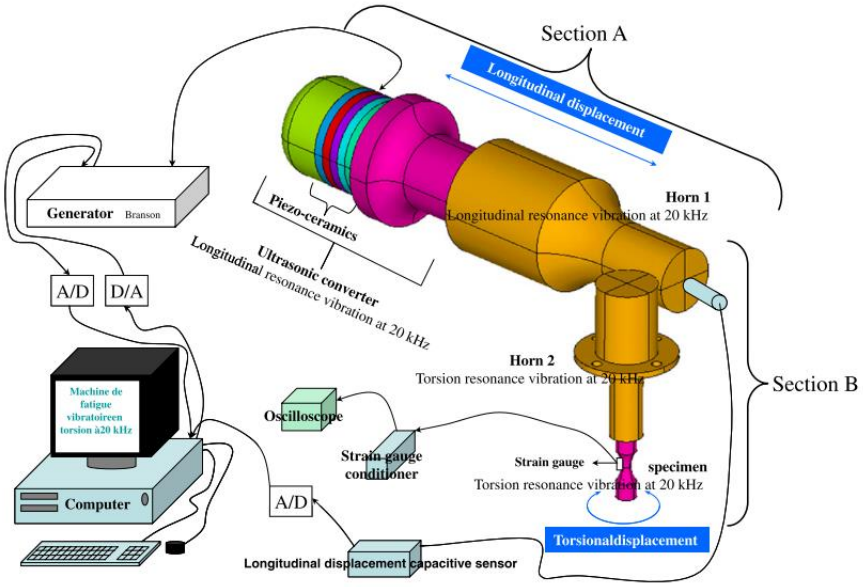

Figure 2-17. Pure torsion ultrasonic fatigue machine scheme designed by Bathias et al. [112].

Just as all ultrasonic machines, the horns and the specimens are induced in specific resonant modes with component displacement and frequency compliance towards achieving the pure torsion stress state of interest.

Following Figure 2-17: Horn 1 (longitudinal horn) is designed to have its first longitudinal resonant mode within the transducer frequency of work, just as a tension-compression ultrasonic fatigue machine horn or booster; Horn 2 (torsional horn) is designed to have the first torsional resonant mode, again within the same 20 kHz frequency. The torsional horn is transversally connected to the longitudinal horn by a tight fit cylindrical pin. The connector pin secures the torsional and longitudinal contact.

The transducer induces the first longitudinal resonant mode to the Horn 1. The pin connection is made so that the longitudinal displacement of the first horn can induce rotational displacement to the torsional horn. Since the torsional horn has the torsional resonant mode at the same frequency that is being excited by the longitudinal horn and the pin, it achieves cyclic torsion resonance. The torsional horn sequentially excites the material specimen, which is also designed to have torsional resonance at 20 kHz.

As the ultrasonic tension-compression specimen, the torsional ultrasonic specimen has an hourglass shape, and it is screwed to the torsional horn. It is important to note that by working in torsion, all resonance associated rigidity is not from the Young's modulus (E), as in tension-compression, but by Shear modulus (G). The overall size of the torsional horn and specimen will be considerably lower due to the considerably lower shear modulus. The same analytical method followed for tension-compression specimens is applied for torsional specimen dimension determination as well as the displacement and stress distribution. The difference is in the wave velocity (see equation(2.2)) since it is governed by rotational waves associated with Shear modulus and the radius dependent shear deformation distribution. The rotational wave velocity is first determined.

$$c = \sqrt{\frac{G}{\rho}} \tag{2.14}$$

For the torsional specimen, only the hyperbolic curve will be considered. Similar to the presented Table 2-1, the L1 constant radius section length equation sequence is determined.

$$\alpha = \frac{1}{L_2} arccosh(\frac{{R_2}^2}{{R_1}^2}) \tag{2.15}$$

$$\beta = \sqrt{\alpha^2 - k^2} \tag{2.16}$$

$$\varphi(L_1, L_2) = \frac{\cos(kL_1)\cosh(\alpha L_2)}{\sinh(\beta L_2)} \tag{2.17}$$

$$L_1 = \frac{1}{K} arctan\left\{\frac{1}{K}\left[\frac{\beta}{\tanh(\beta L_2)} - \alpha\tanh(\alpha L_2)\right]\right\} \tag{2.18}$$

Where the k in equation (2.3) is recalculated with the rotational wave velocity. The displacement and stress distribution can be determined after equations (2.15) to (2.18).

$$\begin{cases} U(x) = A_{0r} \cdot R_1 \cdot \varphi(L_1, L_2)\left[\frac{\sqrt{\cosh(\alpha x)}\sinh(\beta x)}{\cosh(\alpha x)}\right], for\ x < L_2 \\ U(x) = A_{0r} \cdot R_2 \cos\big(k(L-x)\big) \qquad , for\ L_2 < x < L \end{cases} \tag{2.19}$$

$$\begin{cases} \sigma(x) = GA_{0r}R_1\varphi(L_1, L_2)\frac{\sqrt{\cosh(\alpha x)}[\beta\cosh(\beta x)\cosh(\alpha x) - \alpha\sinh(\beta x)\sinh(\alpha x)]}{cosh^2(\alpha x)}, for\ x \le L_2 \\ \sigma(x) = GA_{0r}R_2\sin\big(k(L-x)\big), \qquad , for\ L_2 < x \le L \end{cases} \tag{2.20}$$

After the proposed pure torsion machine by Bathias et al., several other researchers have conducted fatigue experiments with the same setup [113–115]. A new pure torsion machine has later appeared that utilizes a rotational transducer with only a torsional booster and horn [108; 116; 117]. Such setup has a similar design shape as the uniaxial tension-compression ultrasonic machine. Figure 2-18 shows A. Nikitin et al. [116] pure torsional piezoelectric transducer and respective horn and sample.

Figure 2-18. A: Nikitin et al. [116] pure torsional machine with a Branson torsion transducer.

Recently published research has used the new piezoelectric transducer for torsion VHCF testing and compared it with axial tension-compression VHCF results [118–120].

2.3.4.3 Different stress ratios ultrasonic fatigue machines

So far, all mentioned ultrasonic machines can only apply zero mean stress fatigue cyclic testing cycle, R=-1 stress ratio (Figure 2-2). An initial static load method has already been arranged for the tension-compression and pure torsion ultrasonic fatigue methods to achieve different stress ratios. Again, because ultrasonic fatigue machines depend on resonant principles, the application of a static load needs to be carefully designed so as not to disrupt and change the setup resonance. The static load must only be applied in displacement node regions with no displacement. Such ensures a negligible vibration transmission from the ultrasonic setup to the static load applying structure. Otherwise, vibration issues as damping, heat generation or frequency change could affect the ultrasonic method outcome.

A second horn booster set is attached to the free base of the specimen for tension-compression testing. The first and second boosters have a support ring in their respective displacement node, just as R=-1 tension-compression Figure 2-12 ultrasonic machine. A static force can be applied through the two supporting rings, one in each booster in between the specimen. A calculated static load is then applied for a given mean stress, thus having an R≠-1 stress ratio. Figure 2-19 represents a two booster, two horn and specimen setup for R≠-1 stress ratio ultrasonic fatigue. The booster support rings are identified.

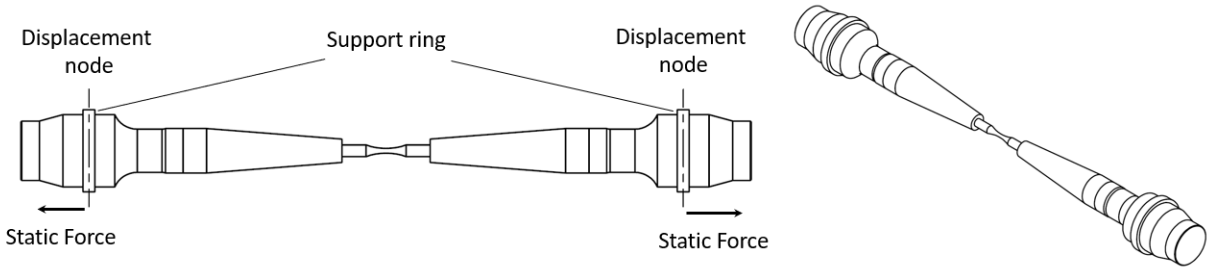

Figure 2-19. Mean stress ultrasonic fatigue machine with two boosters and two horns (2B+2H) and specimen representation.

Several researchers have introduced similar schemes to their tension-compression machine sets for different stress ratio values [121–124]. The two-booster rig is fixed in an electromechanical tensile machine to induce the static load. The fixing rig in the electromechanical tensile machine is similar to the presented Figure 2-14 ultrasonic bending setup.

By having control over the imposed static load, the researcher in [125; 126] has conducted ultrasonic fatigue in which a varying static load was imposed between a set of applied cycles across UFT.

To achieve stress ratios R≠-1 in pure torsion, H. Mayer et al. [127] followed the same explained concept of tension-compression set. The built ultrasonic machine uses a rotational piezoelectric transducer (similar to Figure 2-18). Two booster and horn sets are attached between the bases of the ultrasonic torsional specimen. The static torsional load is then induced through the second booster's support ring.

2.3.4.4 Environmental and fretting ultrasonic fatigue testing

There are also varying ultrasonic fatigue testing methodologies within the mentioned machines to study the environmental impact (Temperature, Corrosion), fretting, air (vacuum) and crack propagation.

For environment impact quantification, two most common ultrasonic test methods are high/low temperatures and corrosion. In high temperatures, a coil is placed around the specimen to achieve temperatures as high as 1500 ºC [128–130]. In low cryogenic temperatures, no deep research has been yet conducted. A study conducted by Bathias et al. [131] was made to titanium specimens at -196º and 253º Celsius. When testing at considerable high and low temperatures, it is fundamental to consider the elastic modulus temperature change when designing the ultrasonic set and specimen. The rigidity dependency on temperature will affect the materials resonance response frequency directly. In [128], the ultrasonic fatigue machine set was modified to ensure the correct fatigue test operation at 650ºC and 1000ºC made to a heat/resistant steel and a single-crystal superalloy. Figure 2-20 shows ultrasonic fatigue testing examples at high and cryogenic temperatures.

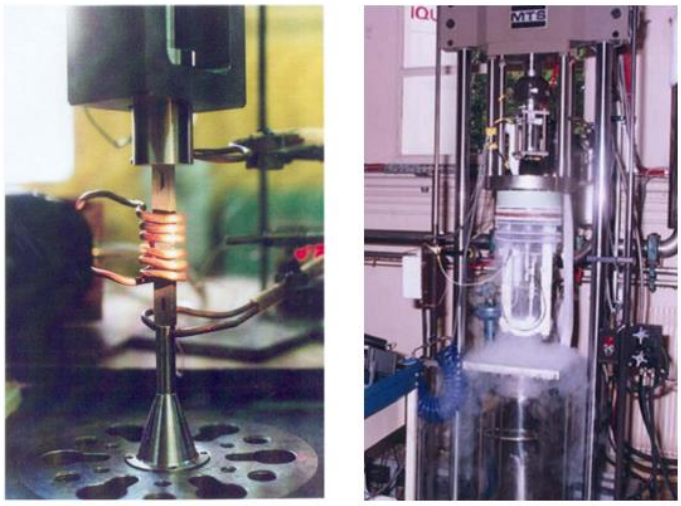

Figure 2-20.Ultrasonic fatigue temperature tests: (A) High temperature with heat coil; (B) low cryogenic temperatures through liquid nitrogen [74].

Corrosion studies have also been conducted by surrounding the specimen in a highly corrosive environment [132–134]. In the referenced research, a direct comparison to the fatigue strength results with no corrosion, with pre corrosion, and artificial seawater flow in real-time was made. To impose a high-corrosive environment, the available free base of the specimen in R=-1 stress ratio ultrasonic tension-compression machine is used. Since the free base allows for a quick application of a high-corrosive environment, Thierry et al. [134] introduced a seawater reservoir directly below the ultrasonic setup. The water was continuously under circulation to achieve high-corrosion on the specimen's surface.

Some researchers have also conducted a comparison of VHCF fatigue results between air and vacuum environments [135; 136]. The air environment impact has an influence on the crack nucleation and propagation within this specific regime. Stanzl-Tschegg and Schönbauer [135] conducted air and vacuum ultrasonic fatigue tests on an AISI martensitic steel. Through the fatigue resistance present change, they concluded that the air environment results in higher crack growth rates, lower stress intensity thresholds, and higher result scatter. Such behaviour was linked to air adverse effects on crack growth due to the corrosive environment provided by the moister and hydrogen embrittlement [137]. The results also showed that air had a higher crack growth threshold, meaning that no considerably slow crack propagation was occurring. Such behaviour was linked to possible oxide-induced crack closure, preventing slow crack growth in a vacuum environment.

Fretting fatigue testing can also be transposed to ultrasonic fatigue testing machines. Fretting fatigue is associated with wear induced by a dynamic interface contact between two components leading to surface damage, stress concentration and, therefore, crack nucleation and propagation. For conventional fatigue testing methods, fretting tests were standardised in 1992 [138]. Fretting is achieved in fatigue by having contact pads with different shapes pressed against the specimen. The cyclic displacement imposed on the specimen will induce wear between the pad and specimen contact.

Ultrasonic fretting fatigue testing is achieved in a similar manner. Induced friction wear is reached by pressing contact pads in the surface of the specimen. The contact region between the pads and the specimens is what differs between conventional and ultrasonic testing. Since the oscillatory friction achieves fretting, the imposed interaction between pads and specimens cannot be placed at the specimen's centre where a displacement node is located (displacement null point). The ultrasonic specimen geometry also changes for it to have a more extended surface at a constant radius for the pad contact. Figure 2-21 shows an ultrasonic fretting fatigue model and the designed specimen geometry by Claude Bathias [74].

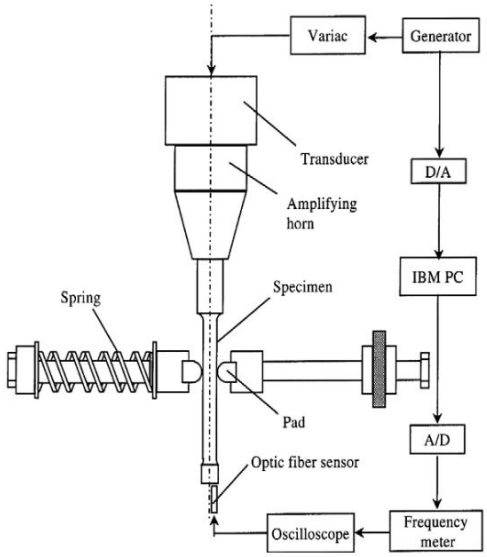

Figure 2-21. Ultrasonic fretting fatigue machine scheme [74].

Just as in conventional fretting fatigue, the normal pads contact force, slip amplitude and stress amplitude is controlled and measured in each conducted fatigue test. While the contact pad spring system regulates the contact force, the slip amplitude is regulated by its location across the length of the smallest cross-section of the specimen. Slip amplitude increases with a higher pad contact distance to the displacement node.

Only a few published research has been done where fretting fatigue was applied to ultrasonic fatigue machines, and all applied the same described method in titanium and steel samples [139–141].

The main purpose of the made description to all built ultrasonic machines and testing methods is to establish better the associated concepts due to the complexity and high frequency of UFT, several intricacies must be well understood and associated with the testing methodology design to consider the obtained fatigue results as reliable. Only then UFT methods can be standardised.

Having established the experimental fatigue basis, a focus on VHCF and influential factors on the fatigue results proceeds. The ultrasonic fatigue method induces damage by an unconventional high strain rate method, which results in new influential issues surrounding induced fatigue. Interesting research focused on specimen size/shape and frequency effects is worth discussing. It has reshaped the geometry of the specimen and the analysis of the stress-life results. However, all described 'rules' to ensure the correct functioning of the ultrasonic test remained untouched.

2.3.5 Size and Frequency Effect

Looking at the extensive description of all ultrasonic fatigue methods, two significant differences to conventional fatigue methods must be acknowledged: the specimen geometry limits and the high tested frequency.

2.3.5.1 Size effect

As explained, all ultrasonic specimens are carefully designed to have specific resonance at the working frequency of the exciting machine. Such requirement limits the specimen shape size and overall dimensions rather than the conventional fatigue established flexible geometry even within the available standards. As the frequency of test increases the size of the specimen decreases. This is simply due to the requiring lowering mass and increasing stiffness to reach higher frequencies. The most common ultrasonic applied frequency of 20 kHz is high enough to result in a considerable fatigue specimen size reduction when comparing to a flexible conventional specimen size.

For a long time it has been well documented that fatigue strength is directly associated with the fatigue region size of a given component/part. As the region size increases, the associated fatigue resistance reduces due to the increased probability of an existing critical size defect, resulting in early fatigue crack propagation and, consequently, failure [142]. This is known as the size effect.

Therefore, the size effect is directly affected by fatigue testing region volume, what is denoted as the risk volume. The size effect on fatigue is not directly associated with the smaller overall specimen size but with the fatigue tested region volume. The full definition of risk volume is still an open debate among the scientific community. Even so, the most followed risk volume concept is described in Yung-li et al. [143] book as the 'volume of material subjected to a stress amplitude larger than 90% of the maximum applied stress'.

The effect on HCF strength was already extensively tested, showing decreased strength with increased risk volume [142–145]. Jonathan et al. applied three different AM Ti6Al4V specimen sizes to study the fatigue size effect [145]. They observed not only a higher fatigue strength in smaller diameter specimens, but the smallest specimen presented a shift from surface to sub-surface crack initiation.

Ultrasonic specimens have lower fatigue region volume due to the average lower testing size and the resulting non-uniform stress distribution. To increase the risk volume, Furuya has employed a dog-bone ultrasonic specimen [146]. The shape does not fully follow the hourglass curvature. It increases the smallest cross-section radius creating a constant radius centre section. Paolino et al. have designed a new ultrasonic specimen geometry denoted the Gaussian specimen [147]. The specimen shape has a centre bulge to increase the risk volume considerably. Figure 2-22 compares Paolino et al. and Furuya ultrasonic specimen shape with the more common geometry.

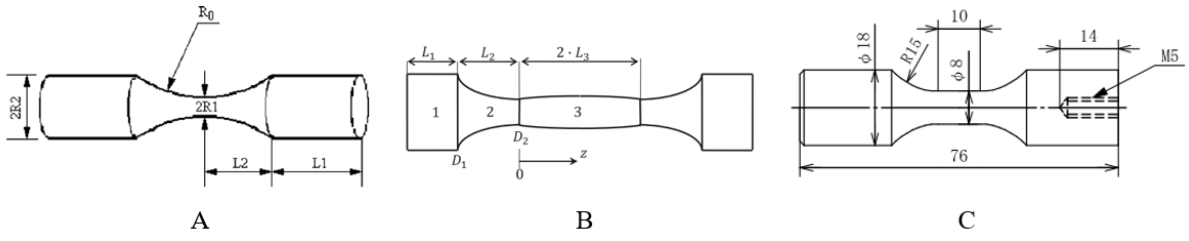

Figure 2-22. Ultrasonic specimen comparison between (A) Conventional hourglass shape; (B) Gaussian specimen; (C) dog-bone specimen.

Furuya tested AISI-4140 [146] and JIS-SUP7 [148] steels with both hourglass and dog-bone geometries. AISI-4140 conventional servo-hydraulic fatigue tests were also conducted with a similar risk volume specimen, which showed similar stress-life results. A standard hourglass shape specimen with a 1.5 mm R1to Furuya AISI-4140 dog-bone specimen presented a change in risk volume from 33 mm^3 to 781 mm^3.

Paulino et al. compared the dog bone and Gaussian risk volume by FEA and by applying strain gauges to different regions of the specimens. The experimental results have proven the ability of both specimens to increase the risk volume. The Gaussian specimens also show the capability to have a relatively constant stress amplitude throughout the bulge risk volume region. Tridello et al. applied the Gaussian specimen to study refined and unrefined AISI H13 steel [99], and SLM manufactured Ti6Al4V [149] having the Gaussian specimens 2300 and 2034 $mm^{3,}$ respectively.

Hongqian et al. [150] studied the size effect of cast aluminium only by increasing the hourglass-shaped specimen smallest cross-section radius. The increased radius changed the 90% maximum stress risk volume from 34 mm^3 to 194 mm^3. Even with a considerably smaller risk volume increase, the fatigue strength showed a clear lower life for the higher radius tested specimens.

2.3.5.2 Frequency effect

Another critical aspect of ultrasonic fatigue testing is the frequency effect on the resulting material fatigue behaviour and strength. The existence of such an effect can be predicted since many materials behave differently in high deformation rates, having higher yield and ultimate stress [151; 152].

Two major frequency effect issues are present in ultrasonic machines: temperature generation and the material microstructure response to high strain rate. The frequency effect direct correlation to the resulting fatigue response is first discussed followed by the generated heat.

Regarding the direct high-frequency effect on materials fatigue resistance, in certain cases, different stress-life results were obtained between ultrasonic and low-frequency conventional testing. The frequency effect on fatigue life was first noticed in 1925 by Jenkin [153], even before Mason's machine. Jenkin tested copper, iron and mild steel at 50 Hz,

500 Hz, 1000 Hz and 2000 Hz cyclic frequencies. All three materials presented higher fatigue strength at higher frequencies. To test considerably high frequencies the same base resonance principal was applied, similar to the 1912 Hopkinson machine [72]. Jenkin with Lehmann [154] conducted a second high-frequency research in 1929 close to 20 kHz cyclic frequency through a built air fluctuation pressure machine inducing vibration in the specimen. The tested copper, two carbon steels, Armco iron and aluminium, showed the same frequency fatigue resistance trend again. However, Jenkin and Lehmann also concluded that a frequency cap is reached when the fatigue resistance increase is ceased. Subsequent research showed no frequency peak was present.

In 1965, Kikukawa et al. conducted fatigue tests at an even higher frequencies up to 100 kHz [155]. They achieved such high frequencies through a ferrite magnetostrictive vibrator and three sets of amplification horns. Two carbon steels were tested, S10C and S20C. Water cooling in combination with cathodic protection was used. The results for all tested frequencies showed an always continuous increase in fatigue strength.

With the UFT research interest and accessibility over the years, several studies with detail related to the impact and effect of high frequencies on the fatigue results and the root causes for such effect [94; 156; 157]. The different steel microstructure phases have been shown to be linked to specific behaviours in high-frequency testing and crack initiation and propagation.

As the published research by J. Bach et al. [158] concludes, in low alloyed carbon steels, the ferrite phase is mainly responsible for higher stress life results when testing at high frequencies. Perlite microstructure phase shows to be responsible for preventing fatigue micro-crack growth related to the VHCF regime, meaning that the fatigue limit concept in HCF can be considered when a given steel microstructure has a predominant perlite volume fraction. Several other high-frequency studies with similar low carbon ferrite-perlite microstructure steels have shown similar results [155; 159–162].

When considering high strength metals, different microstructures will be present, leading to different frequency load effects and different fatigue fracture behaviour. High strength steels and bearing steels are usually associated with austenitic, martensite and bainite microstructural phases.

Furuya et al. [163] conducted a frequency effect fatigue analysis to high strength JIS SNCM439 low-alloy steel with a martensite microstructure. No considerable frequency effect was found. The life to stress amplitude results were associated with inclusion size from low to high-frequency fatigue tests.

Schneider et al. [164] conducted a frequency fatigue study of 50CrMo4 steel and EN AW-5083 aluminium. The specimens were subjected to ambient air and inert argon atmospheres at 400Hz and 20 kHz. The studied steel was heat-treated in two different sequences, one for low strength and one for high strength. Both presented an austenitic microstructure with different grain sizes. Only the high-strength steel presented a negligible frequency strength difference. Both aluminium and low strength steel presented a frequency effect at ambient air conditions. A similar fatigue strength increase from air to argon atmospheres was observed in steel specimens for low- and high-test frequency. On the other hand, the aluminium showed an equal fatigue resistance between low and high frequencies when tested in an inert argon atmosphere. The steel frequency effect was concluded independent of the present atmosphere, but the frequency effect was linked to the surrounding environment for the aluminium.

Using the same material with different heat treatments, the research led by Aiguo Zhao et al. [165] compared ferrite and martensite microstructure's high-frequency fatigue responses. As the material has a higher annealed temperature, a more ferritic microstructure is obtained with a corresponding lower ultimate stress, Vicker's hardness and lower fatigue stress-life strength (in conventional fatigue testing). In this study, a rotation-bending low-frequency 52.5 Hz fatigue test and 20 kHz UFT were performed for frequency effect comparison. When comparing all four different microstructures, from lower strength ferritic to higher strength martensitic microstructures, the results showed: lowered fatigue resistance difference between low frequency and ultrasonic fatigue tests, being almost negligible in tempered martensite; failure in a higher number of cycles; crack initiation transition from surface to internal regions.

When testing in high frequency, the high strain regions generate heat due to the material hysteretic damping and micro-plastic deformation [82]. The heat generated was already mentioned since all shown ultrasonic presented setups have a cooling system [74]. One example of heat generation issues is studying CFRP at high frequencies due to the polymer's high damping material property [89].

The amount of generated heat will depend on material type, microstructure, strain amplitude and rate, the testing fatigue method, and even the manufacturing method.

J. Bach et al. [166] studied the specimen geometry influence on increased temperature generation in ferrite-perlite steel. The generated heat was linked to local microplastic deformations having similar temperature generation for similar strain cyclic amplitudes in two different specimen shapes. The temperature management improvements observed between specimens were linked to increased surface in the fatigue risk volume region, higher surface gauge, better thermal uniformity and, therefore, better specimen cooling. Since the ferritic-pearlitic tested steel had a limited thermal conductivity, the observed improvement may become negligible for higher thermal conductivity materials.

Liu et al. [167] conducted ultrasonic fatigue tests on two sets of specimens machined from forged and rolled bainite/martensite duplex-phase steel rods. The results proved a significant difference in generated heat. Under high frequency forged specimens proved to have higher heat generation, which oxidised the surface of some higher stress amplitude tested specimens. While rolled specimens had negligible temperature change even at higher stress amplitudes. All tests were conducted with compressed air cooling. Also, Liu et al. showed a heat generation peak close to the final fatigue propagation cycles. With the crack nucleation, its propagation will result in a local considerable higher heat generation.

With heat generation associated with microplastic deformation and crack propagation, some studies have focused on their correlation with fatigue resistance. They linked the variation of heat generation throughout UFT with cyclic deformation softening or hardening behaviour of the material [168; 169]. For the same high-frequency testing time, when heat generation increases or decreases, the material is softening or hardening, respectively. Therefore, it can quickly be concluded that the heat generated measurement and its control are required throughout UFT not only to prevent any temperature influence, but to comprehend the material frequency response behaviour and predict the crack nucleation and propagation.

The frequency effect is inherently connected to the tested steel microstructure and its overall strength. Higher-strength steels will generally have a lower frequency effect and a surface to sub-surface and internal crack initiation from HCF to VHCF. The sub-surface and internal VHCF crack initiation are associated with material inclusions and defects. The associated fatigue and characteristic fracture mechanics are described in the following chapter.

2.3.6 VHCF Fracture Mechanics

As previously shown, the resultant fatigue behaviour of metal materials is dependent on many testing parameters and on its microstructure. Such behaviour differences between materials will also change the fatigue fracture mechanics associated with the fatigue regime under study, the VHCF. In the HCF regime, fracture starts predominantly at the surface. Beyond 10^7 cycles, fatigue crack nucleation and propagation at the surface may not occur for certain metals [67]. A fatigue limit within the VHCF regime can supposedly be established for metals where no surface or internal nucleation occurs beyond 10^7 cycles. This behaviour is commonly perceived in low strength steels as ferrite-perlite microstructural steels. No propagation to failure occurs due to the crack closure and microstructural barriers (grain barriers) mechanisms preventing small crack propagation [170; 171].

From low to high strength steels, crack initiation at the sub-surface and internally starts to emerge, and an evident VHCF failure is present. As the hardness and general strength increases, the VHCF regime failure appears and becomes more pronounced [137]. Figure 2-23 shows a stress-life representation from Aiguo Zhao already mentioned study [165] illustrating different steels strength fatigue behaviours.

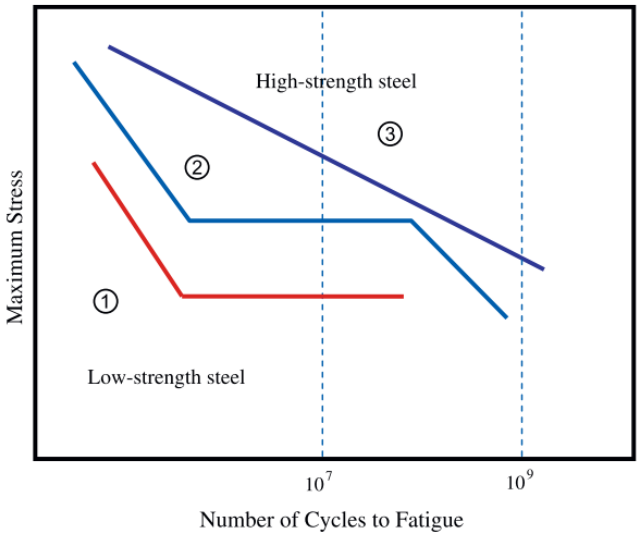

Figure 2-23. Stress-life fatigue schematic of typical carbon and alloy steels. (1) Low strength steel with a clear fatigue limit; (2) mild strength steel with a step-wise shape curve between HCF and VHCF; (3) High strength steel with a clear VHCF regime [165].

In high strength steels, the fatigue fractures in the VHCF regime are predominately nucleated in the subsurface and inside the specimen at inclusions, defects and voids of the material [99; 135; 163; 172; 173]. Considerable research has been dedicated to the VHCF fracture associated mechanisms as well as the related parameters influencing fatigue strength.

The reason for subsurface and interior inclusion and defect crack nucleation was concluded by Bathias and Paris [71] to be related to induced stress concentration. They have concluded that there is more likely higher stress concentration in the subsurface and interior for minor defects or inclusions than in the surface. In other words, subsurface and internal inclusions induce a stress intensity factor high enough for crack nucleation followed by low propagation rate fatigue crack.

Due to VHCF failure in high-strength steels being majorly initiated at inclusions and material voids, the fatigue strength and behaviour across the stress-life (S-N) curves are directly related to the inclusions size, shape, density and location [174]. Different overall fatigue strength can be observed depending on the direction of the loading, indicating that not only the size but also the shape and orientation of the inclusion have a direct effect on the results. Their influence and unpredictable nature induce S-N scatter data in the VHCF region for hard steels. Taizo [175] researched the effect of inclusion geometry on fatigue life and limit of forged and rolled allow steel JIS SCM435. Specimens were manufactured in different directions to the metal rolling procedure. Because the shape of the defects and inclusions were elongated by the forging and rolled process, the VHCF S-N results and crack initiation inclusion shape proved different between the different directional specimens.

Murakami introduced the $\sqrt{area}$ geometric parameter model for determining small cracks or defects induced stress intensity factor, and a threshold value for fatigue failure [176]. The model links a projected orthogonal area of a defect, crack or inclusion to the load direction. Figure 2-24 represents the defect projected orthogonal area to load direction.

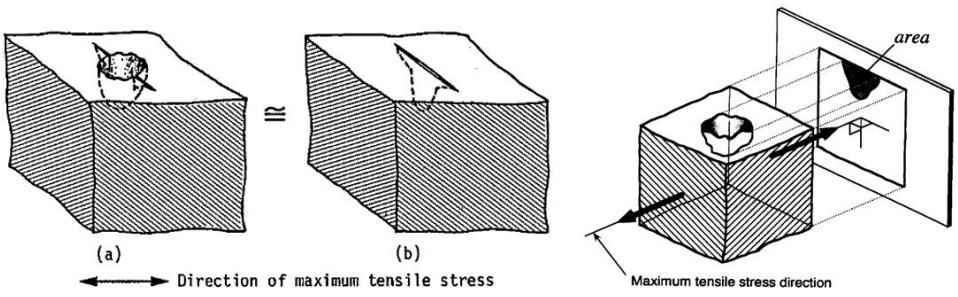

Figure 2-24. $\sqrt{area}$ representation [176].

Since the area directly affects the induced stress intensity factor, the smaller the effective inclusion area, the higher the fatigue life. Surface and inclusion failure can occur in the HCF regime depending on defect shape, size and orientation, leading to an S-N fatigue result with more scatter data. Murakami geometrical parameter is directly correlated with the stress intensity factor. Considering Figure 2-24 tensile load and internal $\sqrt{area}$ defect, the crack nucleation and propagation will be under crack opening mode (Mode I), and the associated stress intensity factor is K_I. For this case, the maximum mode I stress intensity factor across the defect is given by:

$$K_I \cong 0.5 \cdot \sigma\sqrt{\pi\sqrt{area}} \tag{2.21}$$

In the Murakami area model, the higher normal area to stress direction projects the S-N results dependent on the present defects and determines the threshold stress intensity factor range, ΔK_{th}, for crack growth [176]. Murakami and Endo also relate the Vickers Hardness (HV) and crack geometry effect on ΔK_{th} [177]. Murakami established a fatigue limit threshold stress intensity factor, and the respective stress amplitude is given by:

$$\Delta K_{th} = 3.3 \cdot 10^{-3}(HV + 120)(\sqrt{area})^{1/3} \tag{2.22}$$

$$\sigma_w = 1.43(HV + 120)/(\sqrt{area})^{1/6} \tag{2.23}$$

Many VHCF experiments have applied the Murakami geometrical parameter to the resulting fatigue S-N results by measuring the crack initiation defect area. The model's effectiveness is proven by comparing regular S-N fatigue results with the applied model. A VHCF test to SCM435 steel with high HV hardness compares the scatter regular S-N result to the Murakami $\sqrt{area}$ model plot, as shown in Figure 2-25 [137].

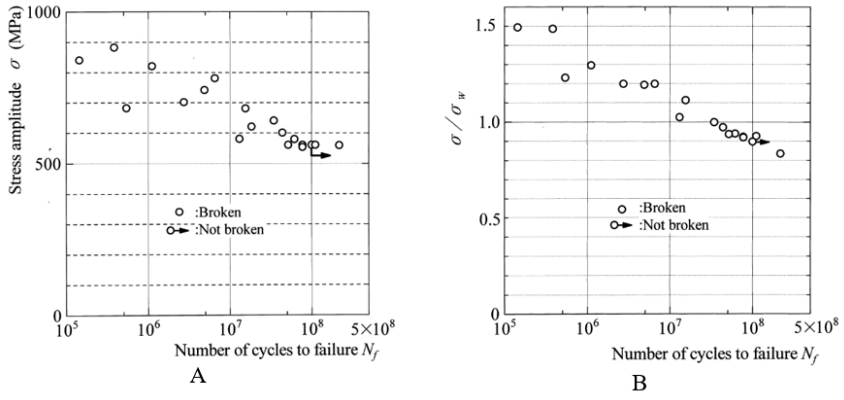

Figure 2-25. SCM435 (A) stress life results with defect crack initiation; (B) modified stress life with calculated $\sqrt{area}$ geometrical parameter σ_w fatigue limit [137].

Figure 2-25 stress fatigue failure σ results to Murakami fatigue limit σ_w prediction indicated an approximate 10% unconservative for a 10^8 cycles lifetime [137]. A study conducted by Qingqing J. et al. [178] compared structural steel with and without surface defects. The surface defect was made to reach a higher stress concentration factor than the present material defect and bring the crack initiation to the surface of the specimen. The surface defect reduced the fatigue strength considerably; almost no failure was achieved in VHCF, and inclusion crack initiation was no longer obtained. Therefore, the experiment was able to prove the fatigue limit by the induced surface stress concentration above the existing defects of the material.

Other studies associated the crack initiation defect location to ΔK_{th} and fatigue strength [175; 179]. Zhiqiang et al. [180] applied numerical methods to determine the effects of pore depth from the surface, pore clustering and size. They concluded that a present sharp stress concentration condition occurs when the pore intercepts the free surface. A high-stress concentration also increases when pores are intercepting or at proximity. Also, as expected, the pore size increased its stress concentration.

The crack nucleation mechanics at inclusions is still a debatable research topic. Once a crack nucleates from the inclusion and extends to the matrix, the inclusion is unbounded and relieved of stresses, being afterwards equivalent to a defect or pore [181].

The propagated fatigue fracture from sub-surface/internal defects presents what was denoted as the fish-eye crack formation. There are key crack propagation stages of the fatigue fish-eye fracture formation when observed by SEM microscope. The unordinary fracture shape was denoted as a fish-eye due to the resemblance created by the several circular-shaped stages. In sequence, the crack propagation stages are defect crack nucleation; Intergranular zone, ‘smooth area’ low crack growth, and macroscopic crack propagation.

The intergranular zone presents a characteristic rough surface. It was denoted as Fine Granular Area (FGA) by Sakai et al. [182], Optically Dark Area (ODA) by Murakami [183], or Granular Bright Facet (GBF) by Shiozawa et al. [181; 184]. This propagation stage has a very low propagation crack growth. Higher FGA areas in fatigue fracture are obtained in lower amplitudes and higher fatigue life cycles, growing until the stress intensity threshold is reached for regular fatigue propagation. It is estimated that FGA formation starts at 5-10% of fatigue life, taking around 90% of fatigue life growing [185]. This region presents a dark rough surface.

Several models try to explain its formation, as in Murakami theory of ‘hydrogen embrittlement assisted crack growth’ [186].

Figure 2-26 show fish-eye fatigue fracture formation from a research conducted by Stanzl-Tschegg et al. [135] on hydrogen embrittlement, together with a representation of the three main stages.

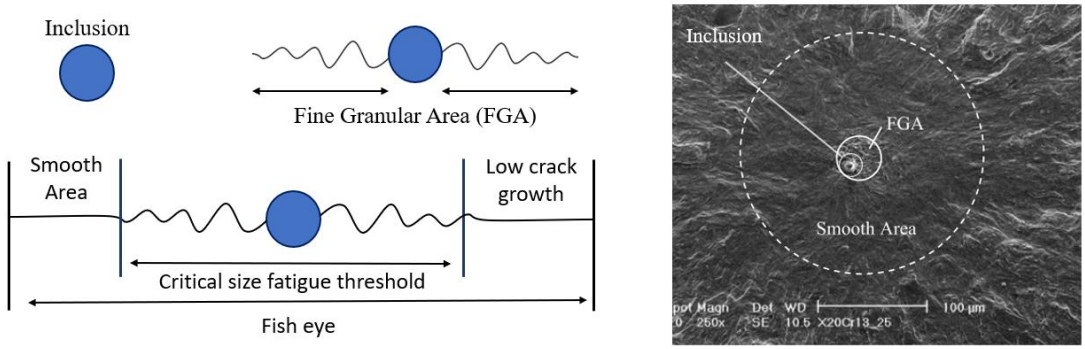

Figure 2-26. The representation of fish-eye formation and Stanzl-Tschegg et al. [135] obtained fish-eye fatigue fracture of AISI420 steel.

The fatigue fracture fish-eye formation initiated at a spherical inclusion followed by the FGA formation with a bright rough surface. Afterwards, a low roughness propagation region denoted ‘smooth area’ is present. This area morphology is associated with low crack propagation [185]. Finally, a similar HCF crack propagation surface morphology is present until the final fracture.

All briefly mentioned fracture mechanics associated with VHCF will guide the analysis of the obtained fatigue fracture surfaces. Much new research revolves around the crack nucleation mechanics and if there is an infinite fatigue life, even beyond 1010 cycles. Only by continuous improvement of fast frequency fatigue-inducing machines and respective methodologies will these present questions be understood, followed by unravelled new problems without certainty of their limit.

3

Finite Element Analysis

3.1 Introduction

Finite element analysis (FEA) proved to be essential for designing all ultrasonic fatigue components. In this chapter, every computed numerical analysis is fully described together with its relevance and the associated results. ABAQUS software was employed for all the conducted FEA. The conducted FEA and experimental results comparison analysis showed significant insights for improving every ultrasonic method conducted in this work. Both physical and numerical efforts were followed together and interactively throughout.

By working in resonance, every major component connected to the transducer needs to be carefully designed to have a specific resonance mode at 20 kHz. Resonance frequency determination requires the density (ρ), Poison ratio (ν), and material's elastic stiffness Young modulus properties considering isotropic materials. Such properties were determined through tensile material testing experiments later described in chapter 4.

FEA made to the tension-compression ultrasonic machine and individual specimens is first presented. They serve as proof of concepts and base explanation for the pure torsion and multiaxial FEA afterwards conducted. Beyond the use of FEA for component and specimen design, more complex analyses were also conducted to expand the ultrasonic setup modal behaviour comprehension and determine the impact of other present variables.

FEA proved essential in developing and improving all three main ultrasonic methods under discussion: pure torsional machine, tension-torsion, and cruciform axial-axial. All three UFT methods underwent modal frequency and steady-state modal analysis to comprehend and quantify the experimental results from which the modal behaviour was improved and/or corrected.

The pure torsional machine FEA and sequenced experimental improvements are presented with the steady-state analysis explanation. FEA was essential for the two biaxial ultrasonic methods in understanding the found issues, devising improved specimen geometries and ultrasonic setups, and planning the required experimental methodology.

3.2 FEA Uniaxial Tension-Compression Specimen Design and Setup Study

The first and well defined ultrasonic tension-compression machine is comprised of the axial piezoelectric transducer, booster, axial horn and testing sample. Before the initiation of the present work the present ultrasonic machine setup (without specimen) was in tension-compression working conditions. Similar to any given standard fatigue test, only the specimen needs to be designed to execute any given ultrasonic tension-compression test. The numerical analysis of the uniaxial tension-compression will first focus on the specimens and afterwards on the full booster-horn specimen setup.

The ultrasonic specimen requirements are the 20 kHz specific resonance under free-free boundary considered conditions that depend on the followed geometry and tested material static properties.

3.2.1 FEA Tension-Compression Specimens

To reach working uniaxial tension-compression and pure torsion specimens, both Bathias et al. [71] (eq. 2.2 to 2.13) and Japanese Welding Engineering Standard WES 1112 [187] (eq. 2.14 to 2.20) described equations were first applied respectively. Such analytical equations provide a base 20 kHz sample geometry close to the final solution, the displacement to stress relation, and their respective distribution.

Two sets of uniaxial tension-compression specimens were designed, manufactured and tested in this work: a conventionally machined metal alloy AISI P20 and AM Selective Laser Melting (SLM) titanium Ti6Al4V. A cylinder bar from standard construction steel was also created and experimentally tested for a frequency behaviour change response analysis. The steel bar 20 kHz length was analytically determined by equation (3.1) [71], followed by FEA.

$$l = \frac{c}{2f} = \frac{1}{2f}\sqrt{\frac{E}{\rho}} \tag{3.1}$$

Where *c* is the wave propagation velocity (equation (2.2)), *f* is the working frequency, E the Young's modulus and ρ the material's density. The cylindrical steel bar conducted experimental analysis and results is further discussed in chapter 5.2.

All analytically calculated tension-compression ultrasonic specimens had a cylindrical hourglass shaped with a hyperbolic variable section curve. The hyperbolic curve is considered a circular r radius curvature for equation simplification. Figure 3-1 presents the final Ti6AL4V specimen model with the Bathias established dimension variables, the circular curve and the M6 thread connection.

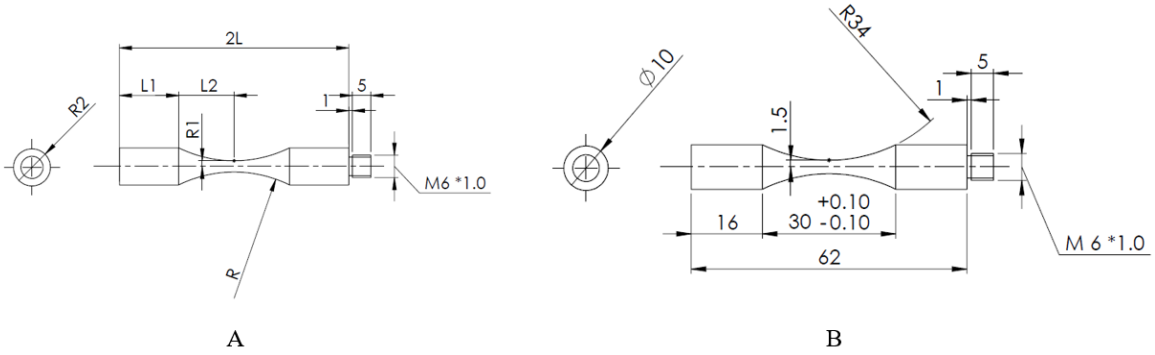

Figure 3-1. Tension-compression ultrasonic fatigue specimen: (A) Bathias dimension nomenclature [71]; (B) final reached Ti6Al4V ultrasonic specimen.

For AISI P20 ultrasonic specimen determination, the applied material properties were obtained by experimental static tests. All static specimens were machined from the same cylindrical bar as the ultrasonic fatigue specimens. The researched titanium was obtained by the SLM powder bed fusion AM process. Since only one complete order request was possible budget-wise, both the static and ultrasonic specimens were manufactured in the same SLM printing sequence. Therefore, the required material static properties for resonance determination were only tested after manufacturing tension-compression. Without experimental

static results the properties were first researched in previous publish research, and only later changed for correctly computation of all analytical, experimental and FEA results.

For the titanium specimens, a 1.5 mm smallest cross-section radius (R_1) was followed, similar to considerable referenced UFT tension-compression published research [103; 132; 161; 163; 173; 188; 189]. For AISI P20 specimens, a 2 mm smallest cross-section radius was applied, resulting in a longer constant cross-section (L_1) dimension and, therefore, an overall higher length specimen. The increased smallest cross-section radius was made to compare specimen overall modal behaviour variability.

FE free vibration frequency analysis followed the analytically determined geometry. L_1 was iteratively changed until a final geometry with the closest working 20 kHz frequency value. ABAQUS FE frequency analysis was applied with a fine Hex quadratic mesh. Figure 3-2 presents Ti6Al4V final specimen dimensions, FEA modal analysis applied mesh, and the tension-compression modal shape deformation sequence.

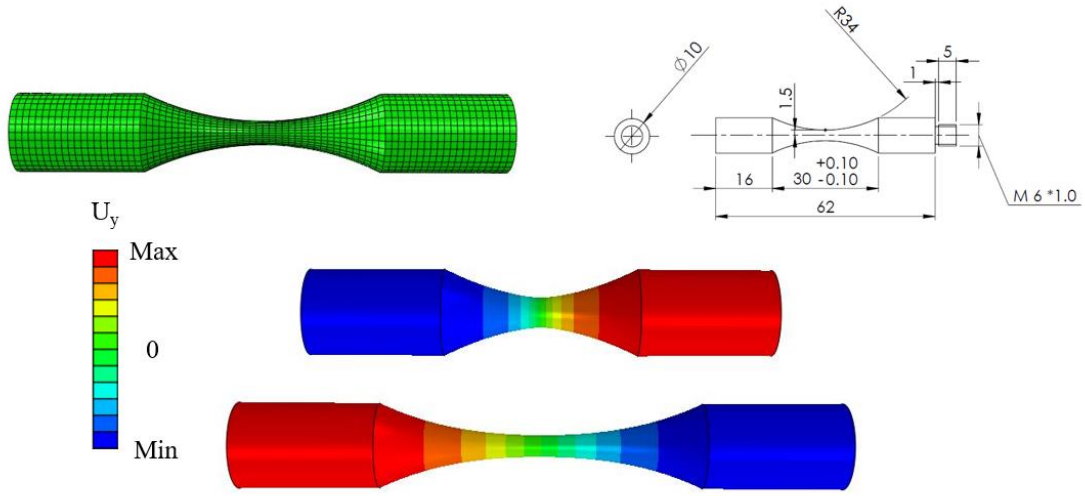

Figure 3-2. Ti6Al4v ultrasonic tension-compression fatigue specimen FEA applied mesh and resonant mode shape representation with axial displacement (U_y) distribution.

Since the Ti6Al4V properties vary significantly with the manufacturing parameters [190], a higher than FEA determined L_1 dimension was required. If the specimens showed a too low frequency, they could always be machined to adjust the frequency of work. If a higher than expected rigidity were obtained, the higher L_1 dimension would compensate it. The obtained Ti6Al4V and AISI P20 tension-compression specimen dimensions are presented in Figure 3-3, directly comparing the two different cross-section sized specimens.

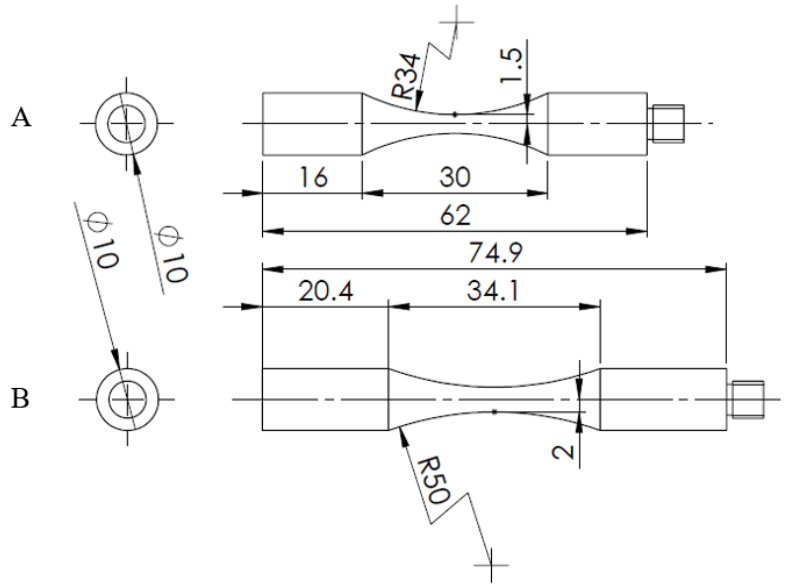

Figure 3-3. Tension-compression ultrasonic fatigue specimen final dimensions [mm] and comparison: (A) Ti6Al4V; (B) AISI P20.

Through the FEA free-free vibration frequency analysis of the specimens alone, a direct comparison is made between it and the presented analytical solution (eq. 2.2 to 2.13) [71]. The main objective was to understand the FEA and the analytical solutions compatibility. A low deviation between the two methods proves the FEA reliability towards a 20 kHz specimen design and stress determination. An analytical solution and FEA link enabled the study to reach a more complex analytical solution for the tension-torsion and the axial-axial cruciform specimens.

The FEA obtained frequency with the analytical determined L_1 is first compared to the FEA ideal 20 kHz L_1 dimension. Table 3-1 presents the FEA free-free boundary condition vibration analysis results of analytically and FEA determined 20 kHz L1 dimension for AISI P20 and Ti6Al4v specimens.

Table 3-1. Free-free vibration FEA frequency results for analytical and numerically obtained L1 dimension.

Specimen Material	**L1 Dimension [mm]**	**FEA resonant frequency [Hz]**
Ti6Al4V	14.4 (analytical E=100 GPa)	20221
	14.8 (FEA final)	19987
	16 (analytical E=110 GPa)	19317
AISIP20	20.1 (analytical E= 202 GPa)	20118
	20.4 (FEA final)	19984

A higher than 20 kHz frequency was always obtained in FE free-free vibration frequency analysis with the static determined Young modulus and analytically determined L_1 from Table 2-1. Through an iterative process, the L_1 dimension is increased towards closer to 20 kHZ frequency specimen. Still, the frequency obtained analytical – FEA low difference will not have a considerable effect regarding the UFT.

The parameterised specimen stress and displacement distributions across its length are also compared between the analytical and FEA solutions. The analytical solution acknowledges two types of specimens, a hyperbolic and an exponential ultrasonic tension-compression specimen. Two fictional uniaxial ultrasonic specimens considering the aluminium used in the ultrasonic cruciform tests were analytically determined through Table 2-1. A cylindrical hyperbolic curve fictional specimen with similar base dimensions as to the used by [14; 191] and Figure 3-1 Ti6Al4V specimen; and a second plane specimen with exponential variable section curve. These specimens were designed to compare each associated distribution of displacement and stress analytical solution to FEA numerical results. They are also later associated with a proposed solution for the cruciform specimens here tested in this work. Very few published ultrasonic fatigue research have employed exponential plane specimen geometry [192].

The hyperbolic and exponential sample dimensions were again analytically determined and afterwards introduced in ABAQUS numerical software. For the analytical displacement and stress solution computation an unitary axial displacement (A_0) was considered. Again, FEA free vibration frequency analysis was computed. The first longitudinal resonant mode describing a tension-compression modal shape is the only of interest for this comparison. Comparing the 20 kHz analytical frequency with the FEA obtained frequency, both specimens presented higher numerical frequency again. The frequency result is within the operation transducer range, and it will not have any detrimental effect on the specimen and ultrasonic setup resonance. Figure 3-4 presents both the hyperbolic and exponential specimens with the axial displacement FEA distribution. The displacement and stress distribution were taken across the specimen's length centre *y*-axis. Figure 3-4 also shows the specimens *y*-axis path where both analytical and FEA distribution results were computed.

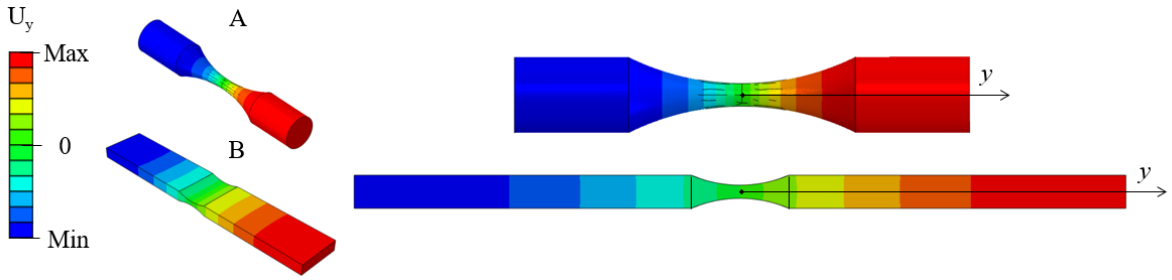

Figure 3-4. Ultrasonic tension-compression hyperbolic (A) and exponential (B) specimens FEA *y*-axis and longitudinal displacement (U_y) distribution.

Both the analytical and FE stress and displacement results were parameterised. Figure 3-5 compares the analytical and FEA displacement and stress distribution solutions across Figure 3-4 fictional specimens y-axis.

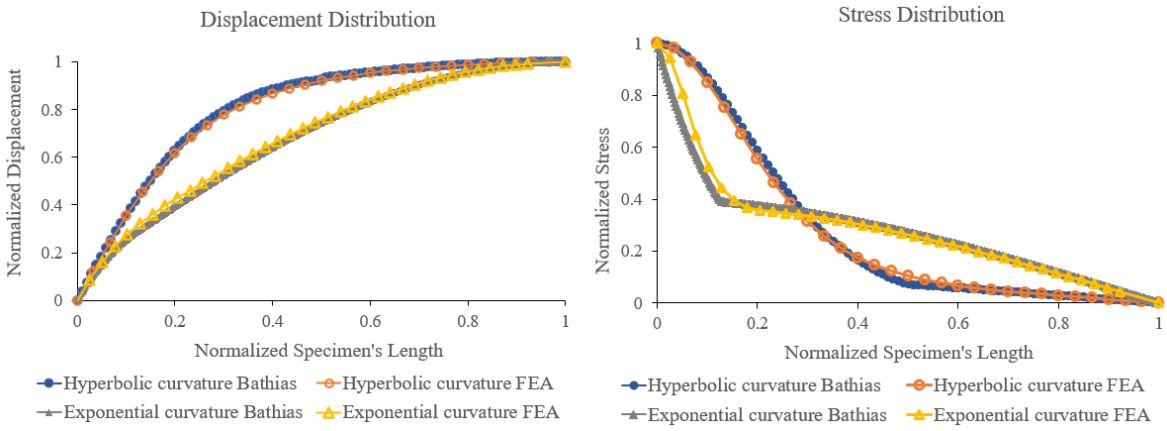

Figure 3-5. Ultrasonic tension hyperbolic and exponential specimens' displacement and stress distribution comparison between Bathias analytical solution and Abaqus FEA frequency analysis.

The results show very good agreement between the two methods. Therefore, the analytical and FEA proved their compatibility and reliability. A behaviour comparison was also made between the AISI P20 and Ti6Al4V different specimen geometry. Both specimens' normalised FEA displacement and stress distributions are compared in Figure 3-6 showing again an excellent agreement.

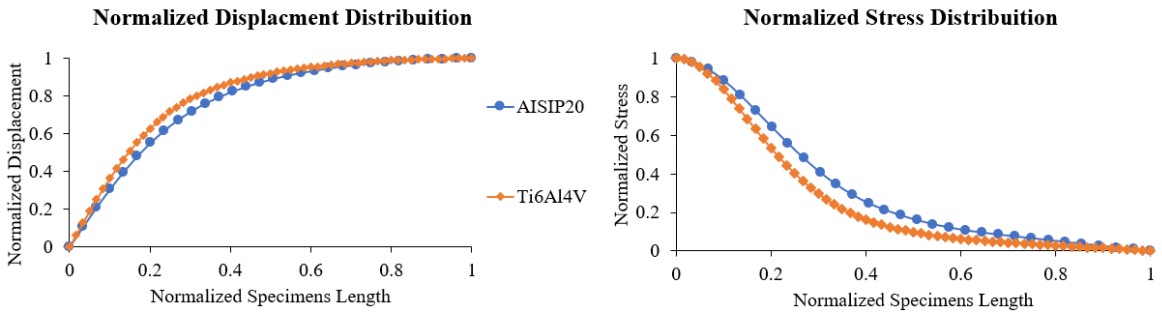

Figure 3-6. Tension-compression ultrasonic AISI P20 and Ti6Al4V specimens normalised axial displacement and stress distribution.

3.2.2 FEA Tension-Compression Setup

After the conducted free vibration FEA frequency to tension-compression ultrasonic specimens, they were attached to the two available setups, tapered and hyperbolic setups. The two available tension-compression setups are composed of the same booster and two different axial horns, the tapered and hyperbolic horns.

The two horns have different shapes, mass, and displacement amplification with the same resonant mode at 20 kHz. The two different horn setups here presented are numerically and experimentally studied to observe any modal improvement a given geometry might bring to the ultrasonic fatigue method.

The two complete setups together with the specimens were numerically analysed in free-free modal frequency and steady-state modal analysis. Both setups free-free modal frequency analysis obtained the desired longitudinal resonant mode at the transducer 20 kHz. This axial displacement distribution and modal shape representation of both tapered and hyperbolic horns are shown in Figure 3-7.

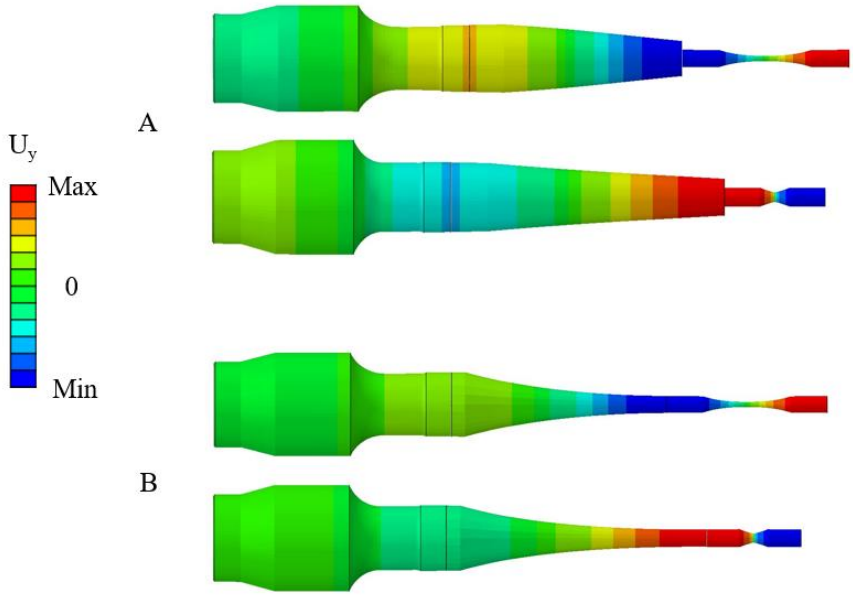

Figure 3-7. Tension-compression ultrasonic fatigue setup tapered horn (A) and hyperbolic horn (B) setups modal shape and axial displacement (U_y) distribution.

As mentioned, a steady-state analysis was afterwards conducted. This numerical analysis applies a unitary force in the transducer booster connection region. The unitary force will replicate the transducer excitation across the established frequency range of 18.5 to 21.5 kHz.

The computed result gives the setup its steady-state response for a given excitation frequency. This numerical analysis is applied to all tested setups in this work. It allows to fully understand the setup excitation response, meaning all resonant modes present inside the frequency range may be excited or not by the axial excitation of the transducer. If an apparent displacement magnitude appears around a given mode's frequency, it has the possibility to be excited by the piezoelectric transducer.

Inside the established 18.5 to 21.5 kHz frequency range the two tested tension-compression ultrasonic setups showed more than one resonant mode in FE free-free modal frequency analysis. Table 3-2 presents the obtained resonant modes and their frequency for both the tapered and hyperbolic setups with the AISI P20 specimen.

Table 3-2. Tension-Compression ultrasonic booster tapered and hyperbolic horn AISI P20 specimen setup free-free vibration FEA frequency results within the 18.5 to 21.5 kHz range.

Tension-Compression Booster Horn AISI P20 Specimen

Tapered Horn		Hyperbolic Horn	
Resonance Mode	**Frequency [Hz]**	**Resonance Mode**	**Frequency [Hz]**
Longitudinal	20006	Bending	18610
Torsional	20027	Longitudinal	19992
-	-	Torsional	20249

From the steady-state modal analysis, the axial stress at the smallest cross-section of the specimen and the axial displacement at the free base are plotted across the frequency range in Figure 3-8.

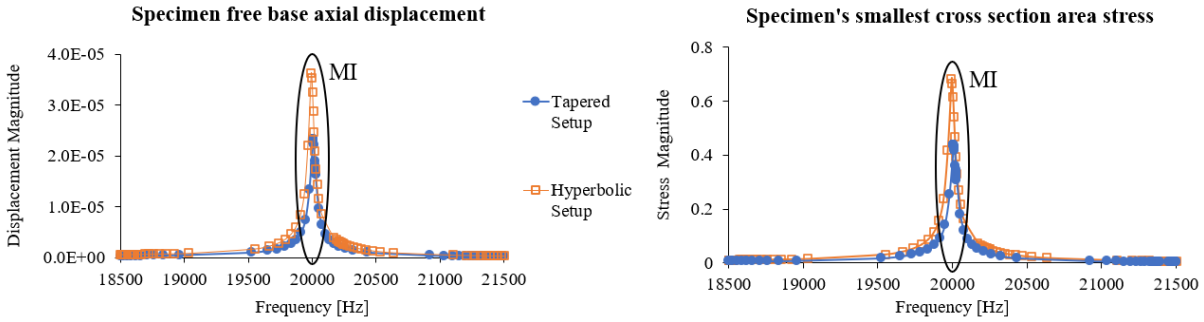

Figure 3-8. Tension-compression booster horn AISI P20 specimen setups. FEA steady-state axial displacement at the free base of the specimen and axial stress at the smallest cross-section area.

Figure 3-8 stress and axial displacement show only one excited resonant mode within the studied frequency range. Since the excited resonant mode is the desired shape and desired stress-induced method, it is denoted the Mode of Interest (MI). MI is identified in Figure 3-8. From the present FE free-free vibration and steady-state analysis, no clear difference between the tapered and hyperbolic horn was taken beyond the displacement amplification. The experimental results will unveil the present modal differences between horns more clearly since the setup imperfections will be present, contrarily to the numerical analysis where all components (booster horn specimen) have an almost perfect 20 kHz resonance.

The steady-state modal analysis can also compute the ratio between the displacement at the specimen free base to tensile stress at the specimen smallest cross-section area. The obtained FEA displacement to stress ratio is afterwards compared to the experimentally measured in chapter 5.3.

3.3 Pure Torsion Machine Design

One main objective of the present work was to build a working pure torsional ultrasonic fatigue machine. A similar Figure 2-18 rotational piezoelectric transducer of the referenced research [116] was intended to be acquired, but it was unfortunately not possible. At present, the device is an under-research Branson transducer that only a few research teams had the fortunate access. The project abandoned the possibility of having a rotational transducer after a considerable time loss requesting it with Branson international personnel. Thereafter, it was decided to build the Bathias et al. [112] Figure 2-17 torsional machine through a longitudinal transducer. All associated study and building process is fully described in the document.

To reach a working pure torsional ultrasonic fatigue machine following Bathias concept design, an interactive numerical-experimental sequence was followed. The machine components setup was sequentially FEA designed, machined, experimentally analysed. All obtained experimental results were then compared to FEA predicted. A methodology was then conducted to two different created setups from those first results. The final obtained setup was capable of conducting UFT in pure torsion.

As described in detail in chapter 2.3.4.2, the Bathias pure torsion ultrasonic machine is composed of two horns, a Longitudinal Horn (LH) and a Torsional Horn (TH). A single pin connects the horns, and the testing specimen is screwed to the TH. The pure torsional setup is shown in Figure 3-9 with an exploded view to perceive its assembly.

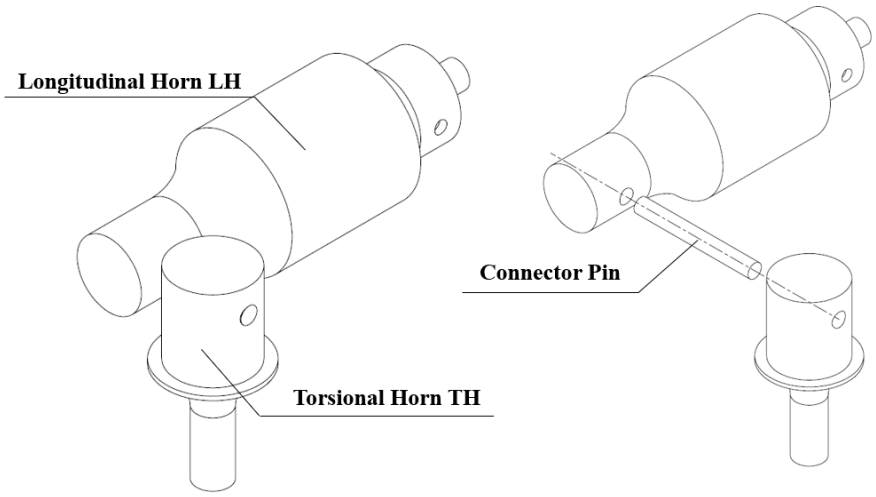

Figure 3-9. Pure torsion ultrasonic fatigue machine representation with an exploded view.

To reach a functional machine, the LH and TH must have the first longitudinal and torsional resonant modes, respectively, at 20 kHz frequency. Both horns and the connector pin were numerically designed and manufactured in Ck45 steel. The connector pin and the respective hole were machined with a thigh H7-k6 adjustment.

Several different horn shapes (LH and TH) were created and numerically analysed separately in FEA free-free vibration frequency. The LH followed a similar geometry to the used booster in tension-compression ultrasonic fatigue machines. Just as the booster, LH has its first longitudinal mode (one displacement node) at 20 kHz and an area reduction for transducer displacement amplification. The final dimensions and mode shape are represented in Figure 3-10.

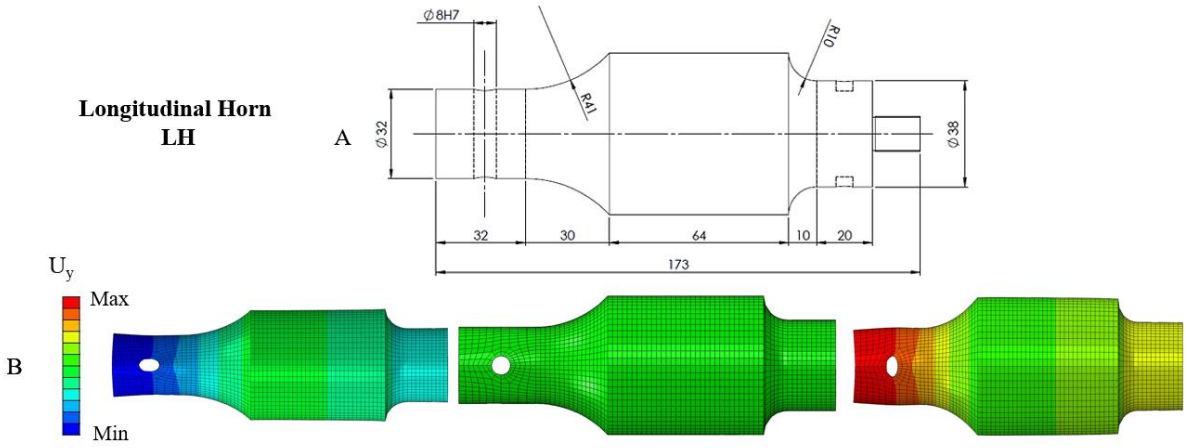

Figure 3-10. Pure torsion Longitudinal Horn (LH) final dimensions (A) and resonant mode shape with axial displacement (U_y) distribution (B).

For the TH, a circular curved variable section was followed. A more considerable area reduction was introduced for rotation displacement amplification. TH resonance follows the first rotational mode at 20 kHz. A support ring was machined in the displacement node region to lean TH on the supporting structure. The machined dimensions and mode shape are represented in Figure 3-11. Figure 3-11 also indicates the L_{th} dimension that will serve to frequency adjust the TH.

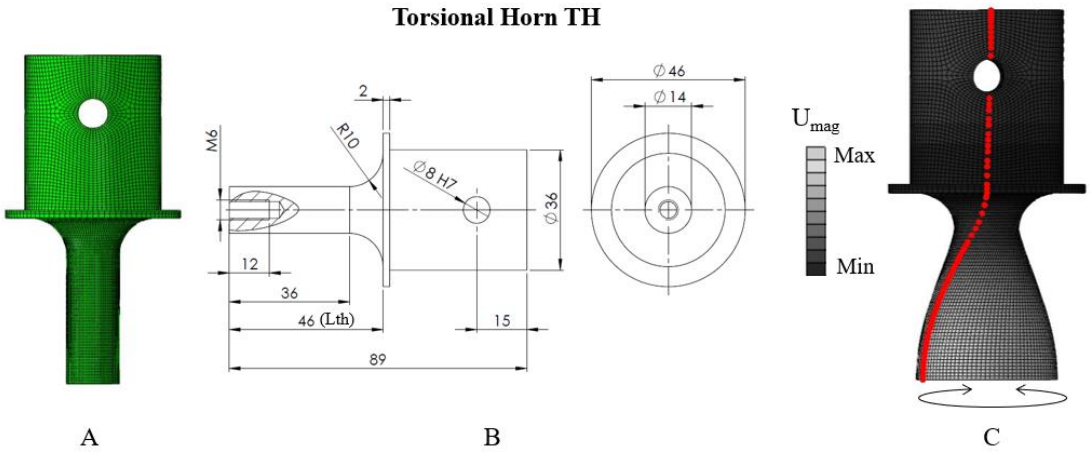

Figure 3-11. Pure torsion Torsional Horn (TH): (A) FE mesh; (B) machined dimensions (C) resonant mode shape with displacement magnitude (U_{mag}) distribution (C).

The FEA frequency of LH and TH results is different if the pin hole is on the assembly or not. The pin connector and the respective hole in each horn influence the final frequency and mode shape. When the pin is inserted in a horn, it is equivalent to having no hole if the contact remains fixed (no slip). Table 3-3 presents the obtained FEA frequency of both LH and TH with and without the pin holes. Table 3-3 also presents the resulting frequency of LH with the pin (no TH) and the complete setup frequency. In frequency modal analysis with more than one component, the contact was established as rough contact, meaning no slip.

Table 3-3. Free vibration FEA frequency results for different pure torsion components combinations.

FEA Model	**Frequency [Hz]**
LH without Hole	20073
LH with Hole	20151
LH with pin	(LH1) 19122; (LH2) 20638
TH without Hole	20062
TH with Hole	20074
Full setup (LH, pin, TH)	20064

LH with pin has two similar modes, LH1 and LH2. Each mode has an equal longitudinal mode shape LH, but the pin has a different phase. In the TH and LH, a higher frequency is obtained when the pin hole is present. This occurs because the hole is located near the stress node (high displacement, low deformation), meaning the associated mass reduction has a higher impact than the loss in rigidity and, therefore, the frequency increases. If the pin to LH link presents slip when excited by the transducer, the horn will show a higher excitation frequency.

All Table 3-3 obtained frequencies will be compared to the experimentally obtained, except for TH with hole. Since the project was not able to attain a torsional transducer, it is impossible to excite TH without the pin.

If the tight pin connection remains fixed in the two horns, the resulting horn resonant frequency will be equivalent to a no-hole response. Therefore, the FE frequency analysis when designing both TH and LH should be conducted to a no-hole geometry.

The dimensional determination and modal analysis methodology applied to the tension-compression specimens was transported for the pure torsional specimens. The exact tension-compression Figure 3-1(A) analytical dimension terminology was followed. The smallest cross-section radius value of 1.5 mm R_1 was considered, R_2 and L_2 dimensions were chosen accordingly, and L_1 analytically determined. Afterwards, the analytically determined geometry was introduced to FEA free vibration frequency for a final L_1 adjustment towards 20 kHz rotational frequency. Figure 3-12 presents the torsional specimen determined dimensions and mode shape representation from the FEA.

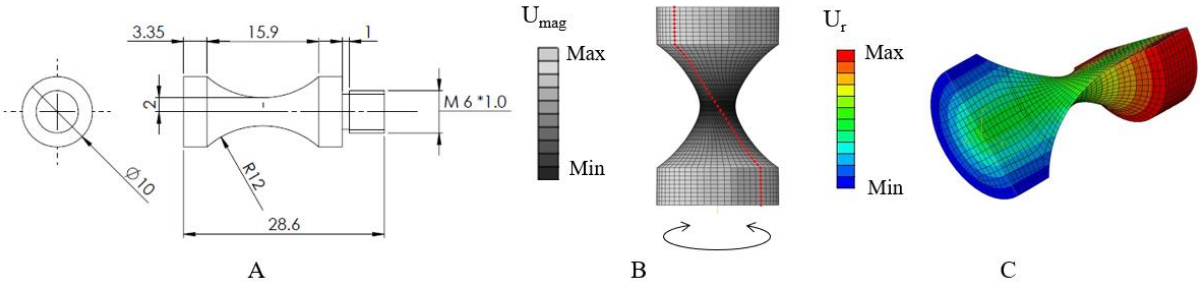

Figure 3-12. Pure torsion ultrasonic fatigue specimen dimensions (A) and mode shape representation with displacement magnitude (U_{mag}) (B) and rotational (U_r) distribution(C).

The experimental results chapter 5.4 will show that a not functioning resonance was obtained when testing the first assembled setup. From a modal analysis of the setup, it was perceived that TH had a considerably lower frequency than predicted. Upon dimensional measurements, the TH L_{th} dimension (Figure 3-11) had a higher dimension than the required. The obtained frequency reduction beyond the transducer operation range in TH occurred due to a higher dimensional sensitivity of all rotational modes. Regarding deformed tensile mode shapes, the frequency of a given component is dictated by its rigidity-mass ratio (considering negligible damping). Since there is only elastic deformation, the rigidity is associated with the Young's modulus (E). However, for torsional mode shapes, the Shear modulus (G) mass ratio dictates the frequency. Because G is considerably lower in steel, the mass must be reduced;

hence smaller specimens and horns, and the rigidity-mass ratio will be more sensitive to changes. Meaning all rotational components have a higher dimensional sensitivity than axial components.

The TH L_{th} dimension (Figure 3-11) was slowly machined to correct the experimentally measured low frequency. Several machine sequences (Mach *x*) were conducted until TH had a frequency as close as possible to LH. The experimental process will be described in more detail in subchapter 5.4. A FEA dimensional sensitivity of the L_{th} was conducted before the machine sequences to limit the taken material between each step. An FEA steady-state modal analysis with a unitary axial excitation force in LH was conducted for each Mach obtained L_{th}.

The FEA and measured points of comparison must be the same. From mode shape inspection of the setup the regions that allow laser measurements and to quantify the setup behaviour are the LH free base stress node, and the free base of the specimen rotational stress node. Both regions are highest displacement locations and allow for to study LH axial resonance and TH and specimen rotational resonance. The measuring experimental setup is fully explained in subchapter 4.4 and represented in Figure 4-26.

The steady-state modal FEA results showed: (i) the excited modes from the transducer axial excitation; (ii) obtained rotational displacement to shear stress ratio and respective distribution; (iii) the displacement phase between the measured laser locations. All obtained steady-state FEA data will later be compared with the experimental FDD modal analysis.

FEA steady-state results for the final LH TH specimen 20 kHz setup excitation show two different modes being excited by the unitary axial force applied in the LH. The two modes have a considerable 1019 Hz frequency difference. Figure 3-13 presents the FEA steady-state obtained magnitude and phase for the experimentally established locations.

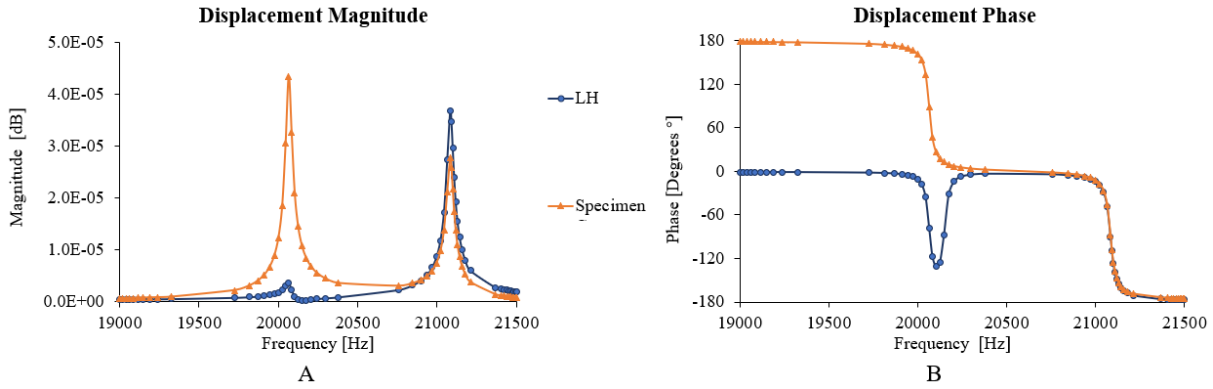

Figure 3-13. FEA steady-state final LH pin TH specimen setup displacement magnitude (A) and phase (B) of the established experimental measured LH and specimen locations.

The intended resonant mode has a much higher specimen rotation to LH axial displacement magnitude ratio, and the two measuring points are in 180º out-of-phase. In the second mode, LH and the specimen will be in-phase. The phase difference allowed for an easy and reliable resonant mode identification.

The ratio between the specimen rotational displacement and induced shear stress was taken from all conducted FEA steady-state analyses. The FEA taken ratio was then compared with the experimentally measured laser displacement and stress measured by strain gauges.

3.4 FEA Tension-Torsion Ultrasonic Fatigue Machine

Outside the present study and all associated research team, no complete or somewhat standardised ultrasonic biaxial tension-torsion fatigue methodology was ever achieved. The complexity of the induced deformation and overall horn and specimen geometry has impeded the development of a complete analytical solution followed by a consistent and proven experimental result.

As it was first introduced in chapter 2.2, tension-torsion is one of the most common conducted multiaxial fatigue testing experiments. It is far from a straightforward task to carry it to ultrasonic fatigue testing machines. With no supporting analytical method and the complex resonant behaviour, the built methodical designing and experimental method would not be possible without numerical software. Every development present in this thesis will undoubtably support future research in multiaxial ultrasonic fatigue methods towards a standardized methodology and possibly an analytical solution.

As this chapter will explain in detail, the studied tension-torsion ultrasonic machine has a complex ultrasonic setup attached to the commonly used longitudinal transducer. The study focused first on in-depth FEA to the first designed and tested setup by Mario et al. [91]. The existing horn and specimen individual and setup complexities were described. An improved horn design and specimen geometry were proposed and tested.

The improved set created the ability to induce and reach tension-torsion fatigue with different stress shear /axial ratios. It allowed for a first base geometry determination method that will only require minor adjustments, just as the conducted procedure for the uniaxial specimens. A devised experimental methodology is also proposed.

To better present all tension-torsion ultrasonic fatigue reached data, improved set and conclusions, an introduction is first made to all base concepts. A first detailed analysis of the setup with no specimen and with the first specimen was conducted and here presented to demonstrate all tension-torsion intricacies. Subsequently, the detailed analysis results are discussed, leading to the new specimen geometries capable of varying the multiaxial stress ratio.

The new setup and specimen design built across the study were experimentally tested, taking the FEA method and results into account. Both FEA and experimental results showed good agreement. However, they also revealed new issues to be improved. From the taken numerical and experimental conclusions two significant recommendations for further improve the machine were analysed in their reliability and are also here presented. The same proven FEA methodology was computed to the two proposed future developments to the setup. All numerical results display significant improvements towards this innovative ultrasonic method.

3.4.1 Introduction to Tension-Torsion Ultrasonic Fatigue

As aforementioned in this study, UFT takes advantage of components resonance to reach high enough strain at considerably high frequencies. To reach a functioning testing method FEA modal analysis of all components are required. Taking the tension-compression ultrasonic machine as an example, all components, booster, horn and specimen, are modally designed to have compliant resonant modes at the transducer frequency of work.

To reach a working multiaxial ultrasonic fatigue method, there are two possible solutions: A uniaxial displacement excitation made to a specimen with a resonant mode where the resultant excited mode shape induces a multiaxial deformation at a single fatigue region; or exciting the specimen in two simultaneous resonate modes with a shared high-stress fatigue region.

The aforementioned Palin Luc et al. [193] ultrasonic biaxial method (chapter 2.3.4.1) follows the first possible solution. The booster-horn setup excites a disk-shaped specimen through a uniaxial displacement. The disk is modelled with a resonant mode where the highest stress region induces a biaxial bending stress state.

Mário Vieira et al. [91] designed and experimentally tested the first tension-torsion booster multi-horn specimen setup from a common construction steel alloy. To reach a biaxial tension-torsion stress state of excitation the second possible solution was followed. The horn-booster setup was specially designed to excite an also unique modelled specimen in a longitudinal and a rotational resonant mode simultaneously. Therefore, the specimen was made to be excited simultaneously in two transversal resonant modes in the same frequency, a complex resonant mode. Mario Vieira et al. special specimen design [91] is shown in Figure 3-14. Figure 3-14 also labels all main dimensions. Different Tr values between the cross-area reduction sections were applied. The intention was to prevent a higher induced stress combination outside the intended fatigue testing region at its centre.

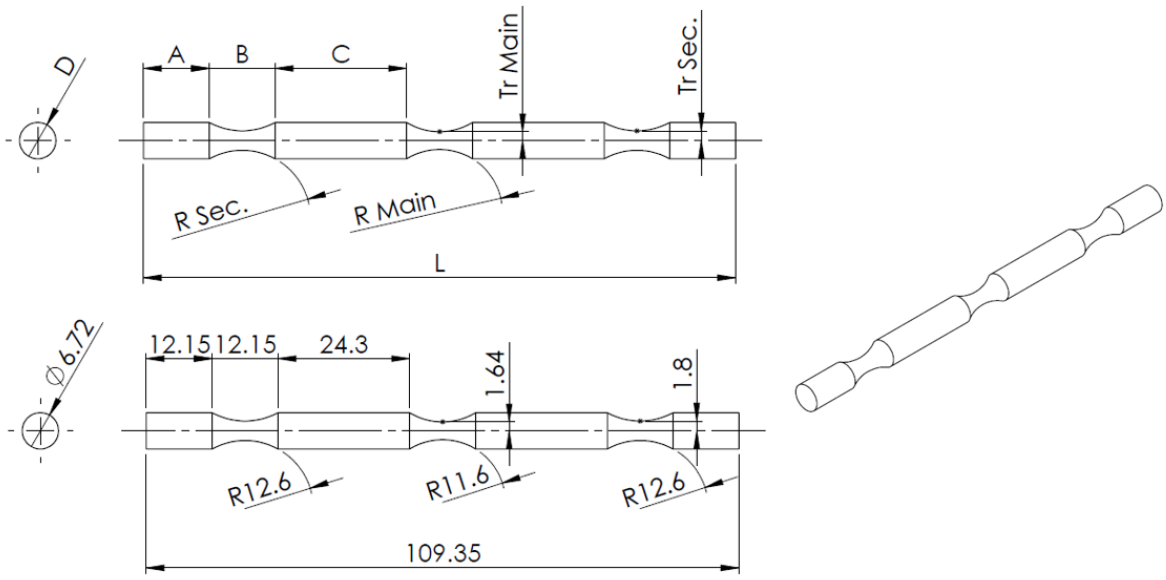

Figure 3-14. Mario et al. [91] first experimentally tested ultrasonic tension-torsion fatigue specimen with key dimension designations.

To excite two resonant modes simultaneously, a compliant biaxial inducing displacement combination was required. The exciting biaxial displacement must have both resonant associated displacement types. While the used booster is the same, a unique horn was designed to induce both longitudinal and rotational waves at the same frequency to the specimen. In other words, a multiaxial horn will induce two types of displacements simultaneously to the specimen, axial and rotational cyclic displacements.

To reach such multiaxial displacement of excitation, the created unique horn design can transform part of the longitudinal waves induced by the piezoelectric transducer into rotational waves. The multiaxial horn (multi-horn) design has two sets of grooves responsible for the wave transformation towards rotational displacement. A representation of booster multi-horn specimen tension-torsion setup is made in Figure 3-15.

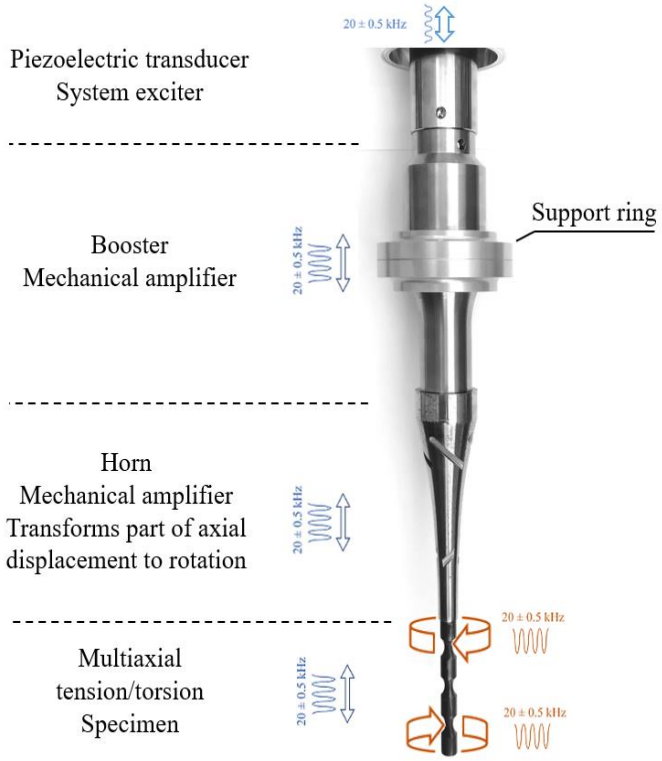

Figure 3-15. Tension-Torsion ultrasonic fatigue machine representation with component designations.

When designing the booster-horn-specimen tension-torsion setup, the existing rotation should be prevented or reduced to a negligible amplitude from reaching the booster and the transducer. The transducer was not designed to work in rotation. Therefore, the rotation distribution was intentionally made to be as low as possible to safeguard the transducer since it may damage it.

3.4.1.1 Multiaxial tension-torsion horn concept

The tension-torsion ultrasonic machine was only made possible with the unique multi-horn design. The axial displacement provided by the booster is transformed partly into rotation through two sets of slits. Therefore, the horn is axially excited in resonance on one end (the highest radius section) and has a biaxial axial/rotation displacement at the other (smallest cross-section). Just as the axial horn from the tension-compression ultrasonic set, the horn also amplifies the displacement from the booster. When designing a multiaxial horn, five parameters need to be considered:

- Working frequency of the desired resonant mode
- Low rotational displacement at the booster-horn connection
- Highest displacement (lowest stress) at the horn-specimen connection
- Rotation axial displacement ratio at the horn-specimen connection
- No considerably high deformation/stress regions

Costa master thesis [194] focused on reaching a working multi-horn design. To reach a working multi-horn geometry that fulfils the pointed four parameters is a complex iterative task using numerical software. The first used by Mario et al. [91] presented deformation at the horn-specimen connection, which did not allow for high power transducer settings, meaning no high stress could be imposed on the specimen and therefore no suitable for UFT.

Costa [194] multi-horn geometry followed a conic shape in the slits section and a hyperbolic curve in the multi-horn specimen connection (SnH). The hyperbolic curvature allowed to reach the necessary highest displacement (lowest stress) in the SnH. After conducting the first UFT with the multi-horn, it changed its behaviour and resonant frequency. The change in frequency indicated a change in its rigidity. This meant a possible fatigue crack was induced in the multi-horn due to a present high deformation region.

A new multi-horn was designed with a total hyperbolic curvature. Every pinpointed parameter was followed, with special attention to high deformation regions. The new multi-horn was used for all the conducted tension-torsion fatigue tests in the present study. The respective multi-horn axial (U_y) and rotational (U_r) displacement distribution in the desired resonant mode is shown in Figure 3-16. The obtained modal frequency of the shown Figure 3-16 FEA result for the multi-horn resonant mode of interest was 20064 Hz.

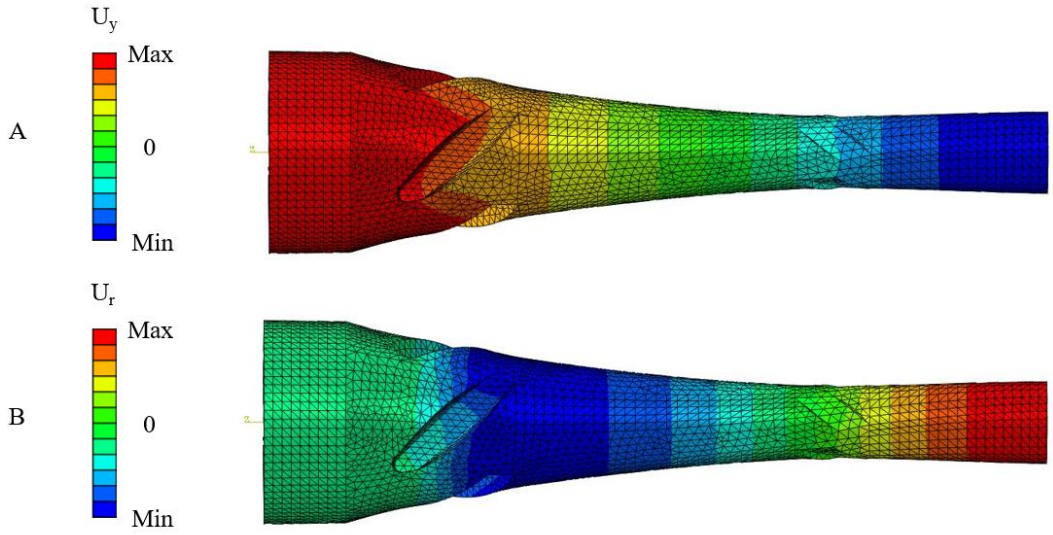

Figure 3-16. FEA Multi-Horn Mode of interest: (A) Axial displacement distribution (U_y); (B) Rotational displacement distribution (U_r).

Figure 3-16 multi-horn rotation distribution shows the desired maximum rotation at the multi-horn specimen connection base (SnH) and a low rotation on the booster-horn connection (SnB). The axial displacement is similar to an ordinary ultrasonic axial horn, having the lowest stress maximum displacement (stress node) at both SnH and SnB. The rotation and axial displacement ratio displacement is an important multiaxial parameter since it will affect the final shear/axial stress ration induced to the specimen. However, this value can only be taken when the multiaxial horn is within the complete setup.

3.4.1.2 Ultrasonic tension-torsion specimen concept

Regarding now the tension-torsion ultrasonic specimen concept and design. Any specimen attached to the multiaxial horn will have an imposed axial and rotational cyclic displacement. To fulfil the resonance ultrasonic machines demands within tension-torsion setup (i.e. to have correctly placed stress and displacement nodes) the specimen must have both an axial and a rotational resonant mode within the transducer working frequency range. Also, both excited modes need to share the same fatigue testing region.

Table 3-4 presents the longitudinal and rotational modes frequency of Figure 3-3.B AISI P20 tension-compression ultrasonic fatigue specimen. As aforementioned in previous chapters, the longitudinal and rotational frequencies are dependent on the Young's and Shear modulus,

respectively. Considering the AISI P20 tension-compression specimen, the frequency of the rotational mode will be considerably lower due to the lower Shear Modulus.

Table 3-4. AISI P20 tension-compression ultrasonic fatigue specimen longitudinal and rotational resonant mode's FEA free vibration frequency result.

AISI P20 Tension-Compression Specimen	
Resonance Mode	**Frequency (Hz)**
1º Torsional	6274
1º Longitudinal	20008
2º Torsional	63403
3º Torsional	66272
2º Longitudinal	84542

Due to the Young's and shear modulus rigidity difference in conventional metals no cylindrical hourglass-shaped specimen (similar to Figure 3-1 uniaxial tension-compression ultrasonic specimen) can have the first longitudinal and first torsional modes with the same frequency. To reach a frequency match between the two modes, the designed specimen has not one but three hourglass cross-area reduction regions. Consequently, the created sample geometry places three rotational displacement nodes in three smaller cross-section areas. Each section will reduce the stiffness, lowering the third mode frequency significantly. The three lower stiffness regions result in a low enough third torsional frequency to meet the first longitudinal mode. The three cross-section reduction sections of the specimen were denoted as 'throats'. A representation of the specimen is shown in Figure 3-17. Figure 3-17 also attributes specific designations to each throat, having Figure 3-15 horn and booster as reference.

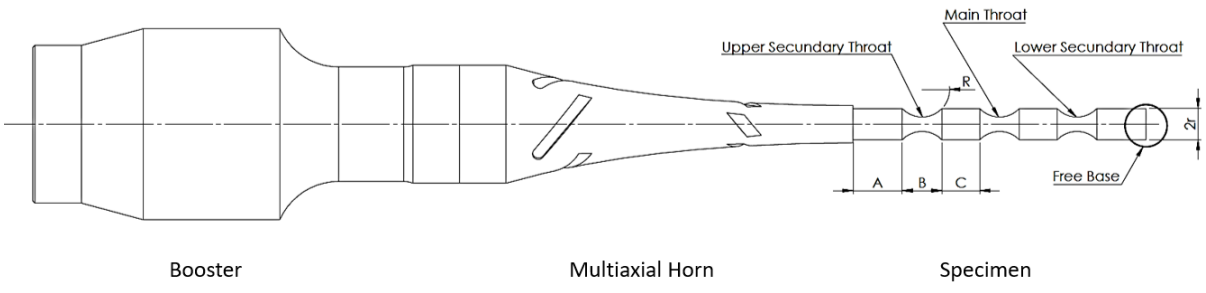

Figure 3-17. Throat designations of the multiaxial fatigue specimen with the initial horn as reference.

The rotational mode excited is designated as the third because of the present three displacement nodes. The longitudinal mode is the first having only one displacement node at the main throat. The reason for three and not two or four throat sections is the ability to have one shared region with axial and rotational displacement nodes, the fatigue testing region.

Both longitudinal and third torsional modes with the respective deformed shape are represented in Figure 3-18 as well as the final complex mode. Observing the individual and resulting complex mode displacement distribution, the main throat has an axial and rotational displacement node and, therefore, the highest stress combination.

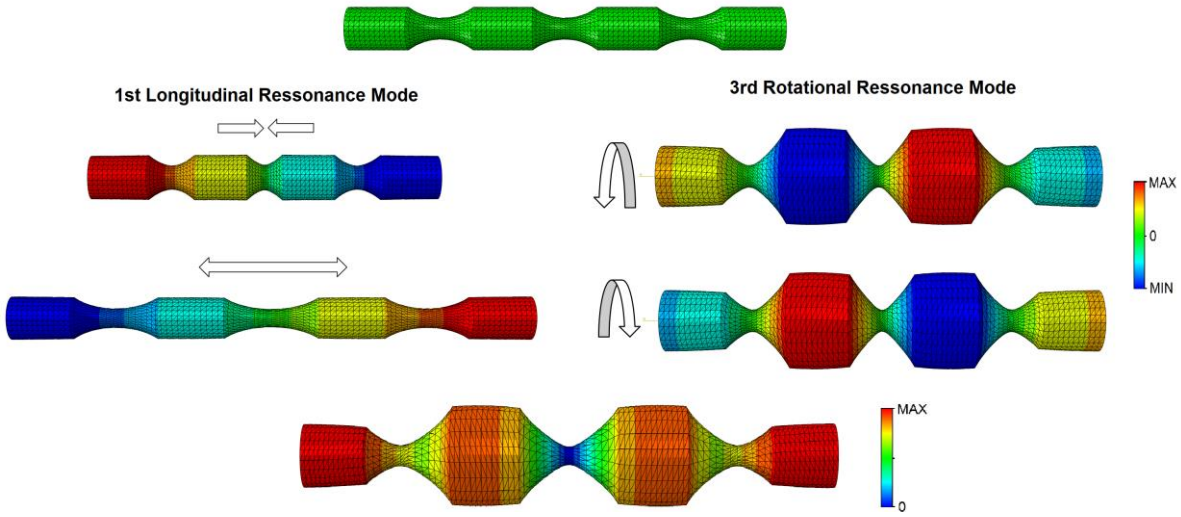

Figure 3-18. Three throated specimen mode shape displacement magnitude and deformed representation for the first longitudinal mode; third torsional mode, and the resulting complex resonant mode.

A more detailed explanation of the tension-torsion specimen concepts and how the specimen shape influences the resonant modes is afterwards made with associated FEA results. From all followed concepts, new improvements were made that allow for different tension-torsion ratios.

3.4.1.3 Multiaxial tension-torsion setup

A full description of the complete setup follows the established base concept of all designed tension-torsion main components. The present tension-torsion ultrasonic machine setup components are attached in the following sequence: axial piezoelectric transducer; booster; multi-horn; three throated specimen.

The booster is the same as the one applied in the tension-compression ultrasonic setup. It serves as a first axial displacement amplification of the piezoelectric transducer. The booster axial displacements will excite the multi- horn in a desired resonant mode that partially transforms the received axial displacement to rotation. The booster multi horn setup resonant Mode of Interest (MI) is presented in Figure 3-19 with the axial (U_y) and rotational (U_r) displacement amplitudes. The rotational displacement (U_r) is taken by cylindrical coordinate system.

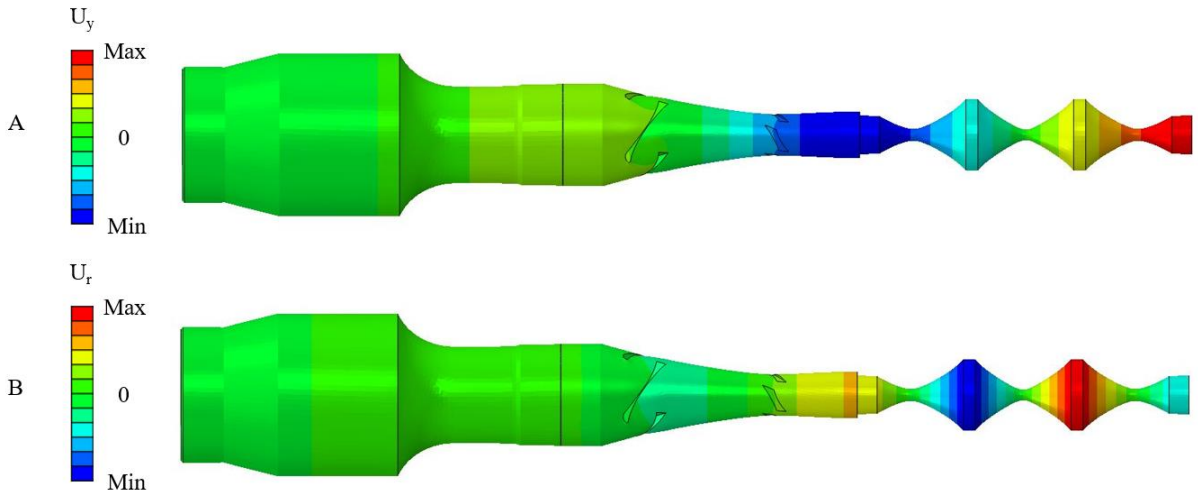

Figure 3-19. FEA tension-torsion resonant Mode of Interest (MI): (A) axial displacement distribution (U_y); (B) rotational displacement distribution (U_r).

The displacement combination at the end of the multi-horn excites the specimen in the mentioned two resonant modes of interest. The rotation and axial displacement multi-horn ratio will influence specimen final shear and axial stress ratio. The resulting associated behaviour will be discussed in detail in the following FEA in-depth analysis of the tension-torsion ultrasonic setup. The final theoretical displacement and stress distribution of the tension-torsion setup is shown in Figure 3-20.

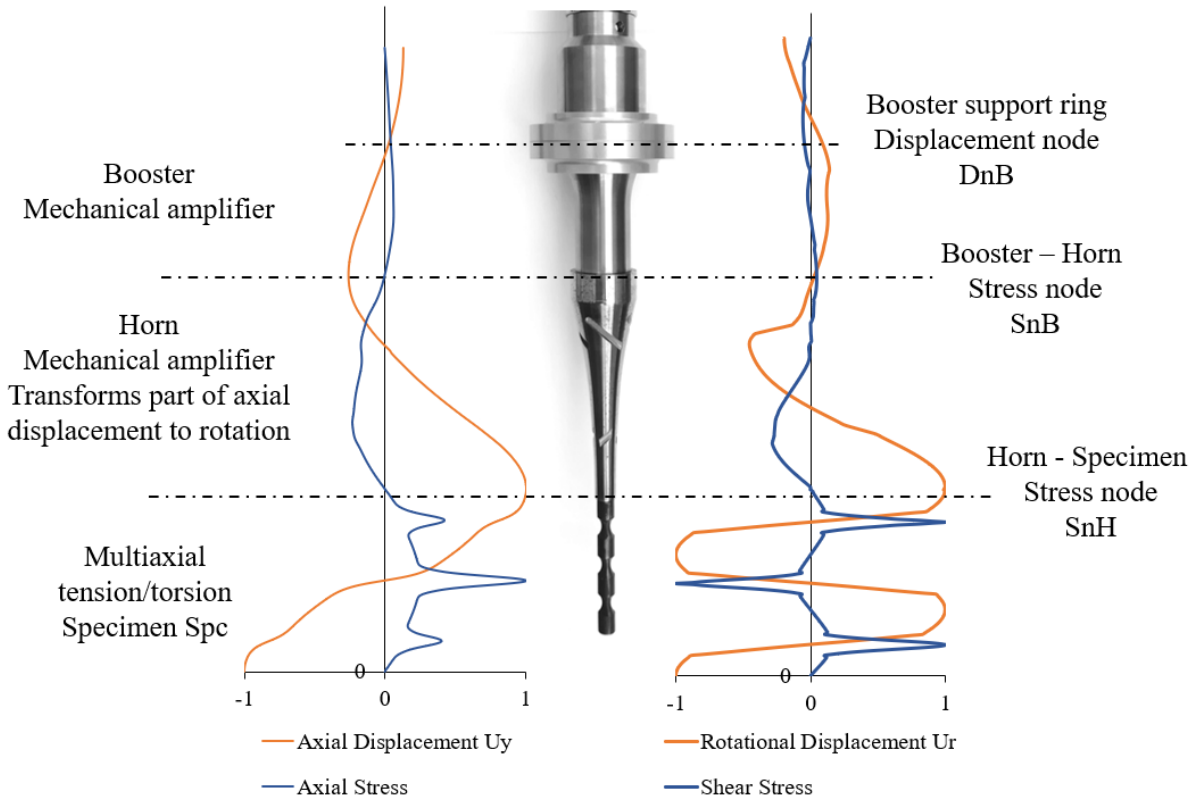

Figure 3-20. Numerical representation of the axial and rotation displacements and corresponding axial and shear stress throughout the first specimen design of the multiaxial ultrasonic fatigue test machine.

The setup is supported by the Booster support ring where the booster displacement node (DnB) is located. Just as both discussed uniaxial tests, tension-compression and pure torsion, temperature control is required as well as a measuring method at the free base. The control and measurements followed across all tension-torsion ultrasonic tests are discussed in detail in the respective methodology subchapter 4.4.3.

3.4.2 FE Analysis

In this section, the FE analysis method and the obtained results are discussed. FEA was conducted to the specimen and all ultrasonic components alone before attaching the complete setup. Regarding the applied multi-horn, since Costa master thesis [194] has already focused on the multi-horn developments and its complex resonant behaviour, this study only briefly discusses its main parameters and intricacies.

The first ultrasonic tension-torsion tests were conducted with Mario Vieira et al. [85] setup. As previously discussed, the first setup showed fundamental working issues that need to be solved. To reach a fully working and improved tension-torsion machine, FE analysis of both the tested setup (no specimen), the first specimen alone (no setup) and the first specimen within the setup were required.

3.4.2.1 The Booster Multi-horn setup (no specimen)

The multiaxial setup FE modal frequency analysis and the resulting excitation from the unitary force steady-state modal analysis were first computed without the specimen. From the free-free boundary conditions FE ABAQUS frequency modal analysis, the booster multi-horn setup presented a 20014 Hz for the resonant MI to be excited. Other resonant modes were present within the 18.5 to 21.5 kHz analysed frequency range. Table 3-5 presents the obtained resonant modes from the free-free modal frequency numerical analysis.

Table 3-5. Booster Multi-Horn tension-torsion ultrasonic fatigue setup FEA free-free modal frequency result.

Booster Multi-Horn setup

Resonance Mode	**Frequency [Hz]**
Bending	19112
Mode of Interest (MI)	20014
Parasite Mode (PM)	20542

Table 3-5 presents three resonant modes obtained within the established frequency range (18.5 to 21.5 kHz): a bending mode; the resonant Mode of Interest (MI) to be excited towards the desired fatigue stress state; and a denoted Parasite Mode (PM). The PMs are here established as a resonant mode with close frequency proximity with a mode shape somewhat coherent with the transducer axial cyclic displacement. PM modes may affect the final excitation MI mode shape induced to the specimen, and, therefore, change the desired fatigue stress state. Further FEA computation through steady-state modal analysis allows to better understand if the detected PMs can reach considerable amplitude through the transducer axial excitation, and if so, will they influence the MI towards an unwanted/unreliable ultrasonic fatigue test.

Showing an approximate 20 kHz MI resonance frequency, the steady-state modal analysis with a unitary force was then computed. In this numerical analysis, a 1 Newton [N] cyclic total force is applied as a pressure in ABAQUS, meaning a uniformly distributed force with a sum of 1N. The applied force is uniformly distributed across the transducer booster connection base. The requested frequency steady-state response was again between 18.5 and 21.5 kHz. The resulting rotational and axial amplitude magnitude and phase are plotted in Figure 3-21 for the established frequency range.

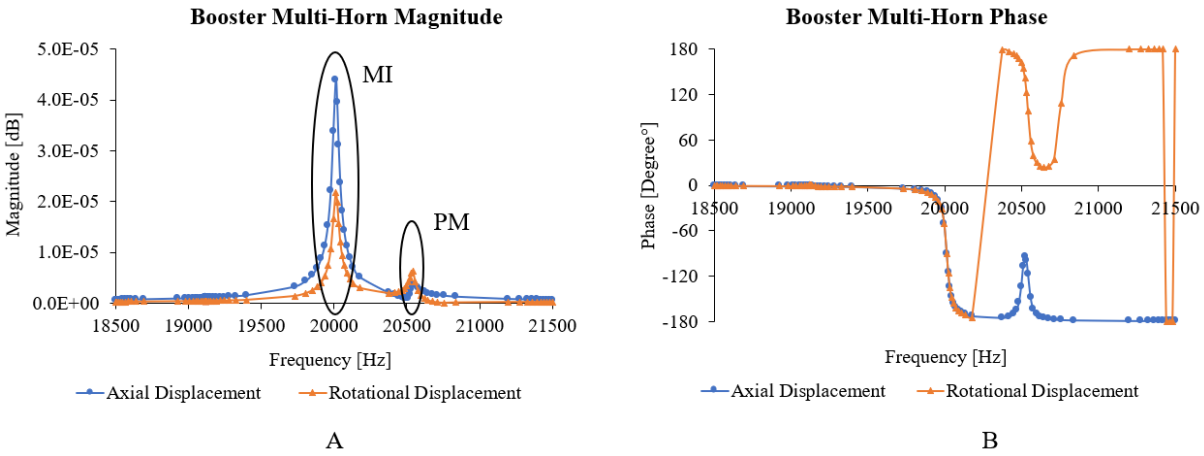

Figure 3-21. Booster multi-horn setup axial and rotational displacement magnitude(A) and phase (B) between 18.5 kHz and 21.5 kHz.

Figure 3-21 identifies two of the three Table 3-5 resonant modes within the analysed frequency range, MI at 20014 Hz and a PM at 20542 Hz. The observed displacement magnitude of the two identified resonant modes proves their ability to be excited through the axial force applied to the booster. For MI, a 0.5 rotation/axial displacement ratio was obtained at the horn/s tip where the specimen will be attached.

Contrarily to a tension-compression setup, the multi-horn setup allows for the excitation of rotational resonant modes due to the slit multi-horn shape. Just as the multi-horn can induce rotation from axial displacement, rotation also induces axial displacement. Therefore, all rotational resonant modes will now have an axial displacement aspect. This present axial displacement allows for predominate rotational resonant modes excitation from axial cyclic force. Since the axial displacement of this PM mode is not predominant, its amplitude is not as considerable as for the MI with the same unitary excitation force. The MI axial and rotational displacement magnitude at the horn's tip is 12 and 3.5 times higher than PM, respectively. Figure 3-22 shows the PM mode shape with the axial and rotational displacement distribution.

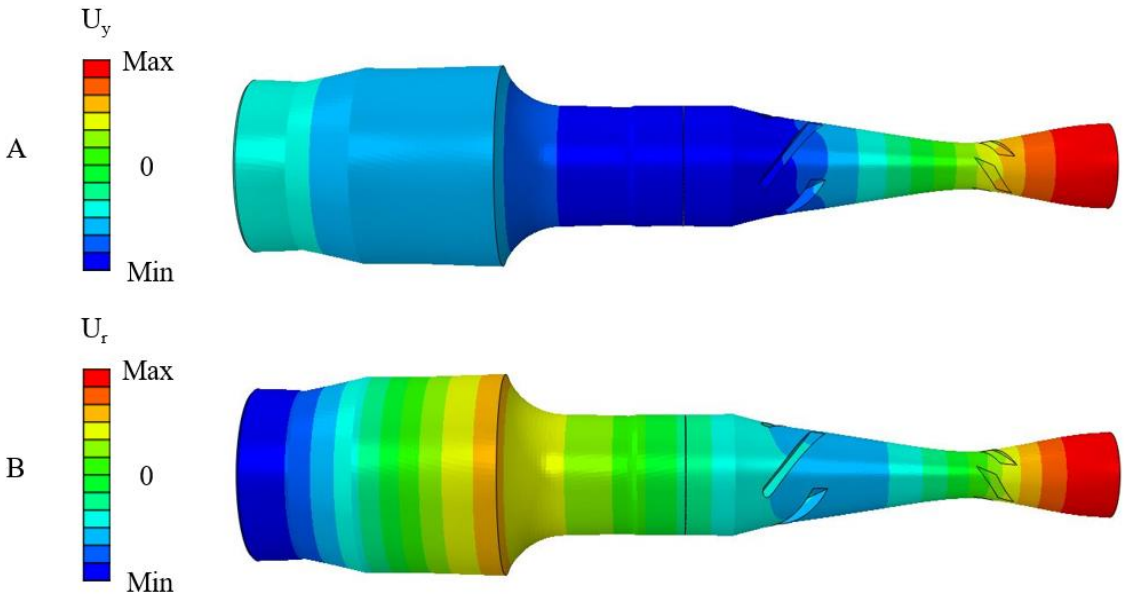

Figure 3-22. Booster multi-horn setup PM mode shape displacement distribution: (A) axial displacement (U_y); (B) rotational displacement (U_r).

As it can be observed in Figure 3-22, PM axial displacement distribution is similar to the MI with a non-zero amplitude at the booster transducer base. Such axial distribution shows the ability to be excited by the cyclic axial force applied to the booster.

Again, since the steady-state analysis tries to replicate the transducer excitation and the experimental frequency scan analysis, Figure 3-21 obtained result shows that with the booster multi-horn setup, only the mode of interest will be present within the transducer working frequency range. PM may be present inside the frequency range if its resulting experimental frequency is lower than the obtained 20542 Hz. The experimental frequency scan proved no PM mode within the transducer frequency range.

Different specimens were then added to the setup that meets the resonance defined ultrasonic component parameters. Being the AISI P20 steel the material applied in this study, several different geometries were created and numerically analysed. However, before the new specimens were created and introduced in the FE software, Mario's specimen was studied in-depth alone and within the presented booster multi-horn setup.

3.4.2.2 First multiaxial three throated ultrasonic specimen

As briefly aforementioned, the first and all subsequently tested tension-torsion specimens were designed with three throats to reach a 20 kHz longitudinal and third torsional resonant mode. Mario's specimen was machined from a common construction steel (E= 200 GPa, ρ= 7800 kg/m^3). The obtained FEA Abaqus free vibration frequencies for longitudinal and torsional modes of the first designed specimen alone are presented in Table 3-6.

Table 3-6: Longitudinal and torsional resonance FEA frequencies of the first designed and tested multiaxial ultrasonic specimen.

First Tension-Torsion Specimen

Resonance Mode	**Frequency [Hz]**
1º Torsional	8816
2º Torsional	17562
3º Torsional	20092
1º Longitudinal	20121
2º Longitudinal	40039

The specimen shows frequency similarity between the two resonance modes of interest. Comparing Table 3-4 uniaxial AISI P20 obtained resonant frequencies with the Table 3-6 multiaxial common construction steel specimen, the third torsional, the second longitudinal, and remaining torsional modes had frequency reduction. This behaviour is related to the newly created throats that reduce the stiffness in the mode's displacement nodes, thus reducing the associated frequency.

The first multiaxial specimen followed certain ratios between Figure 3-14 key dimensions to achieve working specimens. The different specimen sections tracked the rotational wavelength propagation of the third torsional mode. The present study proved that the believed necessary specimen section dimension ratios were not required.

The first specimen dimensional concept follows the displacement wavelength. The wave has: four maximum displacement amplitude sections (four stress nodes), and three no displacement sections (displacement nodes). The stress nodes are located at the extremities and in between throats; the displacement nodes are at the smallest area cross-sections; The resulting wavelength: between the extremities and the secondary throats there is a quarter wavelength; between the secondary throats and the main throat, there is half a wavelength.

From the described wavelength pattern, the length dimension between throats (half wavelength) should be double the length between secondary throats and the extremities (quarter wavelength). Figure 3-23 shows the wavelength and specimen's dimensions relation being a quarter wavelength the dimension A.

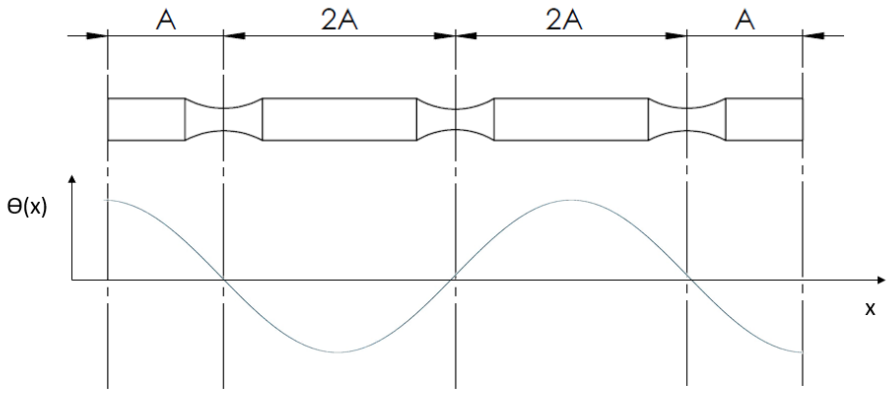

Figure 3-23. Rotational waveform established relationship representation across the multiaxial specimen length.

The resulting wavelength displacement is always in equilibrium, meaning that Figure 3-23 displacement sum is null. With the followed profile, the torsional mode shear stress is theoretically equal in all three throats. With the one longitudinal displacement mode at the main throat, the highest stress combination would theoretically always be at the main throat. The numerically obtained by the present study FEA free-free modal frequency analysis normalized distribution of the rotational and axial displacement, and resulting shear and axial stress across the first three throated specimen is shown in Figure 3-24.

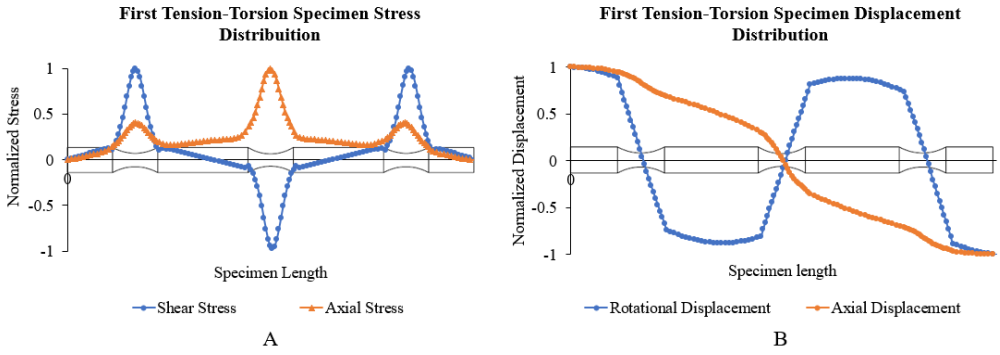

Figure 3-24. First tension-torsion specimen displacement (A) and stress (B) distribution across its length.

Figure 3-24 FEA results of the stress distribution show a similar shear stress amplitude in all three throats and a higher tension-compression stress amplitude at the main throat.

Figure 3-23 rotational wave and Figure 3-24 rotational displacement and shear stress distributions show apparent similarity to the pure torsion specimen. A three throated specimen following the dimensional rule and with equal three throats is, in fact, three 20 kHz pure torsion specimens in sequence. Combined, they will have a 20 kHz torsional resonance frequency with all three rotating sequentially in opposite rotation phases. Mario's specimen does not have the same Tr in all three throats (Figure 3-14). This results in a combination of pure torsion specimens with different but with an average of 20 kHz. Figure 3-25 presents the conducted FE frequency analysis of the pure torsion 20 kHz specimen concept for the first specimen. Since it follows the established wave propagation rule, the L1 length is equal in all three specimens, only the R_1 (Tr) value changes.

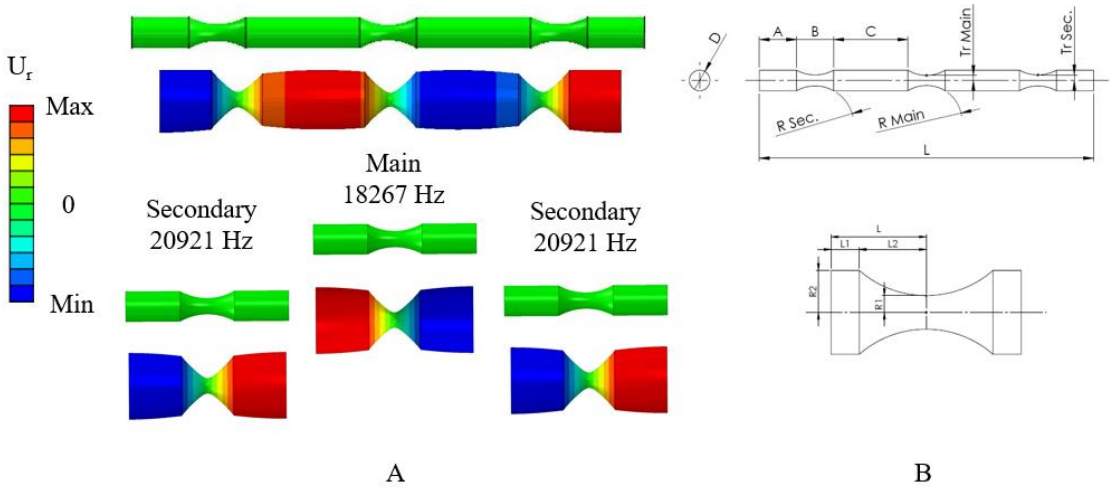

Figure 3-25. Three sequential pure torsion specimens concept with FEA frequency results and rotational displacement (U_r) distribution.

Because of the lower main throat Tr, a lower rigidity is obtained and, therefore, a lower torsional frequency. The average frequency between all three pure torsion idealised specimens is 20036 Hz. This is, as predicted, very close to the final three throat specimen 3º torsional resonant mode (Table 3-6).

When machined and tested, the specimens would only show the predicted behaviour if the established dimensions and shape were rectified with high enough precision that guaranteed the slightest frequency difference of both modes to the booster multi-horn frequency. Strain gauge measurements proved the exciting multiaxial tension-torsion stress state at both the secondary and main throats [195]. Most specimens showed higher temperature generation at the secondary throats and the horn specimen connection region. Only one specimen proved an as predicted higher stress in the main throat.

A sensitivity analysis was conducted to perceive the specimen dimensional influence. Dimensional changes to the specimen were made to all key dimensions (A, B, C, and Tr). Each dimension was altered in equal and symmetrical values alone to quantify their overall impact on the frequency (A ±1 mm; B ±1mm; C ±1mm; Tr ±0.05 mm). The resulting frequency changes for the torsional and longitudinal modes are presented in Table 3-7. Table 3-7 blue mark indicates non-altered key dimension. The constant radius sections R was not changed.

Table 3-7. First tension-torsion specimen dimension to frequency sensitivity analysis results.

First Specimen Dimensions [mm]					**Resonance Frequency [Hz]**	
A	**C**	**B**	**$Tr_{Main\ Throat}$**	**$Tr_{Secundary\ throat}$**	**3º Torsional**	**1º Longitudinal**
12.15	24.3	12.15	1.64	1.8	20092	20121
12.15	24.3	12.15	1.7	1.85	20966	20368
12.15	24.3	12.15	1.6	1.75	19316	19939
13.15	24.3	12.15	1.64	1.8	19790	19690
11.15	24.3	12.15	1.64	1.8	20440	20574
12.15	25.3	12.15	1.64	1.8	19849	19841
12.15	23.3	12.15	1.64	1.8	20351	20408
12.15	24.3	13.15	1.64	1.8	19536	19539
12.15	24.3	11.15	1.64	1.8	20902	20740
Frequency Range (Max-Min)					1650	1201

Tr is the only dimension that, when increased, so does the frequency. Higher Tr values increase the rigidity and, therefore, higher frequency. Tr has the most significant influence on the specimen torsional frequency, while B affects the longitudinal frequency. The third torsional mode higher sensitivity becomes apparent by comparing the frequency changes and range between both modes. Figure 3-26 plots the Tr dimension with the resulting frequency of both modes.

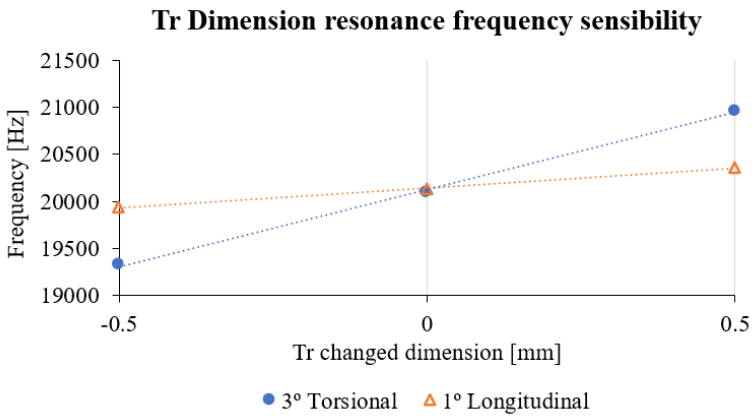

Figure 3-26. Tr dimension influence on longitudinal and torsional resonant modes frequency for the first tension-torsion specimen.

When observing specimen frequency sensitivity and the effect on the stress distribution, it becomes clear that the main issue revolves around specimen rotation. Torsional frequencies are associated with a lower stiffness/mass ratio resulting in smaller pure torsion specimens, more sensitive to dimensional changes. Considering AISI P20 ultrasonic specimens (Figure 3-3 and Figure 3-12), ± 1 mm change in constant radius section L_1 has a ±460 Hz frequency change for tension-compression and ±2535 Hz on pure torsion. Also, three throated specimens have one high deformation region (stiffness associated region) for the longitudinal resonant mode, but the torsional resonance has in all three throats, which means that it relies intensely upon all three throat dimensions.

How specimen frequency differences influence the final induced stress combination can only be predicted and comprehended by the complete setup FEA. The frequency difference between the setup and the specimen's frequency leads to a wave propagation adjustment and deformation profile change. Therefore, the setup resonance frequencies and the resulting deformation across all nearby 20 kHz frequencies must observe.

3.4.2.3 Ultrasonic tension-torsion setup with first multiaxial specimen

The inclusion of Mario et al. [91] specimen to the setup was studied through FEA free vibration frequency and steady-state modal analysis. Both analyses were computed between 18.5 – 21.5 kHz. Again, a unitary axial force was applied in the booster for the steady-state modal analysis. Figure 3-27 shows the steady-state analysis rotational and axial displacement magnitude and phase results taken from the specimen's free base.

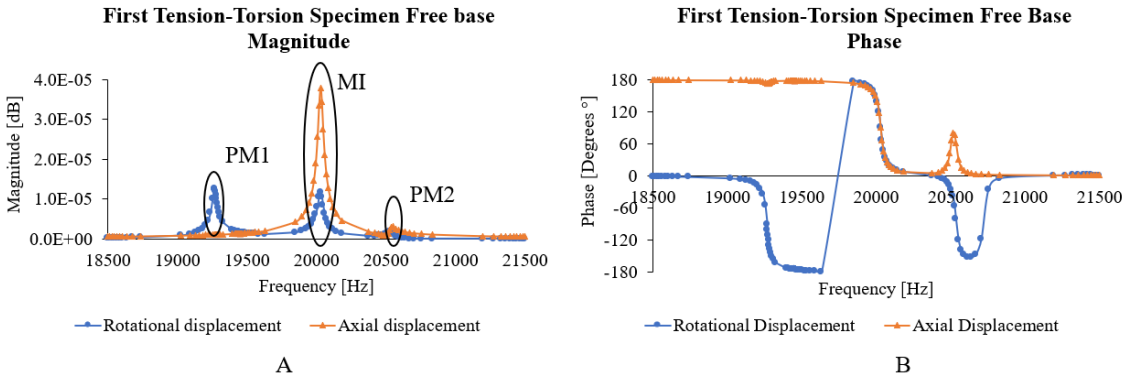

Figure 3-27. Booster multi-horn first specimen setup, free base axial and rotational displacement magnitude (A) and phase (B) between 18.5 kHz and 21.5 kHz.

The shear and axial stress magnitude at the main throat across the same frequency range was also observed from the steady-state modal FEA. Figure 3-28 plots the resulting shear and axial stress magnitude. Both Figure 3-27 and Figure 3-28 identify the excited resonance modes.

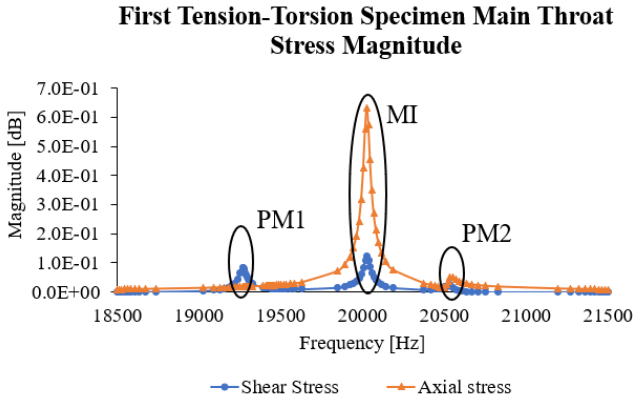

Figure 3-28. Booster multi-horn Mario's specimen setup, main throat shear and axial stress magnitude between 18.5 kHz and 21.5 kHz.

The steady-state results present the excitation of two parasite resonant modes with close frequency proximity to the MI. Obtained bending resonant modes from free vibration frequency analysis had a non-existent excitation magnitude. The denoted PM1 has a lower frequency and the second PM2 has a higher frequency in relation to MI. All proven excited modes presented both axial and rotational displacement. Both PM1 and PM2 have an opposite displacement axial and rotational phase to the MI. Figure 3-29 shows a representation of the three identified resonant modes with the axial and rotational displacement distribution.

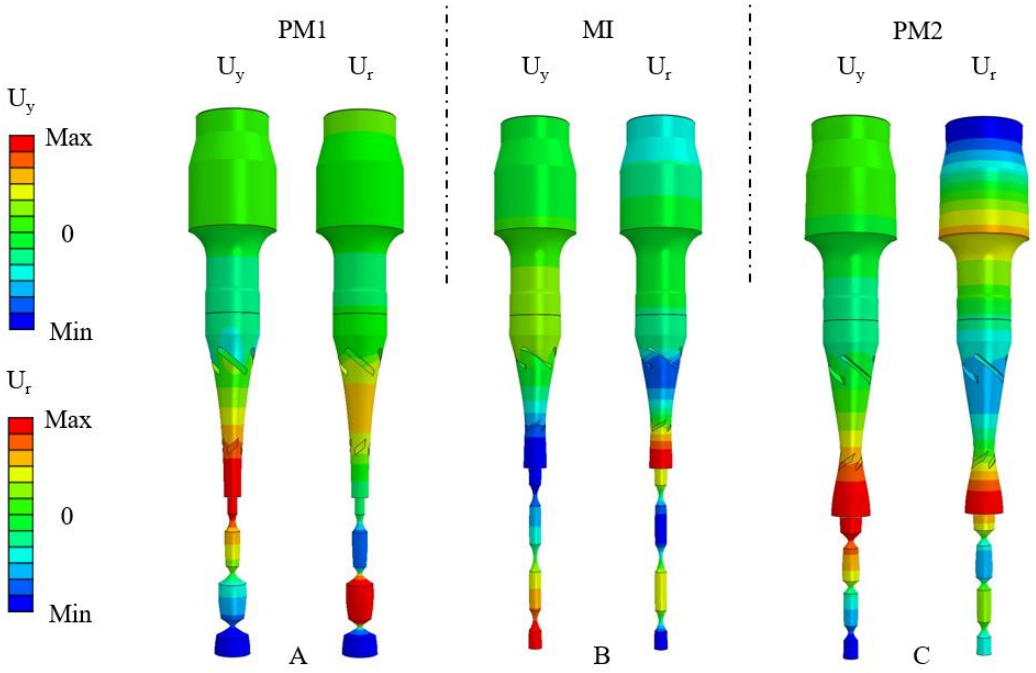

Figure 3-29. Booster multi-horn first specimen setup mode shape U_y and U_r displacement distribution of PM1 (A), MI (B), and PM2 (C).

As predicted, MI presents both axial and rotational displacement, resulting in a shear axial stress combination. With the last machined and tested multi-horn setup here applied in this study, a 0.19 shear/axial stress ratio was obtained. The numerically obtained low shear axial stress ratio with the final ultrasonic multiaxial setup occurs due to a reduction in rotational displacement amplitude in relation to the axial displacement. The lower displacement rotation/axial ratio of the final multi-horn was designed taking the new specimen geometries into account. Such resulted in a lower required rotation to induce the desirable stress ratios on the new specimen design. This also reduced the multi-horn stress combination amplitude at the slits, securing fatigue damage across all conducted UFT.

Both PMs and MI have a stress node (high displacement location) at the free base of the specimen. This region will serve as an excitation magnitude comparison between PMs and MI. Therefore, the free base will be a crucial experimental measuring location for all tested specimens, enabling a direct comparison with all FEA results. The modal frequency FEA and steady-state results comparing all three resonant modes are presented in Table 3-8.

Table 3-8. FEA modal frequency and steady-state results for the complete tension-torsion ultrasonic setup with the first multiaxial specimen.

Tension-Torsion setup with the first tested Specimen

Resonance Mode	FEA Modal Frequency [Hz]	Steady-State Frequency [Hz]	Ur/Uy ratio	Stress Shear/Axial ratio	MI/MP Ur Magnitude	MI/MP Uy Magnitude
PM1	19267	19266	11.74	4.6	0.93	35.32
MI	20028	20028	0.31	0.193	-	-
PM2	20534	20535	0.62	0.48	6.29	12.63

Through modal shape axial and rotational displacement distribution analysis, PM2 comes directly from Figure 3-26 booster multi-horn PM torsional resonant mode. In PM2, the multi-horn has an inverse behaviour of what it was meant (rotation to axial displacement and not axial to rotation). Such low axial displacement allows for its excitation through the cyclic force applied to the booster. PM2 has a considerably lower excitation magnitude in comparison with MI. With the applied unitary cyclic force, MI has 6 times the rotational magnitude and 12/13 times the axial magnitude at the specimen's free base.

PM1 appears only with the attachment of a specimen to the setup. PM1 displays key similarities to MI. PM1 has one less rotational displacement node throughout all setup, meaning it can be described as the previous resonant mode from MI. Just as PM2, PM1 has an overall dominant rotational displacement. However, contrarily to PM2, the rotational displacement is focused on the specimen. This results in the highest stress combination being located at the lower secondary throat. Since rotation is the dominant deformation, considerable higher shear stress is present, resulting in the high 4/5 stress ratio observed in Table 3-8. PM1 excitation magnitude is overall lower than MI. Even with a 35 times lower axial magnitude, the rotation magnitude at the free base is similar to MI, proving the high induce rotation in the specimen by PM1.

Knowing the ability of PMs to be excited through an axial cyclic force in the booster and their possible influence, a sensitivity analysis was afterwards conducted. For comparison purposes, the same altered dimensions (A, B, C, Tr_{Main}, $Tr_{Sec.}$) and respective amplitudes as in Table 3-7 specimen frequency dimensional sensitivity were applied. Table 3-9 presents for each tested dimensional combination, PMs and MI frequencies, MI shear/axial stress ratio at the specimen's main throat, and displacement ratio at its free base.

Table 3-9. Booster multi-horn first tension-torsion specimen setup, dimension to frequency sensitivity analysis results.

First Specimen Dimensions [mm]					Resonance Frequency [Hz]			MI Stress ratio	MI Disp. Ratio
A	**C**	**B**	**Tr_{Main}**	**$Tr_{Sec.}$**	**MI**	**PM1**	**PM2**	**Shear/Axial**	**Free base**
12.15	24.3	12.15	1.64	1.8	20028	19267	20534	0.193	0.310
12.15	24.3	12.15	1.7	1.85	20127	19998	20548	2.164	5
12.15	24.3	12.15	1.6	1.75	20002	18543	20529	0.107	0.125
13.15	24.3	12.15	1.64	1.8	19971	18963	20528	0.159	0.209
11.15	24.3	12.15	1.64	1.8	20086	19620	20542	0.278	0.572
12.15	25.3	12.15	1.64	1.8	19991	19042	20530	0.147	0.223
12.15	23.3	12.15	1.64	1.8	20066	19505	20539	0.276	
12.15	24.3	13.15	1.64	1.8	19950	19173	20525	0.105	0.129
12.15	24.3	11.15	1.64	1.8	20138	19990	20550	1.207	2.717
Range (Max – Min)					188	1455	25	2.059	4.875

Table 3-9 results show a non-desired high stress and displacement ratio variability. The stress ratio should not deviate as much since it impedes a constant and replicable fatigue multiaxial testing research execution. PM2 has a negligible frequency change throughout all made dimensional combinations. Therefore, PM2 has low-frequency dependence on both the specimen's longitudinal and torsional resonance.

On the other spectrum, PM1 has the most frequency change. The PM1 frequency range is parallel to the specimen sensitivity change analysis. This implies that PM1 is more frequency dependent on the specimen's resonance than the remaining setup. This is in line with the observed dominant specimen shear deformation on PM1 modal shape.

When PM1 has a close 20 kHz frequency, MI presents high shear stress in the lower secondary throat. This results in fatigue testing region shift towards the lower secondary throat since its stress combination becomes higher than the main throat.

3.4.2.4 New specimen concepts

Concerning the redesigning tension-torsion specimen, four main objectives were tackled: reduce the high specimen **dimensional sensitivity**; ensure the **higher stress combination at the main throat (fatigue testing region)**; enable a specimen geometry change for achieving **different shear/axial stress ratio;** reach a straightforward **analytical/ numerical geometry design method** for a working 20 kHz tension-torsion specimen.

To guarantee a **maximum stress combination in the main throat** its torsion shear stress was intended to be considerably increased in relation to the secondary throats. A significant shear difference between throats would always guarantee a higher stress combination in the main throat. It was also thought that a higher main throat torsion deformation could reduce the stress ratio variation from specimen to specimen. The frequency associated torsion stiffness would then be more dependent on one throat instead of being equally dependent on the existing three. Therefore, to have higher shear stress in the main than the secondary throats not only self-guards the main throat as the one single fatigue testing region, but it might improve the **dimensional specimen sensitivity.**

The shear stress increase was made possible by reducing the in-between throat sections length. This meant overthrowing Figure 3-23 wave propagation to section length made associations. The concept is to compress the rotational wave propagation in-between throat sections. Therefore, the constant radius sections between throats will have higher rotation leading to higher induced shear stress in the main throat. Figure 3-30 shows the displacement and stress distribution for a reduced length constant radius in-between throat sections.

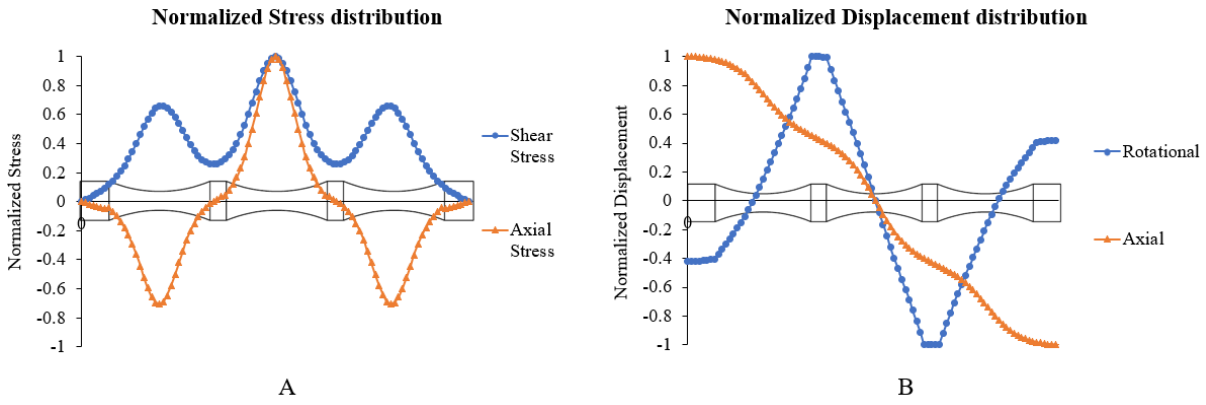

Figure 3-30. FEA normalised stress (A) and displacement (B) distribution of a three throat specimen with the newly established sections.

FEA shows a clear difference in torsion rotation between constant radius sections. Considerably higher shear stress is now induced on the main throat. The axial stress and displacement do not noticeably change distribution tendency and amplitude between throats.

The improved specimen was made with equal throats simplifying any new geometry design. The final geometry has five design variables (A, B, C, D, Tr). Figure 3-31 represents the new specimen geometry and respective variable acronyms. Dimension B, Tr, and R have associated values, meaning the R dimension can be determined with B and Tr. The dimension R can be determined by equations (3.2) and corresponding solution (3.3).

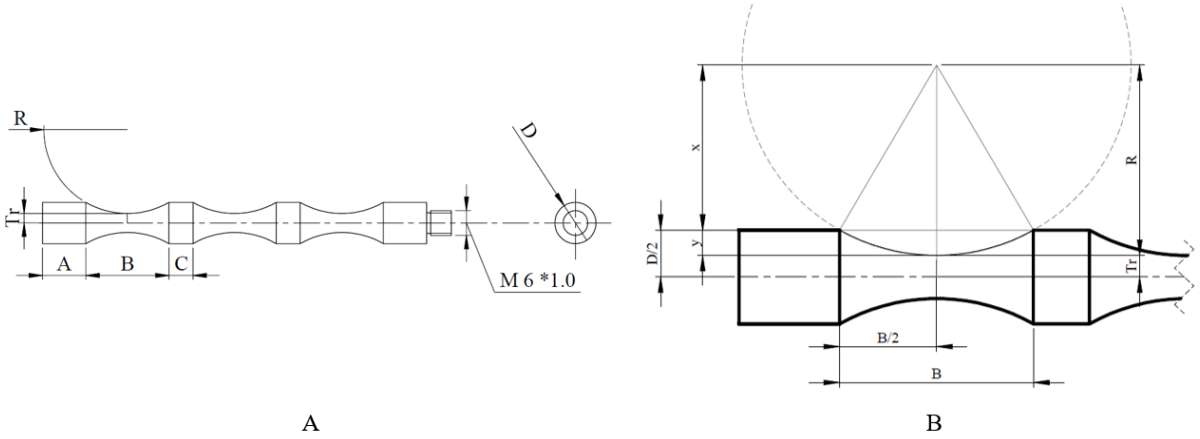

Figure 3-31. Multiaxial specimen: (A) Dimension variables acronyms for the multiaxial specimen; (B) Geometric throat constraints.

$$\begin{cases} \frac{D}{2} = Tr + y, D = 10 \\ y = R - x \\ x = \sqrt{R^2 - \left(\frac{B}{2}\right)^2} \end{cases} \tag{3.2}$$

$$R = \frac{Tr^2 - TrD + \frac{B^2 + D^2}{4}}{D - 2Tr} \tag{3.3}$$

A, B and C are the lengths of each section, D is the cylindrical bodies diameter, which was re-established as 10 mm (equal to the applied in uniaxial specimens), R is the radius of the hourglass shape, and Tr is the throat smallest cross-section radius.

Between materials and research objectives, there are different stress combinations of interest. Hence, the ability to change the **Tension-Torsion stress ratio** was one primary objective when redesigning the specimen. Before this study, the only known method believed possible was to change the axial/rotation ratio induced by the multi-horn. A different multi-

horn for different stress ratios of interest would be impractical and expensive. The demonstrated capability to manipulate the shear distribution showed it was possible to achieve stress ratios without changing the horn.

Several specimens were designed and tested with different throat B and Tr combinations to describe how the stress shear/axial ratio varies and its main variables. All such specimens were under FEA alone and with the complete setup. Three specimens were chosen to conduct further in-depth FEA and to be experimentally tested. All experimental results were compared with the obtained numerical. The chosen geometries shown in Figure 3-32 have diverse B and Tr combinations for widespread overall behaviour comparison.

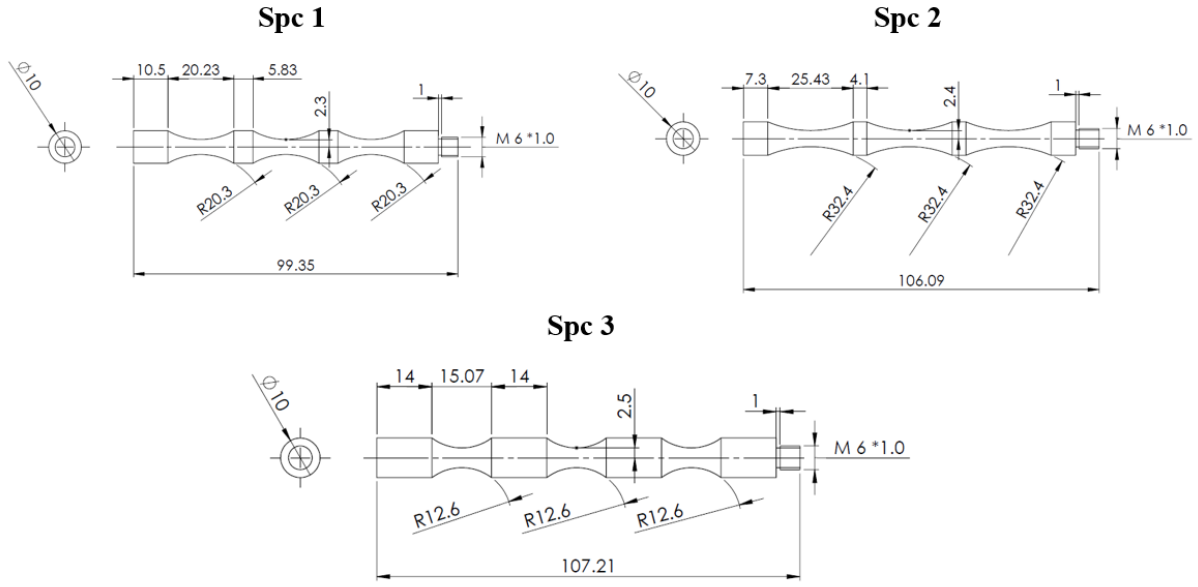

Figure 3-32. Chosen and machine Tension-Torsion new specimens (Spc*x*).

Only Spc2 results are fully shown to simplify the in-depth FEA presentation. Spc1 and Spc3 are discussed throughout the analysis, and the complete results are presented in Annex 2. Figure 3-32 specimens underwent the same sensitivity analysis conducted to Mario's specimen. The same dimensional variation was imposed on all four key dimensions (A, C, B, and Tr). Table 3-10 presents the Spc2 resulting frequency changes for each dimension combination.

Table 3-10. New Spc2 tension-torsion specimen dimension to frequency sensitivity analysis results.

Spc2 key Dimensions [mm]				Resonance Frequency [Hz]	
A	**C**	**B**	**Tr**	**3º Torsional**	**1º Longitudinal**
7.3	4.1	25.43	2.4	19992	20002
7.3	4.1	25.43	2.45	20588	20212
7.3	4.1	25.43	2.3	19371	19777
8.3	4.1	25.43	2.4	19847	19365
6.3	4.1	25.43	2.4	20170	20696
7.3	5.1	25.43	2.4	19164	19772
7.3	3.1	25.43	2.4	20968	20233
7.3	4.1	26.43	2.4	19414	19472
7.3	4.1	24.43	2.4	20585	20554
Frequency Range (Max-Min)				1804	1331

Spc2 and Spc1 proved a slightly higher frequency change in both modes when compared to the first specimen. For Spc3, a minor frequency change was observed. No dimensional sensitivity change conclusion can be withdrawn from the minor differences between Spc and the first specimen. By comparing first specimen Table 3-10 with the new specimens, the overall mm to Hz influence on both modes has changed. Figure 3-33 compares the first specimen with Spc2 for each dimension frequency influence over third torsional mode separately.

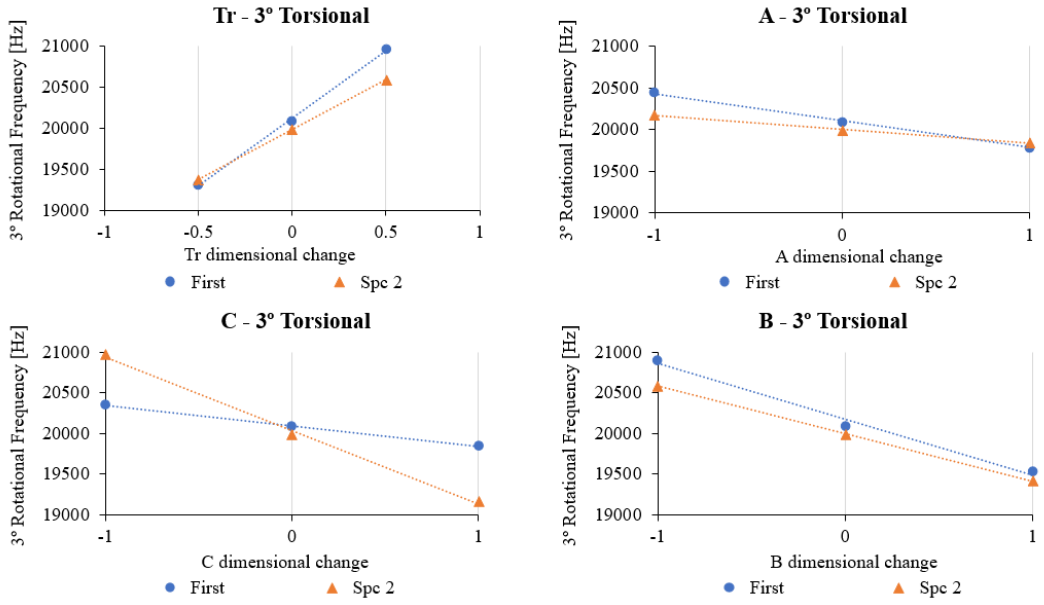

Figure 3-33. First and Spc2 dimensional frequency effect comparison.

As expected, there was a reduction in the Tr influence from the first to the new specimens. Still, Tr has the most significant mm to Hz influence. One crucial observation is the change in the dimensional sensitivity associated with the C section. Spc1 and Spc2 have a considerably higher rotational concentration at the C section. Consequently, this dimension now has a more profound impact on the overall torsional frequency. Spc3 lower C frequency change occurs due to the higher C dimension. It reduces C section rotation concentration resulting in an in-between behaviour to the first and Spc1 and Spc2.

A **new analytical/ numerical geometry design methodology** was studied with the acquired modal behaviour knowledge. As previously presented, both uniaxial and pure torsion have an analytical method to reach a working 20 kHz specimen. The method can be easily implemented to reach a working base geometry. Achieving a proven analytical method for preparing and executing a given fatigue test is to standardize it. This is the primary goal of any multiaxial ultrasonic method discussed in this study. The analytical method for both uniaxial and pure torsion ultrasonic specimens, and the here described for a three throat specimen geometry prediction and associated shear/axial stress ratio are sequentially presented step by step in Annex A1.

The first and further tested specimens, as the multiaxial test conducted by Henrique et al. [196] to railway wheel steel, were obtained iteratively by FEA. This meant readjusting all dimensions towards a final 20 kHz solution. Such a method required considerable time and knowledge on the individual dimension effect in each of the two resonant modes of interest. The method is impractical and not standardizable.

When following Figure 3-23 dimensional rule, the multiaxial specimen was proven to be, in fact, three equal and sequential pure torsional specimens (Figure 3-25). Therefore, the pure torsion analytical method could determine the respective torsional specimens. With the applied change to the C section length, the specimen is no longer equivalent to three 20 kHz sequential pure torsional sets. To transfer the pure torsion 20 kHz analytical method again, we need to observe node by node (both stress (Sn) and displacement (Dn)) for only half the specimen. Figure 3-34 presents the rotational displacement distribution for half the specimen's length with all nodes identified, three different divided sections (Ts), and relevant dimension designations.

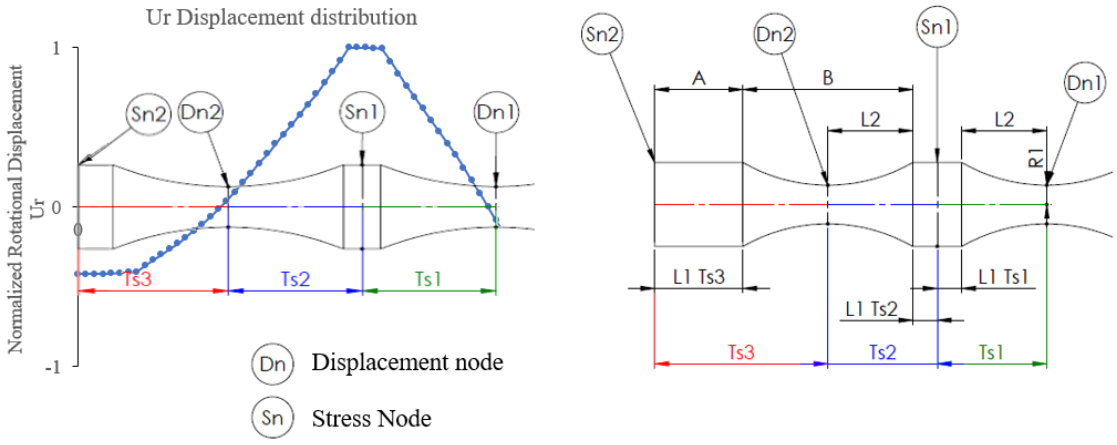

Figure 3-34. Half a three throated new specimen rotational displacement distribution with stress and displacement nodes identification, key dimension designations, and three pure torsion section Ts.

The Ts-sliced half specimen sections were attributed to pure torsion specimens. The main throat section (Ts1) was proven to be a 20 kHz specimen. Meanwhile, the two secondary throat sections (Ts2 and Ts3) were associated with two pure torsion specimens with a combining 20 kHz mean frequency. Ts2 with a lower constant radius section ($L_{1,\ Ts2}$) has a higher than 20 kHz frequency, while Ts3 has a lower than 20 kHz frequency with a lengthier constant radius section ($L_{1,\ Ts3}$). Then non 20 kHz frequency of Ts2 and Ts3 can be linked to the lower rotation and the lower shear-induced stress in the secondary throats.

$L_{1\ Ts2}$ and $L_{1\ Ts3}$ can be analytically determined from the pure torsional analytical solution. The difference is in equation (2.3) applied frequency, *f*. The method remains the same, only the assigned frequency changes. Different combinations of Ts2 and Ts3 frequencies are possible. One example is to combine *f*=24000 Hz for Ts2 and *f*=16000 Hz for Ts3.

Unfortunately, a 20 kHz first longitudinal frequency cannot be guaranteed considering a three pure torsion 20 kHz specimen set. Due to geometry increased complexity, the tension-compression analytical method cannot be directly brought towards the three-throat geometry. Considering the same Tr in all three throats, only one Ts2 and Ts3 combination has a 20 kHz longitudinal frequency. Unfortunately, to the author's knowledge, there is no possible direct correlation between all possible Ts2 and Ts3 combinations and the desired 20 kHz longitudinal frequency. From a large group of different AISI P20 FEA determined specimens, a base prediction can be made to the Ts2-Ts3 combination length using the analytical tension-compression method. Table 2-1 hyperbolic tension-compression L_1 determination sequence of equations are applied with B and Tr throat dimensions for an equivalent L_{axail} of a one throat

specimen. Due to the secondary throats reduced stiffness, L_{axial} must be rectified. The first prediction for Ts2-Ts3 combination length is to consider 80% of the determined L_{axial}. The frequency combination of Ts2-Ts3 with the analytically determined 80% L_{axial} must be iteratively determined.

With Ts1, Ts2, and Ts3, the whole geometry dimensions are introduced in FE software for final readjustments. This process allows for a 20±1kHz resonance prediction that can be easily corrected by adding or removing A and C lengths.

Since only one specimen is possible for each throat combination, we can conclude that the **tension-torsion stress ratio** is overall dependent on the B and Tr combination. Other specimens with different secondary throat dimensions to the main throat allow for a change in the stress ratio. However, in the study, only all equal throats specimens were manufactured. The final obtained stress ratio is also dependent on the axial/rotation ratio of the multi-horn, as it can be predicted.

The method to predict the stress ratio of a given specimen was initially fully numerical again. Frequency modal FEA were conducted to all obtained specimen geometries within the booster multi-horn set.

A stress ratio is obtained from the main throat shear and axial stress amplitude taken from the torsional and longitudinal resonant modes. In FEA, stress amplitude can be taken from each of the two resonant modes of interest, considering a unitary displacement amplitude on the Sn with the highest respective displacement. The final induced stress ratio result is dependent on the multi-horn specimen SnH displacement ratio. The final complete setup excited stress ratio can be predicted by knowing the rotation axial displacement ratio in the SnH and applying it to the specimen.

The final setup stress ratio is determined through equation (3.4) with the specimen alone resonant modes stress ratio, the displacement ratio between its stress nodes Sn1 and Sn2 ($U_{Sn1/Sn2\ ratio}$), and the complete setup displacement ratio at the SnH region ($U_{SnH\ ratio}$).

$$\sigma_{setup\ ratio} = \frac{U_{SnH\ ratio}}{U_{Sn1/Sn2\ ratio}} \sigma_{specimen\ ratio} \tag{3.4}$$

As mentioned, the no specimen setup horn displacement ratio at MI was 0,5 rotational/axial. When all created AISI P20 specimens were attached, a consistent SnH displacement ratio of 0.41±0.05 ($U_{SnH\ ratio}$) was obtained. The resulting FEA $U_{SnH\ ratio}$ of the tested specimens will later be seen in the subsequent chapter. This taken stress ratio serves as a

first FEA prediction. A complete setup steady-state analysis is the final FEA stress ratio prediction for a given specimen geometry.

The proposed analytical method can also predict the **shear** and **axial** stress for a unitary displacement on the Sn with the highest displacement (Sn1 for rotational, Sn2 for axial, Figure 3-34), utilizing the three pure torsion sections and the determined axial equivalent tension-compression L_{axial}.

The **shear stress** at the main throat is easily determined through the Ts1 section that follows a 20 kHz pure torsion specimen. The pure torsion analytical method, equations (2.14) to (2.20), is calculated with a unitary displacement A_{0r} to the Ts1 geometry. The obtained stress is on par with the FEA unitary A_{or} displacement at the stress node Sn1. From more than 15 different designed AISI P20 multiaxial geometries, a lower than 4% stress difference was obtained between FEA and the shear stress analytical solution.

A correction from the tension-compression analytical method must be made for the **axial stress**. Again, the tension-compression method cannot correctly describe the displacement and stress distribution behaviour due to the specimen geometry complexity. From a substantial group of eighteen different multiaxial specimens, an equivalent constant section L_{eq} was determined to the analytically determined one throat specimen L_{axial}. The equivalent L_{eq} can be attained by extrapolated equation (3.5), solely dependent on L_{axial}.

$$L_{eq} = -0.0227L_{axial}^2 + 0.7112L_{axial} \tag{3.5}$$

The L_{eq} is then applied to the axial analytical method (eq. 2.2 to 2.13) with a unitary A_o displacement at Sn2. The axial displacement proved a higher error difference between the FEA and the analytical method. Still, a lower than 10% error was obtained, with only very few specimens showing higher than 5%. Figure 3-35 compares FEA shear and axial stress amplitude to the described analytical method for several different AISI P20 specimens. The induced FEA and analytical stress amplitudes are associated with a 1 μm displacement amplitude A_o and A_{or} at the specimens Sn2 and Sn1, respectively.

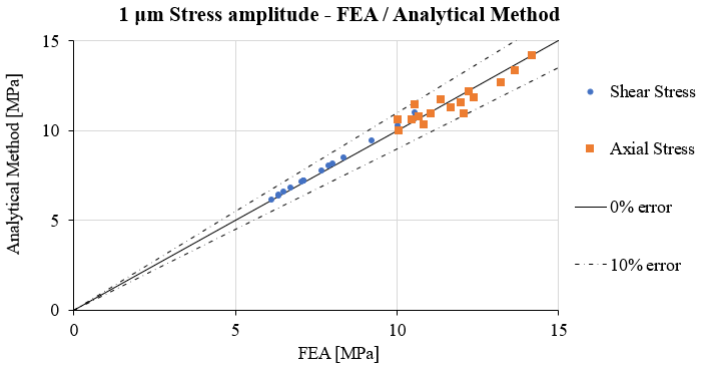

Figure 3-35. Axial and rotational one µm displacement to stress [MPa] comparison between the proposed analytical method and FEA results.

After the axial and shear stress amplitude analytical determination, the final stress ratio for a given booster multi-horn setup is again determined by equation (3.4). Like in FEA, to calculate the final induced stress ratio the Sn2/Sn1 rotational ratio of the specimen needs to be determined, together with the multi-horn displacement excitation ratio

Across all created AISI P20 three throat specimens, the Sn2/Sn1 rotation ratio has an exponential correlation to the Ts3 frequency. Figure 3-36 plots the Ts3 torsion section with the associated Sn rotation ratio for the AISI P20 specimens set with the respective exponential obtained trendline equation. An ASI P20 specimen with a 20 kHz Ts3 section (following Figure 3-23 wave propagation rule) is also included.

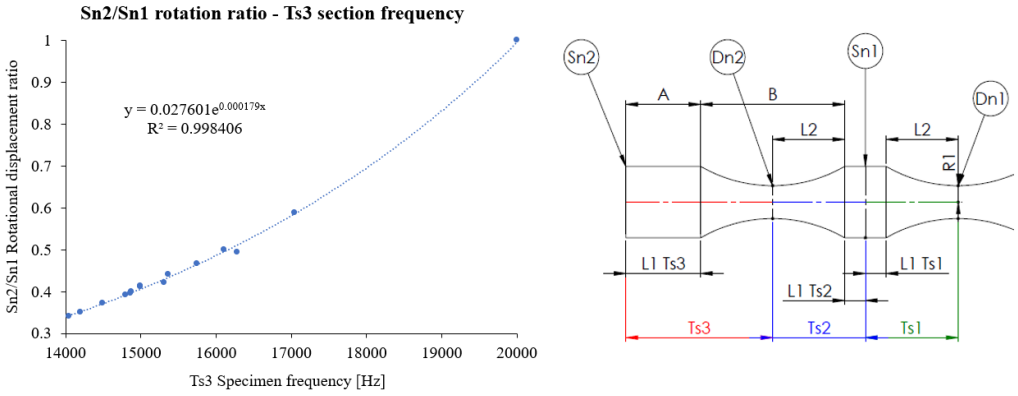

Figure 3-36. Sn2/Sn1 rotation ratio relation to the Ts3 section frequency.

Figure 3-36 proves that the lower frequency of the Ts3 section results in a lower displacement, leading to higher shear stress in the main throat Ts1. If a different Tr dimension is applied to the secondary throats, the Ts3 frequency to Sn2/Sn1 ratio still follows the same Figure 3-36 trend. One presented point in Figure 3-36 comes from a specimen with a higher Tr dimension in the secondary throats.

A new base three-throated specimen was achieved with: **higher stress combination in the fatigue testing region** (Main throat), **different stress ratios** for the same booster multi-horn setup, and less time-consuming **specimen geometry determination method** together with a stress ratio prediction method. Regarding the **lower dimensional sensitivity**, the new specimens showed a small improvement for a lower B dimensional value. The overall diameter increase may ease the machining process, which in turn results in an overall lower frequency deviation. The in-depth specimen analysis must now be applied to the complete setup. Only the FEA with the complete ultrasonic setup can be compared to the conducted experiments and their results.

3.4.2.5 Tension-Torsion booster multi-horn setup with new specimens

The complete booster multi-horn specimen setup must undergo an FE in-depth analysis to study the made improvements thoroughly and compare any conducted experimental result of the three different AISI P20 Figure 3-32 Spc specimens. Such conducted FEA also served to comprehend the present issues for future improvements. Again, two different numerical analyses were conducted, free-free modal frequency and steady-state modal analysis.

Several key details were taken from the conducted FEA to a set of different AISI P20 specimens:

- Maximum stress combination difference between the specimen and the multi-horn;
- The with and without specimen booster multi-horn displacement ratio (rotation/ axial displacement);
- Specimen frequency changes effect on the final setup excitation and stress combination at the main throat;
- Comparison between the predicted analytically and numerically determined stress shear axial ratio;
- How does the close frequency parasite modes influence the final excitation;
- Displacement at the free base to stress at the Main throat relation of the experimentally tested specimens;

As previously mentioned in the multi-horn introduction design, one necessary constraint for a correct design is preventing high deformation-induced regions. This ensures no fatigue-induced damage to the multi-horn as UFT is conducted. Two major deformation regions are present at the multi-horn slips within the complete setup with all specimens. The von Mises failure criterion was used to compare the high-stress regions. Figure 3-37 shows the higher stress regions of the multi-horn on one full setup.

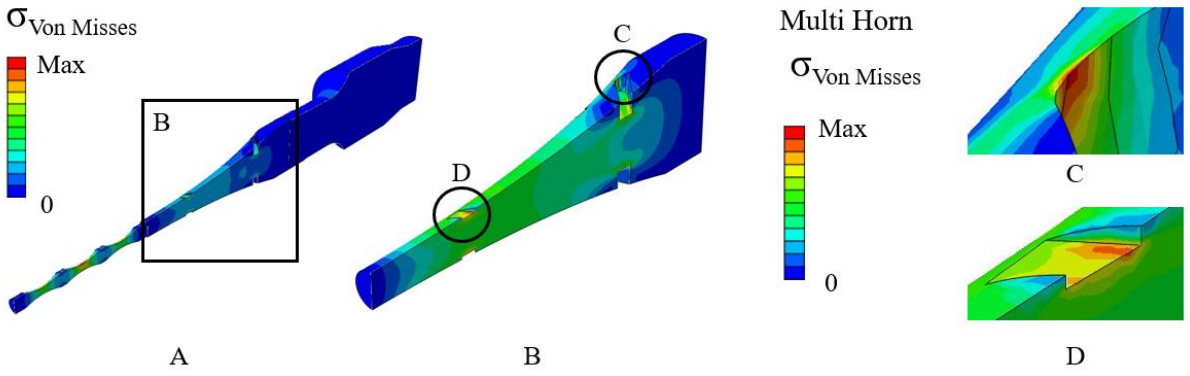

Figure 3-37. von Mises Multi horn stress amplitude analysis: (A) comparing the complete setup; (B) multi-horn Von Misses stress amplitude results; (C) upper slips high-stress region; (D) lower slips high-stress region.

Due to the local stress concentration, a mesh refinement was conducted in the multi-horn slit regions. In all conducted FEA, the multi-horn presented a reasonable lower stress combination amplitude to the specimen's main throat. The machined and tested multi-horn was painted black for temperature control via a thermal camera. No heat generation was perceived across any experiment or fatigue conducted test. Therefore, no high-stress amplitude was ever induced, and after all conducted experiments, no fatigue failure, no frequency, and no behaviour changes were observed by the final multi-horn.

Several essential data were taken from the conducted FEA analysis: The resulting frequency; highest stress combination location; main throat stress shear/axial ratio; rotational/axial displacement ratio at the specimen's free base and at the multi-horn specimen connection (SnH).

All created AISI P20 geometries presented the highest stress amplitude combination in the main throat. The resonance frequency between all numerically analysed specimens varied between 20000 and 20048 Hz. Table 3-11 presents Figure 3-32 three new specimens within the complete booster multi-horn setup: MI and two PM1 and MP2 frequencies; the SnH

displacement ratio; Specimen's free base displacement ratio, and the stress shar/axial ratio at the main throat.

Table 3-11. FEA free-free modal frequency results for the new Spc within the booster multi-horn setup.

	Resonance Frequency [Hz]			Stress ratio	Disp. Ratio	
Specimen	**MI**	**PM1**	**PM2**	**Shear/Axial**	**SnH**	**Free base**
SPC 1	20015	19417	20490	0.78	0.41	0.41
SPC 2	19989	19342	20496	0.61	0.41	0.41
SPC 3	20001	19268	20485	0.64	0.41	0.44

The same dimensional sensitivity analysis conducted on Mario's specimen (Table 3-9) was replicated to Spc specimens. Even when the specimen's frequencies were far from the ideal 20 kHz, the highest stress combination remained at the main throat. Such was not the case for the first specimen. Table 3-12 presents A, B, C, and Tr computed dimension combinations for Spc2 with the obtained setup frequencies, stress ratio at the main throat and displacement ratio at the free base. Spc1 and Spc3 results are presented in Annex 2.

Table 3-12. Booster multi-horn Spc2 tension-torsion specimen setup, dimension to frequency sensitivity analysis results.

Spc 2				Resonance Frequency [Hz]			Stress ratio	Disp. Ratio
A	**C**	**B**	**Tr**	**MI**	**PM1**	**PM2**	**Shear/Axial**	**Free base**
7.3	4.1	25.43	2.4	19989	19342	20496	0.61	0.41
7.3	4.1	25.43	2.45	20125	19787	20543	1.47	1.14
7.3	4.1	25.43	2.35	19954	18801	20484	0.32	0.18
8.3	4.1	25.43	2.4	19893	19241	20482	0.57	0.35
6.3	4.1	25.43	2.4	20129	19476	20527	0.65	0.50
7.3	5.1	25.43	2.4	19950	18572	20482	0.26	0.15
7.3	3.1	25.43	2.4	20290	19931	20629	2.55	1.88
7.3	4.1	26.43	2.4	19902	18826	20479	0.32	0.20
7.3	4.1	24.43	2.4	20172	19808	20547	1.42	1.05
Range (Max-Min)				397	1359	150	2.29	1.72

A considerable shear/axial stress variation was still observed in Spc2. Comparing all results with the first specimen, Spc1 and Spc3 lowered the shear axial ratio variation. Spc3 showed the most considerable improvement with a 0.87 stress ratio variability from the 2.06 of the first specimen. Still, the dimensional and frequency sensitivity is considerable and needs further improvements. From the setup FE analysis and associated experimental results, two improvements are proposed with already associated FEA.

The dimensional methodology improvements did always guarantee the required highest stress combination. The focused rotation in-between the main throat does not allow for a higher stress combination at the secondary throats. This also results in a considerably lower displacement ratio variation on the specimen's free base.

Close observation of the first and Spc results shows a link between the specimens 3º torsional mode, the setup PM1 and the stress ratio variability. As the 3º torsional mode increases, so does the PM1 and the resulting MI stress ratio. The Table 3-9 and Table 3-12 conducted analysis to the first and all Spc proves the link between the three. Figure 3-38 associates the specimens 3º torsional and longitudinal mode with PM1 and MI.

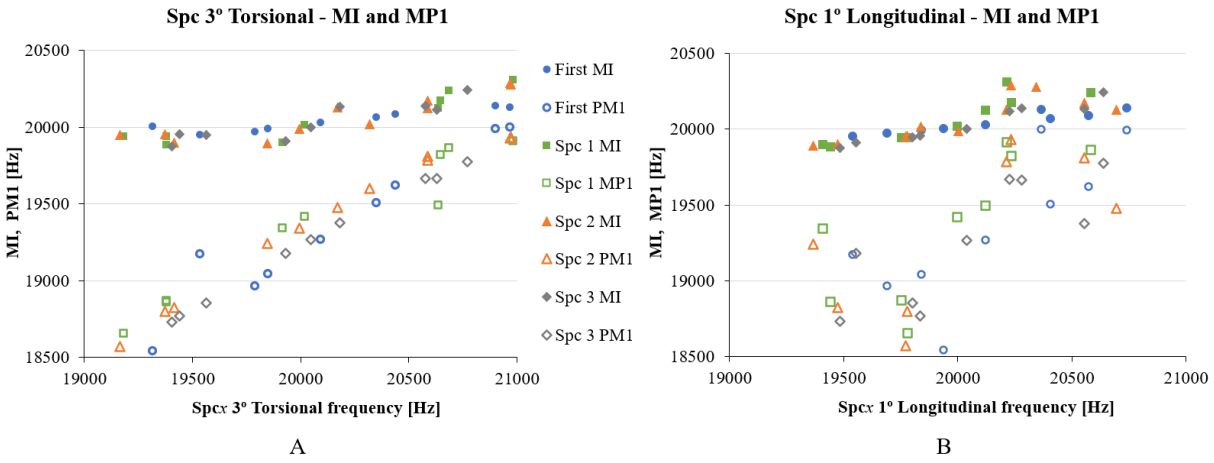

Figure 3-38. First and Spc specimens 3º Torsional (A) and 1º Longitudinal (B) frequency to MI and PM1 booster multi-horn setup frequency.

A clear trend is shown in Figure 3-38, whereas the 3º Torsional specimen mode increases, so does PM1 considerably. MI also increases with the 3º Torsional mode but not as substantially. The specimen's longitudinal mode shows an uneven distribution with PM1, indicating a negligible effect on PM1 frequency. The longitudinal mode shows a link with the MI frequency trend. However, this trend is not as pronounced when the PM1 reaches a close

frequency to MI. This is because the MI is becoming more predominantly dominated by rotation deformation with closer PM1 frequencies.

With the increase in PM1 frequency, so does the MI stress ratio, indicating a higher shear stress amplitude. Since PM1 has a high shear inducing stress, as previously shown, the stress ratio increase can be associated with it. Figure 3-39 shows how PM1 is associated with the final MI stress ratio.

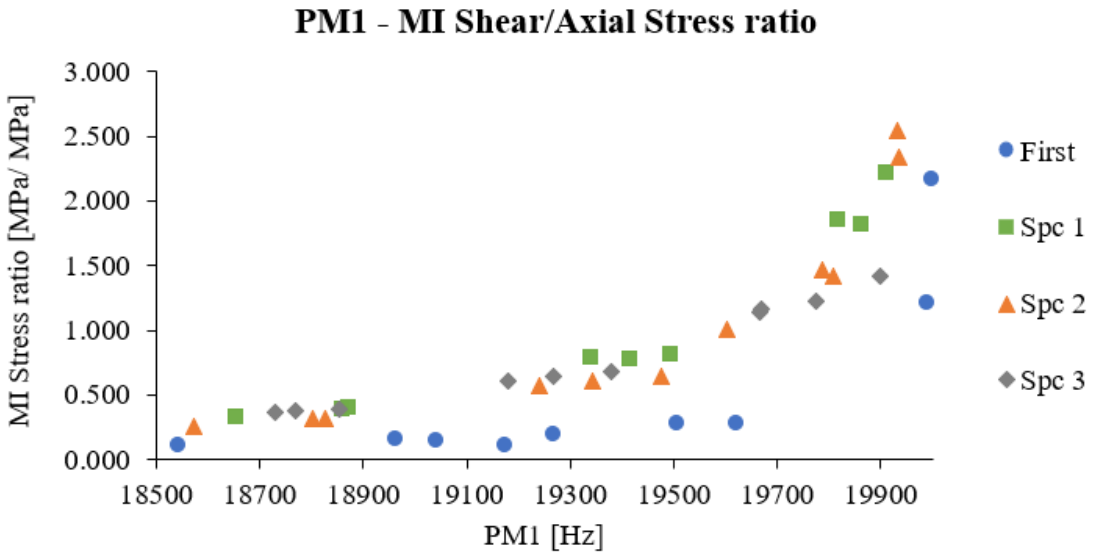

Figure 3-39. Sensitivity analysis PM1 frequency to MI obtained shear/axial stress ratio for the first, Spc1, Spc2 and Spc3 specimens.

A clear stress ratio increase tendency with the PM1 frequency can be perceived in Figure 3-39. The first specimen has a lower variation in lower PM1 frequencies. However, as it reaches closer to MI frequency, the stress ratio has a peak. Again, Spc3 shows its lower stress ratio variability with a more stable and favourable result.

Steady-state modal analysis followed the FEA free-free modal frequency. The Spc2 stress and displacement magnitude and phase is presented in Figure 3-40.

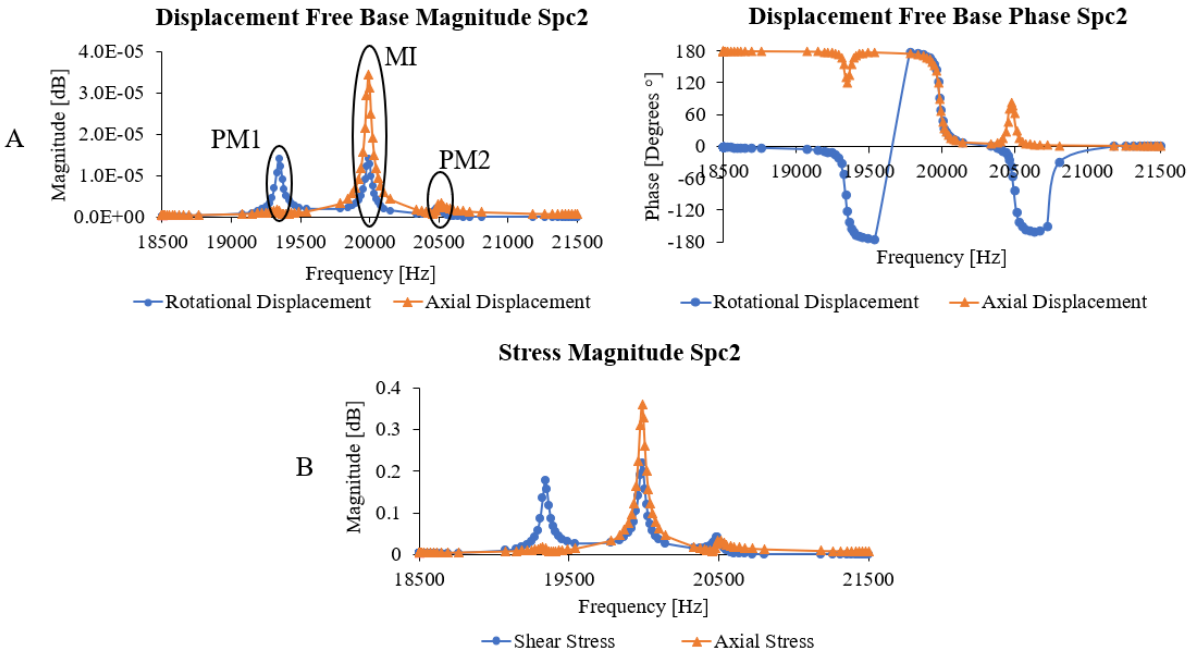

Figure 3-40. Booster multi-horn Spc2 setup steady-state modal: (A) rotational and axial displacement magnitude and phase; (B) shear and axial stress magnitude.

PM2 presents an almost negligible axial and rotational displacement. Just as it did with the first specimen (Figure 3-27). Spc show a high rotational magnitude with resulting high shear stress in PM1. However, PM1 has a considerably lower axial magnitude than MI. Both PMs have an opposite rotational and axial phase to the MI. The phase between measured locations will identify the excited modes experimentally. The FEA modal frequency and steady-state Spc2 results comparing all three resonant modes are presented in Table 3-13.

Table 3-13. FEA free-free modal frequency and steady-state results for the booster multi-horn tension-torsion Spc2 ultrasonic setup.

Booster multi-horn Spc2 setup Steady-State modal

Resonance Mode	FEA Modal Frequency (Hz)	Steady-State Frequency (Hz)	Ur/Uy ratio	Stress Shear/Axial ratio	MI/PM Ur Magnitude	MI/PM Uy Magnitude
PM1	19342	19326	9.24	11.57	0.99	22.29
MI	19989	19989	0.41	0.61	-	-
PM2	20496	20496	0.74	1.24	6.01	10.8

The resulting steady-state analysis of all new Spc free bases are parallel to the first specimen. PM1 has a dominant specimen rotational deformation with a similar amplitude to MI. Such high rotational magnitude can be excited even with 22 times lower than MI axial magnitude. The negligible effect of PM2 is also again proven with both low rotational and axial displacement magnitude.

A rotational and axial displacement magnitude relation to shear and axial stress can be taken from steady-state. A linear displacement to stress relation is proven numerically to all analysed specimens. Figure 3-41 presents Spc2 displacement to stress ratio for both axial to axial and rotational to shear when excited in the MI frequency.

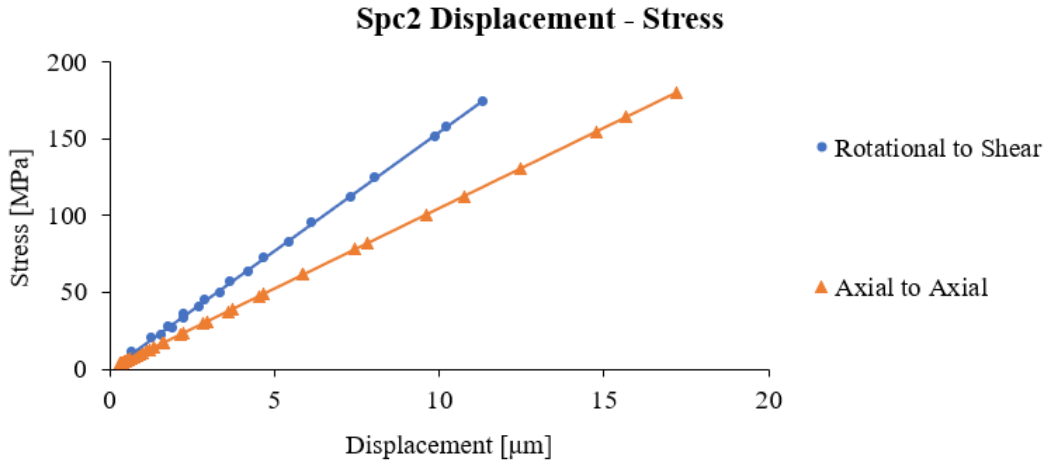

Figure 3-41. Spc2 MI displacement at the free base to induced stress at the main throat.

All obtained and here presented steady-state results will be compared with the conducted experimental measurements to the three new Spc specimens. The FE steady-state results later compared to the experientially obtained are: MI and PM frequency; main throat stress ratio; rotational and axial displacement at the free base to shear and axial stress amplitude at the main throat, respectively.

The proven compatibility between the FEA and the experimental results was utilised to explore possible improvements to this complex new multiaxial fatigue method. Recommendations for future improvements are presented in the next chapter considering all numerical and experimental data.

3.4.2.6 Future improvements to be implemented

One major problem remains with the reached solutions and improvements to the tension-torsion setup, shear/axial stress ratio variability between specimens. The present variability does not allow for experimental repetition with consecutive similar stress ratios.

The rotational response change in the specimen will always be an issue. The torsional modes have shown a higher frequency sensitivity to dimensional changes, and the induced torsional resonance is always dependent on the longitudinal of the complete setup. In other words, the specimen torsional mode will always depend on the exciting frequency for the longitudinal excitation. The longitudinal excitation creates the rotation through the multi-horn into the specimen.

To mitigate the specimens stress ratio variability, future improvements must take into consideration: the specimen key dimensions should be retained as much as possible, and a more imposing/controlling specimen rotation excitation through the booster multi-horn should be established, the never changed components. Two different solutions are here presented and studied through FEA:

- Transform the three throated specimens into three different separate sections.
- Application of a second booster multi-horn tension-torsion setup similar to non-zero mean stress ultrasonic fatigue machines.

From the described specimen FE analysis, the three throated geometry proved that three consecutive pure torsional specimens could represent it. This depiction of the specimen allowed for the described analytical method. From such a conclusion we can assume that specimen can indeed be machined separately into three specimens and attached sequentially to the multi-horn. Therefore, the actual fatigue specimen would only be the main throat Ts1 section (Figure 3-34). The remaining secondary throat section would be one single set used throughout all fatigue tests. Since the main throat is the single fatigue testing region, only the Ts1 pure torsion specimen will fail and be replaced between UFT. A representation of the detached three throat specimen is made in Figure 3-42.

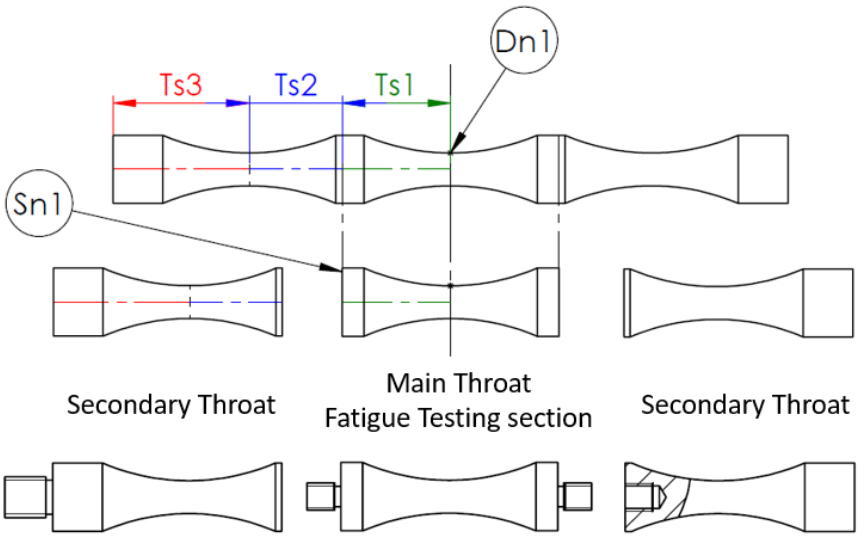

Figure 3-42. Three throated specimen transformation to three pure torsion sections cut representation with an example of the screw method between each section.

The specimen segmentation main objective is to lower geometry variability between specimens. Approximately 2/3 of the complete three throated specimen will remain between UFT, and, therefore, there will be a considerable reduction of stress ratio variability associated with geometrical differences. The amount of material needed to be machined is also reduced, which also represents a lower manufacturing cost.

The sectioned tension-torsion specimen is proven possible only if the deformation at the connections has low amplitude. This is a requirement in all ultrasonic fatigue machine components. From the already presented displacement and stress distribution FE analysis, there are rotational stress nodes Sn between the idealised three pure torsion sections Ts (Figure 3-34). The Sn1 stress nodes between the secondary and main throat ensure low shear stress at the proposed connection. Only the axial stresses can be detrimental to the in-between specimen parts connection.

Spc2 resulting axial stress and displacement distribution in the MI with stress nodes Sn and the displacement nodes Dn indicated is shown in Figure 3-43. The Sn1 point associated with rotation is where the supposed separation of the three specimens would be made.

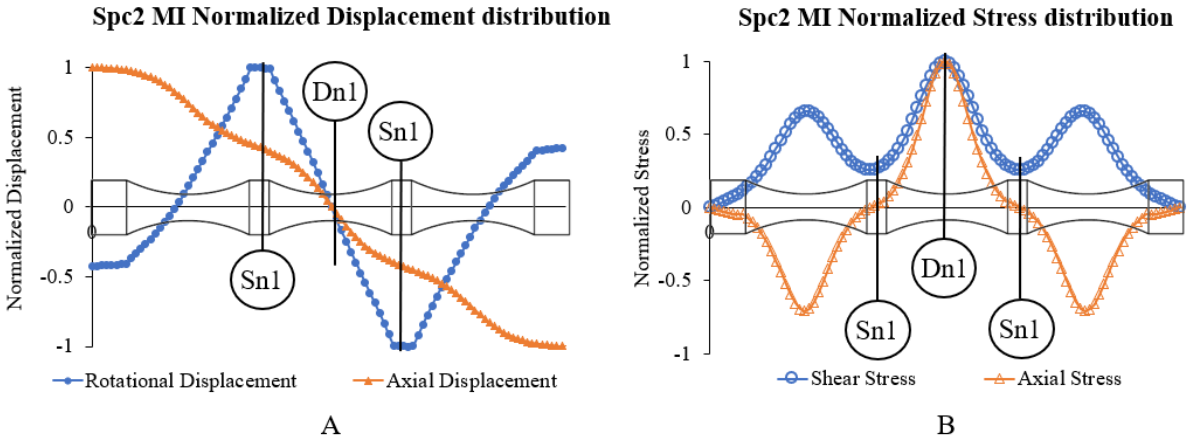

Figure 3-43. Spc2 MI normalised displacement (A) and stress (B) distribution within the booster multi-horn setup.

From the axial stress distribution, Sn1 has an expected induced axial stress. The resulting amplitude is considerably lower to the maximum point at the lowest cross-section area of the main throat. For the specimen Spc2, Sn1 axial stress amplitude is 26% of the maximum point at the Dn1. The results do not fully confirm the ability to retain the connection across a fatigue test in high axial stress amplitude. Even so, the considerably lower deformation in Sn to the fatigue testing region leads to the possibility of conducting a full fatigue test using a three-part specimen.

The final analysed and recommended improvement to be experimentally tested in future research focuses on diminishing the PM1 influence on the setup excitation. As observed, the PM1 has a non-negligible influence on the final MI deformation. Just as the MI, PM1 can be excited by the transducer axial cyclic displacement and induce high shear stress. This was proven to be one primary reason for the resulting stress ratio variance. The experimental results will also prove that this could prevent the ultrasonic machine from exciting the setup on the desired resonant mode, and therefore, excite the PM1 instead.

A found solution to diminish this issue was made from observing the rotation displacement distribution of the AISI P20 specimens within the setup. In PM1, the rotation distribution is non-symmetrical across the specimen's length, contrarily to the MI. This also results in a non-symmetrical shear stress distribution across the specimen. Figure 3-44 shows the Spc2 PM1 rotational displacement distribution within the booster multi-horn setup. It also plots the rotational displacement and resultant shear stress across the specimen's length in detail. The MI rotational displacement and shear stress distribution across Spc2 length is also shown as a reference.

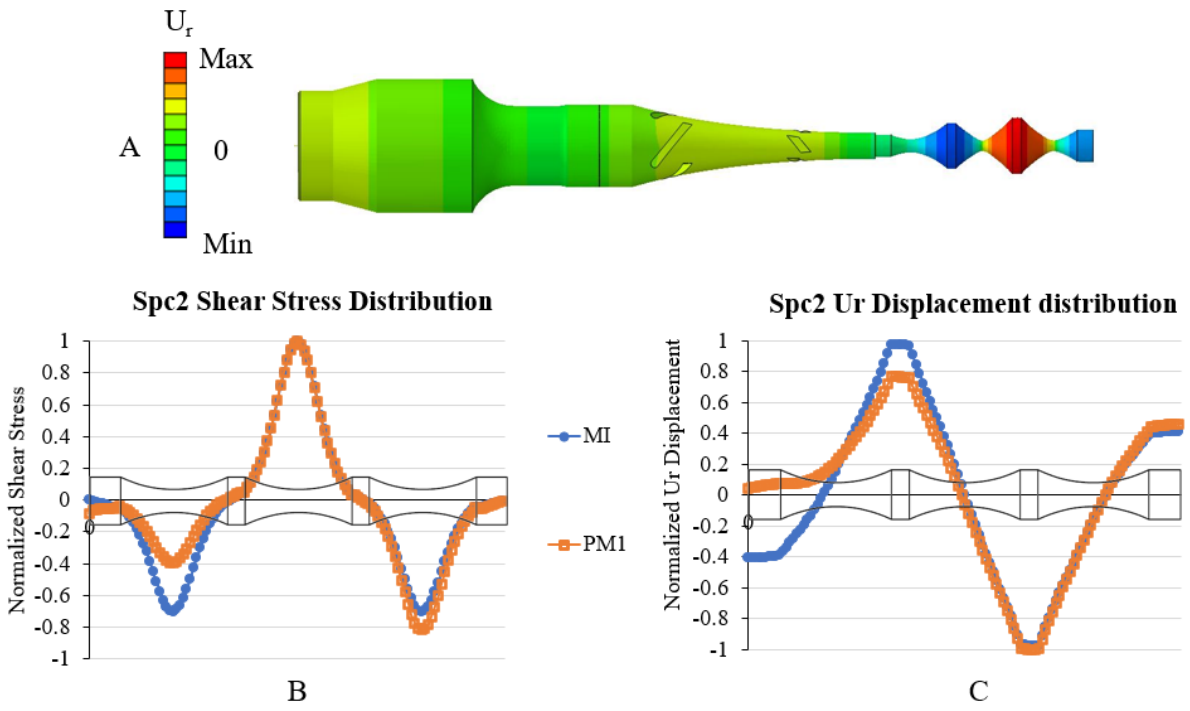

Figure 3-44. Booster multi-horn Spc2 PM1: (A) mode shape rotational (U_r) displacement distribution; and resultant Spc2 MI and PM1shear stress (B) and rotational (U_r) displacement (C) distribution.

Through Figure 3-44 the rotational displacement non-symmetry is easily observed. The low rotational displacement at the multi-horn specimen connection will induce undesirable shear stress. As it will later be experimentally proven, PM1 induced shear stress at this location will result in considerable heat generation.

The found solution was to ensure a symmetrical rotation across the specimen's length through a second booster and multi-horn. This second set is attached to the free base of the specimen, similar to the non-zero mean stress ultrasonic fatigue machines (Figure 2-19). Figure 3-45 shows the two booster two multi-horn (2B+2H) Spc2 specimen setup resulting MI axial and rotation displacement distribution.

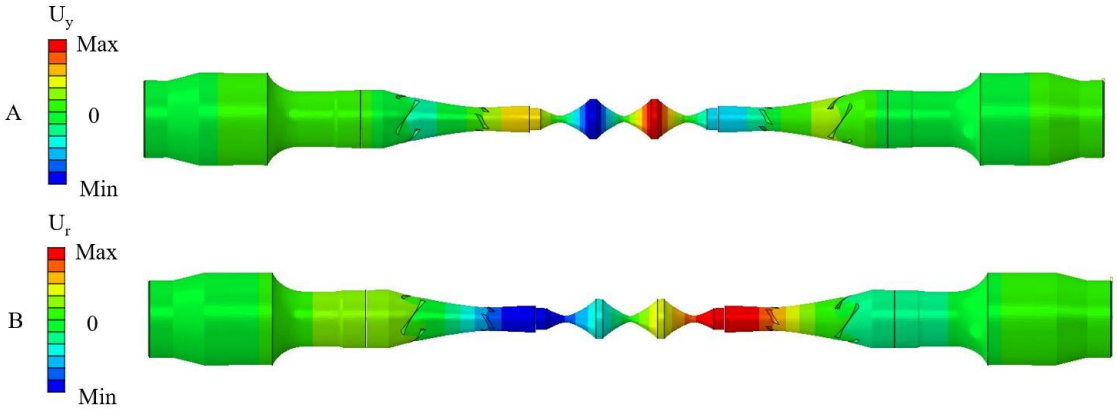

Figure 3-45. FEA Two Booster Two Horn (2B+2H) Spc2 MI mode shape: (A) Axial displacement distribution (U_y); (B) Rotational displacement (U_r).

Figure 3-45 MI presented a 20016 Hz frequency by FEA free-free modal frequency. The PM1 presented a considerably diminished 18515 Hz frequency from the single booster multi-horn Spc2 19342 Hz. PM1 also shows a different rotation displacement distribution. The displacement and induced stress are now fully symmetrical, with a predominant deformation at the main throat. Figure 3-46 presents the PM1 rotation distribution (U_r) across the 2B+2H Spc2 setup and the specimen's length.

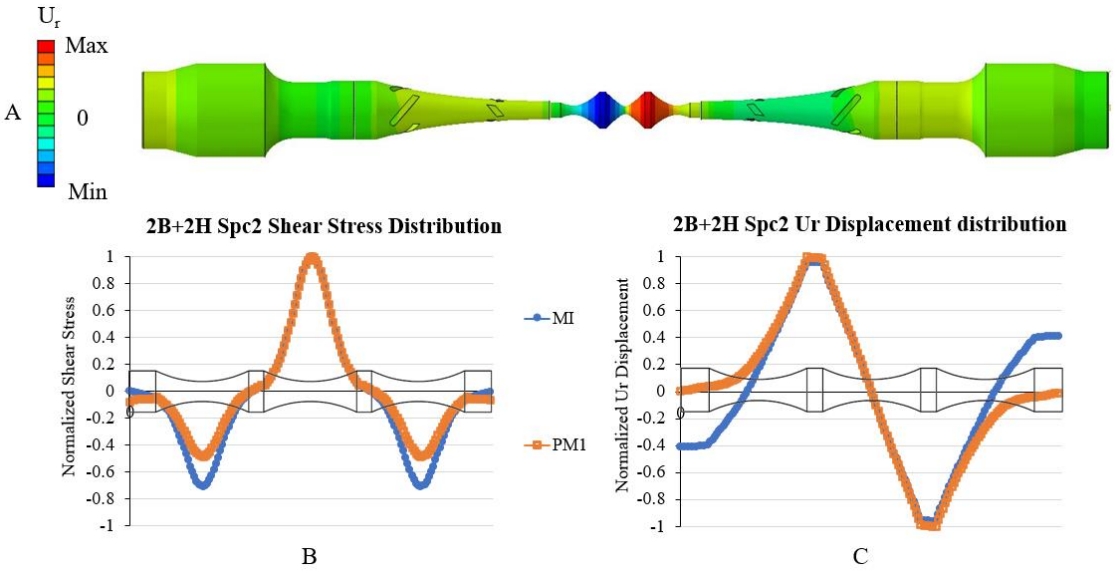

Figure 3-46. 2B+2H Spc2 PM1 rotational displacement (U_r) and shear stress distribution with MI Spc2 as reference.

The already shown sensitive analysis was again conducted with Mario's and Spc specimens to demonstrate the resulting improvement. For representation purposes, only Spc2 results will again be shown, just as in previous chapters where a sensitive analysis was shown

for specimen alone (Table 3-10) and within booster multi-horn setup (Table 3-12). The first, Spc1 and Spc 3 results for the same conducted 2B+2H sensitivity analysis are presented in Annex 2. The same dimensional differences to specimens were inserted into FEA to thoroughly compare the 2B+2H resulting improvement. Table 3-14 presents 2B+2H Spc2 sensitivity analysis: MI, PM1 and PM2 frequencies; stress ratio at the main throat; displacement ratio at a multi-horn specimen connection; and the overall range between all computed results.

Table 3-14. 2B+2H Spc2 tension-torsion setup, dimension to frequency sensitivity analysis results.

Spc2				Resonance Frequency [Hz]			Stress ratio	Disp. Ratio
A	**C**	**B**	**Tr**	**MI**	**PM1**	**PM2**	**Shear/Axial**	**Base**
7.3	4.1	25.43	2.4	20012	18508	20517	0.60	0.41
7.3	4.1	25.43	2.45	20061	18946	20420	0.84	0.37
7.3	4.1	25.43	2.35	19978	18063	20410	0.45	0.44
8.3	4.1	25.43	2.4	19945	18492	20398	0.60	0.39
6.3	4.1	25.43	2.4	20078	18524	20429	0.60	0.44
7.3	5.1	25.43	2.4	19972	17734	20411	0.37	0.44
7.3	3.1	25.43	2.4	20095	19340	20418	1.26	0.29
7.3	4.1	26.43	2.4	19948	18038	20408	0.43	0.41
7.3	4.1	24.43	2.4	20089	18988	20420	0.88	0.38
Range (Max-Min)				150	1606	31	0.89	0.15

The sensitivity analysis shows a considerable reduction in MI and MP2 frequency variance and, most importantly, a lower change in stress ratio. The Spc2 2B+2H stress ratio range is 71% lower than the single booster multi-horn setup. From close observation, PM1 has a higher frequency change in 2B+2H. PM1 frequency is lower, but it appears as the mode is even more dependent on the specimen's torsional frequency.

The displacement ratio at the second multi-horn specimen connection (previous free base) is more consistent and closer to the 0.41 SnH ratio for a single booster horn setup. The same conclusions were taken from all tested Spc and Mario's specimen.

Just as conducted with the single booster multi-horn setup in Figure 3-38, the 2B+2H setup PM1, specimen resonant modes and MI stress ratio were linked. Figure 3-47 associates the specimens 3º torsional and longitudinal mode with 2B+2H PM1 and MI.

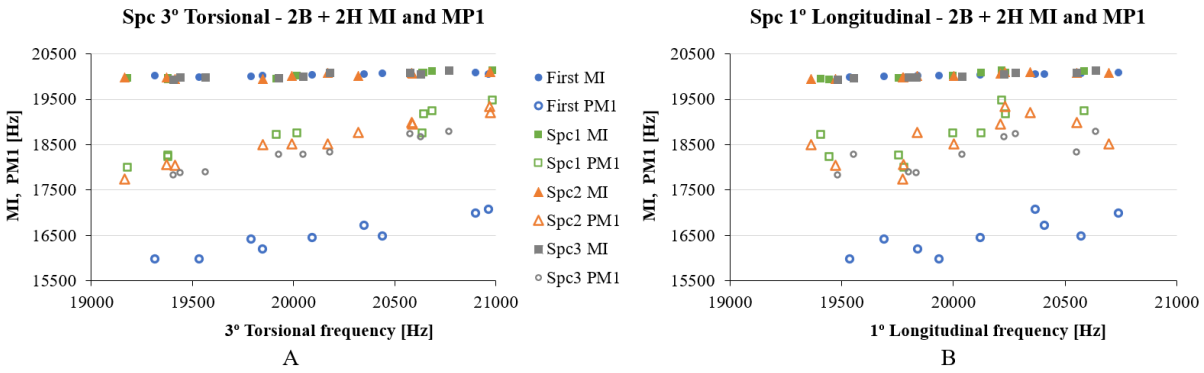

Figure 3-47. First and Spc new specimens 3º torsional (A) and 1º longitudinal (B) frequency to MI and PM1 frequency 2B+2H setup.

The same observed trend where the PM1 increases with the 3º Torsional specimen mode is also present. MI also increases with the 3º Torsional mode but not as substantially. The specimen longitudinal mode shows a somewhat distribution with PM1 which indicates small effect on PM1 frequency.

Even with a considerable frequency difference, PM1 higher shear stress can still be linked to the MI final stress combination. Again, with the increase in PM1 frequency, MI stress ratio increases, indicating a higher shear stress amplitude for the same displacement transducer excitation. Figure 3-48 shows how PM1 is associated with the final MI stress ratio. Figure 3-48 also plots the single booster multi-horn Spc2 stress ratio as reference.

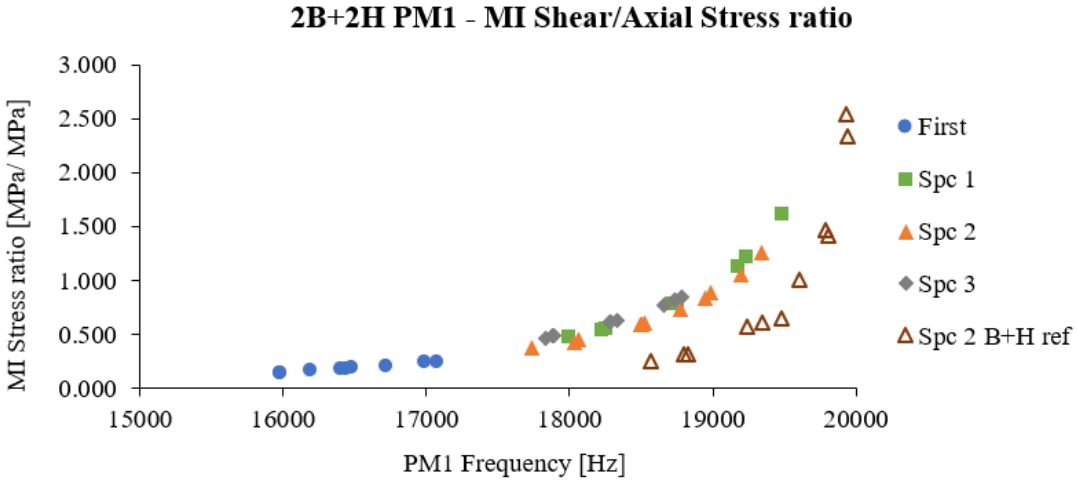

Figure 3-48. Sensitivity analysis 2H+2B PM1 frequency to MI obtained shear/axial stress ratio for the first, Spc1, Spc2, Spc3, and Spc2 in single booster multi-horn as reference.

The 2B+2H lower variable stress ratio becomes clear in Figure 3-48. All specimens present a lower stress ratio influence over the PM1 frequency, meaning a more consistent tension-torsion UFT method with lower specimen dimensional dependency. Spc3 and first have the lowest stress shear/axial ratio change with ±0.19 and ±0.12 from the starting 20 kHz specimen base model, respectively.

The 2B+2H first specimen PM1 has a lower frequency value and a lower stress ratio change. The associated shear rigidity of this specimen is lower due to its thinner shape, resulting in a lower PM1 frequency. Also, the overall lower mass and rigidity results in a less predominant frequency influence over the setup overall mode shape and frequency.

A FE steady-state modal analysis was again conducted with a unitary force applied to one of the attached boosters. Again, the same 18.5kHz to 21.5kHz frequency range was applied. Figure 3-49 presents the magnitude of the axial and shear stresses at the main throat, and the magnitude and phase of the rotational and axial displacements for one of the multi-horn specimen SnH regions. There was no considerable difference between the two SnH regions, showing the 2B+2H symmetry response.

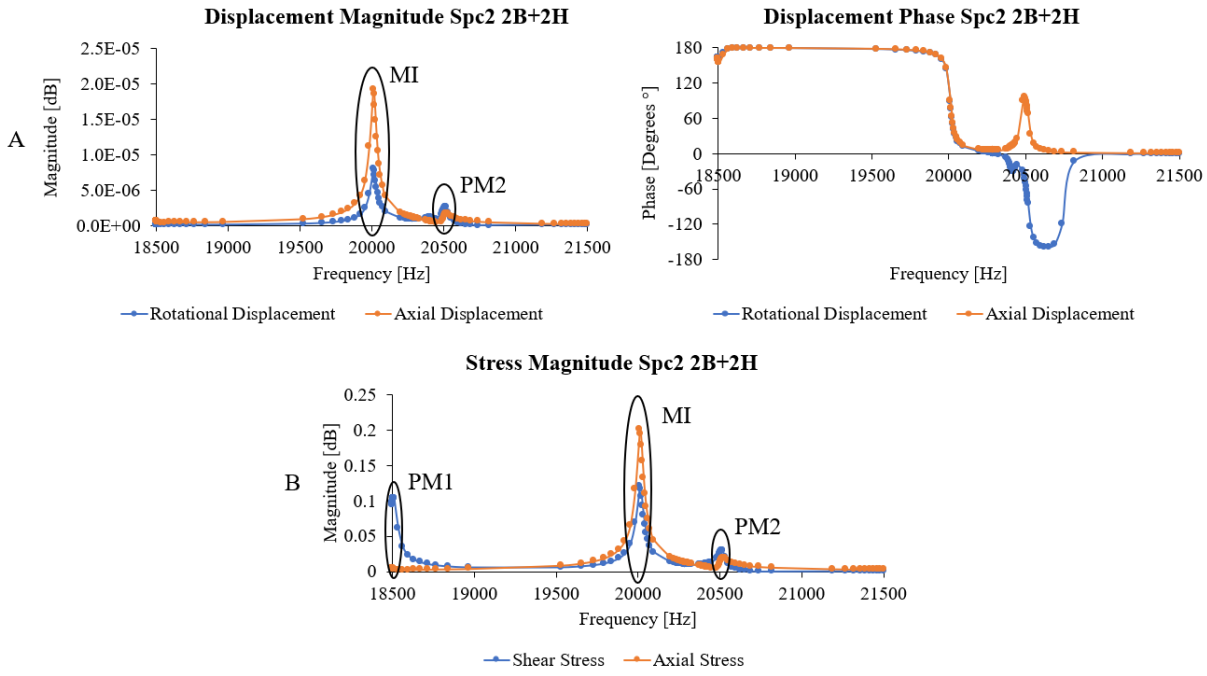

Figure 3-49. 2B+2H Spc2 setup steady-state modal: (A) rotational and axial displacement magnitude and phase; (B) shear and axial stress magnitude.

The PM1 is barely visible within the established frequency range of study. Just as for the single booster multi-horn setup, the displacement phase is different between MI and PMs. The 2B+2H Spc2 modal frequency FEA and steady-state results comparing all three resonant modes magnitude is presented in Table 3-15.

Table 3-15. FEA free-free modal frequency and steady-state results for 2B+2H Spc2 ultrasonic setup.

2B+2H Spc2 setup Steady-State modal

Resonance Mode	FEA Modal Frequency (Hz)	Steady-State Frequency (Hz)	Ur/Uy ratio	Stress Shear/Axial ratio	MI/PM Ur Magnitude	MI/PM Uy Magnitude
PM1	18508	18508	0.16	26.88	86.40	34.33
MI	20012	20012	0.42	0.60	-	-
PM2	20515	20515	1.56	1.60	3.02	11.37

2B+2H Spc2 PM1 presents a considerable lowered U_r and U_y magnitude to the single booster multi-horn Table 3-15. Such is due to the Sn2 multi-horn specimen connection region has become for PM1 a rotational displacement node. The low to null displacement can be observed in the previously shown Figure 3-49. The lowered U_y indicates a lower excitation magnitude. PM2 continues to be present with a similar

The 2B+2H setup has thus proven to be a promising improvement in obtaining a more reliable and consistent ultrasonic fatigue tension-torsion method. It will also allow for imposing a constant mean deformation, both axial and/or rotational, which increases the biaxial fatigue machine research range. There might only be one experimental difficulty to the author's knowledge: the specimen rotation measurement. The applied experimental specimen rotation measuring method might no longer be possible. If not, future experiments need to be carefully thought out to fashion a new rotation measuring method. Since there is no free base, the conventional axial measuring methods can only be applied to the opposite booster from the transducer. The specimen's axial displacement can be mathematically determined from the known booster multi-horn amplification.

Another conclusion can be taken for future research from the specimen alone, the complete single booster multi-horn specimens, the 2B+2H FEA study. The specimen's impact on the setup rigidity is vital to the final stress ratio and excitation frequency. Future specimens should reduce rigidity mass ratio through a lower constant radius D (Figure 3-31). It is not

recommended to go as low as Mario's 3.36 mm for manufacturing and design purposes. The specimen should also follow a C to A geometry ratio similar to Spc3 that showed the lowest stress ratio variability between all here presented Spc.

3.5 In-plane Cruciform Ultrasonic Fatigue

The second studied biaxial method focuses on axial-axial cruciform ultrasonic fatigue. Such a new ultrasonic methodology was developed in collaboration with Bournemouth University. They have modelled and machined all tested geometries, while this study conducted detailed FEA and experimental analysis in our LEM^2 laboratory.

Experimental tests presented issues with the specimen's dynamic behaviour which are explained within this section. Suggestions on how to improve the specimens or at least avoid these issues are presented based on FEA. FEA also provided the tools to reach an analytical calculation method relating the measured displacement to the induced biaxial stress at the specimen's centre.

3.5.1 Introduction to Ultrasonic Cruciform Fatigue

In a similar manner to the tension-torsion development concept, the designing of cruciform ultrasonic fatigue testing was achieved by resonance analysis of potential geometries. The achieved biaxial ultrasonic method follows the second possible described resonant method: one resonant mode at 20 kHz, compliant with the axial excitation of the ultrasonic setup, with a resonant mode shape that induces multiaxial deformation in one fatigue testing region.

Therefore, cruciform geometries were modally studied to reach designs capable of achieving resonance at the piezoelectric transducer frequency, with displacement compliance to the booster horn setup and consequent strain of interest at one region. Diogo Montalvão et al. [197] iteratively reached two initial different ultrasonic cruciform geometries.

The cruciform geometries were designed following Baptista et al. [62] optimised conventional cruciform geometry and dimensional relations made for small size, low thickness specimens and ensured maximum stress on its midpoint. FE frequency free vibration modal

analysis was used to determine the dimensions iteratively with the desired resonant mode shape at 20 kHz.

Two different geometries were first studied and manufactured to induce transverse axial-axial plane stress state: in-phase tension-tension (First T-T) and out-of-phase Tension-Compression (T-C). Both specimens' geometry followed the optimised Baptista geometry. The T-T and C-T mode shape and displacement magnitude distribution are represented in Figure 3-50 from the FEA modal results of two 20 kHz geometries.

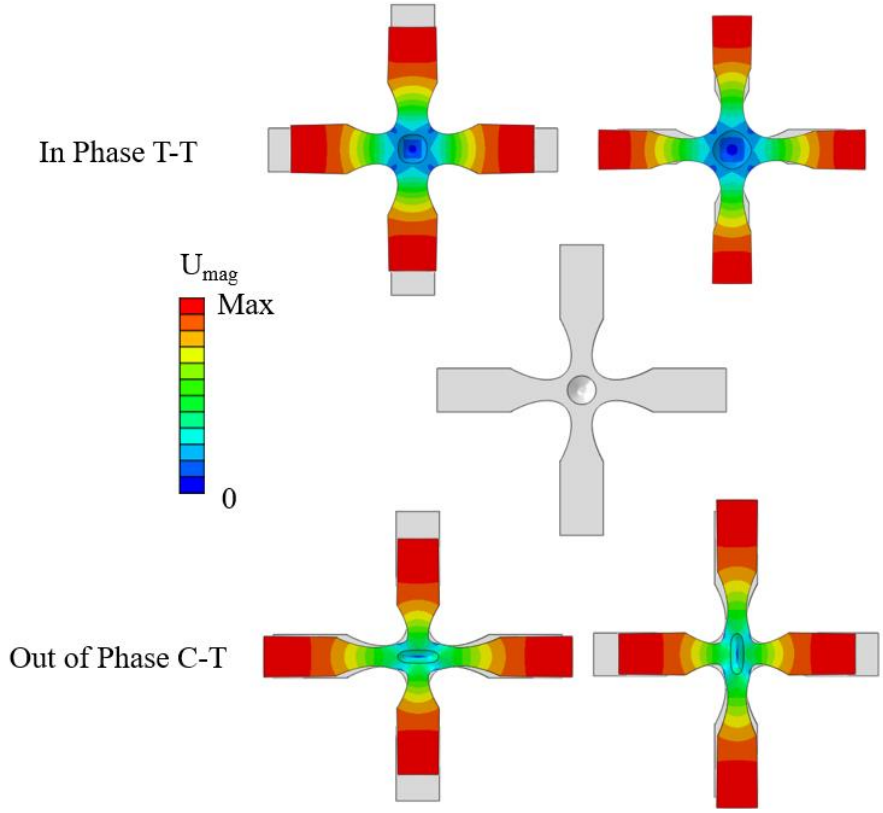

Figure 3-50. In phase T-T and out of phase C-T cruciform resonance mode shape and displacement magnitude distribution.

As observed in Figure 3-50, in both T-T and C-T cruciform specimens there is a maximum axial displacement at all the tips/extremities of the arms (stress node). With this uniaxial maximum displacement behaviour, both cruciform resonant modes have a compliant displacement with the booster axial horn tension-compression ultrasonic fatigue setup. Such compliance and the present stress node make the excitation of both resonant modes possible. Figure 3-51 shows a representation of the booster axial horn cruciform ultrasonic fatigue machine setup with each component identified.

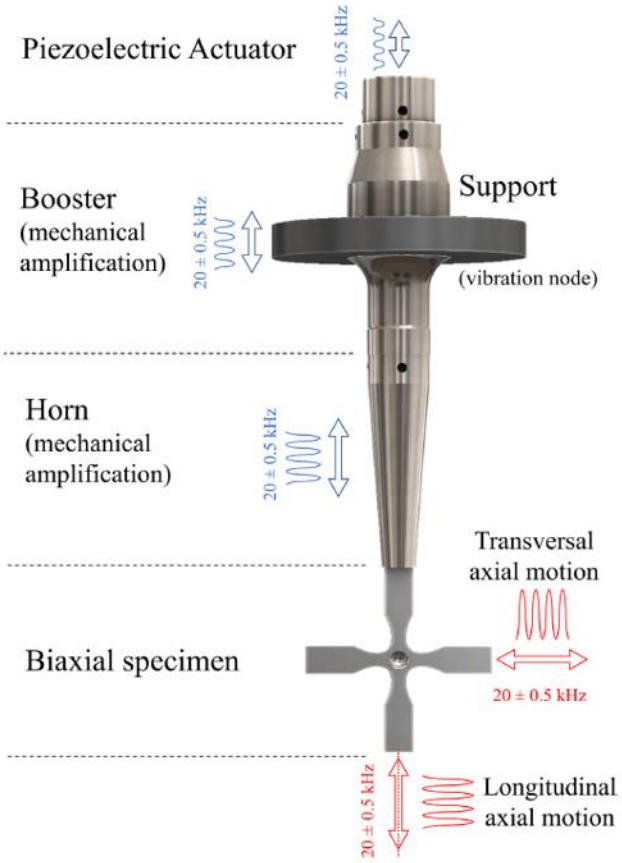

Figure 3-51. Transducer booster horn cruciform setup representation [198].

The ultrasonic cruciform full setup works similarly to the tension-compression ultrasonic described setup. The machine is supported by the booster support ring (displacement node). Both the booster and the horn amplify the transducer cyclic axial displacement, and every component has a threaded connection at a stress node. All attached components, including the specimen, have a 20 kHz specific mode shape resonance.

All cruciform geometries were designed to reach a unitary axial-axial ratio. Non-unitary axial-axial cruciform were also analysed and are under research [198]. The new geometries with non-unitary axial-axial ratios were reached by altering the length ratio between cruciform arms. The non-unitary ratios are out of this study's scope, so no results are presented.

Unitary ratio cruciform specimens were modally analyzed in detail with and without the booster horn setup. FEA was crucial in improving the ultrasonic cruciform method and creating a proposed analytical solution. All results were compared with experimental modal analysis, strain measurements and power to displacement mode shape behaviour. All tests and FEA calculations were repeated for the two available axial horn booster setups.

3.5.2 FE Cruciform Analysis

All FEA to cruciform geometries were computed simultaneously with experimental measurements. FEA proved a vital tool for understanding the cruciform deformation behaviour, setting the experiment measurements requirements, and establishing a working experimental methodology through an analytical solution.

Similar to the conducted FEA study for uniaxial tension-compression and tension-torsion, the specimens alone and the complete setup were first numerically analyzed in free vibration FEA frequency and then in FEA steady-state modal.

3.5.2.1 Cruciform specimen

Three different unitary axial-axial ratio specimens were FEA analyzed and experimentally tested: the first design and machined in-phase T-T specimen (F*x* T-T); a second new in-phase T-T specimen (N*x* T-T); and an out-of-phase (C-T x). All cruciform specimens were numerically designed and machined in aluminium 6082-T651. The second in-phase T-T specimen's group was manufactured with the intent of improving the observed issues in the first F T-T specimens. Figure 3-52 presents the three different cruciform specimens under discussion with the respective designations.

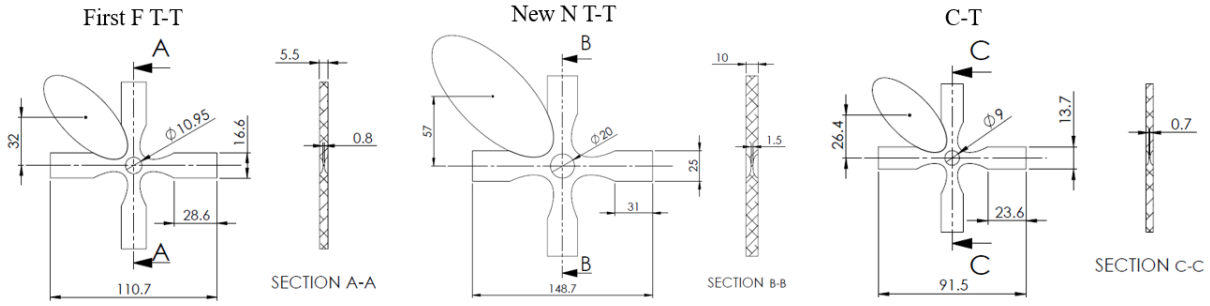

Figure 3-52. Cruciform ultrasonic fatigue specimens: In phase first F*x* T-T and new N*x* T-T; Out of phase C-T *x*.

As previously mentioned, to achieve a 20 kHz cruciform specimen, an iterative dimensional change procedure was conducted. The shape and dimensions relation equations follow the Baptista et al. [54] optimisation. The study collaborator Bournemouth University research team computed all three 20 kHz cruciform presented geometries. They conducted all free-free modal frequency analysis through ANSYS numerical software. Our team also conducted the tested material static properties determination. The final 3D geometries and

machined specimens were then handed over for detailed FEA, experimental analyses, and fatigue testing.

A first FEA frequency in free-free modal frequency analysis was conducted. The numerical analyses of all three cruciforms showed an undesirable close frequency modal resonant shape with a compliant axial displacement. Again, the undesirable resonant mode was denoted as a Parasite Mode' (PM), and the intended mode to be excited as the Mode of Interest (MI). As previously explained, PMs are resonant modes that have frequency proximity to the MI that may influence/alter the final induced mode shape. The complete setup FEA computation and experimental results will later prove PM's excitation. Figure 3-53 shows for a T-T cruciform both MI and PM resonant modes modal shape in displacement magnitude distribution.

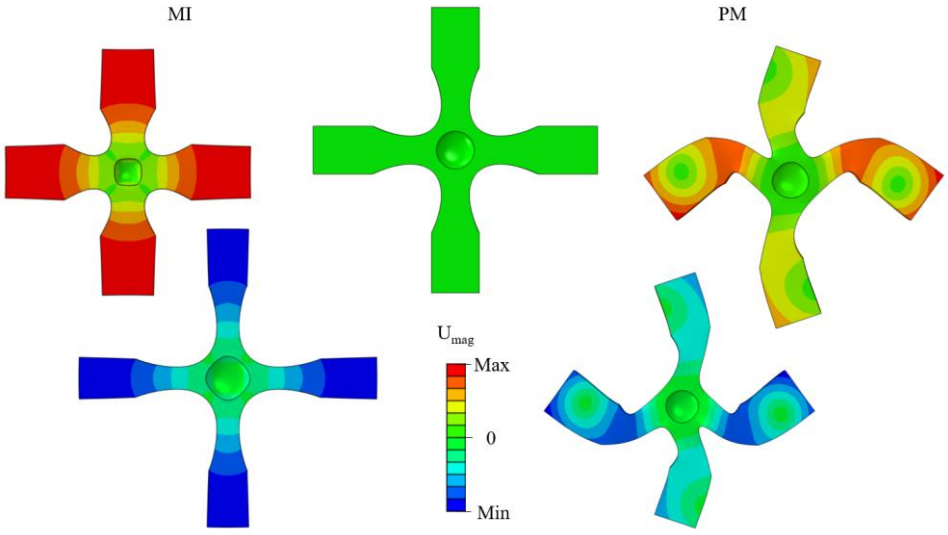

Figure 3-53. Cruciform T-T resonant modal shapes in displacement magnitude: Mode of interest (MI); Parasite mode (PM).

PM modal shape has an axial horn compliant displacement at one of the cruciform arms pairs and a denoted 'flapping motion' on the orthogonal pair. The obtained frequency from FEA results in free vibration for the given geometries is presented in Table 3-16.

Table 3-16. FEA free-free modal frequency results for all three cruciform ultrasonic geometries.

FEA frequency resonant mode [Hz]	**F*x* T-T**	**N*x* T-T**	**C-T *x***
MI	20000	20003	20096
PM	19481	20718	22576

C-T specimens prove a considerably higher frequency difference between MI and PM. The original F T-T has the lowest 519 Hz PM frequency difference regarding MI. The new N*x* T-T specimens were designed to have a higher than F*x* T-T frequency difference, having a 715 Hz difference. The followed FE detail analysis of the cruciform within the setup will better show the PM impact on the final modal shape.

3.5.2.2 Cruciform ultrasonic fatigue setup

As will later be described in detail in the experimental results (chapter 5.5.2), the first experiments showed functioning C-T specimens and only one working in-phase F T-T. F T-T cruciform specimens showed a non-negligible PM resonant deformed shape. Due to their non-working as pretended resonance, deformation occurred in the specimen-horn connection. Initially, some specimens could not even be induced at higher power transducer settings.

As predicted, the PM displacement compliance to the axial displacement transmitted by the horn and a close frequency value to the working 20kHz allowed for its excitation. Consequently, it was concluded that the final behaviour of the specimen was a combination between the resonant MI and the close PM.

A new T-T design (N T-T) was created from the same aluminium 6082-T651 to correct the described PM effect. The new design followed the same iterative methodology but also considered the frequency difference between PM and MI.

From the FE free vibration frequency analysis of all three geometries in both axial horns, the results show cruciform PM (Figure 3-52) being excited by the horns and the intended MI. The obtained frequencies are shown in Table 3-17 for all three specimens in both axial horn booster setups.

Table 3-17. Free vibration FEA frequency results for all three cruciform ultrasonic geometries within the two axial horns booster ultrasonic setups.

FEA frequency resonant mode [Hz]	**F*x* T-T**		**N*x* T-T**		**C-T *x***	
	Tapered	**Hyper**	**Tapered**	**Hyper**	**Tapered**	**Hyper**
MI	20004	19999	20004	20001	20010	20025
PM	19612	19576	20551	20606	21444	

Considering the closest MI to PM setup with the hyperbolic horn, the F T-T specimen has a 540 Hz difference, while N T-T presents a 605 Hz. The given N T-T specimen MI to PM frequency does not present a sharp frequency improvement. However, as it will later be observed experimentally, all N T-T specimens had similar behaviour and a MI correct excitation, contrarily to most F T-T. C-T specimens showed a 1434 Hz frequency difference for the same setup, resulting in no considerable PM influence over the MI.

Modal FEA comparison without and with booster horn setup (Table 3-16 and Table 3-17, respectively) presented considerable PM frequency differences. Since the PM shows displacement compliance with the booster-horn set, just like the MI, the PM working frequency approaches the booster horn working frequency. In other words, PM to MI frequency difference is lower when considering the setup assembly. This is more easily observed in C-T specimens, where PM goes from 22576 Hz in specimen alone to the hyperbolic setup 21444 Hz. The considerable modal frequency difference between with and without the booster horn setup proves that the complete setup analysis is always required to compare FEA with the experimental results.

Figure 3-54 shows both MI and PM mode shapes for the new N T-T specimen's vertical and horizontal axial displacement distribution with the booster tapered horn setup.

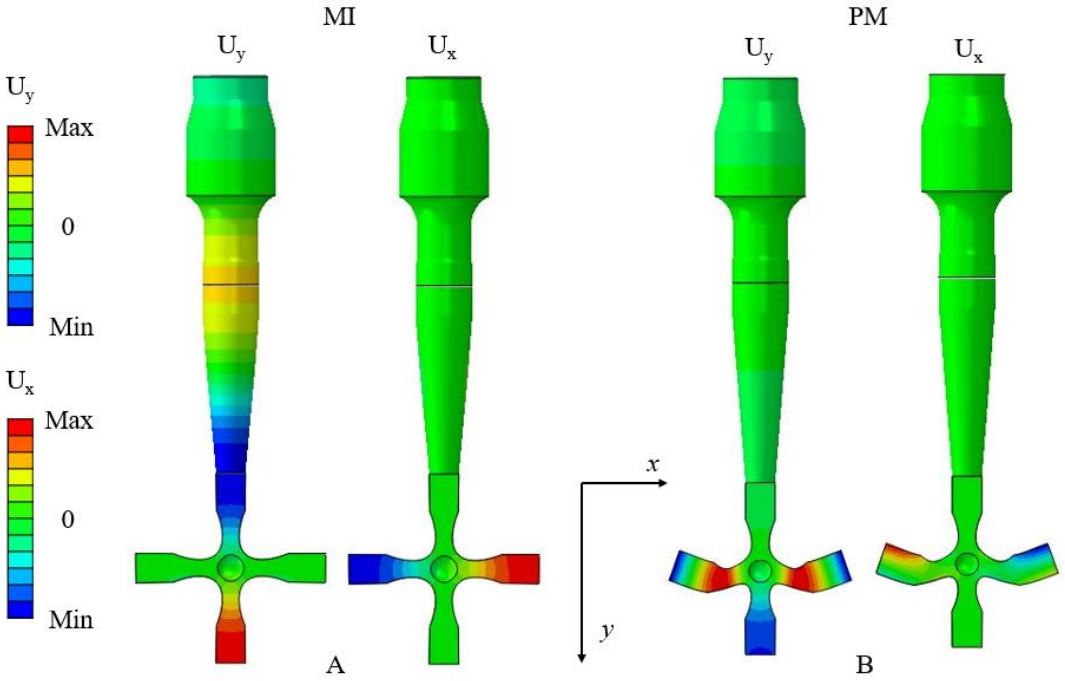

Figure 3-54. MI and PM vertical (U_y) and horizontal (U_x) axial displacement distribution of the booster tapered horn N T-T ultrasonic setup.

All experimental displacement measurements points and respective directions were devised from the FEA taken MI and PM mode shape. MI highest displacement regions (stress nodes) are at the arms tips, horizontal arms in the *x*-direction and vertical arms in the *y*-direction. The PM mode also has two highest displacement locations: a vertical flapping displacement of the perpendicular arms to the setup length, the horizontal arms, and the vertical displacement of the vertical lower arm.

Figure 3-55 shows in detail the complete setup PM vertical displacement distribution across the horizontal arm. The flapping vertical displacement amplitude is not constant throughout the arm's length. It has a vertical stress node at the tip and a displacement node around the middle of the arm's length.

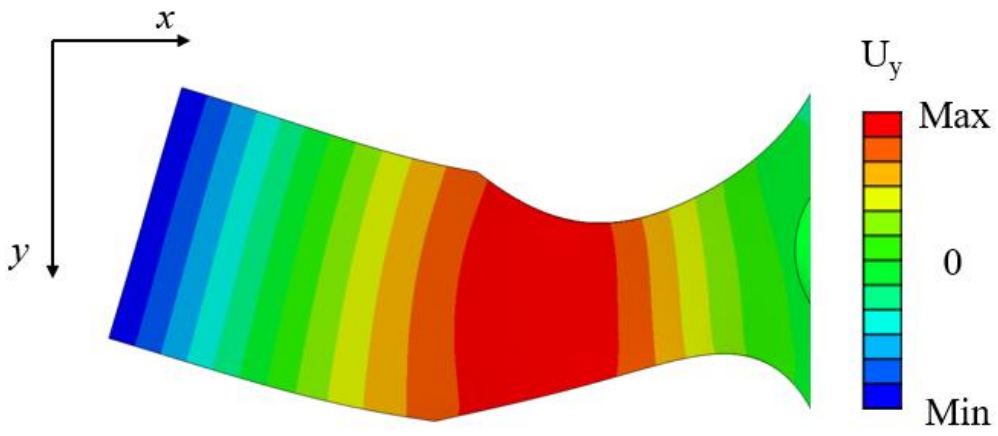

Figure 3-55. Cruciform complete setup PM vertical axial displacement (U_y) distribution across a horizontal arm.

An experimental measurement made along the arm from the taken FEA conclusion proved the excitation of the PM mode and its disruptive influence in the first F T-T specimens [92]. The arms' tip highest vertical displacement will be a measuring point location for experimental and more complex steady-state FEA.

It is important to note that the modal frequency FEA presents the resonant modes shape and frequency independently. Even without the PM influence, there was a vertical displacement of the horizontal arms. Steady-state analysis was conducted to understand better and characterise the vertical displacement occurrence. The conducted steady-state modal analysis follows the same method as in tension-compression and tension-torsion setup. A cyclical unitary force is applied to the booster, and the resulting vibration excitation is determined for an 18.5 to 21.5 kHz frequency range.

Three points of interest are taken from the steady-state. These points are the same as the applied measuring experimental locations. Figure 3-56 shows the experimental measured locations. Figure 3-56 presented experimental conducted setup is again shown and described in the experimental methodology chapter (chapter 4.4.3.2, Figure 4-28). The three taken points are: vertical displacement of the vertical free arm (Laser 1, L1); horizontal displacement of the horizontal arms (Laser 2, L2); and the vertical displacement at the horizontal arm's tip (Laser 3, L3). The laser L designations are attributed to link FEA to the experimental results.

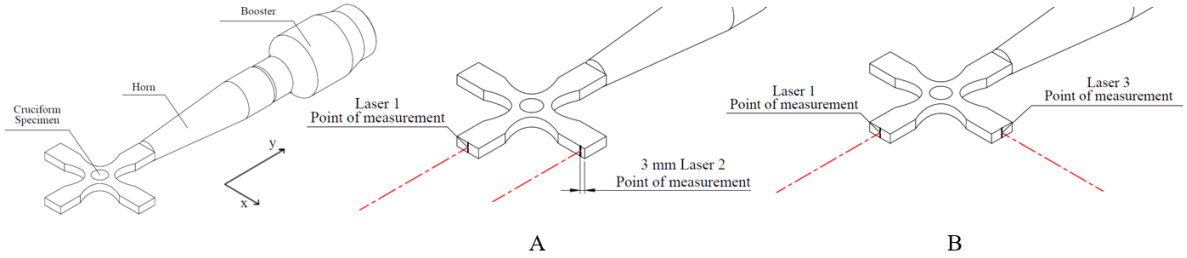

Figure 3-56. Cruciform Laser A and B laser placement setups for modal FDD and power to displacement analysis.

The 'flapping motion' proved unavoidable even with a high-frequency difference between MI and PM, such as for C-T specimens. The 'flapping motion' is associated with how PM shape is formed. The always present frequency difference between the specimen and the booster horn setup will affect the specimen deformation equilibrium, resulting in a displacement node dislocation. A higher or lower specimen frequency will move the displacement node slightly up or down, respectively. Not having the displacement node at the midpoint, the overall vertical displacement readjusts to equilibrium. The 'flapping motion' compensates and brings vertical displacement equilibrium to the final excited mode shape.

The steady-state analysis shows the vertical displacement change as the setup is under different frequency excitation. The vertical displacement is almost nonexistent when the setup is excited closer to the specimen's own frequency. On the contrary, for further away frequencies, the vertical displacement increases.

Figure 3-57 shows all three points of interest across the frequency established range for the new N T-T specimen within the booster tapered horn. The phase between the three points is also plotted in Figure 3-57 across the frequency range.

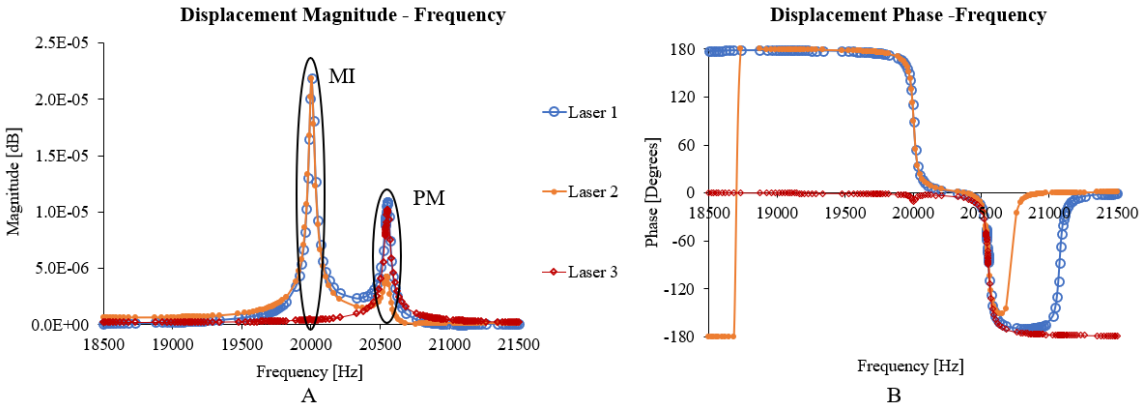

Figure 3-57. Booster tapered horn N T-T cruciform setup steady-state modal laser 1 to 3 displacement magnitude (A) and phase (B).

Just as with the tension-torsion FE analysed setups, several other resonant modes are present within the studied frequency range. Only MI and PM have a compliant mode shape with the transducer excitation. Laser 1 and 3, associated with PM mode shape, have a considerable displacement magnitude at the PM frequency. A phase change between laser 3 and 1/2 after MI to PM is present. It will allow easy experimental resonant mode identification.

Table 3-18 shows the obtained frequency and the magnitude ratio between lasers. Experimentally Laser 1 is the referenced measure; therefore, the calculated numerical ratios also have Laser 1 as the reference.

Table 3-18. Complete setup ultrasonic cruciform steady-state laser ratios in MI and PM frequencies.

Specimen	**Horn**	**MI L1/L2**	**MI L1/L3**	**PM L1/L2**	**PM L1/L3**	**L1 MI/PM**
F*x* T-T	Tapered	1.00	33.28	1.66	0.82	1.90
	Hyperbolic	1.00	34.06	2.03	0.69	2.07
N*x* T-T	Tapered	1.00	50.63	2.59	1.07	2.01
	Hyperbolic	1.00	48.89	3.50	0.87	2.21
C-T *x*	Tapered	1.05	36.75	0.37	0.65	3.34
	Hyperbolic	1.04	44.11	-	-	-

The booster hyperbolic C-T PM frequency is outside the steady-state scope of analysis, and therefore no displacement magnitude and phase were taken. Every resonant mode outside the established range was considered to never influence the result. From the F T-T to N T-T, a slight improvement is observed by Table 3-18 in both horn setups. The L1 and L2 have a lower PM magnitude in relation to MI. L3 also has a lower magnitude value in MI for N T-T

cruciform. Therefore, N T-T specimens present a lower PM magnitude of excitation and a lower overall influence over the final MI mode shape excitation.

The ‘flapping’ PM motion showed to always be present even with an almost perfect 20 kHz frequency numerical specimens and setup. The arms flapping will not only affect the horizontal laser L2 measurement, but it can also influence the final induced stress. As it will later be proven by experimental measurements, the ‘flapping motion’ will increase or decrease the L2 amplitude depending on L2/L3 phase. Therefore, understanding the ‘flapping motion’ is vital when defining a measuring methodology and respective analytical solution towards the fatigue region induced stress determination.

A detailed analysis of the steady-state results was again conducted to understand how it is induced and what affects its amplitude. From observation of the cruciform deformation across the frequency within a given setup, the ‘flapping motion’ was deduced.

The tension-compression ultrasonic specimen mode shape has proportional deformation in both directions. Half the specimen stretches/compresses in an equal amount from the displacement node at the center. The same applies to the cruciform specimen. The vertical and horizontal arms deform in equilibrium with the center displacement node as the symmetry axis. This is only achieved in the natural frequency of the resonant mode of interest MI. If the specimen is forced to be excited at a different frequency, the wave propagation will be different, and the displacement node (symmetry axis) may change. The frequency difference is inevitable since the booster horn and specimen will never have a perfect 20000 Hz frequency. For the tension-compression specimen, this effect is negligible. This effect is also negligible regarding the cruciform vertical arms, just as the axial specimen. However, for the horizontal arms, the symmetry axis deviation forces an orthogonal deformation to compensate for the non-symmetry, the ‘flapping motion’. A higher or lower forced frequency will move the displacement node up or down, respectively. The node tends towards the low stiffness regions, the smallest cross-section area in the cruciform midpoint. Nevertheless, a slight deviation still occurs.

To better perceive the described behaviour, the N T-T specimen was subjected to a steady-state FEA without the booster horn setup. The excitation unitary force was directly applied on one considered vertical arm. This analysis showed how the specimen responds when excited with higher and lower frequencies than its natural frequency. The vertical displacement across the same frequency range was computed for the L1 and L3 locations. Figure 3-58 shows the L3/L1 ratio across 18.5 to 21.5 kHz.

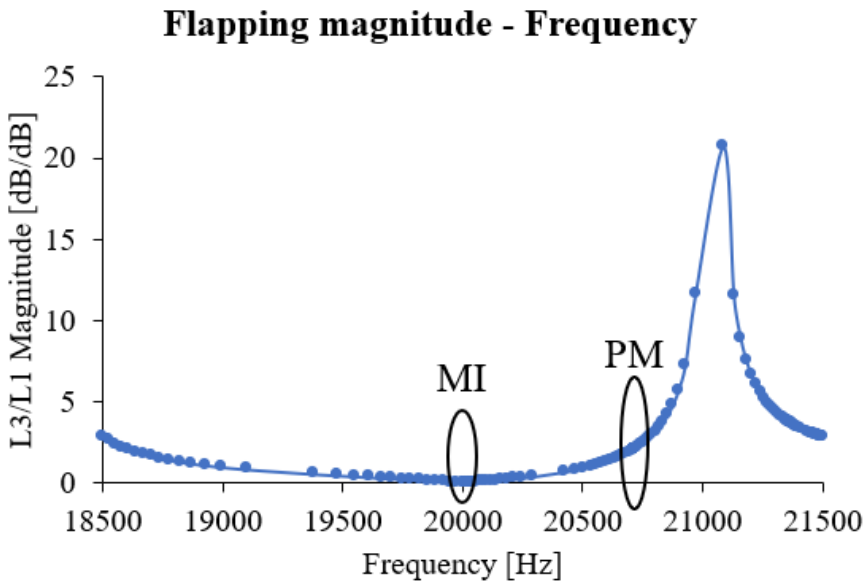

Figure 3-58. 'Flapping motion' study FEA steady-state L3/L1 result.

As perceived, at the specimen natural MI frequency, no flapping motion is present. In lower and higher force excitation frequencies, the flapping motion increases. We can deduce from the results that the 'flapping motion' is not only associated with the PM. It is also caused by the frequency difference between the specimen and the setup. It is this 'flapping' behaviour that will lead to the PM modal shape. Figure 3-59 shows the vertical cruciform displacement in natural frequency and higher and lower excitation frequencies. The colour scale was limited to perceive the horizontal arms vertical displacement distribution.

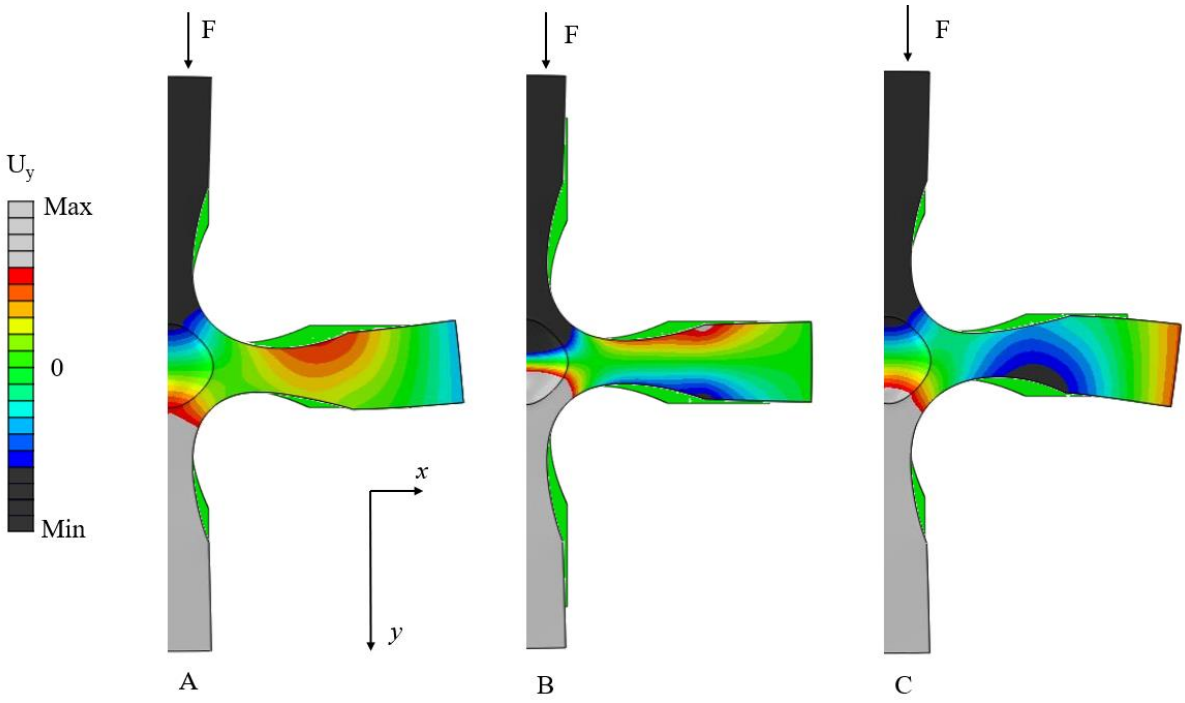

Figure 3-59. N T-T cruciform steady-state analysis vertical displacement distribution response for frequency of excitation: (A) MI -100 Hz; (B) MI; (C) MI +100 Hz.

The formation and phase of the ‘flapping motion’ can be perceived between Figure 3-59 A and C with lower and higher excitation frequencies. The phase to which the vertical ‘flapping motion’ (L3) has concerning the vertical displacement of the vertical arm (L1) will change by the specimen-setup frequency difference. For Figure 3-59 N T-T cruciform, ‘flapping motion’ is in-phase when exciting the specimen in higher frequencies (C) and out-of-phase in lower frequencies (A).

The analysis also shows a unitary only L1/L2 ratio at the natural frequency. Both FEA and experimental measurements show that the ‘flapping motion’ will increase the horizontal displacement amplitude when in-phase and decrease in out-of-phase.

The following proposed analytical solution was only achieved through FE in-detail analysis together with experimental results. The discussed concepts will bring the ultrasonic tension-compression analytical solution method to cruciforms, and it will also allow for the determination of FEA displacement to stress ratio, later compared with the experimentally obtained. The steady-state results linked the displacement and stress between each arms’ direction. Displacement to stress ratio has a linear behaviour as expected, since the specimen is deforming in the linear-elastic domain, and it will be compared with the laser measurements and strain gauge experimental procedure.

3.5.2.3 Analytical solution

The proposed analytical solution's main objective is to provide a deterministic process for the induced stress within the UFT. The already presented tension-compression analytical solution method measures the highest displacement amplitude at the specimen's free base and determines its relation to the induced stress. Having a reliable analytic method allows for the execution of UFT without the use of strain gauges and standardizes the ultrasonic fatigue methodology.

The following analytical concept considered the cruciform geometry as two figurative perpendicular plane specimens with one shared fatigue testing region. The associated stress is then determined by measuring the displacement at each cruciform arm's end (the free base of the figurative uniaxial specimens).

Two different combinations of axial specimens' are possible from the cruciform geometry. Each combination was considered as 'Slices' (S*x*) made to the cruciform arms. Plane S specimen defining dimensions were then associated with the cruciform dimensional variables of Baptista et al. [46]. Figure 3-60 shows the two possible 'slices' (S1 and S2) in a cruciform specimen with Baptista et al. cruciform and Bathias tension-compression specimen variable designations.

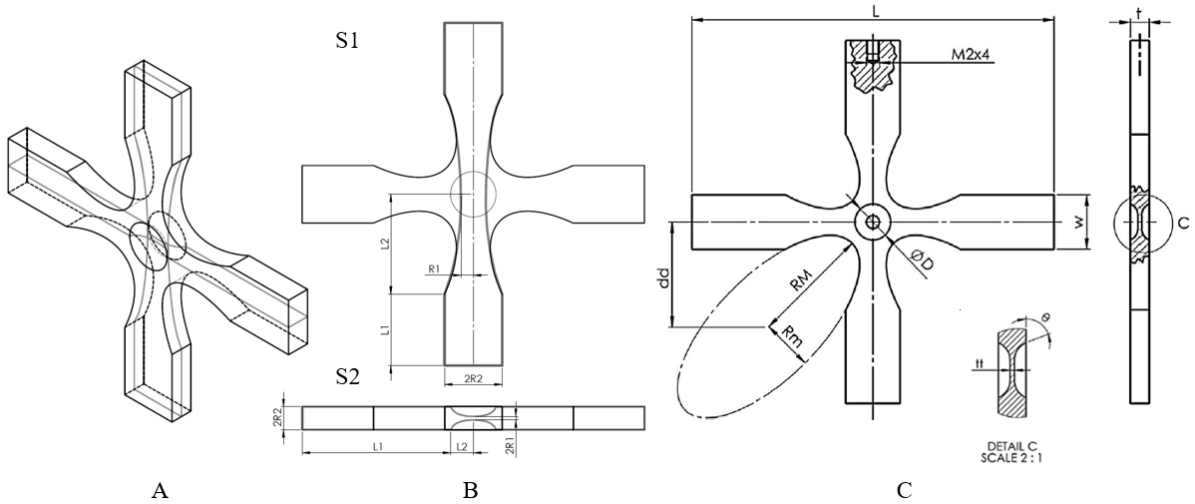

Figure 3-60. Cruciform equivalent uniaxial plane S specimen representation: (A) 3D cut representation; (B) S1 and S2 dimensional variables; (C) Optimised geometry by Baptista et al. [54].

For S1 and S2 slices, one equivalent dimension needs to be determined: R1 for S1; and L_1 for S2. The determined dimensions will ensure an equivalent 20 kHz uniaxial specimen. For S1, R_1 is iteratively determined by changing its value until the cruciform equivalent L_1 is equal

to the determined by the tension-compression analytical method. L_1 for S2 is determined following base tension-compression methodology, just as analytically conducted to the ultrasonic tension-compression specimens. Both S1 and S2 follow an exponential curvature.

FEA's cruciform arms stress distribution is not as straightforward as the uniaxial specimen's overall distribution. The S plane figurative specimen that presents the lowest stress gradient difference is chosen accordingly. Figure 3-61 compares S 'slices' with the New T-T (N T-T) and C-T specimens FEA obtained stress gradient results. An Approximation is also plotted for both presented specimens' results.

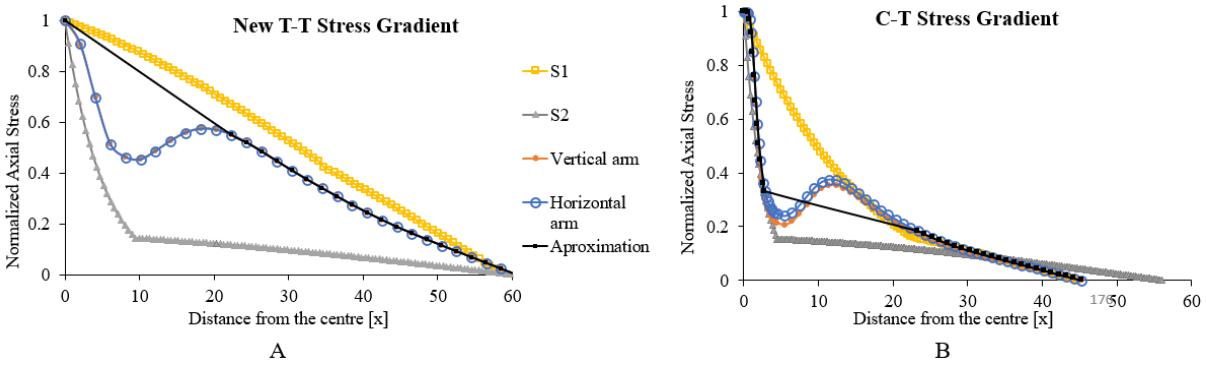

Figure 3-61. Normalised stress distribution of N T-T (A) and C-T (B) vertical and horizontal arms, corresponding S1 and S2 'slices'; made Approximation.

The resulting distribution across the arms to the centre differs significantly between T-T and C-T specimens. From Figure 3-61 observation, the S stress distribution that better represents the cruciform arm's Approximation made is chosen. The T-T specimens follow the S1 distribution, while C-T specimens follow closer to S2. The cruciform varying stress distribution tendency is associated with the complex deformation occurring in the specimen's connection between the arms. The Approximation made was only considered after studying the stress distribution across the complete volume of the arms and the arm-to-arm connecting region.

C-T specimens have a stress increase before the arm-to-arm connection, followed by a subsequent decrease reaching the connection region. While T-T specimens only present a change in the arm-to-arm connection region with low deformation in the centre line and a high at the corner between arms. Figure 3-62 associates Figure 3-61 stress distribution to the FEA arms geometry stress distribution regions.

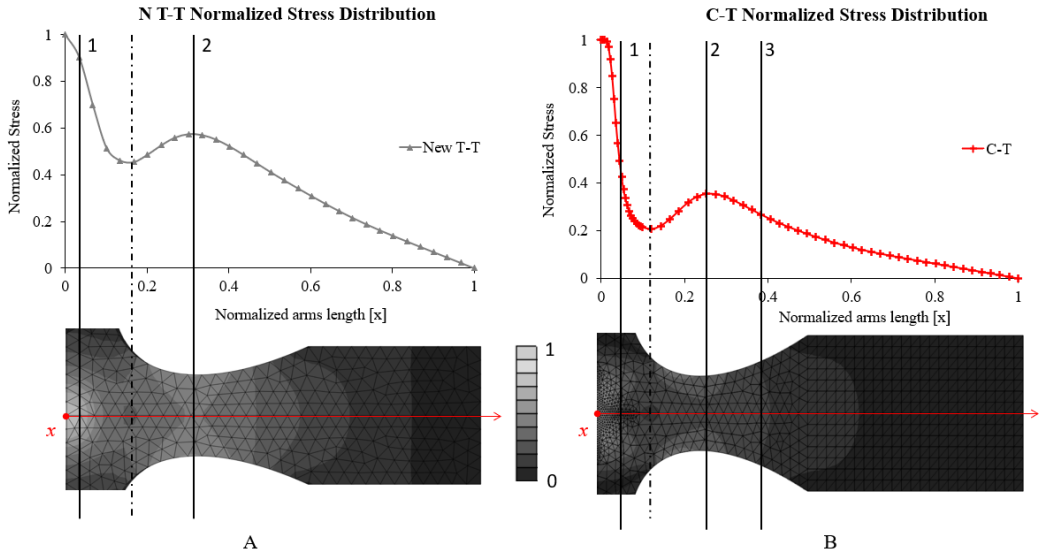

Figure 3-62. N T-T and C-T normalised stress distribution across the length of one arm.

By FEA, the irregular stress distribution was proven not influential on the initial and final tendency and all specimens' maximum centre stress amplitude. There is still a continuous stress increase tendency from the arms tip towards the centre. From Figure 3-62, a normalised stress distribution applied to the identified regions can be considered since the cross area does not present and uniform stress distribution. Therefore, the made Figure 3-61 Approximation that follows the stress distribution initial and final tendency was considered applicable for the analytical stress determination.

The still present stress distribution differences between the selected S*x* and the Approximation are adjusted through Strain energy (*U*). The energy input made by the ultrasonic setup will correspond to the total strain energy of the sample if no damping effects and connection friction between components are considered. Hence, the total U will be equal between cruciform arms and the 'Slices'. Since the S slices are designed from the cruciform, they have a similar volume distribution as the cruciform arms, and therefore were considered as equal. If the volume distribution is considered equal and the total energy input is the same, the only variable difference is the stress distribution. The logic concept is represented in equations (3.6) to (3.8).

$$U = \int \frac{\sigma^2}{2E} dV \tag{3.6}$$

$$U_{cruciform} = U_{Slice} \tag{3.7}$$

$$\frac{\sigma^2_{cruciform}}{2E} dV \equiv \frac{\sigma^2_{Slice}}{2E} dV \rightarrow \sigma_{cruciform} = \delta \cdot \sigma_{slice} \tag{3.8}$$

The strain energy correction is conducted through the stress distribution area. The strain energy is added or removed if the S stress area is higher or lower. The area difference compensation factor (δ) is then introduced in tension-compression exponential curvature analytical solution for the strain distribution. The resulted equation (3.9) for the considered exponential curve becomes

$$\begin{cases} \varepsilon(x) = EA_{0i}(1+\delta)\varphi(L_1, L_2)[\beta\cosh(\beta x) - \alpha\sinh(\beta x)]\exp(-\alpha x), for\ x \le L_2 \\ \varepsilon(x) = E \cdot k \cdot A_{0i}(1+\delta)\sin\big(k(L-x)\big) \qquad\qquad , for\ L_2 < x \le L \end{cases} \quad (3.9)$$

Where ε_i is the strain and A_{0i} is the measured displacement amplitude in the *i* direction (*x* horizontal arm, *y* vertical arms). Equation (3.9) is applied for both the *x/y* measured displacement amplitudes. Figure 3-63 shows the determination of area difference compensation factor (δ) from the N T-T specimen stress distribution plotted in Figure 3-61.

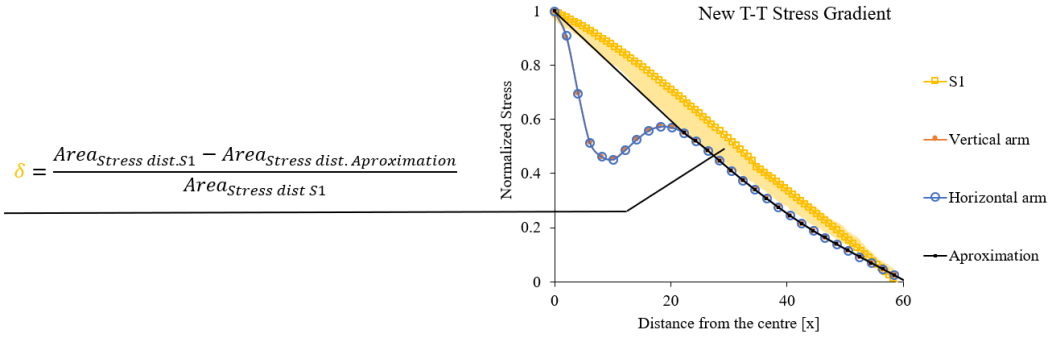

Figure 3-63. Area difference compensation factor (δ) determination method for N T-T cruciform specimen.

As previously perceived, all tested ultrasonic cruciform specimens exhibit a 'flapping motion' resulting in higher or lower horizontal arm *x* displacement (A_{0x}) amplitude depending on the flap movement phase with the vertical arms *y* displacement (A_{0y}). The associated motion is independent of the excited resonant mode (T-T or C-T) and independent of the cruciform geometry.

The hereby proposed correction associates the *x-y* amplitude difference and not the geometry itself. The designated 'flapping motion' factor (γ) is then introduced in equations (3.9) through the area difference factor (δ). The flapping motion factor was empirically determined through all the measured amplitudes and strains. Two different factors were empirically for each 'flapping' motion phase. Equation (3.10) shows the flapping motion correction to be applied in accordance with the x-y amplitude differences.

$$\begin{cases} \gamma = \delta_{x,corrected} = \left(\delta - 1.75\frac{A_{0x}-A_{0y}}{A_{0y}}\right), & for\ A_{0x} \geq A_{0y} \\ \gamma = \delta_{x,corrected} = \ (\delta - 0.75\frac{A_{0x}-A_{0y}}{A_{0y}}), & for\ A_{0x} \leq A_{0y} \end{cases} \quad (3.10)$$

The Hooke's law for isotropic materials is afterwards calculated with null shear strain for the determination of the midpoint (x=0; y=0) biaxial stress state.

$$\begin{bmatrix} \sigma_x \\ \sigma_y \\ \sigma_{xy} \end{bmatrix} = \frac{\mathrm{E}}{1-\nu^2}\begin{bmatrix} 1 & -\nu & 0 \\ \nu & 1 & 0 \\ 0 & 0 & 1-\nu \end{bmatrix} \cdot \begin{bmatrix} \varepsilon_x \\ \varepsilon_y \\ 0 \end{bmatrix} \quad (3.11)$$

As explained, FE steady-state analysis can determine a displacement to stress ratio. The 'flapping' motion factor (γ) can also be applied to FEA determined ratio towards an corrected experimental stress determination solution. The FEA displacement to stress ratio can be correctly applied with γ to the measured *x* displacement (A_{0x}). For FEA, γ equation (3.12) is calculated directly to A_{0x} followed by the numerical determined ratio for stress determination.

$$\begin{cases} A_{0x,corrected} = A_{0x}\left(1 - 1.75\frac{A_{0x}-A_{0y}}{A_{0y}}\right), & for\ A_{0x} \geq A_{0y} \\ A_{0x,corrected} = A_{0x}\ (1 - 0.75\frac{A_{0x}-A_{0y}}{A_{0y}}), & for\ A_{0x} \leq A_{0y} \end{cases} \quad (3.12)$$

The analytical and FEA methods for displacement to stress were applied and compared with the strain gauge results for all three tested cruciform geometries.

4

Material, Equipment and Experimental Methodology

4.1 Introduction

In this chapter lays the experimental base of this work. Every used and improved equipment, in every conducted experiment test, on all applied materials are described in detail.

The study revolved around the built ultrasonic fatigue machine in the mechanical and materials testing laboratory in Instituto Superior Técnico. The already built ultrasonic machine was under intense improvements in electronics, data acquisition and supporting structure before the beginning of all experimental testing. The improvements also considered the assembly of the new pure torsion ultrasonic fatigue machine. All introduced additions and enhancements are presented in detail as all present and used equipment.

All simple mechanical testing experiments for material mechanical properties determination are also discussed. As explained, it is imperative not only for fatigue characterisation but also for ultrasonic specimen design to determine static material properties such as Young's modulus, yield stress, hardness, and metallurgical phase. The methodology and associated results are presented for every tested material except aluminium. All aluminium ultrasonic experiments were done in conjunction with Bournemouth University, where all static mechanical properties determinations were made.

For the titanium alloy ultrasonic specimens, a 3D structured-light scanning and roughness quantification was conducted for all specimens before and after being polished. The scanning and polish procedure is fully described, and the polish treatment changes on the surface roughness.

After the used machines, equipment description and static experiments, the methodology for all ultrasonic fatigue conducted tests is thoroughly presented for every conducted test and specimen.

4.2 Material Static Characterisation

Three different materials were put under mechanical analysis: Aluminium 6082-T651; steel alloy AISI P20; Ti6Al4V titanium alloy. The Bournemouth University conducted all static characterisation tests on the tested aluminium.

All Ti6Al4V specimens were manufactured by the SLM AM method in a single printing sequence. AISI P20 samples were machined by conventional methods from one acquired cylindrical profile. Table 4-1 presents the chemical composition for AISI P20 and Ti6Al4V.

Table 4-1. AISI P20 and Ti6Al4V Eli Grade 23 chemical composition.

AISI P20 Chemical Composition [%]							
Fe	Mn	Cr	Ni	Mo	C	S	Si
0.95	1.39	1.88	1.01	0.17	0.36	0.001	0.27
Ti6Al4V Eli Grande 5 Chemical Composition [%]							
Ti	Al	C	V	Y	Fe	O	N	H
0.88	6.5	<0.08	4.5	<0.005	<0.25	<0.13	<0.05	<0.012

The Young's modulus is one main property for designing and executing ultrasonic fatigue tests. All tested materials required tensile experiments tests for Young's modulus determination. The ASTM E8 / E8M standard test method and specimen design for tensile testing of metallic materials were carried out in an Instron 5566 electromechanical tensile machine. An Instron clip-on strain gauge was applied to all conducted tensile tests and removed before facture. All tensile specimens were lightly polished to remove visible damage that could have influenced the final fracture and overall results.

All tensile test strain/stress results were plotted and evaluated. Figure 4-1and Figure 4-2 shows the calculated stress/ strain result from the AISI P20 and Ti6Al4V tensile tests, respectively.

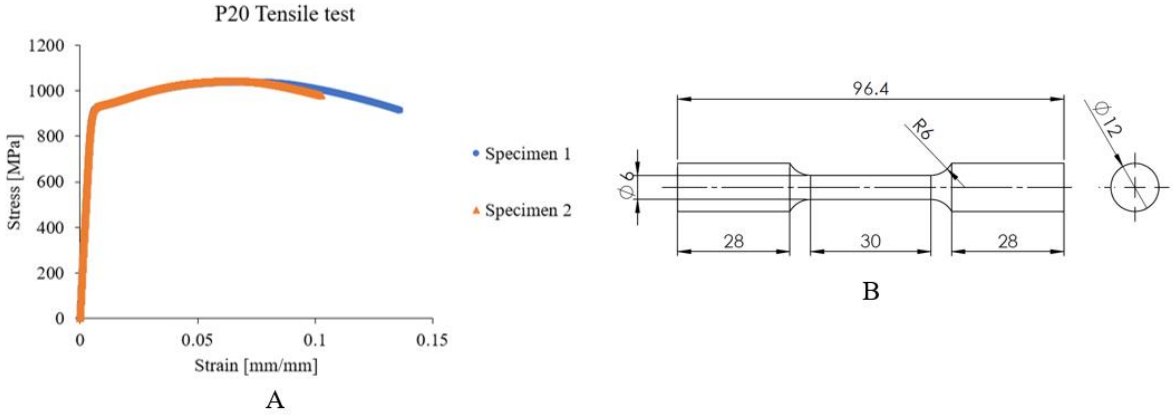

Figure 4-1. Ti6Al4V Static tensile experiment: (A) Stress-strain obtained curve; (B) Tensile specimen technical drawing.

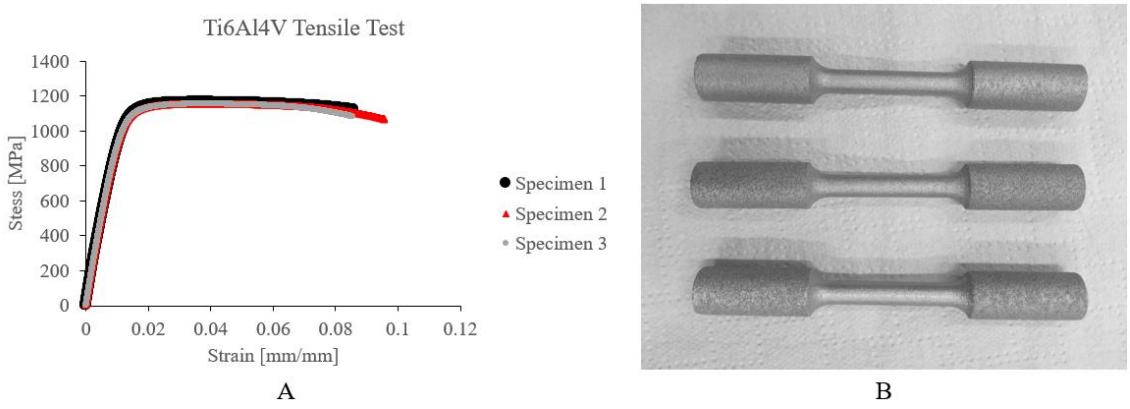

Figure 4-2. Ti6Al4V Static tensile experiment: (A) Stress-strain obtained curve; (B) Tensile specimens.

The Young's modulus, yield stress, and tensile strength were determined from all conducted tensile tests. Both materials showed ductile deformation and fracture surface behaviour.

Vickers hardness tests were also conducted on every tested material. A section of the AISI P20 cylindrical bar profile was cut for hardness testing, while for Ti6Al4V, a tested tensile specimen was cut in several sections. Both samples were tested across their diameter and in all different sections. No considerable variance was measured across their diameter on both Ti6Al4V and AISI P20. All tested surfaces were first polished to a mirror-like finish.

A Ti6Al4V tensile specimen was cut into four sections along its length. The purpose of the test was to understand if the distance from the printing heat plate had an effect on the hardness distribution of the material Figure 4-3 shows the sectioned specimen with respect to the printing direction.

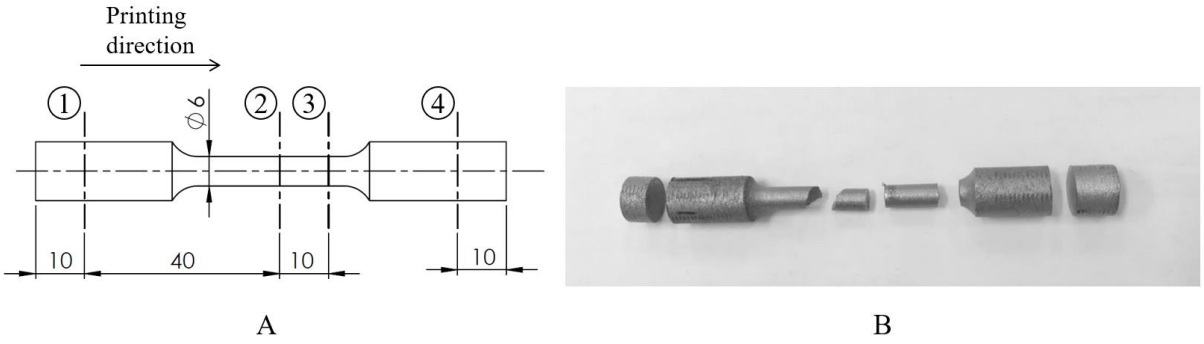

Figure 4-3. Tensile specimen sliced sections for hardness and micrography analysis.

Table 4-2 presents the average value and deviation between all measured results from tensile and hardness conducted experiments.

Table 4-2. AISI P20 and Ti6Al4V material static properties.

Material	**Young's Modulus, E [GPa]**	**Yield Stress, $\sigma_{0.2\%}$ [MPa]**	**Ultimate Stress; σr [MPa]**	**ε_{max} [%]**	**Vickers Hardness [HV]**
Ti6Al4V	100 ±2	1031 ±5	1161 ±10	8.9±0.5	380-420
AISI P20	202 ±3	923.5 ±4.5	1040 ±4	11.5±1.5	308-330

4.2.1 Surface and Dimensional Analysis

The ultrasonic fatigue research associated with Ti6Al4V experiments studied the influence of surface roughness on fatigue strength within the VHCF regime. Both rough (as-built) and polished specimens were subjected to UFT to study the surface effect on the VHCF regime. All fatigue results from cycle to failure and fatigue fracture mechanism were then compared. The impact on surface polish treatment is associated with the surface roughness and depth of removed material. To quantify the removed material, optical structured-light scanning (SLS) was made in all specimens. As for the surface roughness quantification, an interferometer machine was used.

The proceeded polish treatment was made in several sequences. Different grid sanding papers were sequentially applied up until a final 5000 grit paper. Only the specimen's hourglass throat was polished to maintain the base geometry unchanged as much as possible. Ultrasonic machines work with resonance; changing the specimen base geometry by post-treatment may alter its resonance frequency. Since the resonant specimen deformation is not uniform along its length, being considerably higher in the centre, the maintained rough surface on the remaining regions will not cause unpredicted failure when testing. The effect of the polishing treatment in the ultrasonic specimen behaviour is later shown in chapter 5.2.

As the specimens were polished, the surface was continuously checked through an optical microscope. The process was only finished when no visible defects were present. Figure 4-4 shows an example of a specimen's surface treatment sequence, from an as-built surface (Figure 4-4.A) to a mirror-like polished surface (Figure 4-4.F).

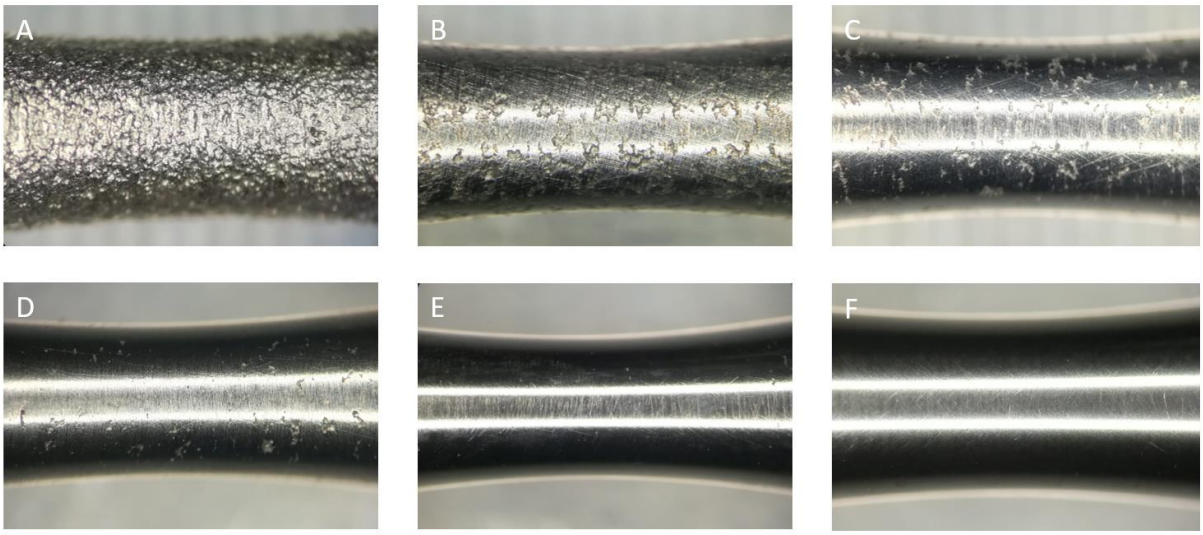

Figure 4-4. Ti6Al4V specimen surface polishing sequence from A to F.

As shown in Figure 4-4.A, the as-built surface quality of the specimens manufactured by SLM presents a considerable high roughness. The surface roughness was measured at different points in the SLM ultrasonic fatigue and tensile specimens through a Profilm 3D interferometer. Figure 4-5 compares the resulting interferometer surface representation of a

rough and polished surface. Figure 4-6 presents the obtained low surface roughness plot for a polished surface.

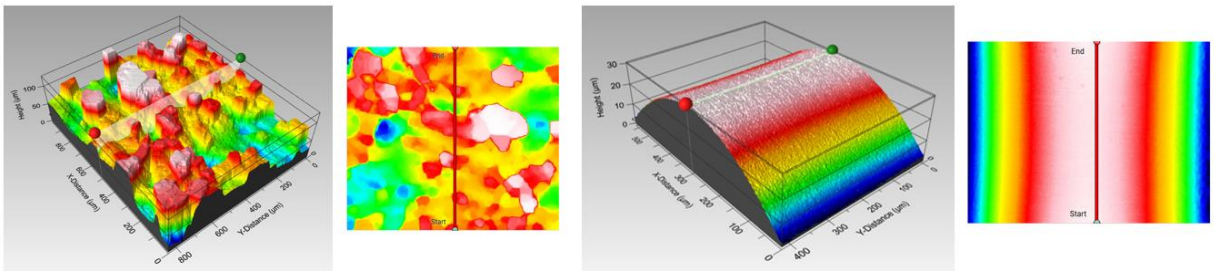

A B

Figure 4-5. Interferometer rough surface results: (A) 3D representation; (B) Top view; (C) Line surface plot.

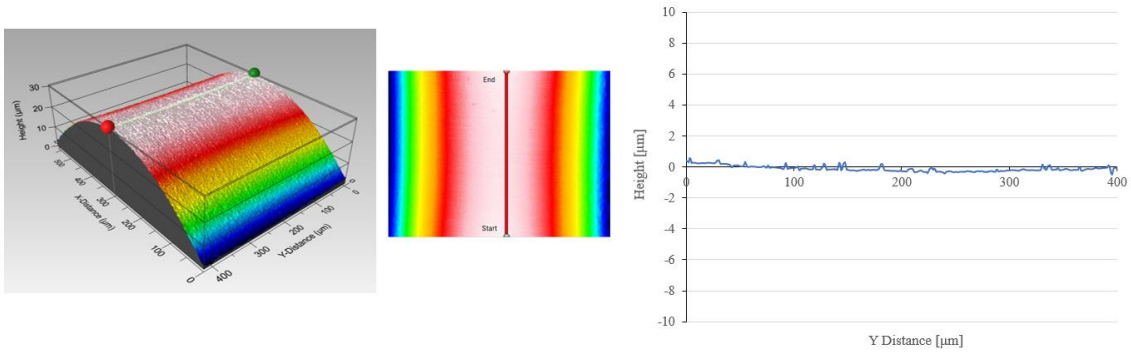

A B C

Figure 4-6. Interferometer polished surface results: (A) 3D representation; (B) Top view; (C) Line surface plot.

Table 4-3 shows the average arithmetic mean deviation (Ra), maximum height (Rz), maximum peak height (Rp) and maximum sample peak to valley height (Rz1max) following the parameters definition of the standard ISO 4287 [34].

Table 4-3. Average ISO 4287 norm surface roughness.

[µm]	**Ra**	**Rz**	**Rp**	**Rz1max**
As-built	2.04	10.16	5.14	21.81
Polished	0.09	0.89	0.46	1.18

The SLS Zirkonzahn S600 machine was provided by Faculdade de Medicina Dentária faculty of University of Lisbon. The used machine is fully automated with two high-resolution, high-speed cameras having a scanning precision of 10 micrometres. It was made for dental applications, but it could scan all specimens. SLS method can achieve high precisions within a considerable low scanning time, but it also brings some challenges and limitations. Any reflecting or transparent surface will damage the resulting quality or will not even appear in the

scan. A first 3D scan with a rough and polished specimen showed the errors associated with metallic surfaces. A thin layer of anti-reflection spray was applied to all specimens. Since all available supports were intended for dental moulds, custom support for the machine was machined to correctly fix all specimens at the centre. A line and a dot reference mark were made to the specimens. The line and dot functioned as a 3D analysis enabling a correct overlap of the two made scans of the same specimen (rough and polished). The machined support, the line and dot referenced, and an SLS scan in progress are shown in Figure 4-7.

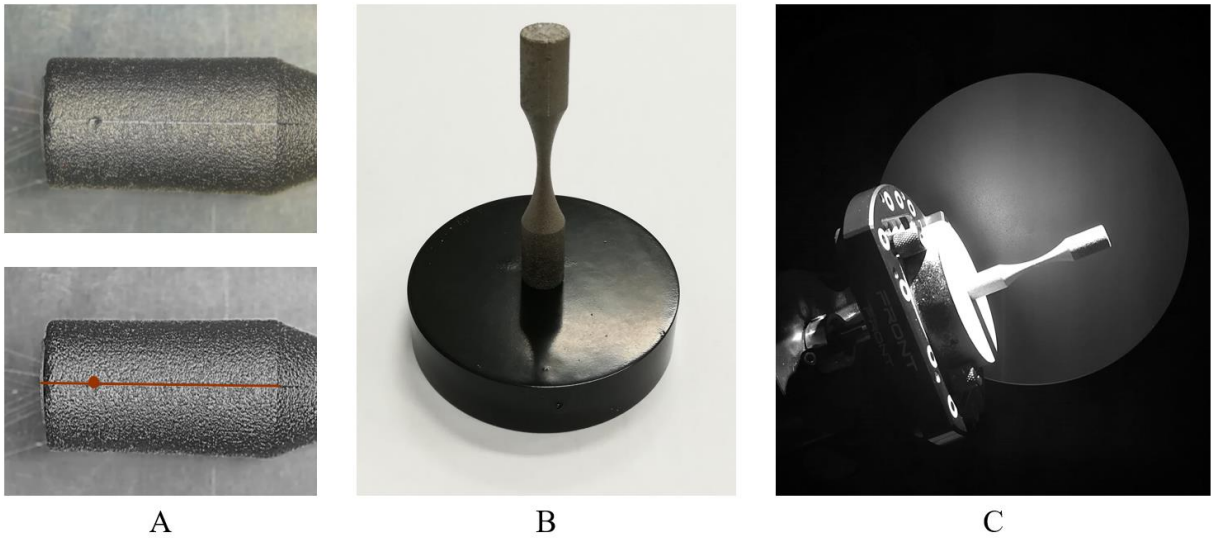

A B C

Figure 4-7. Ti6Al4V 3D analysis: (A) reference dot and line; (B) machined base and specimen; (C) SLS scan in progress.

The SLS scans also provided a dimensional tolerance quality of the SLM AM method. Table 4-4 shows the average measured value and the respective deviation of all base ultrasonic specimen dimensions.

Table 4-4. Polished Ti6Al4V ultrasonic specimen 3D scan measured dimensions and lowest cross-section variance.

Specimen	**Dimensions [mm]**			**Lowest cross-section diameter [mm]**	
Nº	L_1	R_2	L_2	Before polishing	After polishing
6	16.09	9.89	30.05	3.05	2.94
7	16.1	9.93	29.99	3.09	2.96
8	16.1	9.84	29.99	3.02	2.92
9	16.07	9.91	30.19	3.01	2.94

The removed layer was quantified by the SLS scan dimensional differences between a specimen as-built and polished state. A removed layer between 40-55 μm was measured, having only one specimen a higher 75 μm removed layer. The removed layer complies with the interferometer highest and lowest surface peak range oscillating from 40 to 80 μm between measurements, with a 55 μm average value between all conducted roughness measurements.

4.2.2 Microstructure Analysis and Defect Quantification

In subchapter 2.3.5, referenced research has shown that the material microstructure strongly influences its mechanical behaviour and fatigue response to high cycle deformation. Metallurgical phase analysis was therefore conducted. As in the hardness test, a section of the AISI P20 acquired profile was cut and analysed. For Ti6Al4V, the hardness Figure 4-3 samples sections were used.

AISI P20 presented a martensitic structure. Figure 4-8 presents two different magnifications of the martensitic structure.

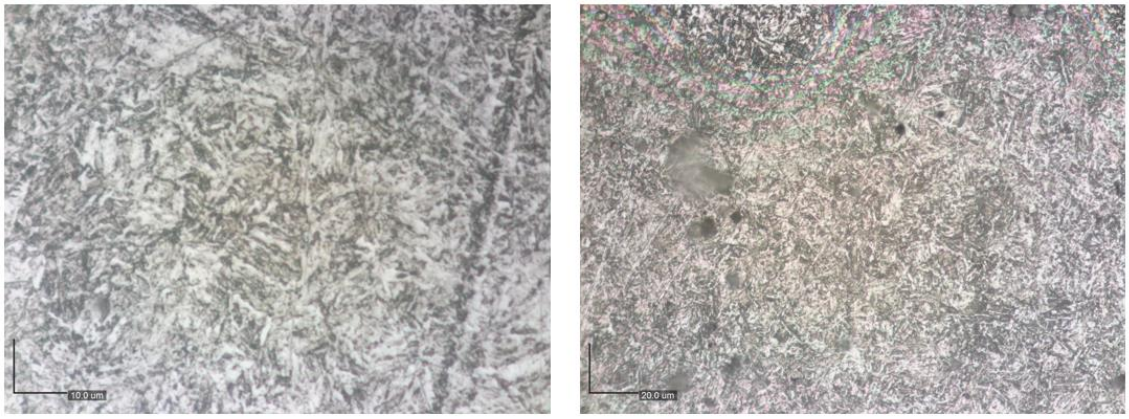

Figure 4-8. AISI P20 microstructural result analysis: (A) 40x; (B) 100x.

The Ti6Al4V obtained phase and grain size did not present any considerable differences between the observed sections at different printing heights. Figure 4-9 shows the Ti 6Al4V microstructure obtained from Figure 4-3, section 1.

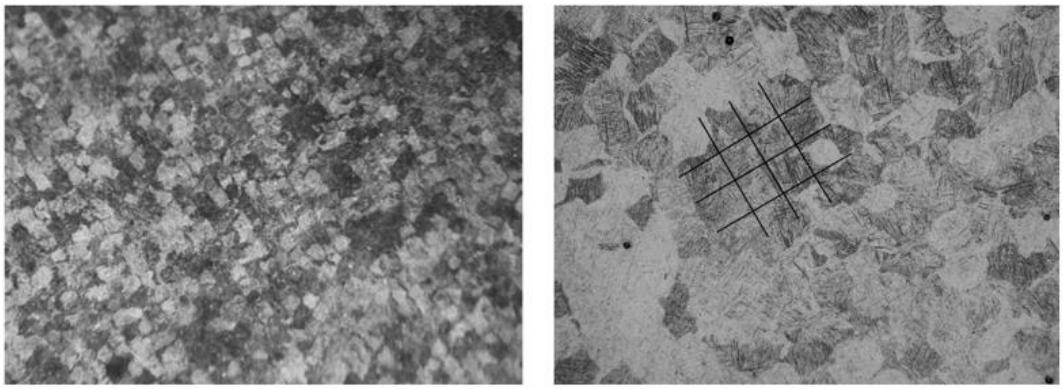

A B

Figure 4-9. Ti6Al4V microstructural result analysis of section 1: (A) 4x; (B) 100x.

The microstructure displays martensite with fine α/α' titanium phase plates. The non-present beta phase is associated with the SLM rapid beam scan and cooling rate [199]. A thorough Figure 4-9 observation shows that alpha phase plates have a square grid pattern. Following Thijs et al. research [200] in SLM Ti6AL4V printing scheme impact on the microstructure, the square grid microstructure results are related with a rotating printing direction between layers.

The type, size, shape, and density of all the observable defects were quantified from the sliced sections surfaces and fatigue fractures. Figure 4-10 shows examples of all the different observed defects observed by SEM: inner gas pores, smooth facet and lack of fusion.

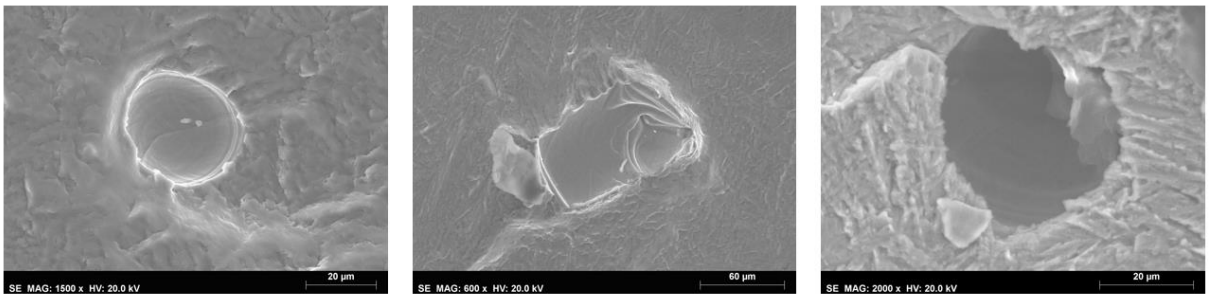

A B C

Figure 4-10. SEM observed different types of observed defects: (A) Inner gas pore; (B) Smooth facet; (C) Lack-of-fusion.

From all observed surfaces, the pores spherical shape varies in radius between 6 and 58 μm, with a 27 μm average between all measured pore diameters. No difference in pore density from the centre to the free surface was observed. A considerably higher number of pore defects were present in all observed surfaces than lack of fusion and smooth facets defects.

4.3 Ultrasonic Fatigue Machine Structure and Equipment

A new structure was built to suit all the new developments studied and experimentally tested. The new structure was designed to have: a new ultrasonic pure torsion device, new ultrasonic setups for uniaxial and multiaxial testing, complex experimental analysis, and various equipment.

The newly built structure took into consideration the construction of the new pure torsional ultrasonic fatigue and the existing and improved uniaxial and multiaxial. Both machines use all available equipment with different required supports and adjustments. Thus, the rig was designed to have both machines together with the ability to interchange or add the necessary measuring and controlling equipment.

Bosh skeleton profile provided the necessary versatility in rearrangements of all used equipment. Three stone slabs were placed, two on the base and one under a sensor placement table. The stones provided structure stability and reduction of unwanted vibration. Rubber was placed between every tone slab and the structure. Figure 4-11 presents the built structure rig photographs with the two ultrasonic machines, the DAQ system with interchanging channels, and all measuring equipment and colling system.

Figure 4-11. Built ultrasonic structure rig and (A) Pure torsion machine; (B) DAQ system; (C) tension-torsion setup with cooling system and temperature pyrometer control sensor.

Each ultrasonic piezoelectric machine has its respective piezoelectric transducer, controller and components set. Both share the measuring equipment and Data Acquisition DAQ systems. A dual-channel Laser Polytec OFV 2802 doppler vibrometer machine (Figure 4-12) is used for displacement measurement and for strain gauge experiments, single or rosette strain gauges, the Dynamic Wheatstone bridge hardware strain signal conditioner.

Figure 4-12. Polytec OFV 2802 doppler-vibrometer: (A) fibre interferometer; (B) Laser output lens; (C) Controller electronics unit.

Figure 4-13 shows the used dynamic Wheatstone bridges, Strain Gauge Conditioning Amplifier 2310. The strain output measurement comes in ±10 volts. Gain calibration is required for the output voltage – strain relation.

Figure 4-13. Dynamic Wheatstone 2310 Signal Conditioning amplifier.

One pyrometer for each machine was employed to measure and control the specimen's temperature. A Thermal camera was also employed to identify where the highest temperature generation regions for every tested specimen were.

From temperature to strain, all mentioned measuring equipment returns a voltage analogue output to the DAQ system. The DAQ has an analogue to digital converter for computer data recording. All data in each channel was recorded with a 300 kHz minimum acquisition rate. The DAQ system also controls the Branson piezoelectric transducer's power and on/off through its signal generator controller. Figure 4-14 shows the overall equipment scheme for tension-compression and tension-torsion setups. The same equipment scheme is followed for the pure torsion and cruciform setups.

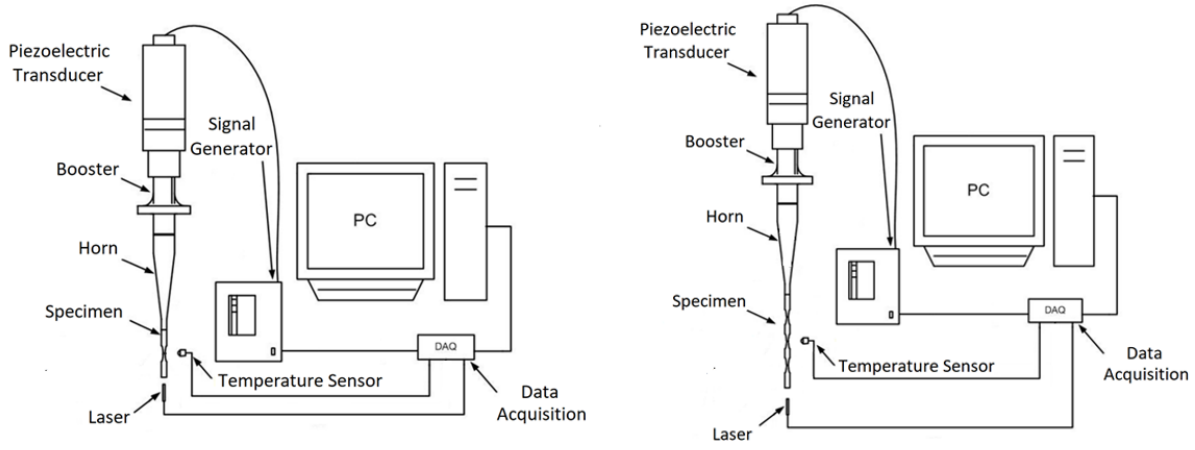

Figure 4-14. Ultrasonic fatigue machine measuring and controlling equipment scheme.

All conducted experiments' control and acquisition of data were made through a LabView software program and two National Instruments DAQs hardware. Significant improvements were also made to the LabView controlling software. The new LabView designed software has higher control over all testing variables. The new software enables:

- DAQ acquisition rate adjustments;
- Easy measuring equipment change and addition;
- pulse-pause fatigue test control with interchangeable pulse and pause time;
- Fatigue tests with or only by temperature control with easy temperature high and low input limits;

- Modal experimental testing and power-displacement calibration testing with low experimental times to safeguard both the specimen and applied strain gauges;
- Average temperature, displacement, power, cycles and frequency across the complete fatigue testing;
- The new software also allows for easier troubleshooting and a no transducer test simulation for verification

All recorded data is exported as a column base .txt file and afterwards imported to Matlab software for displacement analysis, stress calculations and modal analysis.

4.4 Ultrasonic Fatigue Experimental Theory, Setup and Methodology

4.4.1 Introduction

The following chapter focuses on the proceedings and methodology for modal, strain gauge and UFT experiments for all conducted ultrasonic fatigue methods.

Two main measuring experimental methods were applied: Strain gauges and laser displacement measurements. Strain gauges and laser measurements were used in all different tested specimens. From the displacement measurements, a modal analysis was conducted. The chapter introduces first the theoretical background surrounding strain gauges and frequency modal analysis.

Strain gauges were applied to the fatigue testing regions of at least one of each specimen gemetry to quantify the induced deformation at different transducer settings. A full description is made of strain gauge preparation and placement procedure, the used equipment, and the stress calculation method for all types of induced deformations.

Laser displacement measurements were made at specific points on all specimens and horns. All made experiments were done for displacement amplitude quantification and modal analysis. The complete followed procedure is also described with the associated calculations.

4.4.2 Strain and Frequency Analysis Theoretical Background

4.4.2.1 Strain gauge theoretical background

Strain gauge experimental requirements and Hoffmann's book [201] followed equations were employed. The theoretical base concept behind strain gauges is the changing electric resistance of a material when deformed. When a wire is stretched or compressed, the electrical resistance increases or decreases, respectively. Strain gauges are resistors composed of a wire grid, two terminals for each grid and a cover. By measuring the strain gauge resistance variation with induced deformation, the strain can be computed with its correlation to electrical resistance change. A few examples of different strain gauges are shown in Figure 4-15.

Figure 4-15: Strain gauge examples.

There are lines and marks for the proper alignment in the strain gauge's cover. The higher wire grind length should be aligned to the strain measurement direction of interest.

As mentioned, the strain measurement is made by the resistance variance of the strain gauge. The relation between the resistance variation and strain is a strain gauge property named Gage Factor, K that follows equation (4.1).

$$Gage\ Factor = K = \frac{dR/R}{\varepsilon} \tag{4.1}$$

To measure strain gauge resistance variation (dR) Sir Charles Wheatstone devised a specific circuit. He self-named it the Wheatstone bridge. The Wheatstone bridge is composed of four resistances with the same Ohm value when no deformation is yet applied. The way the measurement is made and calculated depends on the number of applied strain gauges and their placement in the component under testing. Figure 4-16 shows a representation of the Wheatstone bridge, where the R_i are the four different resistances that can be strain gages, U_B is the input voltage, and the V_0 is the output voltage.

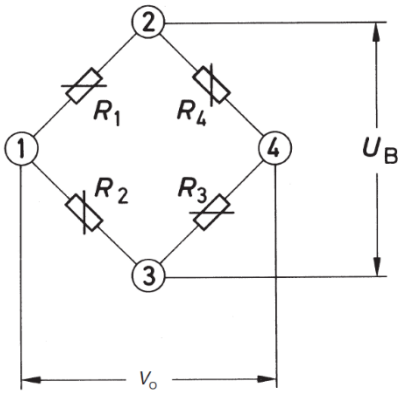

Figure 4-16. Wheatstone bridge circuit representation

One, two or four strain gauges can be applied corresponding to a quarter, a half and a full Wheatstone bridge, respectively. Each bridge has different relations between resistances, input and output voltage and the resulting strain.

Testing strain gauges at different temperatures to ambient or/and considerable temperature variation affect the base electric resistance and gauge factor. This strain gauge altering effect can be compensated by two different means. All strain gauges come with temperature compensation and gauge factor variation functions to apply to the measured results. Another method is to apply a temperature reference strain gauge within the bridge under the same subjected temperatures but without deformation.

In all conducted experiments, only a quarter bridge was applied. No temperature compensation method was required. Every experiment was conducted in a manner to which no considerable temperature was generated and induced to the strain gauge. Therefore, only the related equations for the quarter bridge without the temperature effect are here presented.

An output voltage is measured when deformation occurs, and, therefore, a resistance variation is created in the strain gauge. When there is no deformation of the material, thus no deformation of the strain gauge and therefore no resistance variation, no output voltage is measured (in a calibrated circuit). The voltage measurement is then transformed into strain values. Equation (4.2) associates the output voltage with the strain values in a quarter bridge.

$$\varepsilon = \frac{4V_0}{KU_B} \tag{4.2}$$

Where ε is the measured strain, K is the gage factor, U_B is the input voltage, and V_0 is the output voltage. The strain transformation to stress is made by applying Hooke's law with the properties of the materials. Since every conducted experiment was within the tested samples' elastic behaviour, only the Young's Modulus and the Poisson's ratio are required.

For one-gauge strain measurement, if the strain gauge was adequately aligned to the deformation direction, only Hooke's law equation (4.3) is required for stress determination.

$$\sigma = E \cdot \varepsilon \tag{4.3}$$

For torsion and multiaxial specimens, a 45º rosette strain gauge was applied to measure three strains` components simultaneously. The three strain gauge components with one shared area can fully determine the strain /stress field. Equations (4.4) and (4.5) are applied to calculate two normal strains and one shear strain for the desired x-y coordinates. The rosette strain gauges have a specific numbering for each gauge. The applied numbering is the same in all used strain gauges.

$$\begin{cases} \varepsilon_2 = \varepsilon_x(\cos(\theta_1))^2 + \varepsilon_y(\sin(\theta_1))^2 + \gamma_{xy}\cos(\theta_1)sin(\theta_1) \\ \varepsilon_3 = \varepsilon_x(\cos(\theta_2))^2 + \varepsilon_y(\sin(\theta_2))^2 + \gamma_{xy}\cos(\theta_2)sin(\theta_2) \\ \varepsilon_1 = \varepsilon_x(\cos(\theta_3))^2 + \varepsilon_y(\sin(\theta_3))^2 + \gamma_{xy}\cos(\theta_3)sin(\theta_3) \end{cases} \tag{4.4}$$

$$\gamma_{xy} = \varepsilon_{xy} + \varepsilon_{yx} = 2\varepsilon_{xy} \tag{4.5}$$

Where ε_1 ε_2 and ε_3 are the measured gauge strains, θ_1, θ_2 and θ_3 the angles of a measured strain to the x-axis, ε_x and ε_y the normal strains in *x* and *y* direction respectively, and ε_{xy} the shear strain. The θ angle relation between strain gauges and the x-axis is shown in Figure 4-17 for the applied 45º rosette strain gauge. The gauge number sequence is also indicated in Figure 4-17.

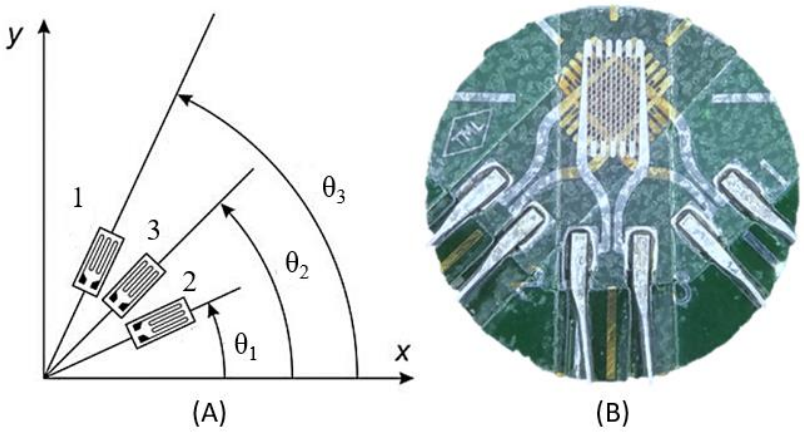

Figure 4-17: (A) Strain rosette alignment and numbering; (B) 45 º rosette strain gauge used.

For isotropic material plane strain to stress calculation, the Plane stress Hooke's law equation (4.6) is as follows:

$$\begin{bmatrix} \sigma_x \\ \sigma_y \\ \sigma_{xy} \end{bmatrix} = \frac{\mathrm{E}}{1-\nu^2} \begin{bmatrix} 1 & -\nu & 0 \\ \nu & 1 & 0 \\ 0 & 0 & 1-\nu \end{bmatrix} \cdot \begin{bmatrix} \varepsilon_x \\ \varepsilon_y \\ \varepsilon_{xy} \end{bmatrix} \tag{4.6}$$

Where E is the Young's modulus, ν is the Poisson's ratio, σ_x and σ_y the normal stresses in x and y direction respectively, and σ_{xy} the shear stress. The Shear modulus is not directly applied in the calculation equation (4.6) methods for the shear stress. It can be related to the Young's modulus by equation (4.7).

$$\mathrm{G} = \frac{\mathrm{E}}{2(1+\nu)} \tag{4.7}$$

4.4.2.2 Frequency and modal analysis theoretical background

As aforementioned, all ultrasonic fatigue machines induce resonance as the means to achieve high deformation at such high frequencies. So, it is imperative and significant to use modal analysis methods and base theories to fully characterise the frequency response behaviour. Through modal analysis, the non-desired effects can be understood leading towards corrective solutions. Improvements are then made to the setups and again, a new complete analysis of the final fatigue and induce deformed shapes are conducted and compared.

A modal analysis theoretical background is first made to introduce all concepts associated with conducted modal experiments to the specimens in different booster horn setups and the two multiaxial ultrasonic machine setups. The modal behaviour of all tested setups was studied in its transient state, steady-state, and free vibration.

Looking at the ultrasonic fatigue machine in service, there are two main stages when a vibration excitation is applied, force vibration and free vibration. The excitation of the piezoelectric material creates the force vibration within the transducer through a varying imposed electric current. The cyclic deformation of the piezoelectric material will excite the components setup attached to the transducer and maintain under vibrations state; thus, we have a forced vibration. When the transducer is turned off, the system will no longer have an applied cyclic force and will vibrate freely, and thus it is now in a free vibration condition.

When in free vibration, the displacement amplitude will exponentially drop until the system comes to a rest. For a system in free vibration, the time related to the reduction of the

displacement amplitude is called the Free Decay. A representation of the force vibration and the free decay is shown in Figure 4-18.

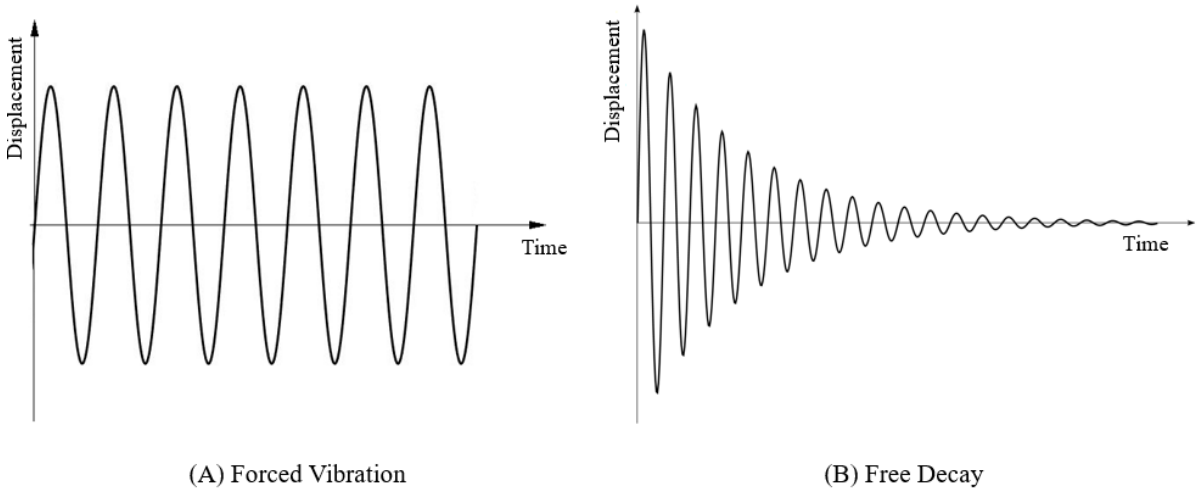

Figure 4-18: Cyclic deformation representation when in: (A) Forced vibration (B) Free decay

The initial response of a resonance excited system by constant cyclic forced vibration is termed the transient state. In this first instance, the amplitude is not stable and harmonic. A harmonic stable and periodic state is reached as the excitation progresses, termed the steady-state. A representation of the transient to steady-state is presented in Figure 4-19.

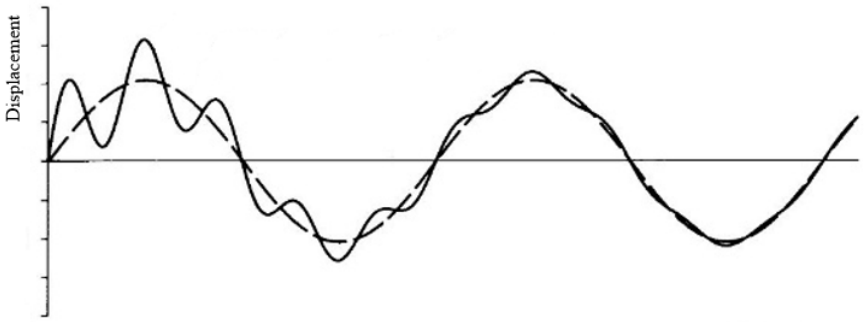

Figure 4-19: Displacement representation of a system from the initial transient to a steady-state.

The damping material property is responsible for the Figure 4-18.B free decay response. Considering a single degree of freedom system, if there were no material damping, the system would, in free vibration, continuously be in harmonic motion with constant amplitude at the undamped natural frequency, ω_n.

$$\omega_n = \sqrt{\frac{k}{m}} \tag{4.8}$$

Where *k* is the stiffness, and *m* is the system's mass. The present under study ultrasonic fatigue systems have multiple degrees of freedom, meaning they have an infinite natural frequency vibration modes. The free vibration decay will have a combination of all natural frequencies. Since free vibration response depends on the initial conditions, the ultrasonic fatigue machines free vibration response will be predominantly on the natural frequency of the excited vibration mode.

The damping value will determine the system's exponential decay and influence the final oscillating frequency, known as the damped natural frequency, w_d.

$$\omega_d = \omega_n\sqrt{1-\xi^2} \tag{4.9}$$

ξ is the viscous damping. Since the damping effect is directly associated with the free decay response, it can be determined through the exponential amplitude decay. From the amplitude values and n cycles, until the system comes to a rest, it is possible to derive the logarithmic decrement following the presented equation (4.10).

$$\delta_n = ln\frac{X_i}{X_{i+n}} = \frac{2n\pi\xi}{\sqrt{1-\xi^2}} \tag{4.10}$$

When the viscous damping has a considerably lower value ($\xi << 1$), equation (4.10) can be simplified to:

$$\delta = \frac{1}{n}ln\frac{X_i}{X_{i+n}} = 2\pi\xi \tag{4.11}$$

The absolute amplitude reduction in the free decay follows a viscous damping exponential curve, as equation (4.12) describes. Figure 4-20 represents the exponential curve amplitude reduction of a free decay with the associated X_i values taken for the viscous damping calculation. Figure 4-20 was taken from the based knowledge followed in this report, Nuno Maia and Silva's book 'Fundamentals of modal analysis' [76].

$$X(t) = X_n e^{-\xi\omega_n t} \tag{4.12}$$

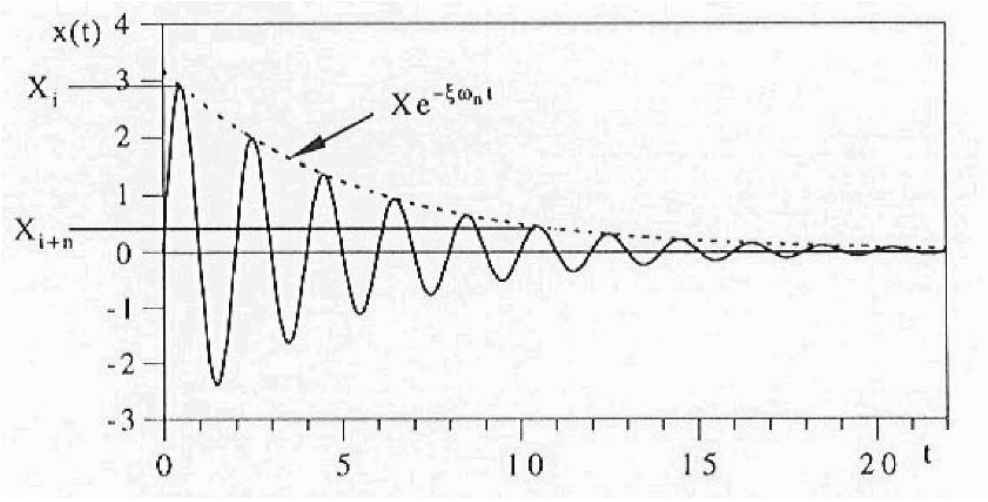

Figure 4-20: Free decay representation with the exponential curved defined by the viscous damping [76].

From equation (4.12), the viscous damping is determined. Again, for low damping systems ($\xi<<1$) hysteretic damping can be related to viscous damping through the following equation (4.13) [202].

$$\eta = 2\xi \tag{4.13}$$

Frequency Response Function (FRF) is defined by experimental modal analysis to quantify a system frequency response behaviour. To determine a system FRF key parameters need to be measured to describe the system modal response. Depending on the measured signal, the made calculations are different, but two fundamental values are necessary: the output motion and the excitation force. The motion can be measured in terms of displacement, velocity or acceleration. Even though there is varying nomenclature to the different motion measured FRF, the followed terminology by Maia and Silva [76] in harmonic excited systems is:

$$\alpha(\omega) = \frac{Displacement\ response}{force\ excitation} = Receptance \tag{4.14}$$

$$Y(\omega) = \frac{Velocity\ response}{force\ excitation} = Mobility \tag{4.15}$$

$$A(\omega) = \frac{acceleration\ resposnse}{force\ excitation} = Accelerance \tag{4.16}$$

The unknown cyclic excitation force is one limitation of currently available transducer-based UFT methods conducted in this research. Such limitation is due to specimen excitation's size and applied mechanism. The unmeasurable force between horn and specimen inhibits the complete calculation of a specimen’s FRF.

One modal analysis method specially devised for such output-only systems and structures under unknown load was created, the Frequency Domain Decomposition (FDD) method. FDD was intentionally developed for buildings and bridges where the force input, like those produced by cars or wind, is unmeasurable [203; 204]. Most research where the FDD was computed was civil engineering structures, as Zhang et al. have described [205].

The FDD method theory bases itself on the relationship between the unknown inputs and the measured responses through the Power Spectral Density (PSD), afterwards decomposed by taking into a set of single degree of freedom systems using the Singular Value Decomposition (SVD). SVD is only applied to specific frequencies determined by the PSD peaks. Following the FDD algorithm, the PSD relationship is firstly presented in equation (4.17).

$$G_{yy}(j\omega) = \bar{H}(j\omega)G_{xx}(j\omega)H(j\omega)^T \tag{4.17}$$

Where $G_{xx}(j\omega)$ is the power spectral density (PSD) matrix (r x r) of the input, r being the number of inputs, $G_{yy}(j\omega)$ is the (m x m) PSD matrix of the m responses, $H(j\omega)$ is the (m x r) FRF matrix, and the overbar and superscript T denotes the complex conjugate and transpose, respectively.

The SVD is then taken for specific frequencies of the matrix:

$$G_{yy}(j\omega_i) = U_i S_i U_i^T \tag{4.18}$$

Where U_i is the unitary matrix holding the singular vectors $u_{ij,}$ and Si is the diagonal matrix holding the singular scalar values $s_{ij.}$ Near a PSD matrix peak corresponding to a resonant mode related to a frequency $\omega_{k,}$ the first singular vector u_{i1} estimates the related mode shape.

The method has the best results when the applied load to the system is random or white noise; the system is lightly damped; and when the mode shapes close in frequency modes are geometrically orthogonal. As described later, the system-imposed load sequence for the FDD determination is not random as recommended.

4.4.3 Experimental Ultrasonic Machines Methodology

4.4.3.1 Strain gauge placement and measurement methodology

The correct strain gauge model was first selected for every strain measurement experiment. The determination of strain gauge type is dependent on the overall size, deformation of interest to be measured, and the material.

A single strain gauge extensometer was applied for all tension-compression ultrasonic fatigue samples. Otherwise, in pure torsion, tension-torsion and cruciform samples, rosette 45º extensometers with three strain gauges were required.

Different materials have different thermal expansion coefficients. To reduce the associated thermal expansion effect error, strain gauges have different temperature compensation coefficients to better test different materials. If not appropriately compensated, the material thermal expansion will induce misleading strain values from the strain gauge.

All acquired and applied strain gauges with the respective number of gauges, thermal expansion resistance and gauge factor are presented in Table 4-5.

Table 4-5. Experimentally applied strain gauges specifications.

Strain Gauge	**Nº of Gauges**	**Resistance Ohm [Ω]**	**Gauge Factor, K**	**Thermal Expansion, α [10^{-6} / K]**
HBM 1-LY11-0.6/120	1	120 ± 1%	1.78 ± 1.5%	10.8
TML FRA-1-11	3	120 ± 0.5%	2.08	11
TML FRAB-1-17	1	120 ± 0.5%	2.10	17
TML FRAB-1-23	3	120 ± 0.5%	2.10	23

The strain gauge applying methodology is similar between different specimens. All strain gauges are bonded with adhesive in the ultrasonic sample's displacement node. These are the fatigue testing regions where the displacement is null and the deformation the highest.

First, the determined fatigue region of interest is polished and cleaned with acetone. All specimens were polished in a turning lathe machine at low speeds to achieve a uniform surface. Figure 4-21 shows a cruciform and a tension-torsion specimen fixed in the turning lathe.

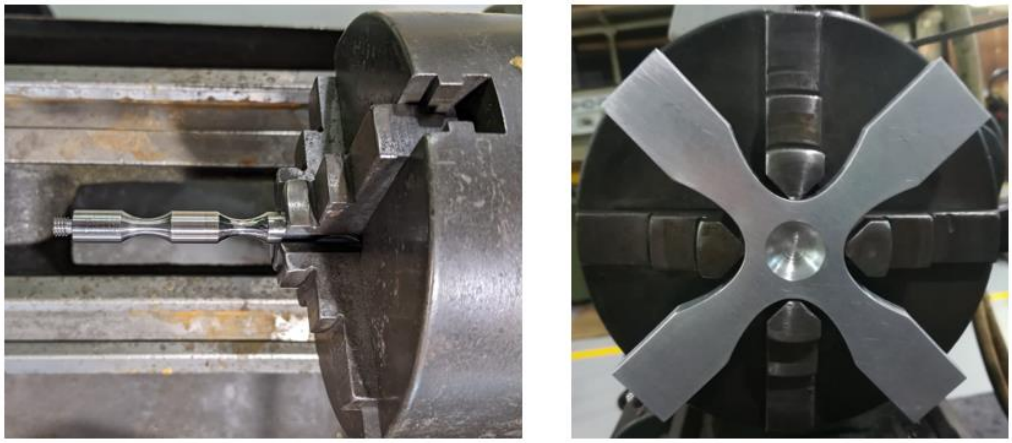

A B

Figure 4-21. Turning lathe for surface polishing: (A) Tension-Torsion specimen; (B) Cruciform specimen.

Polished specimens were marked to pinpoint the correct alignment of the strain gauge placement. The throat midpoint was ink marked in length and radius for tension-compression and tension-torsion specimens. For the cruciform specimens' lines were scratched along the arms, thus pinpointing the centre and the correct gauge alignment.

Due to the specimen's shape and overall small fatigue testing area the acquired strain gauges are the smallest in area provided by HBM and TML. To correctly place and align such a small size strain gauge in such a small tight region is a hardship and precision task. After the surface treatment and made alignment guidelines, a small amount of adhesive was applied, and the strain gauge was placed as centred and aligned as possible.

Figure 4-22 shows the attached strain gauges to a cruciform and a tension-torsion specimen through a magnifying lens.

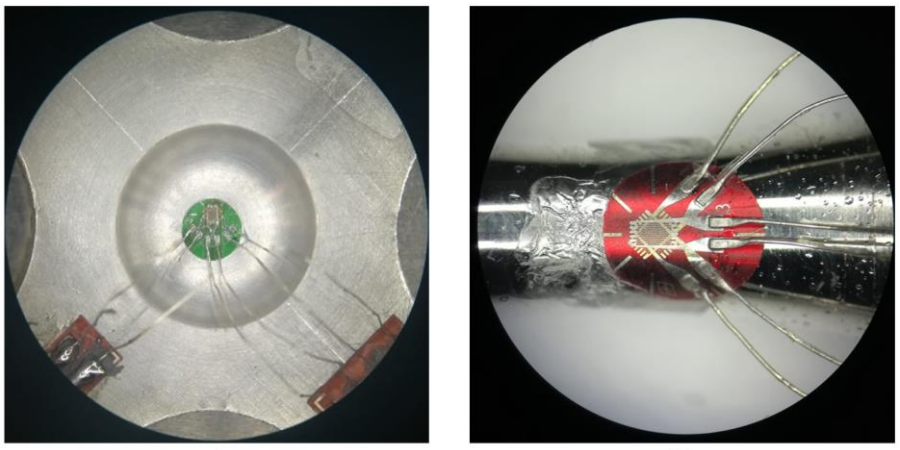

A B

Figure 4-22. Magnified rosette strain gauges applied to (A) N T-T cruciform; (B) Spc2 tension torsion specimen.

All the strain gauge connections were subsequently soldered to strain connectors and secured with electric tape. Figure 4-23 shows a tension-torsion and a cruciform specimen with a glued strain gauge, the guiding lines, the strain connectors and the electric tape securing the soldered cables.

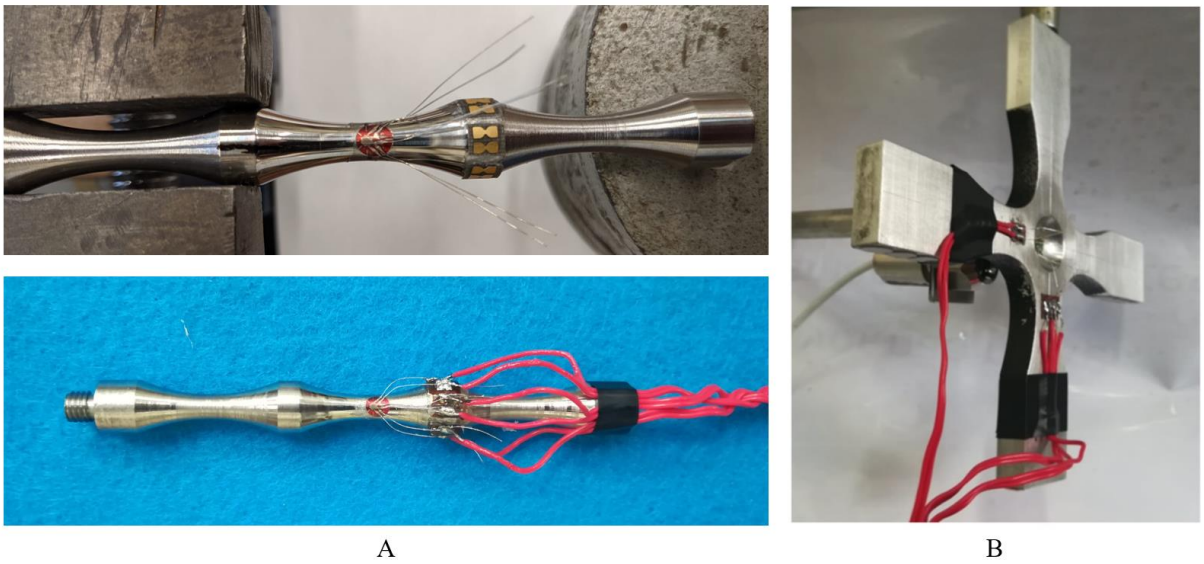

A B

Figure 4-23. Rosette strain gauge, the guiding lines, the strain connectors and the electric tape securing the soldered cables in: (A) tension-torsion three throat specimen; (B) N1 T-T cruciform specimen.

Three Dynamic Wheatstone 2310 Signal Conditioning amplifier bridges were used to obtain each individual strain gauge value. Three dynamic bridges were simultaneously connected to the National Instruments DAQ for the 45º rosette strain gauges. Each DAQ channel had the same 300 kHz acquisition rate.

For each strain gauge specimen different power transducer settings were applied in a pulse time sequence. The applied pulse time interval was carefully chosen. The time under resonant excitation should be as short as possible to ensure low-temperature variation and low damage to the strain gauges, but long enough to reach a stable, steady-state strain cyclical amplitude result. Just as any material, all strain gauges have fatigue failure. Hence, to have the most valuable results from each strain gauge, every experiment needs to be as short as possible.

The followed rosette strain gauge stress calculation for the cruciform ultrasonic specimens case is here shown as an example. The position of the rosette strain gauge and its relation to an established x-y coordinate system is first established. Figure 4-24 shows two different placed rosette strain gauges in cruciform N1 and N2 T-T with the considered *x-y* axis.

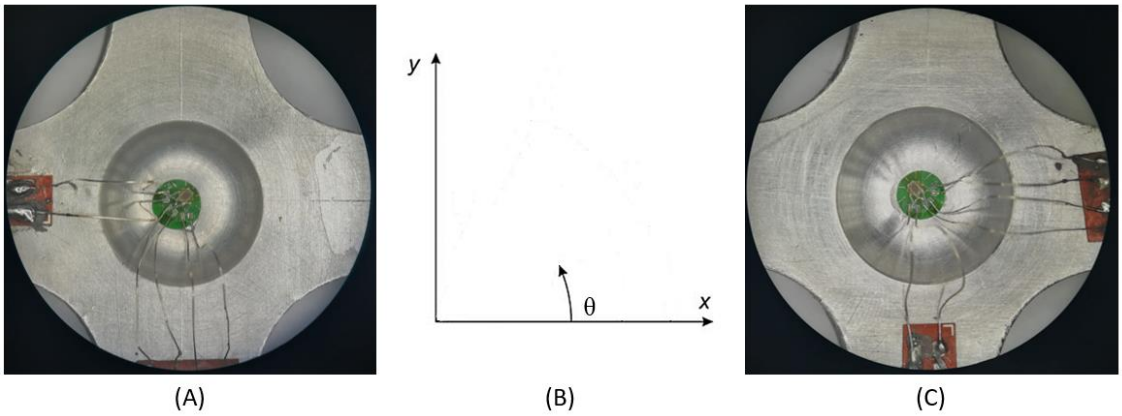

Figure 4-24. Strain gauge relation to the established x-y coordinate system: (A) cruciform 1; (B) coordinate system; (C) cruciform 2.

The angles for each cruciform specimen strain gauge are presented in Table 4-6.

Table 4-6. N*x* T-T cruciform strain gauges x-y coordinate system angles.

Angle	**N1 T-T**	**N2 T-T**
θ_1	0º	90º
θ_2	45º	135º
θ_3	90º	180º

Through the angles in Table 4-6, the normal and shear strain in the x-y direction were determined by equation system (4.4). Equation system (4.19) and equation (4.20) for strain x-y normal and shear strain are associated with the cruciform 1 and 2 strain gauge angles, respectively.

$$\begin{cases} \varepsilon_2 = \varepsilon_x \\ \varepsilon_3 = \frac{\varepsilon_2}{2} + \frac{\varepsilon_1}{2} + \frac{\gamma_{xy}}{2} \\ \varepsilon_1 = \varepsilon_y \end{cases} = \begin{cases} \varepsilon_2 = \varepsilon_x \\ \gamma_{xy} = 2\varepsilon_3 - \varepsilon_1 - \varepsilon_2 \\ \varepsilon_1 = \varepsilon_y \end{cases} \tag{4.19}$$

$$\begin{cases} \varepsilon_2 = \varepsilon_y \\ \gamma_{xy} = 2\varepsilon_3 - \varepsilon_1 - \varepsilon_2 \\ \varepsilon_1 = \varepsilon_x \end{cases} \tag{4.20}$$

Through Hook's law equation (4.6), the two normal and shear stress were then calculated. A stress combination result from a steady-state strain measurement is shown in Figure 4-25.

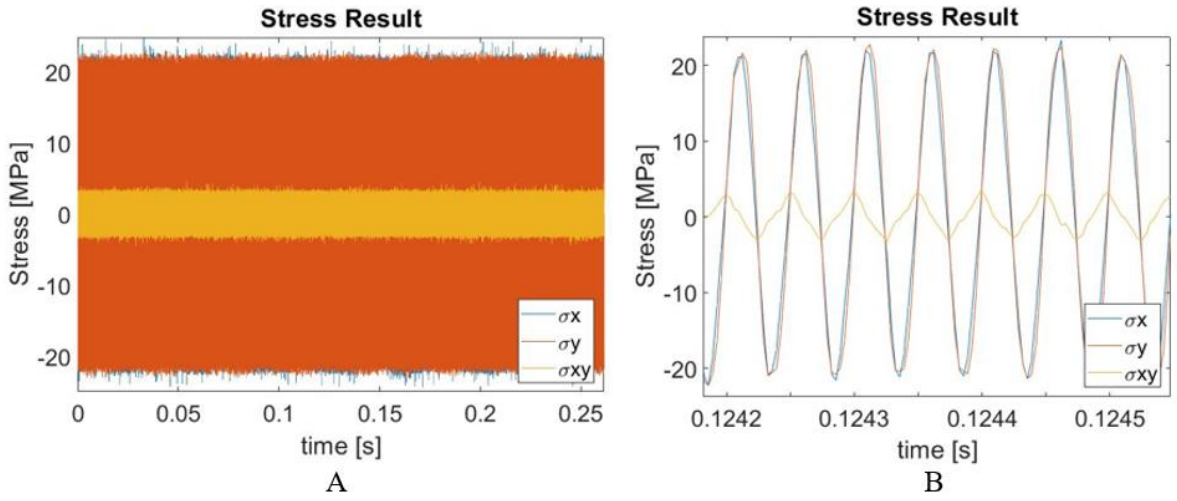

Figure 4-25: Stress combination result for a cruciform rosette strain gauge: (A) overview; (B)Zoomed view with harmonic signal.

Figure 4-25B overview and zoomed view of the rosette strain gauge measurement shows constant harmonic strain amplitudes when in steady state vibration. Max, min and average stress values were taken. A linear plane regression plot is then made with *x* and *y* axial and shear average stress values from each power setting.

4.4.3.2 Modal analysis and displacement measurement methodology

Two different modal response experimental analyses were conducted: A modal shape constant frequency resonance steady-state analysis and an FDD frequency Sweep-Sine modal analysis. The two modal experiments have different induced excitation sequences. The excitation sequence together with the followed methodology is here described.

The experimental setup in both modal experiments was similar in used measuring equipment and their respective placement. The Polytec dual-channel laser vibrometer was used in all modal experiments, measuring the velocity response in key high displacement mode shape location points. A temperature sensor was also applied as a protective system trigger preventing the specimen from any sudden temperature rise that could lead to material changes. All laser measurements were recorded to a computer using a National Instruments DAQ system controlled by the improved LabView algorithm.

The two modal analysis vary in excitation force, frequency and power transducer settings. Regarding first the modal shape frequency resonance steady-state analysis, also denoted as the power to displacement analysis. In this experimental analysis the induced

resonance frequency of all under study setup remains constant. Different transducer power amplitude settings are then sequentially applied. In each setting, the setup is excited until the resonance steady-state is reached. The increase in transducer power amplitude should show a linear increase in measured displacement amplitude for correctly working setups.

A frequency scan sweep sequence was conducted instead of a constant frequency for the FDD Sweep-Sine modal analysis. The 'frequency scan' is a control pre-programmed setup evaluation system of the transducer controller software. A Sweep-Sine frequency setup excitation is conducted within the piezoelectric transducer frequency range (20±0.5 kHz). The transducer 'frequency scan' consists of an harmonic axial excitation that sequentially increases in frequency in a stepwise manner, from 19450Hz to 20450 Hz at 1 Hz each 100 ms. The experimental laser displacements are recorded throughout the complete sequence until there is no more measurable displacement.

The FDD analysis was only conducted on the pure torsional and multiaxial specimens (Tension-torsion and cruciform specimens) ultrasonic methods with the two available Laser Doppler vibrometer channels measuring simultaneously.

The projected experimental laser setups, the measured locations and directions for each tested ultrasonic fatigue setup, were determined by both FEA frequency analysis in free-free no boundary conditions vibration and steady state modal analysis. FEA software is always first used to ensure the resonant mode of interest frequency is in the mid working range of the transducer. Beyond the resonant mode associated with the ultrasonic fatigue test, the frequency and shape of others close to 20kHz are considered since they could influence the final specimen exciting shape and deformation. The laser measurements must focus on the stress node regions, i.e. the highest displacement locations, of the mode of interest (MI) and all determined as possibly influential resonant modes (Parasite Modes-PM). For each modal shape the stress node's location are comprehended and their respective direction and phase. The experimental setup is then arranged with aligned laser positions to the FEA reached stress nodes. Therefore, the experimental setup is constructed around the hypothesised influential resonant modes. The made measurements enable to quantify and proof which resonant modes have a non-negligible excitation and effect on the final mode shape.

For the pure torsional ultrasonic machine, one laser measurement was on the longitudinal horn, and the second was pointed at the specimen. The two-laser combination was made to have both the longitudinal resonance mode of the LH with the torsional mode of the

TH and specimen. Similar to the Mario et al. [85] rotation measuring method for tension-torsion specimens, a pair of groves were machined in the free base of the torsional specimen. The laser measuring setup and the machined grooves are represented in Figure 4-26.

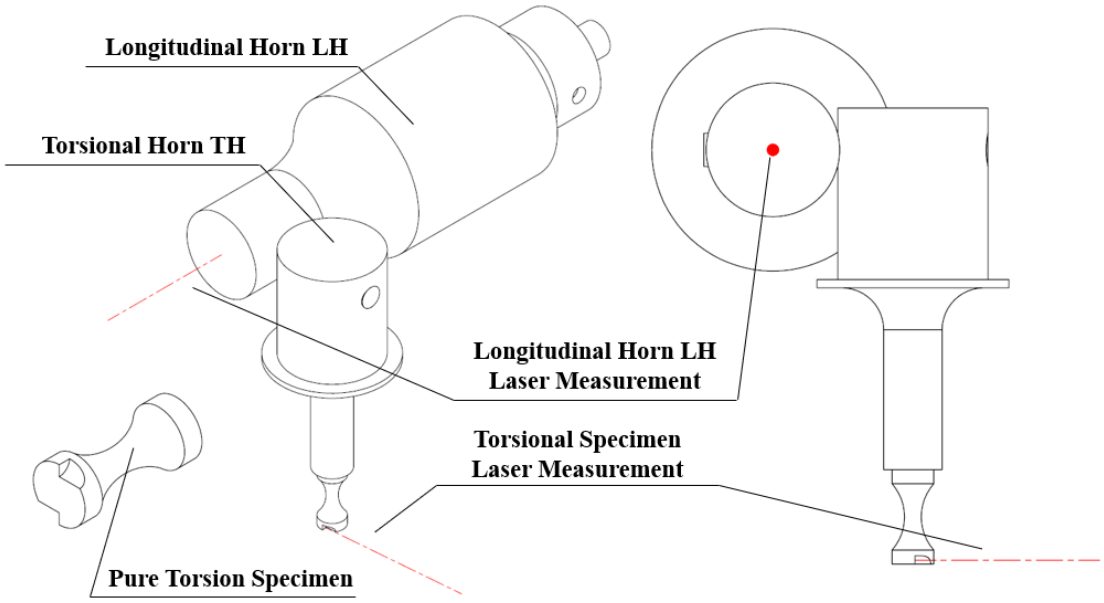

Figure 4-26. Pure torsion laser placement setup for modal FDD and power to displacement analysis.

To apply the specimen grove measured displacement (A_0) towards the analytical solution, a transformation must be made. The method measures axially, but rotation (A_{0r}) must be applied to the pure torsion analytical solution. Equation (4.21) makes the measurement transformation:

$$A_{0r} = \arctan(A_0 \cdot R_2) \cdot R_1 \tag{4.21}$$

Equation (4.21) R_2 and R_1 are the specimen base and smallest cross section radius dimension variables already present in Figure 3-1. Tension-Torsion experimental laser placement focused both lasers at the specimen free end base. The axial displacement is measured by a laser aligned with the specimen's length, just as tension-compression specimens. Similar grooves to the pure torsion specimens (Figure 4-26) were also machined for the rotational measurements. The drawn setup measures the axial and rotational frequency response of the specimen simultaneously. Figure 4-27 shows the tension-torsion laser measuring scheme for modal FDD and power to displacement analysis.

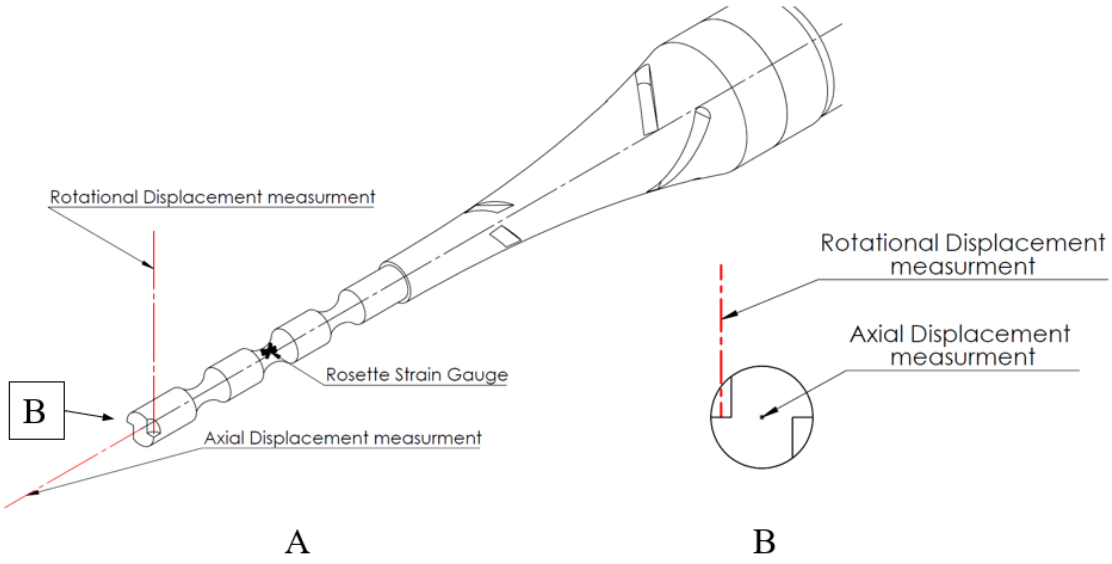

Figure 4-27. Tension-torsion laser and strain gauge placement setup for modal FDD and stress to displacement ratio analysis.

When considering the cruciform specimens, the FEA modal analysis was vital in establishing the laser locations and directions of measurement. Two different resonant modes were required to be included in the modal analysis. All the response coordinates are at the cruciform ends, where the anti-nodes of the two intended modes' highest displacement locations are. Three different measurement points were thus determined based on the FEA results of the cruciform specimens with the horn and booster setup assembly. Due to the inability to measure three displacement locations simultaneously, two different runs were conducted, setup A and B.

Setup A focuses on two measurement points where both modes under analysis have high displacements: Laser 1 (L1) measures the vertical displacement on the vertical arm for the MI; laser 2 (L2) measures the vertical displacement of the horizontal arm associated with the PM; Laser setup B associates the displacement axial-axial ratio between vertical and horizontal arms having; again Laser 1 measuring vertical displacement on the vertical arm; Laser 3 (L3) measuring the horizontal displacement of the horizontal arm.

Since L1 laser location and displacement direction coincide with the two modes, it was established as the reference measuring point between laser A and B setups. Figure 4-28 shows an ultrasonic set representation and the experimental laser setups A and B described above.

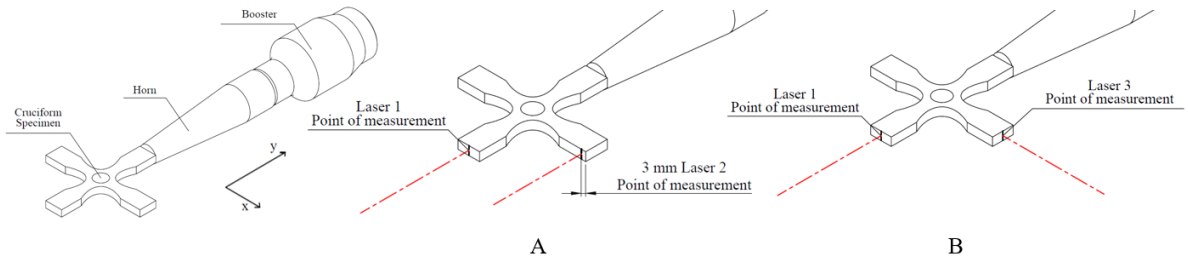

Figure 4-28. Cruciform Laser A and B laser placement setups for modal FDD and power to displacement analysis.

The LabView software directly outputs the displacement amplitude from steady-state constant frequency analysis. All laser recorded data was imported to a Matlab script for the FDD analysis and its respective graph plotting.

4.4.4 Ultrasonic Fatigue Testing Methodology

Having all experimental analyses conducted for all the specimens with the proven desired behaviour, UFT was initiated.

Across all tested ultrasonic fatigue methods, the trailed procedure is similar for the most part. From having the established desired material to research in VHCF through ultrasonic fatigue until the fracture surface final analysis, all ultrasonic fatigue tests follow generally the sequence:

- Static mechanical properties and microstructure determination.
- Specimen design.
- Planning measuring and control system setup.
- Specimen resonance test and deformation response analysis.
- Establishing pulse-pause sequence, temperature control parameters and cooling system.
- Fatigue testing.
- Unveiling the Fatigue fracture by tensile machine.
- Fatigue fracture analysis.

The first four steps have already been discussed. Necessary static mechanical properties were conducted to all tested materials. The uniaxial specimen designs were modelled by analytical equations and refined by FEA software. Multiaxial specimens were fully modelled by FE software. The modal and deformation method determination and analysis methodology was already described at length. For both uniaxial and multiaxial UFT, each experimental analysis and methodology was adapted to the resonance associated behaviour. All key measuring locations were numerically determined, and displacement and strain measurements were conducted.

Along with the fatigue tests, three major parameters must be measured: temperature, displacement and /or strain, and frequency.

In UFT, the specimens have temperature generation on the high deformation fatigue region. The study structure was equipped with cooling fans pointed at the specimen and horn, and compressed air pointed at the fatigue testing region. Similar to Lage et al. [83] followed methodology, temperature control was continuously monitored with a pyrometer. The temperature control prevents the material sample from reaching a high enough temperature that could disrupt the fatigue results. When the temperature limit is reached the transducer is turned off, and the specimen cooled. Lage fatigue testing methodology only applied temperature control, meaning that the transducer will be in operation until the temperature limit is reached. In the improved LabView software, a time control pulse-pause system was implemented similar to other tested research [95; 118; 206]. In pulse-pause time control, the temperature is still continuously measured and controlled. The programmed time control establishes a transducer in operation interval and a cooling interval. Both states will work in sequence until the ultrasonic fatigue experiment comes to a stop. Figure 4-29 shows a UFT output representation when under pulse-pause control.

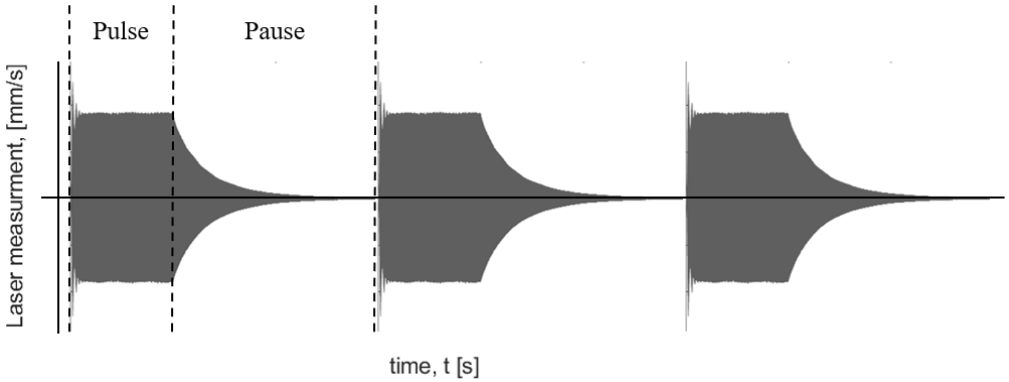

Figure 4-29. Pulse-pause time-controlled UFT method representation.

The measurement of the output response of the specimen is also made across the UFT. The displacement measurement serves as the fatigue cycle counting method and induced stress control. From the displacement, the frequency of work can also be determined. The measurement setup is where the UFT methodology changes between specimens and induced stress combinations, just as in the modal and deformation analysis methodology. One single displacement laser is applied in the free base for tension-compression, multiaxial tension-torsion; two simultaneous lasers at the extremities of the cruciform arms; and for pure torsion one laser at the longitudinal horn.

Because the working concept of UFT is achieved by the modal resonance of a given material sample, the final failure of the specimen will not be the occurring catastrophic failure observed in conventional fatigue testing. Meaning the specimen will not fully fracture in the ultrasonic machines. The working frequency remains relatively constant as the specimen is being tested until a fatigue crack nucleates and propagation is initiated. As the fatigue crack propagates, the specimen stiffness decreases, and consequently, the resonance frequency also decreases, as equation (4.8) shows on a single degree of freedom system. When the fatigue crack reaches a certain size, the specimen reduced frequency brings the complete ultrasonic setup frequency below the transducer 19450 Hz to 20450 Hz frequency range. Consequently, the transducer controller registers an out-of-frequency range overload, and the fatigue test comes to a full stop. The DAQ system is connected to the controller and the transducer controller overload signal interrupts all measurements. The specimens must then be fully fractured in a tensile machine to make the fatigue fracture surface visible.

In this study, the electromechanical Instron 5566 and servo-hydraulic Instron 8874 were used to break all specimens after losing resonance in the applied setup. Due to the small pure torsion specimen size, two cylindrical bars were machined to ensure a correct clamp fixation on the utilised Instron machines. Figure 4-30 shows a pure torsion, a tension-torsion and a cruciform specimen being fully fractured in the mentioned Instron machines.

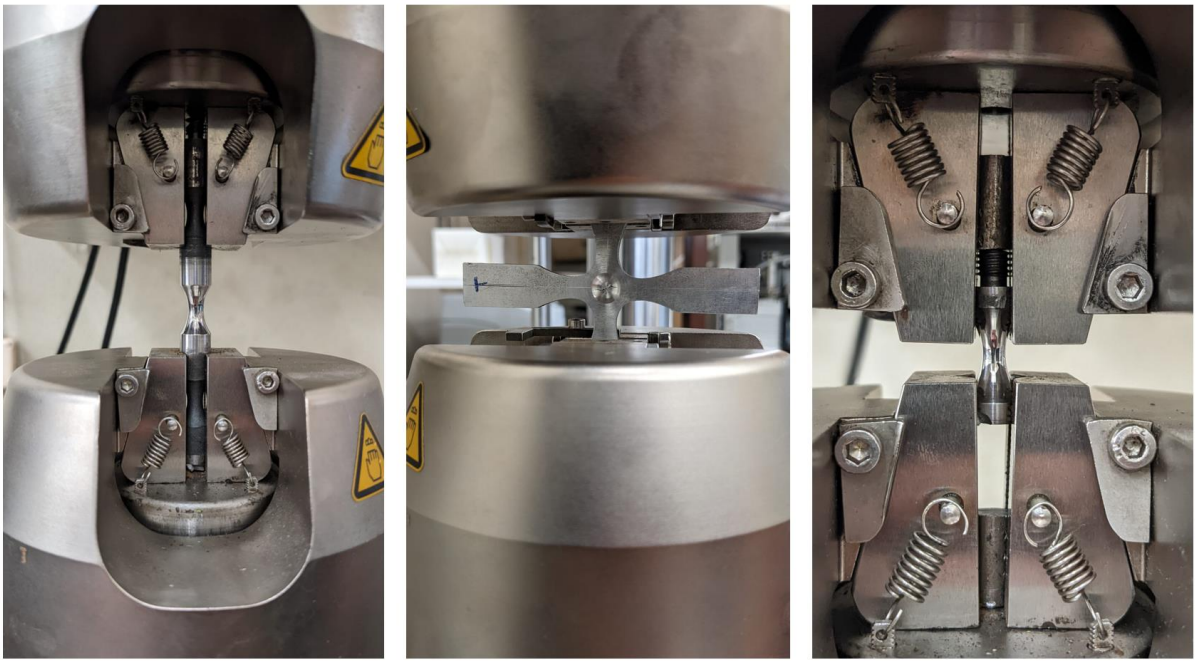

A B C

Figure 4-30. Ultrasonic fatigue samples ultimate fracture: (A) tension-torsion Spc3; (B) F T-T cruciform specimen; (C) pure torsion specimen.

After having the specimens fractured by conventional mechanical means, a primary optic microscope analysis was conducted to the fracture surface. Afterwards, a section from the specimen is taken with the fracture surface for Scanning Electron Microscope (SEM).

5

Ultrasonic Fatigue Results and Analysis

5.1 Introduction

The present chapter details the experimental results for the developed ultrasonic fatigue machines. For all tested samples, the respective modal shape and frequency response study, fatigue stress-life, and fracture surface analysis are shown in such sequence. The modal shape and frequency response experimental results were compared to the numerical simulations obtained by ABAQUS FE software. The obtained fracture surfaces morphologies and presented details are compared to published research.

A first introduction modal response analysis was made with a steel bar. It served as a presentation base for the remaining modal results shown and as an analysis of the two uniaxial booster horn setup responses. The steel bar experimental vibration response was conducted for the two uniaxial setups present in this study, tapered and hyperbolic horns. The two axial horns setups were numerically and experimentally applied to all tension-compression ultrasonic specimens and cruciform specimens.

All uniaxial tensile ultrasonic results are then presented. Both available uniaxial setups and both AISI P20 and Ti6Al4V specimens were compared in their modal behaviour. All modal results took into consideration the different smallest cross-section radius.

Pure torsional machine modal improvements progression is followed with the in-depth FDD conducted modal analysis. Afterwards, all associated specimen results as displacement and strain measurements, fatigue life, and fracture surfaces are shown.

Tension-torsion results are shown again in a similar sequence. The modal analysis results are first shown with the resulting comparison to the FEA results. Tension-torsion specimens displacement and stress amplitudes were also measured in the two axial booster horn setups.

Cruciform modal analysis of the resonant Mode of Interest (MI) and the Parasite Mode (PM) is first shown, followed by the displacement measurements made in both experimental introduced laser setups. Two stress-induced analytical solutions were proposed from the modal analysis, displacement and strain measurements together with FEA results. The strain gauge, FEA, and the analytical solution stress for each given measured displacement were compared.

5.2 Uniaxial Transducer-Booster-Horn Modal Behaviour

A first preliminary frequency analysis was conducted for the three applied horns: tapered, hyperbolic and tension-torsion multi-horn hyperbolic. The working frequency was first determined for all three horns without the booster (Table 5-1) and afterwards with the booster (Table 5-2). The ultrasonic pure torsion rig fixed the transducer horn setup to test all horns without the booster.

Table 5-1. Transducer horn setups working frequency [Hz].

Transducer			
Booster	Tapered	Hyperbolic	Tension Torsion Multi-Horn
20208 Hz	20083 Hz	20083 Hz	20160 Hz

Table 5-2. Transducer booster and horn setups working frequency [Hz].

Transducer and booster		
Tapered	Hyperbolic	Tension Torsion Multi-Horn
19996 Hz	20022 Hz	20112 Hz

All tested setups present a working frequency within the transducer range. The horns frequency setup values tend towards 20 kHz when other parts are attached to the booster. Such tendency occurs because the transducer is designed to have a high frequency alone and, therefore, the more components are added (with 20 kHz design), the closer to 20 kHz the setup becomes. The booster multi-horn frequency has the highest +98 Hz to the FEA obtained.

Having all setups working frequency, a modal amplitude transducer power to axial displacement analysis was conducted. The resulting axial displacement amplitude for sequential transducer amplification settings was compared between the tapered, hyperbolic and multi-horn, all with the booster. The shape and radius ratio between the three horn ends is different, resulting in different amplification factors. The hyperbolic horn has a higher base radius factor. Therefore, it was expected to have a higher displacement for the same transducer power setting. The measured amplitude in several power transducer settings is shown in Figure 5-1 for all Table 5-2 with booster setups.

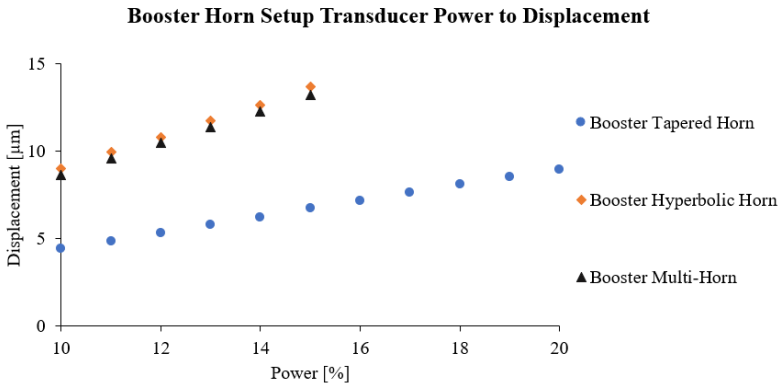

Figure 5-1. Transducer power to axial displacement amplitude of the booster horn setups: tapered: hyperbolic; multi-horn.

As expected, the Tapered horn setup showed the lowest amplitude, with 2.1x times lower amplitude than the hyperbolic, the highest amplifier horn, and 2x times lower than multi-horn.

As previously mentioned in subchapter 3.2, a simple constant cross-section cylindrical steel bar was manufactured for a detailed frequency response analysis of the two available tension-compression ultrasonic setups.

A standard construction steel (E=200 GPa; ρ=7800 kg/m^3) was machined with a 10 mm diameter and a considerably higher length than the calculated from the presented equation (3.1). The length reduction is associated with mass reduction and the centre radius with bar rigidity. As explained, the bar was first progressively machine in its length and afterwards in the centre radius.

For every bar machined step, the following measured and determined data was: working frequency; power-displacement relationship; transient to steady-state period; highest transient to average steady-state amplitude value; and the amplitude variation in steady-state.

The bar was first excited in the hyperbolic setup within the transducer range with a 134.8 mm length. Prior to this length, the Tapered horn excitation was already possible. At 134.8 mm, the tapered horn setup was excited at 19822 Hz. The tapered horn has a higher mass and rigidity and, therefore, a 'stronger' influence on the final Transducer-Booster-Horn-Sample resonance frequency. Therefore, the sample's own frequency can be further away from the pretended 20 kHz and still be excited within the transducer frequency range. All the applied bar mass and rigidity changes proved the tapered horn's lower frequency sensitivity, having a lower variation between each machining iteration. The obtained frequency for each bar length and centre diameter steps for both the tapered and hyperbolic horn is plotted in Figure 5-2.

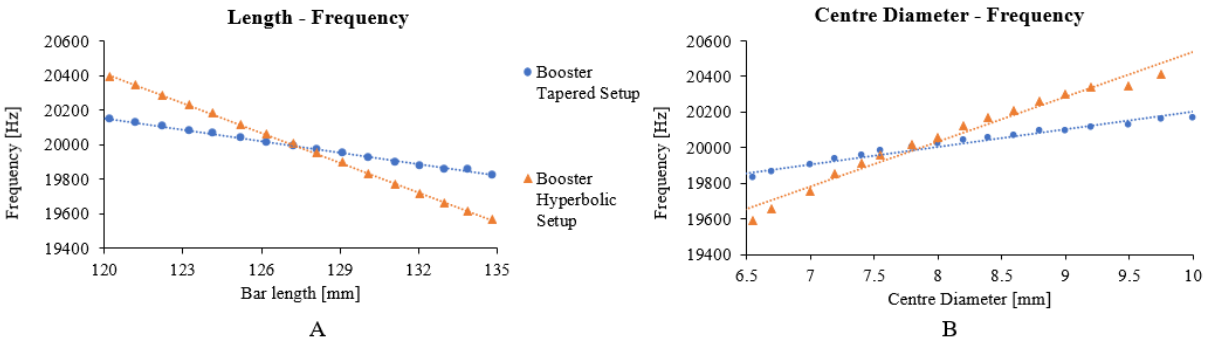

Figure 5-2. Cylindrical bar length (mass) (A) and centre (rigidity) (B) diameter to frequency results for tapered and hyperbolic horn setups.

As expected, the decrease in length decreases mass and, therefore, increases the frequency. Contrarily, the decrease in centre diameter results in a decrease in rigidity and, therefore, a decrease in frequency. Both present a somewhat linear change in frequency. The lowered rigidity presents a less agreeable linear behaviour. This occurred because the machine method applied for the centre diameter has an unavoidable and considerable mass reduction. If a more careful pinpoint centre diameter reduction were to be conducted, the results would show a more linear agreement.

The resonance transient to steady-state and the final free decay can be easily observed from laser response observation. Figure 5-3 shows the force vibration, identifying the transient state, the steady-state and the free decay of one conducted response analysis.

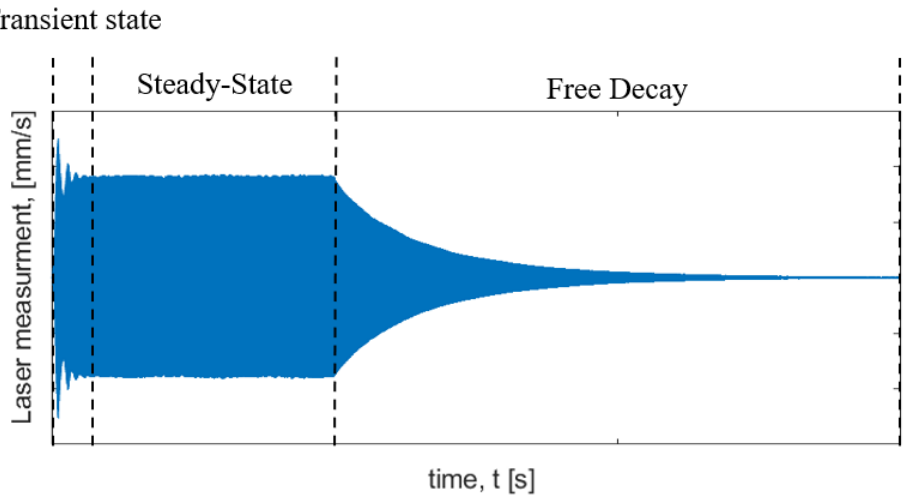

Figure 5-3. Steel bar at constant frequency excitation with transient state, steady-state and free decay represented.

The time from transient to steady-state was also determined in all experimental steps. No considerable variation was noticeable between machined experiment steps. The tapered setup showed a shorter 0.06 seconds transient state, while the hyperbolic setup averaged 0.08. Such time difference has no considerable effect on the overall fatigue imposing results of the two teste horn setups.

Considering the highest amplitude occurring in the transient state, the tapered horn showed a considerably higher value in relation to the steady-state average amplitude. The tapered setup presented an average of 29%, while the hyperbolic setup showed a considerably lower 16%. The resultant lower hyperbolic transient amplitude is believed to be associated with the lower setup frequency influence of the hyperbolic horn. With a lower mass and rigidity horn the working frequency will be closer to the specimen's own frequency resulting in a more coherent resonance and lower transient amplitude variation.

When the setup reaches the steady-state, the max amplitude presented an irrelevant 2% average fluctuation between both setups. No considerable change in the amplitude fluctuation at steady-state was perceived between all experimental steps.

From all taken results of the steel bar vibration study, every displacement test afterwards conducted took into consideration the transient to steady-state time. It also helped to perceive the advantages and disadvantages between the hyperbolic and tapered setups. The continuous result comparison between the two different setups will follow and expand the taken conclusions.

5.3 Tension-Compression Ultrasonic Fatigue Testing Results

5.3.1 Strain and Displacement Measurements

This study's tension-compression tested ultrasonic specimens (AISI P20 and Ti6Al4V) were analysed and compared in their modal transducer power to displacement amplitude and variation response. Both the tapered and hyperbolic horn setups were applied. The Ti6Al4V specimen's displacement measurements were also made and compared before and after the conducted polish treatment. A single gauge extensometer was also applied to one specimen in both tested tension-compression sample sets.

Since the hyperbolic horn setup has a 2.1 times higher amplification than the tapered, the specimen variance comparison between the AISIP20 and Ti6Al4V was made to the lowest 10% power setting for hyperbolic setup and 20% for the tapered setup. Figure 5-4 presents the obtained displacement amplitudes for both setups. Ti6Al4V Figure 5-4 presented results are with the specimens before the polishing treatment.

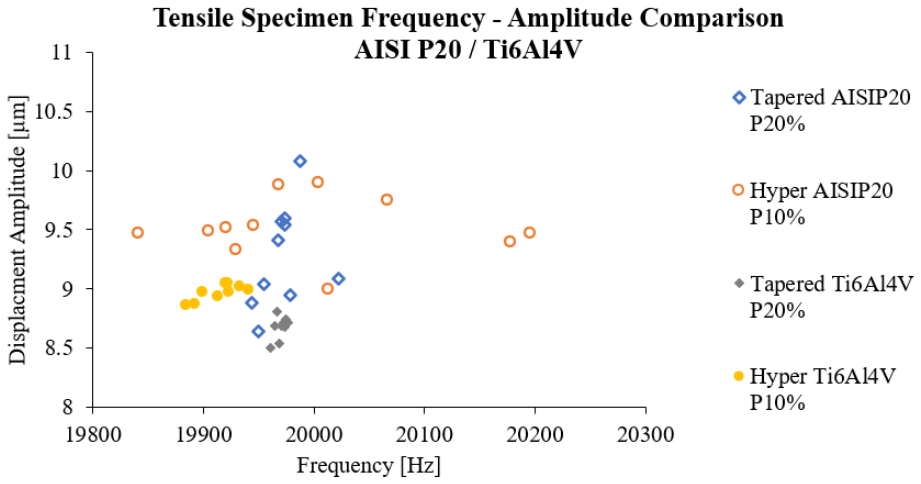

Figure 5-4. AISI P20 and Ti6Al4V displacement comparison for 10% (P10) and 20% (P20) power setting in the hyperbolic and tapered setup, respectively.

Ultrasonic tension-compression higher radius AISI P20 geometry presents a higher frequency and amplitude variability between specimens. This higher variability occurs due to the AISI P20 higher rigidity and mass, making the setup more sensitive to the specimen frequency difference. Both sample sets show a higher amplitude tendency when closer to the booster-horn setup respective frequency. Table 5-3 presents Figure 5-4 frequency and amplitude ranges for both material samples and setups.

Table 5-3. AISI P20 and Ti6Al4V displacement and frequency range comparison between the hyperbolic and tapered setup.

Material	Setup	Frequency range [Hz]	Displacement range [µm]
AISI P20	Hyperbolic	226	0.57
	Tapered	78	1.44
Ti6Al4V	Hyperbolic	77	0.23
	Tapered	37	0.41

Just as the steel bar test results, the hyperbolic setup presented between all specimens a considerably higher frequency spectrum and a lower displacement amplitude spectrum. Such tendency is proven in both material samples.

Half the obtained as-built Ti6Al4V specimens were subjected to a surface polish treatment (Figure 4-4) after the shown modal analysis. New power to displacement measurements were again made with the polished central region. Figure 5-5 shows the displacement amplitude to frequency of excitation results for Ti6Al4V as-built and polished specimens.

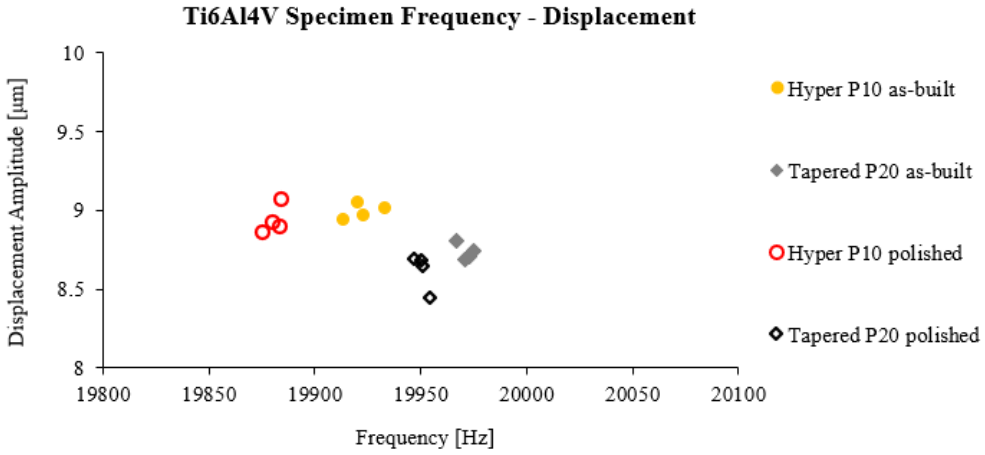

Figure 5-5. Ti6Al4V as-built and polished frequency-displacement comparison.

Just as the tested cylindrical bar, the specimen's resultant excitation frequency lowered since the central region (displacement node) rigidity was reduced. The tapered setup had the predicted lower frequency change. Tapered setup frequency changed -21±2 Hz, while the hyperbolic setup presented a -42±8 Hz change.

The resultant displacement amplitude lowered with the obtained further away frequency from the booster horn setup. One only specimen showed a similar mass variation behaviour to the steel bar analysis, increasing displacement amplitude with lower rigidity and frequency. The amplitude differences are negligible.

The transducer sequentially applied power for displacement amplitude measurement serves as a specimen calibration. The analytical described method is then calculated with the measured A_0 displacement amplitude obtained for each applied power setting. The subsequent power/displacement correlation to stress is linearly proportional since the induced deformation is within the elastic region. The required transducer amplitude settings to achieve the desired fatigue stress are determined from the taken linearity.

For both tested tension-compression specimens, strain measurements were also conducted. Just as for the conducted sequential power displacement amplitude measurements, the same power sequential settings were applied for strain measurements. Again, both axial booster horn setups were tested. The measured strain was transformed to stress by Hooke's law (subchapter 4.4.2 equation (4.2)) with the static material determined properties. The resultant stress for each power setting was compared with the analytically calculated stress. Figure 5-6 plots the analytically calculated stress and strain gauge measured results for one AISI P20 specimen.

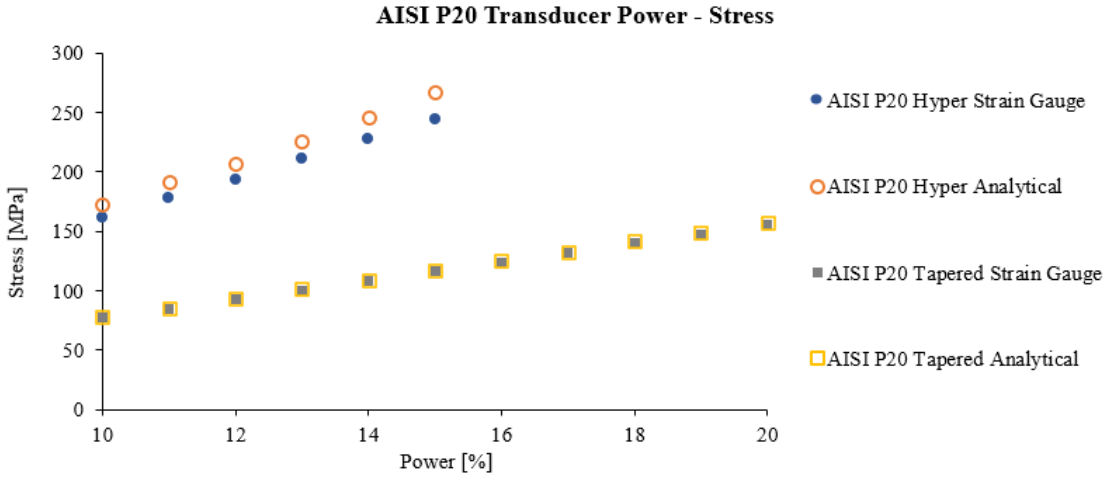

Figure 5-6. AISI P20 strain gauge and analytical solution stress amplitude for different transducer power settings.

A 7.7% and 0.8% average stress difference for the hyperbolic and tapered setup was obtained between the analytical calculation method and experimental strain gauge, respectively.

Regarding the AM titanium Ti6Al4V, strain gauge measurements were only made to polished specimens. Due to the as-built rough surface from the SLM manufacturing method, no reliable strain gauge measurement was possible. Figure 5-7plots Ti6Al4V analytically calculated, and strain gauge measured stress amplitudes for both the tapered and hyperbolic horn booster setups. From Figure 5-6 and Figure 5-7 analysis, the hyperbolic set showed an average of 2.2 times higher amplification than the tapered set. The amplification with and without specimen remains similar (Figure 5-1).

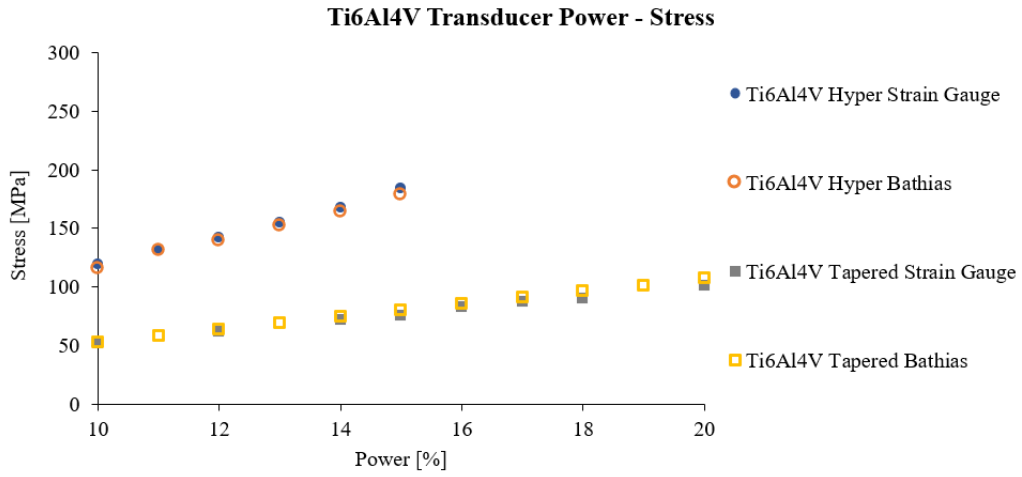

Figure 5-7.Ti6Al4V strain gauge and analytical solution stress amplitude for different transducer power settings.

A low average 2% and 4.3% difference was measured for hyperbolic and tapered setup, respectively. An overall lower stress difference between analytical and strain gauge results was observed in the Ti6Al4V than in AISI P20 specimens.

Both strain gauges show a lower tendency across all determined stress points. The analytical method determined the stress at the highest point while the stain gauges measured an average deformation of their own area, resulting in lower stress amplitude. Also, because of both the specimen and stain gauge small size and round shape, there are inevitable strain gauge placement deviations that will result in lower strain measurement.

As mentioned in the FEA tension-compression chapter (3.2), a numerical displacement to stress relation was obtained from the computed steady-state modal analysis. The FEA displacement at the specimen’s free base was associated with the fatigue region's stress at a surface point on the smallest cross-section area.

The three applied stress determination methods, analytical, strain gauge and FEA, were compared to both tested materials in the tapered and hyperbolic booster horn setups. Figure 5-8 for AISI P20 and Figure 5-9 for Ti6Al4V compare the three methods stress for the measured displacement.

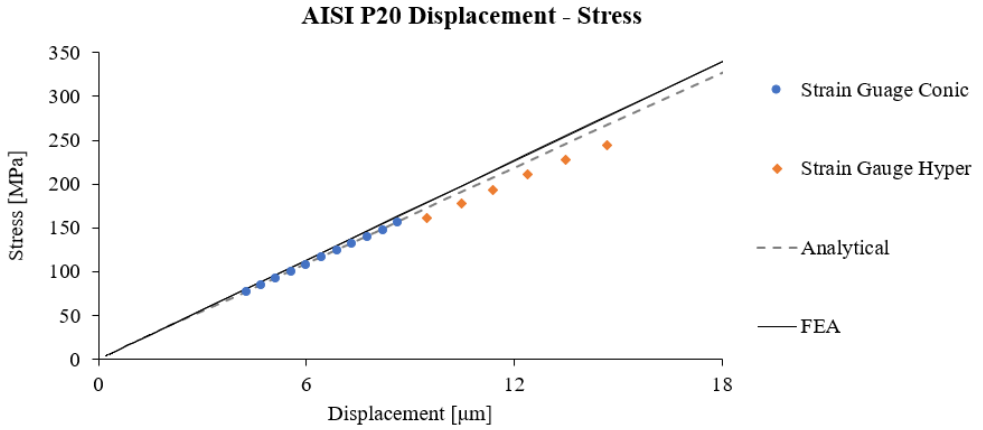

Figure 5-8. AISI P20 Tension-compression displacement to stress comparison between the analytical method, experimental strain gauges and FEA.

Looking carefully at Figure 5-8 and Figure 5-9, the FEA has higher stress to displacement ratio in both materials. AISI P20 FEA has a low 4% deviation from the analytical method. The AISI P20 FEA increase is associated with the hourglass shape's stress concentration. From careful FE analysis of the AISI P20 specimen stress distribution, a 1.035 stress concentration factor is present at the smallest cross-section. If the FEA displacement to stress relation is taken from the centre point of the smallest cross-section area, the FEA method difference to the analytical is below 1%.

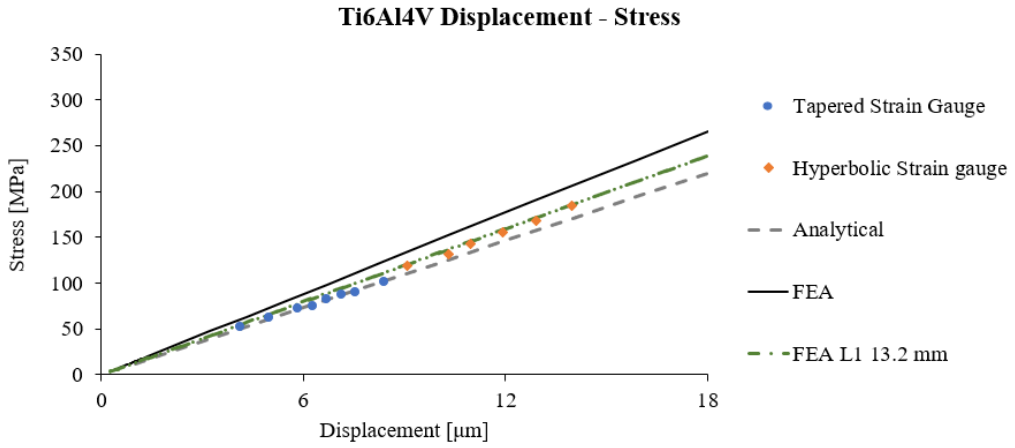

Figure 5-9. Ti6Al4V displacement to stress comparison between the analytical method, experimental strain gauges and FEA.

For the Ti6Al4V, a significant 20.8% difference is present. A second FEA analysis was conducted considering the ideal 20 kHz L_1 13.2 mm dimension for the later obtained mechanical static properties. As explained, Ti6Al4V specimens were designed and manufactured without conducting static properties determination experiments. The lower than predicted Young's modulus and the already increased L_1 dimension differed considerably from the ideal 20 kHz specimen. As it can be perceived, The FEA results for the ideal L_1 dimension present a considerably lower 8.8% difference to the analytical method. Ti6Al4V hourglass shape presented a 1.038 stress concentration factor, reducing the analytical difference to 4.8%.

The two specimen geometries are now compared in their modal response to the vibration excitation. The AISI P20 higher smallest cross-section area specimens present strain and displacement measurements with higher variability between each tested specimen. However, the AISI P20 specimen geometry suggests a better analytical solution agreement to all the stress determination applied methods, strain gauge and FEA. AISI P20 specimen also slightly increases testing volume, has a lower surface stress concentration, and has a more practical strain gauge placement shape.

No undeniably more desirable modal behaviour tension-compression geometry can be fully drawn from the made measurements. The increased smallest cross-section radius proved only a slight overall improvement. Nonetheless, both geometries showed the intended behaviour and proved both the FEA and analytical solution reliability.

5.3.2 Fatigue Testing Results and Fracture Surface Analysis

5.3.2.1 AISI P20 steel

The AISI P20 specimens were all machined from the same extruded round bar. All specimens were polished with high-grade sandpaper to a mirror-like finish. Afterwards, a black heat resistant paint was applied, and the already presented power to displacement calibration was conducted for all specimens.

Through a thermographic camera, a heat generation analysis of the first tested specimens was conducted. The thermographic camera is utilised while the specimen is under high deformation. This analysis not only serves as a last proof of the correct fatigue testing region, the specimen centre, but it helps visualize the heat dissipation and ensure no other

undesirable heat generation regions are present. Figure 5-10.A shows a thermal camera image of an AISI P20 specimen under higher deformation. For demonstration purposes of unwanted behaviour, the same AISI P20 specimen was placed in the multi-horn. Since it does not have a torsional resonance at 20 kHz, shear stress will be induced at the specimen horn connection region. Such stress will result in heat generation. Figure 5-10.B presents the undesirable heat generated between the specimen and the multi-horn.

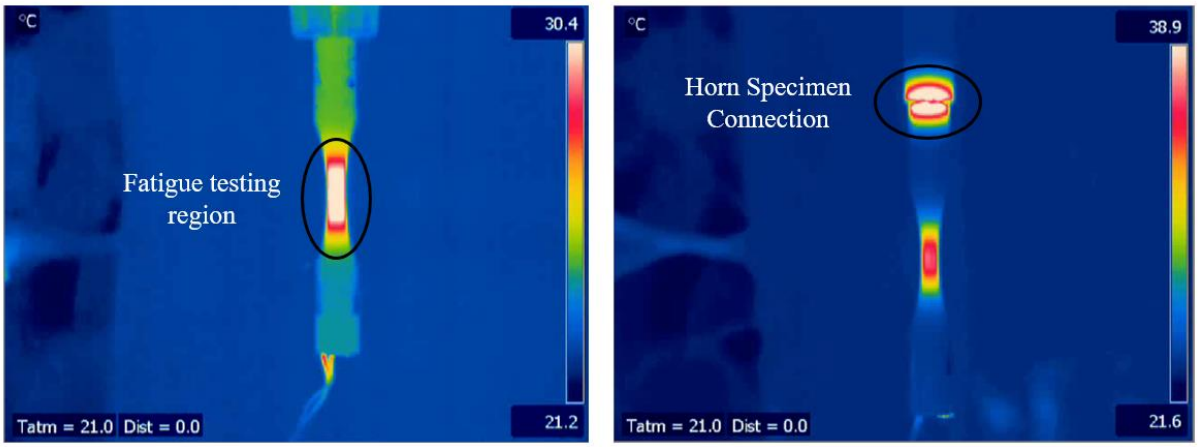

A B

Figure 5-10. Thermal camera UFT heat generation: (A) AISI P20 tension-compression test; (B) AISIP20 uniaxial specimen attached to the multi-horn setup demonstration showing unwanted heat generation.

UFT was only conducted after the displacement transducer calibration, the shown agreement between the strain gauges and the analytical method, and a final thermal image test. A pulse-pause time-controlled UFT was conducted with secondary temperature control with a pyrometer. The pulse and pause time was adjusted between specimens to ensure fast and even temperature fatigue tests. UFT pulse and midpoint temperature established range: 100 ms to 200ms in-service time; 20º to 40º at specimen midpoint.

Figure 5-11 presents the stress-life results with the specimen's respective fatigue life. The sample number depicted in the graph does not reflect the tested sequence. The fatigue failed and run-out specimens that did not achieve failure after 1E09 cycles are separately identified.

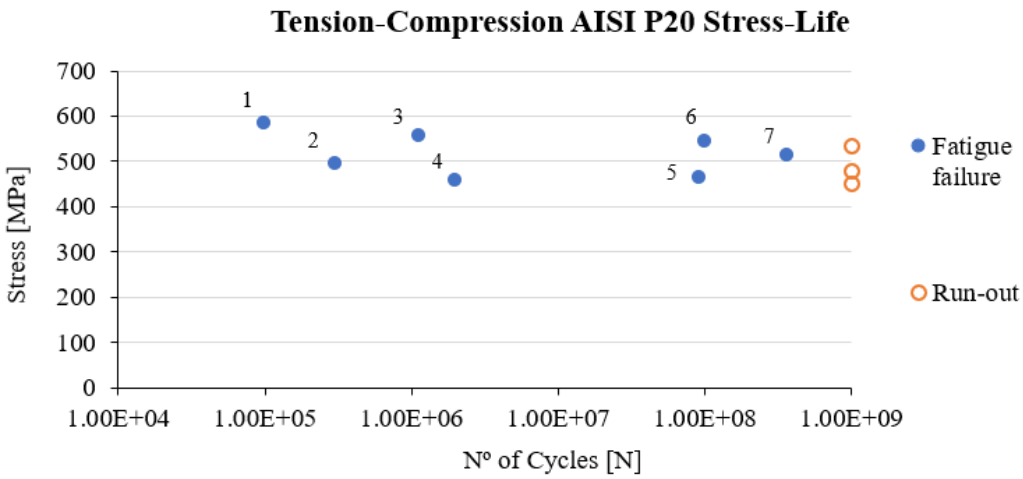

Figure 5-11. AISI P20 Tension-Compression R=-1 UFT stress-life fatigue results.

An almost asymptote considering the fatigue stress-life scatter results can be observed in Figure 5-11. As described in chapter 2.3.6, Figure 2-23, the results are on par with mild strength steels where the VHCF behaviour is almost asymptote. For such metals, the crack initiation is primarily focused on the surface.

Scanning Electron Microscope (SEM) was utilised for fatigue fracture surface analysis. Most fatigue crack initiations occurred at the surface. All specimens with one exception presented a surface crack initiation. All surface-initiated specimens presented a 0° crack initiation angle.

VHCF failed specimens with surface crack initiation do not present the fish-eye formation. A dark area is obtained around the surface crack initiation location. Afterwards, an observable mode I crack propagation is present until the fatigue crack limit. The mode I region presents a continuously growing crack propagation rate. The same crack initiation and propagation are seen between HCF and VHCF specimens. Figure 5-12 compares HCF specimen 3 and VHCF specimen 12 surface crack initiation morphology.

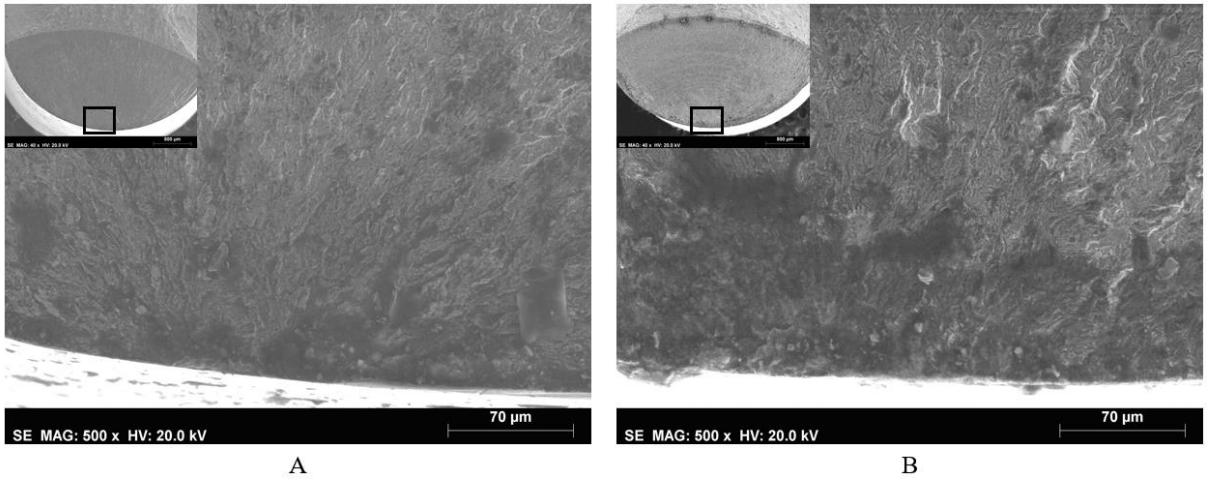

Figure 5-12. SEM 500x Surface crack initiation region: (A) HCF specimen 3; (B) VHCF specimen 7.

Both HCF and VHCF figure crack initiations have a dark area followed by a high crack propagation rate. The VHCF dark region tends to have a larger area followed by minor crack propagation indentations.

Jiang et al. [178] conducted tension-compression UFT to martensitic structural steel with considerably higher strength. A straightforward higher life for a lower stress and internal crack initiation at the surface was obtained. However, specimens with induced surface defects showed a similar stress life behaviour to the AISI P20 obtained. VHCF was still reached but with considerably lower stress amplitude and with a similar asymptote behaviour to AISI P20 Figure 5-11. Therefore, HCF and VHCF presented similar stress amplitudes, and all specimens had a surface crack initiation. Surface crack propagation also did not show FGA formation. Area Electron Diffraction analysis showed no grain refinement on surface crack initiated specimens. The same dark area morphology was observed on the initiation area, followed by a crack propagation mode I.

Specimen 1 presented the only internal crack initiation from a spherical inclusion. Figure 5-13 shows the specimen fatigue crack surface and the inclusion in detail with the respective diameter. Energy Dispersive Spectroscopy (EDS) for the chemical composition analysis was conducted to the inclusion and outside the inclusion. The EDS results are presented in Figure 5-14.

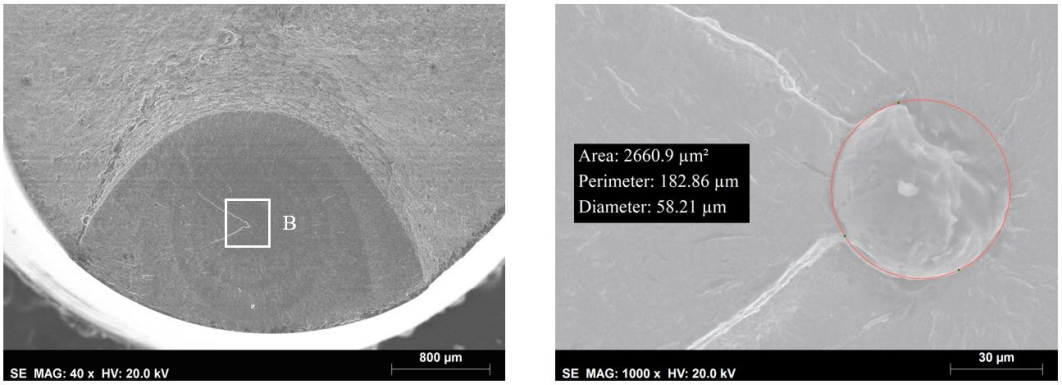

A B

Figure 5-13. Internal crack initiation specimen 1: (A) 40x fatigue fracture surface overview; (B) 1000x crack initiation inclusion with measured diameter.

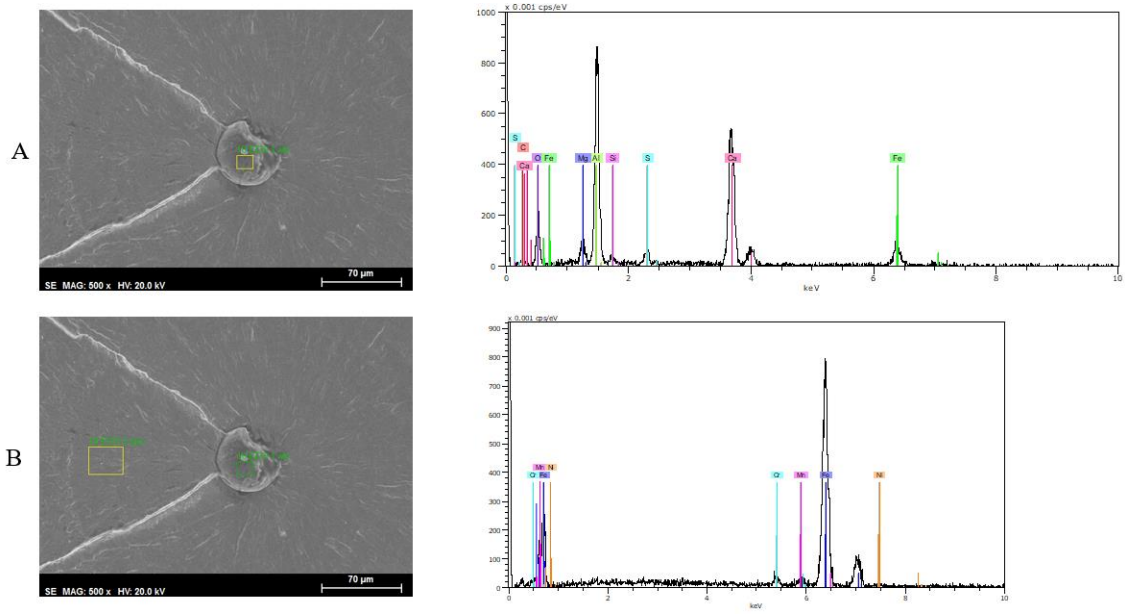

Figure 5-14. EDS chemical composition comparison: (A) spherical inclusion; (B) AISI P20 fatigue fracture surface.

The inclusion showed to be composed of aluminium oxide with considerable percentages of aluminium, oxygen, calcium and manganese. Similar shaped and chemical composed spherical inclusions were found in ultrasonic fatigue tested steels research [178; 207; 208]. The obtained chemical composition outside the inclusion is on point with Table 4-1 AISI P20 chemical composition, having a dominant iron percentage, chromium, manganese, and nickel.

5.3.2.2 Ti6Al4V titanium alloy

Ti6Al4V UFT was first conducted to as-built specimens. For both as-built and polished specimens, unordinary UFT failure occurred. Because UFT technology works with resonance, no complete failure of the testing sample is achieved, as previously explained. As the fatigue crack grows, the stiffness decreases, and consequently, the resonance frequency also decreases. As the crack reaches a considerable size, the specimen resonance frequency brings the ultrasonic set's frequency below the transducer range, and the experiment comes to a stop. Afterwards, the specimen is fully fractured at an electromechanical or servo-hydraulic machine (Figure 4-30). However, most tested titanium specimens were fully fractured in UFT conditions. One assumption for such behaviour is due to the low overall weight compared to other most commonly UFT tested metals, the specimen frequency decrease was not significant enough to decrease the used ultrasonic setup below the transducer range. The machine only came to an out-of-frequency range stop when the specimen had a complete failure. Another assumption is due to the assumed residual stresses later discussed with the fatigue fracture surface.

The initial high-stress level was applied. According to the previously resulted stress-life, the succeeding applied amplitude stress was adjusted for failure within the VHCF regime. Figure 5-15 presents the stress-life results with the specimens respective fatigue life, initiation region, defect size and distance from the surface (regarding sub-surface crack initiation). The sample number depicted in the graph does not reflect the tested sequence.

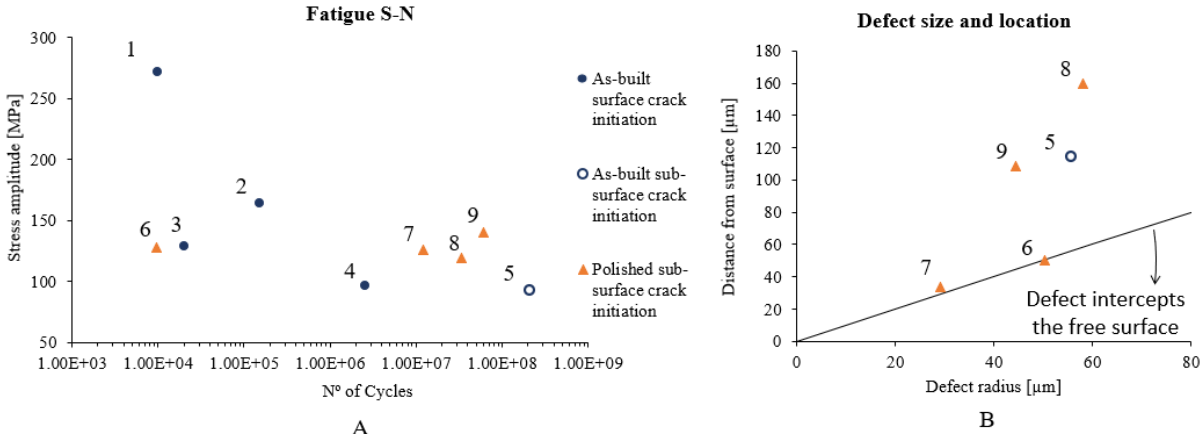

Figure 5-15. Ti6Al4V: (A) Tension-compression R=-1 UFT stress-life fatigue results for as-built and polished ; (B) crack initiation defect size to distance from the surface.

Polished VHCF regime failed specimens proved a 30 to 40% stress amplitude increase for a similar life time. 10^6 to 10^9 cycles failed as-built specimens had an R=-1 amplitude range between 90-100 MPa; Polished specimens presented 120-140 MPa. Both the as-built and polished specimens presented, in Figure 5-15, two results with lower than expected life, specimens 3 and 6 (around 10 thousand cycles). The lower life appears to be associated with defects considerably outside the measured defect average size.

From as-built fatigue fracture observation, crack initiation occurred predominantly at the surface. Specimen 4 presented multi-surface crack initiation locations. Only the highest cycles to failure specimen 5 presented crack initiation at a pore defect in the sub-surface region. Figure 5-16 shows the observed as-built SEM fractures and crack initiation of specimen 4 (Figure 5-16.A) and specimen 5 with defect radius and distance to surface (Figure 5-16.B).

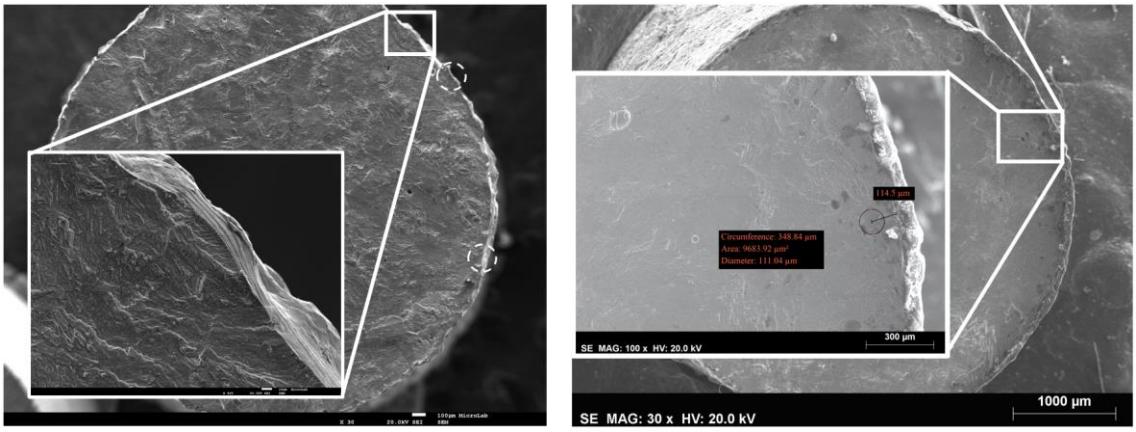

Figure 5-16. SEM fracture surface images: (A) surface-initiated specimen 4; (B) Sub-surface-initiated specimen 5.

In opposition, all polished specimens presented crack initiation at the sub-surface region originating from pores and smooth facets. These results are aligned with VHCF testing research of Ti6Al4V [190; 209–211].

Polished specimens, numbers 7, 8 and 9, presented the fish-eye formation with the Fine Granular Area (FGA) around the pore or smooth facet. UFT conducted experiments in the referenced research [209] presented similar crack initiation in defects and FGA formation. The limits of the fish-eye were not evident in the taken SEM images. Figure 5-17 shows specimen 8 fracture surface identifying the smooth facet defect responsible for crack initiation, its size, distance from the surface and the FGA limits.

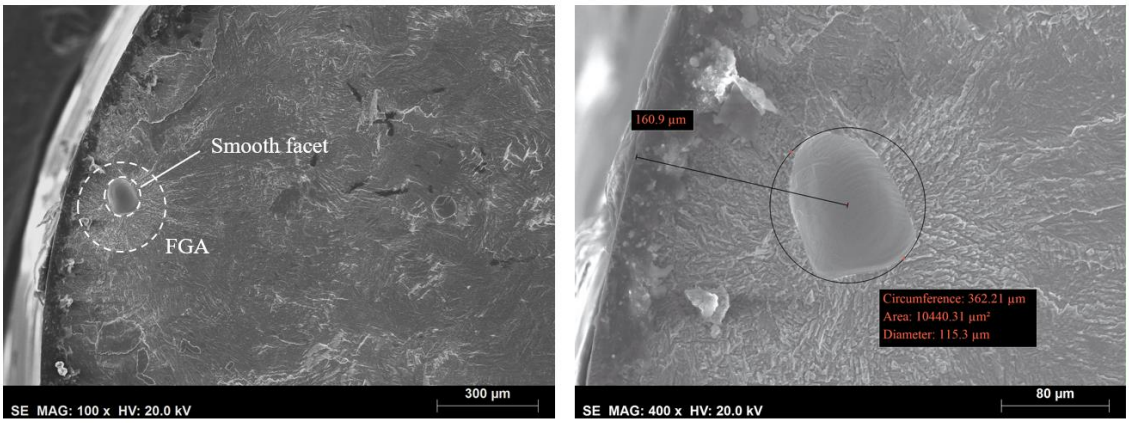

Figure 5-17. SEM fracture surface of specimen 8: (A)sub-surface smooth-facet responsible for the crack initiation and FGA region; (B) Smooth facet size and distance from the surface.

The as-built and polished specimens presented two results with lower than expected life, specimens 3 (as-built) and 6 (polished). Just as specimen 4, specimen 3 showed multiple surface crack initiation. No apparent reason for lower life was perceived. For Specimen 6, the premature failure initiated at a pore intercepting the free surface. The respective pore defect had a similar radius to the specimen 5 crack initiation. According to the Zhiqiang et al. investigation on the pore position [180], a sharp increase in stress concentration occurs when the pore intercepts the free surface. A 37 % higher stress amplitude to specimen 5 and intercepting the surface edge can justify the premature specimen 6 life span. Specimen 7 had the smallest defect crack initiation radius, similar to specimen 6, but the defect does not intercept the free surface. Figure 5-18 shows the specimen 6 and 7 crack initiation pore on the edge of the free surface. No FGA is perceived in specimen 6.

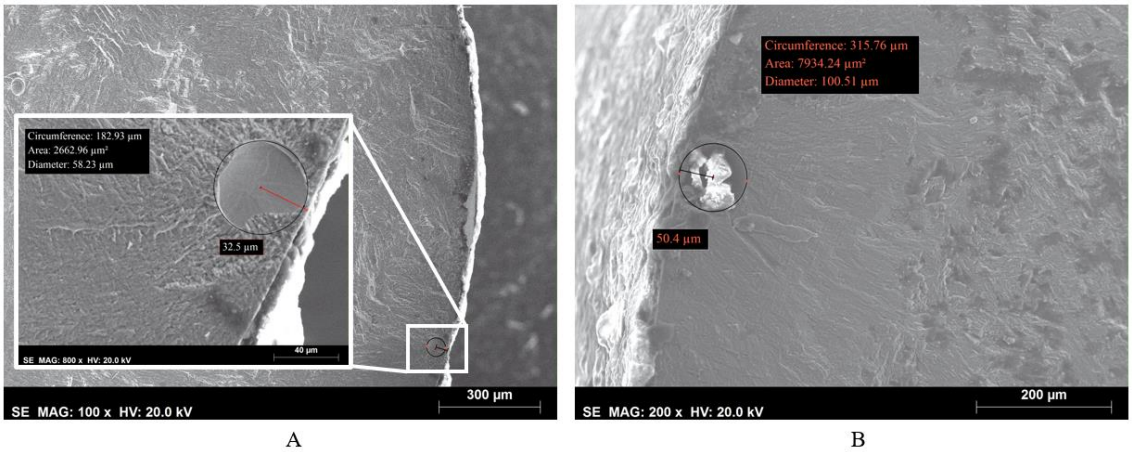

Figure 5-18. Sub-surface crack initiation pore radius and distance from the surface: (A) Specimen 7; (B) Specimen 6.

From a detailed analysis of all life-stress and fracture surfaces results, four different parameters were shown the most relevant, surface roughness, defect size, defect location, and residual stresses. Surface roughness, defect size and morphology were already correlated with fatigue strength in HCF, especially in the VHCF regime [66; 190; 209–212]. Most crack-initiated defects presented a radius above the measured 27 μm average from all observed and radius sized pores and smooth facets. The fatigue crack-initiated defects were located close to the edge of the surface. When comparing referenced fatigue fractures, the present work did not have a single internal crack initiation specimen.

Moreover, all specimens presented a peculiar fatigue fracture area shape. Both the crack initiation location and fracture surface differences can be associated with present residual stress. As mentioned, no post-SLM heat treatment was conducted. Residual stress is a complex subject that is printing parameters-dependent [213], such as shape, thickness [214] and distance from the build plate [215]. Abdul et al. [216] crack growth experiment have shown the presence of residual stresses in SLM Ti6Al4V. The residual stress was observed to be in tension around the surface and compression internally, resulting in a lower crack propagation area until total failure. Abdul lower crack propagation area can be correlated with the uncommon observed total failure in the ultrasonic fatigue machine. Casavola et al. [214] have also proven tensile residual printing direction stress at the surface.

The surface residual stresses may have contributed to fatigue crack nucleation and propagation, justifying the surface/sub-surface crack initiation trend and no internal crack initiation. The fracture surface shape comparison also suggests the presence of the described residual stress. An observed higher surface crack propagation on the surface could have been related to present tensile residual stress. Figure 5-19 compares the obtained fracture surface shape with the obtained by other researchers heat-treated Ti6Al4V ultrasonic specimens.

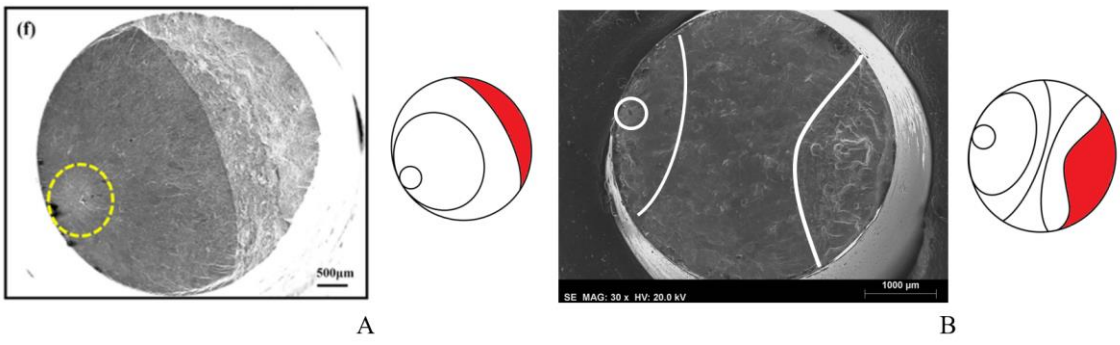

Figure 5-19. Fracture surface shape comparison: (A) ordinary VHCF fatigue fracture shape by Qian et al. [212]; (B) obtained fracture surface shape.

5.4 Pure Torsion Ultrasonic Fatigue Testing Results

As first mentioned in the FEA analysis of the ultrasonic pure torsion components and machine analysis (chapter 3.3), the first torsional horn TH1 presented a considerably lower frequency than expected. To rectify TH1 frequency, the length of its lowest radius constant section (L_{th}), was progressively machined (Mach *x*). The complete setup (LH, pin and TH) was fixed in a milling machine to progressively reduce L_{th} and, therefore increase TH frequency. Figure 5-20 shows a representation of the Mach process and the fixed setup on the milling machine. The TH1 horn was never detached from the setup across all conducted Mach sequences because the pin is tightly fixed between TH and LH. To remove it repetitively could have resulted in unwanted damage to any of the three components.

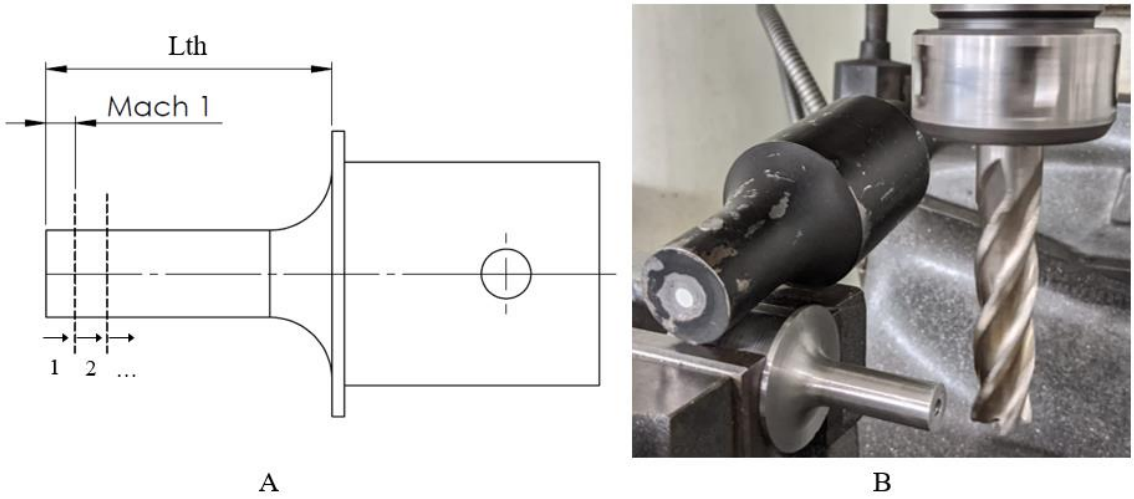

Figure 5-20. (A) Mach sequence representation; (B) pure torsional setup (LH, pin, and TH) fixed on milling machine.

For each Mach, a modal analysis was conducted to the complete setup. Across the modal analyses, two different specimens were used for the measurements following the Figure 4-26 experimental setup. A rosette strain gauge was applied to one of the specimens. This specimen was only applied in the pure torsion ultrasonic setup in specific sequences. Because strain gauges are easily damaged across the conducted tests, the number of measurements was limited to ensure it would function until the last sequence. The no strain gauge specimen was applied in all Mach.

The Mach sequences were conducted to two equal torsional horns (TH1 and TH2). The first applied TH1 was machined beyond the wanted frequency point, while TH2 was machined until the closest frequency to LH. TH1 Mach sequences served as a guide for a final TH2.

The modal analysis, displacement and strain measurements results are now presented. UFT was conducted after reaching the working ultrasonic pure torsion setup, followed by SEM analysis of the fatigue fracture surfaces.

5.4.1 Modal FDD analysis

Before attaching the pin connector and the TH1 to the LH, FDD analysis of the LH alone was conducted. Also, an LH with the pin (no TH) FDD was also conducted. It is not possible to conduct an experimental modal analysis of the THs alone without a rotational piezoelectric transducer.

As aforementioned in FEA results, the pin hole in LH and TH has a frequency resulting influence. The pin hole changes the overall geometry and reduces the mass, resulting in an increased frequency. The obtained frequency and displacement response with and without the hole and pin was different, as the FEA free vibration frequency Table 3-3 predicted. The resulting LH with pin FDD analysis is presented in Figure 5-21 and compared to the equivalent steady-state FEA analysis. The FEA steady-state to LH with hole (no pin) is also present for comparison purposes. Figure 5-21 identifies the denoted LH1 and LH2 resonant modes and the PSD frequency region associated with the transducer excited stepwise frequency range (from 19450 to 20450 Hz).

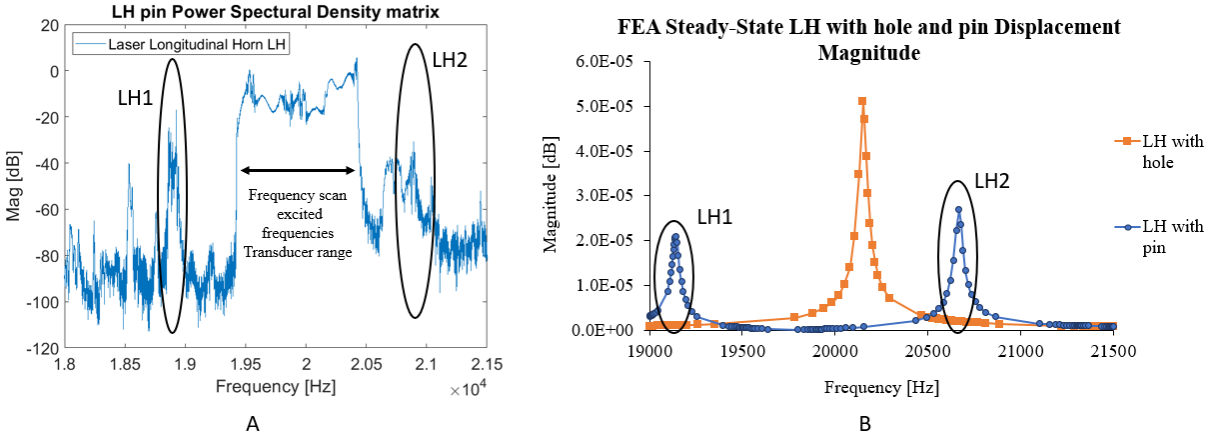

Figure 5-21. LH with pin FDD comparison with FEA steady-state result with identified LH1 and LH2 resonant modes.

The PSD transducer frequency scan region (19450 to 20450 Hz) presents a higher magnitude than other frequencies since the excitation sequence did not follow the recommended random excitation for FDD modal analysis. The resulting FDD shows two resonant modes outside the frequency range of the transducer, just as FEA predicted results. The LH1 mode with around 18926Hz (FEA: 19122 Hz) and LH2 mode with 20890 Hz (FEA: 20638 Hz). Within the frequency operation range of the transducer, there is no working resonant mode. The LH with pin behaviour will occur on the complete setup when there is slip between TH and the pin. The resulting frequency LH no pin FDD has one resonant mode at 20101 Hz (FEA: 20151 Hz).

The obtained frequencies from the LH analysis are different from the obtained by FEA. The difference is associated with FEA to experimental differences, machining tolerances and material property variability. These are the expected and unwanted differences that the study developed methodology intends to prevent and, therefore, ensure the correct functioning of the ultrasonic machine.

After the LH alone and with the pin analysis, the first TH1 was connected. An FDD modal analysis was conducted without any machining step (as-built). For both TH1 and TH2 machined sequences, the FDD analysis proved the existence of a second excitable resonant mode. This was also observed by the FEA Figure 3-13 steady-state modal analysis. The obtained amplitude and phase between the two measured points for both detected modes was in compliance with the FEA results. Figure 5-22 plots the setup frequency of excitation for all L_{th} dimensions from TH1 and TH2 Mach sequences and compares them to the respective FEA obtained frequencies.

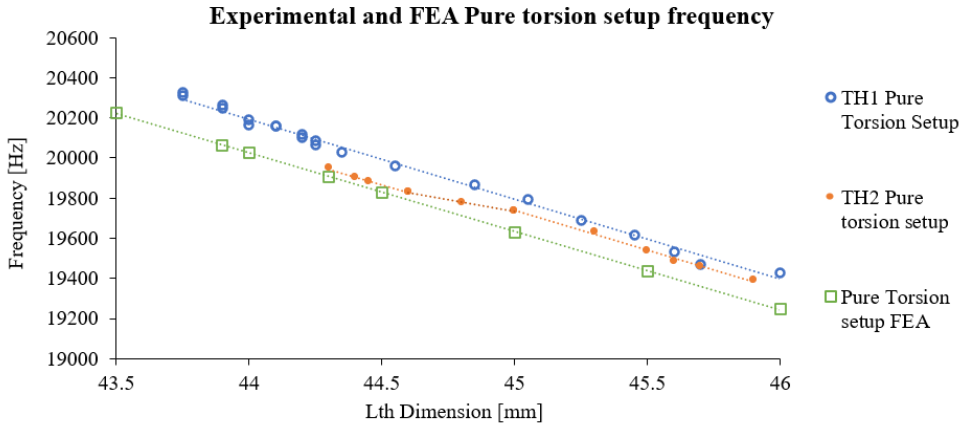

Figure 5-22.Experimental and FEA comparison of pure torsional setup frequency for all TH Lth dimensions.

As expected, after each Lth dimension reduction, the TH frequency increased. The frequency linearly increased with each Mach, similar to the steel bar mass reduction experiment. The setup frequency increase is parallel to the FEA obtained. Figure 5-22 also shows the frequency variability associated with machining tolerances and material properties variability. A frequency difference is present for similar L_{th} dimension values between two TH horns machined through the same Computer Numerical Control (CNC) method, with the same material batch, following the same technical drawing.

The final reached TH2 Lth dimension was 44.3 mm, frequency equivalent to FEA 43.9 mm. If the FEA dimension was followed, the setup had already surpassed the working frequency without a possible readjustment.

For the two THs, FDD analyses were conducted between all Mach. TH1 was machined beyond the frequency point of interest. From the complete Mach sequence, several undesired behaviours were observed:

- The transducer could not maintain the same frequency state when testing at constant frequency in the initial Mach sequences. This meant that high-frequency changes were continuously applied by the transducer controller when conducting displacement measurements. The excitation frequency only became constant in Mach with TH frequency closer to the LH horn.
- The ultrasonic machine made an acute sound in the first and last Mach when in constant frequency excitation. The sound was dimmed and practically muted in closer TH frequencies to LH. This implies a non-correctly working setup with possible slip/friction between components.
- Higher transducer amplitudes resulted in TH movement from the LH contact.
- When observing both the FDD analysis and the associated lasers frequency scan output, an LH resonant mode within the frequency transducer range does not appear in full detail. In some TH1 Mach, the FDD could still detect the torsional setup resonance and the LH1 and LH2 resonant modes.

The observable behaviours were correlated with slip in the TH. When testing the complete setup, if the connector pin presents slip with given horn, the resulting setup resonant shape and frequency will tend towards two possible outcomes. When slip occurs in the LH horn the modal response will tend towards LH alone result. In the TH, the displacement amplitude

will decrease, the setup frequency will change, and the LH will behave similarly to it alone with pin.

The modal result when testing the setup was a mixture between the complete torsional setup and the LH with pin only setup. Figure 5-23 presents the frequency scan laser output and FDD result for TH1 machine sequence 1 (Mach1). Both the torsional setup resonant mode of interest and LH with pin LH1 and LH2 resonant modes are identified in Figure 5-23.A PSD matrix. The resulting laser output exhibits a low amplitude with similar behaviour to LH pin output and one higher rotation amplitude associated with the torsional resonant mode.

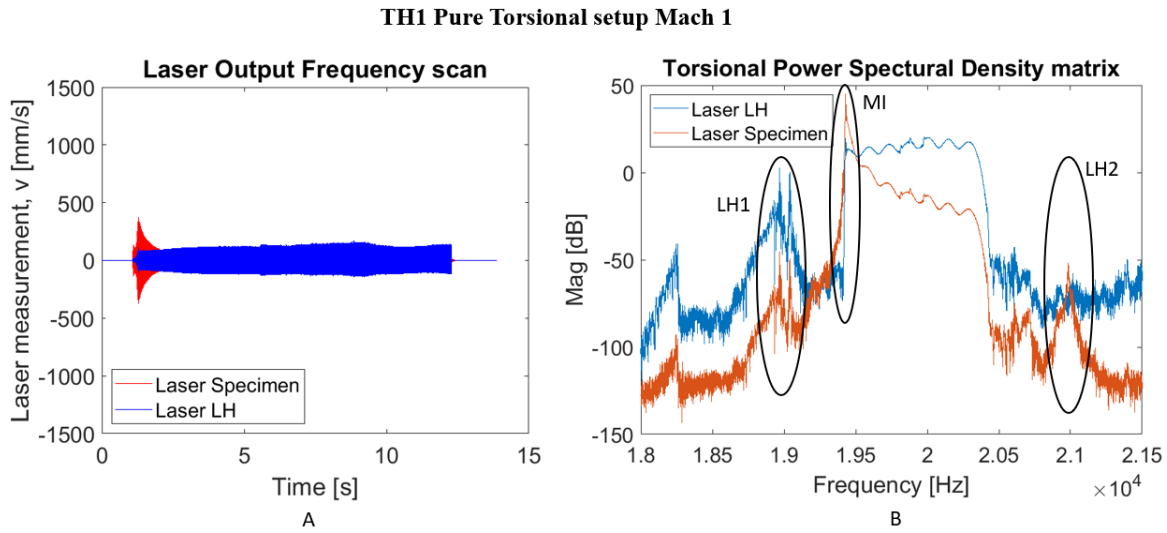

Figure 5-23. TH1 pure torsional setup Mach 1 frequency scan: (A) laser output; (B) FDD PSD result with identified resonant modes.

As TH1 Mach sequences progressed, the slip behaviour diminished, the rotational displacement amplitude increased, and the LH resonance within the frequency range of the transducer appeared and had a sequential increase in amplitude.

TH2 was manufactured, assembled and sequentially machined, taking into account all results and conclusions from the TH1 setup.

One significant improvement was the pin TH link made with a tighter fit. This resulted in improved TH2 behaviour, even from the as-built first FDD analysis. For comparison and to convey the resulting improvements made to TH2, Figure 5-24 shows TH1 and TH2 frequency scan laser output of different Mach stages.

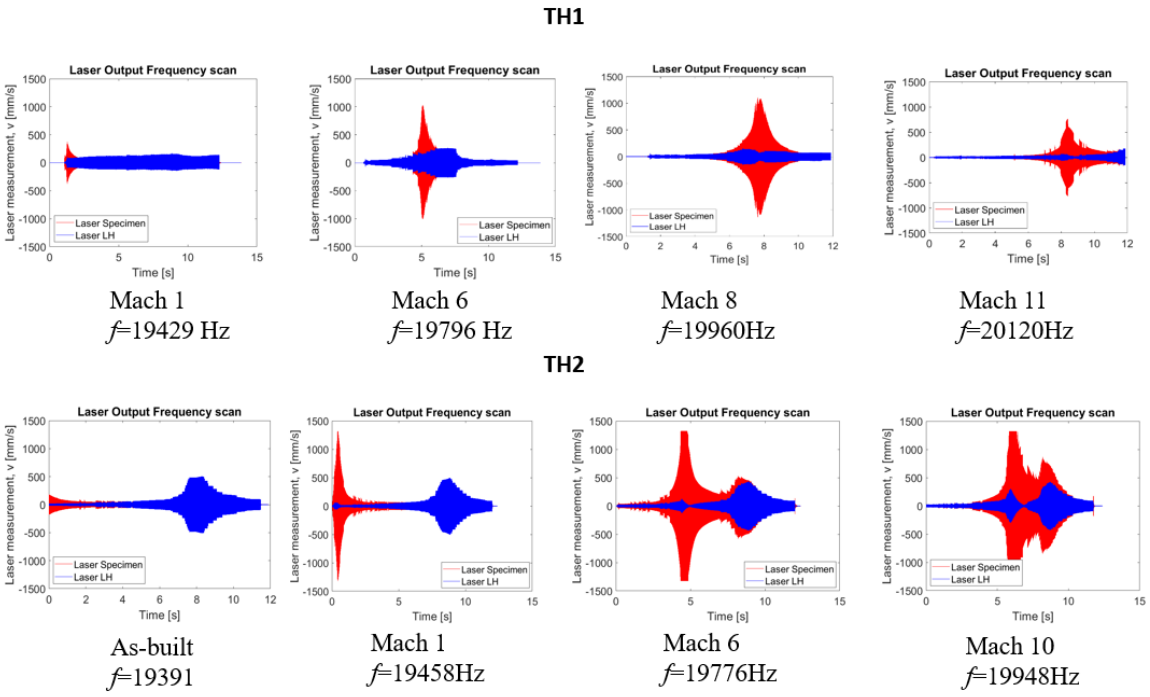

Figure 5-24. TH1 and TH2 laser output comparison for different Mach stages.

From TH2 Mach 1 to Mach 10, a second resonant mode appears after the mode of interest. The mode did not appear in TH1 and has similar behaviour to the predicted by FEA, only its frequency is considerably lower. From a close study of FDD and observations of the machine in high transducer settings, the second mode appearance was linked to two possible hypotheses: the much higher rotation across the Mach achieved by the tighter fit pin had a TH slip after the resonant mode, or the LH horn instead of the TH had pin slip.

It was concluded that the present second mode showed that the connection to the pin was still not correctly secured, especially in high power settings. A resulting loss of contact between TH1 and TH2 with LH in higher transducer amplitudes did not allow for UFT high rotational excitation. A new TH support to the structure was produced to impede the TH2 movement. To achieve this TH support ring was fixed to the structure with an applied force in the LH direction.

This last made improvement increased the second mode frequency and resulted in a considerable increase in specimen rotation. All laser rotational measurements were no longer reliable because the increased rotation reached the limit of the equipment capability, clipping the output signal. However, strain gauge measurements were still possible. The pure torsion MI resonant mode also had an increase in its frequency. Figure 5-25 compares the laser output of

TH Mach 10 with and without the made fixed support with the resulting FDD frequencies of MI and the second PM.

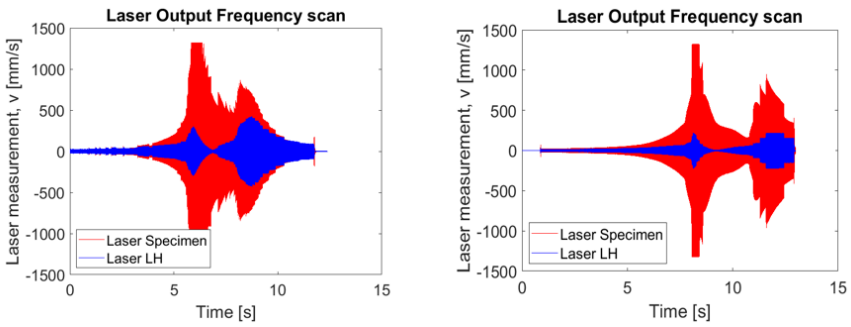

Mach 10
MI f = 19948 Hz
PM f = 20122 Hz

Mach 10 (with new support)
MI f = 20050 Hz
PM f = 20330 Hz

Figure 5-25. Frequency scan laser output comparison between the first Mach 10 with the applied new TH fixing support to the stand structure.

From both the laser output and FDD, the new support addition improved the frequency response of the pure torsion ultrasonic setup. The output is more stable across all excited frequencies, and an increased 106 Hz frequency difference between MI and PM was obtained.

In conclusion, the established experimental procedure allowed for a guaranteed functional pure torsional machine with proven UFT failed specimens. However, the setup should be improved. Even at low transducer settings, the built LH TH setup achieved a too high rotation displacement for the present laser equipment to measure. Therefore, the LH and TH geometry should be changed to ensure a lower rotational amplification, preferably the LH horn. By reducing the LH displacement amplification, the pin will be subjected to lower displacement and deformation, reducing the slip possibility between the two horns.

5.4.2 Strain and Displacement Measurements

Across the Mach sequences, after FDD modal analysis, the setup was excited in constant frequency. Both displacement and strain measurements were made at different transducer amplitude settings. As previously explained, to protect and ensure consistent strain gauge measurements, the second specimen with the strain gauge was spatially applied between machined sequences.

With the measured displacements at the free base, the presented analytical equations were applied for stress determination at the smallest-cross section of the specimen. The analytically obtained stress amplitude was then compared with the strain gauge and with the steady-state FEA results. Figure 5-26 compares the displacement to stress analytical ratio to the experimentally measured by laser and strain gauge and the steady-state FEA determined ratio.

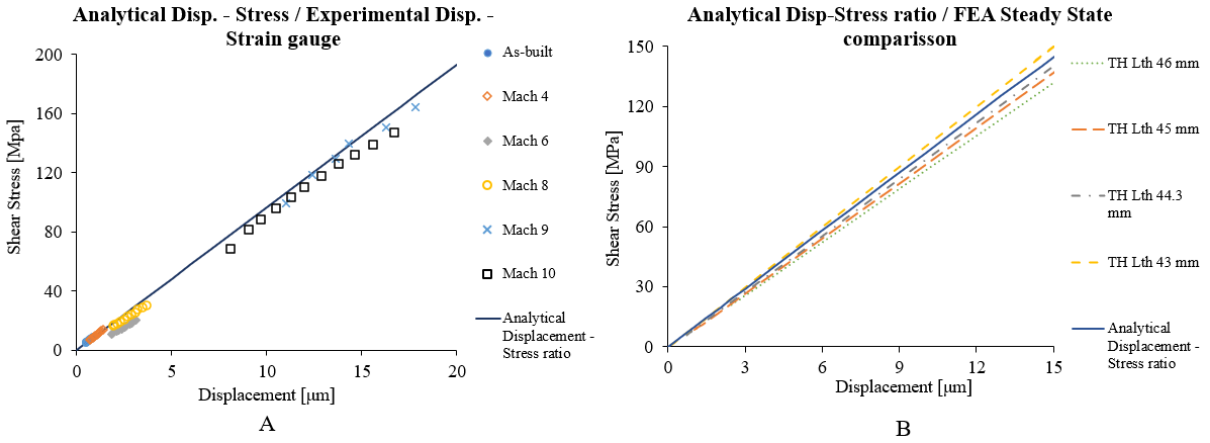

Figure 5-26. Pure torsion, displacement to stress ratio comparison between analytical, experimental and FEA.

The last machined sequence (Mach 10 without the new base) analytical solution presents an average +7.2% error to the stress amplitude measured by the strain gauge. The previous Mach sequences and the as-built also show an acceptable error difference as it can be perceived by Figure 5-26. The specimen machine groves have shown an acceptable experimental measuring method for the determination of the applied shear stress.

The FEA analysis presents a lower -2.6% error difference when considering the final Mach 10 TH2 A dimension (44.3 mm). The FEA results show an even lower -1.3% difference when considering the FEA determined TH A dimension of 43.9 mm.

The strain gauge results present an overall lower stress amplitude in association with the measured displacement. This can be associated with the area of measurement of the strain gauge. Due to its size, the strain gauge measures the average strain in one given area and not one single point as in the analytical and FEA solutions. The specimen and strain gauge size and shape also make strain gauge application very difficult to ensure correct alignment and exact placement in the smallest cross-section area (fatigue testing and highest stress amplitude region).

5.4.3 Ultrasonic Pure Torsion AISI P20 Fatigue Results

Having reached a working pure torsional ultrasonic machine setup, a first thermal camera temperature analysis was conducted. This first experiment is conducted at a high enough transducer power setting, meaning high strain, to reach a distinct heat generation. No laser or strain gauges are used in this experiment. The high heat generation on the centre of all tested specimens proved the high-stress region and no induced deformation and friction on the TH specimen connection region. Figure 5-27 shows a pure torsional specimen excited in resonance under a thermal camera.

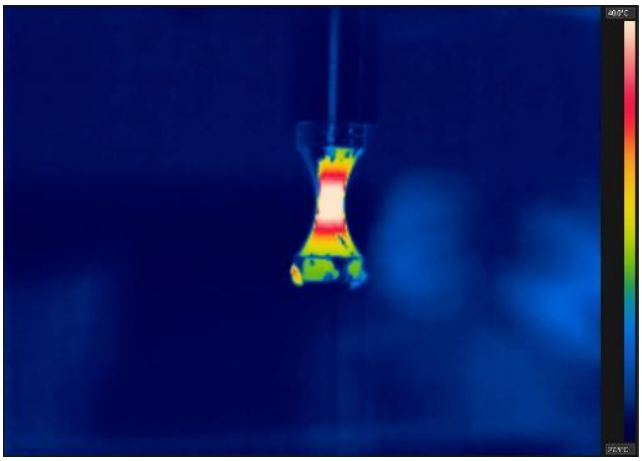

Figure 5-27. Thermal camera UFT heat generation of a pure torsion AISI P20 specimen.

A thermal analysis was also conducted in the remaining setup. There was no clear heat generation location. However, when testing at high transducer power settings for UFT, an increased heat between TH and LH was detected. A cooling fan was added to reduce the generated heat and prevent damage to the pin LH and TH setup.

Since the resulting rotational displacement had a too significant transducer axial displacement amplification, no reliable laser measurements were possible and, therefore, no specimen calibration. In this instance only strain gauge specimen calibration was possible. Only a small number of specimens were possible to be correctly under UFT. Figure 5-28 presents the pure torsion stress-life results with an attributed sample number. The number sequence does not reflect the tested sequence.

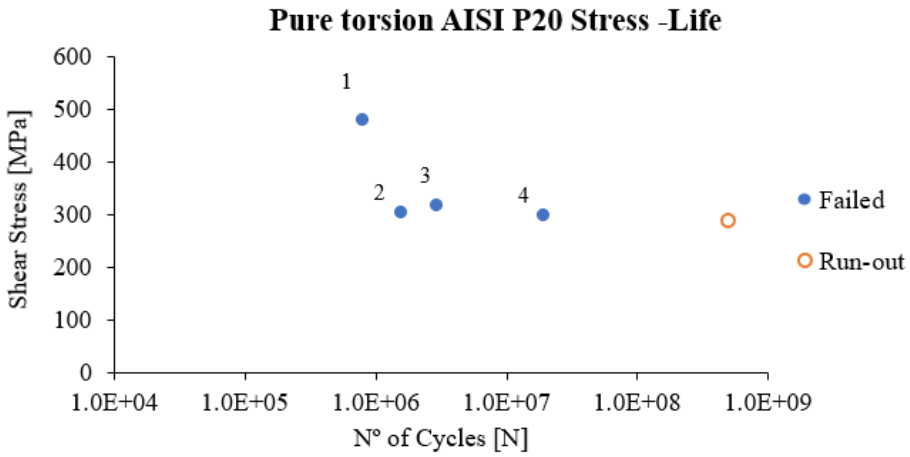

Figure 5-28. AISI P20 pure torsion R=-1 S-N fatigue results.

Even with a small set of fatigue failed specimens, asymptote shape behaviour is obtained beyond the HCF regime, similar to tension-compression S-N results (Figure 5-11). After fatigue crack propagation and loss of resonance, the specimens were fully fractured in a servo-hydraulic machine as presented in Figure 4-30.

All torsional specimens exhibit a crack initiation at the surface. Crack initiation occurs at the point with a low angle associated with the highest shear stress plane mode II. Afterwards, the crack propagates at an increasing angle with radial marks (shear bands). In some specimens, the crack bifurcated. Figure 5-29 shows microscopic images of the specimen 3 fatigue fracture surface and crack initiation location. Figure 5-29 identifies the fatigue fracture surface and final fracture achieved by the servo-hydraulic machine. High heat generation marks are also visible in Figure 5-29 in the first stages of crack propagation. An almost zero degrees angle is present in the crack initiation region, followed by a continuous increase in crack angle.

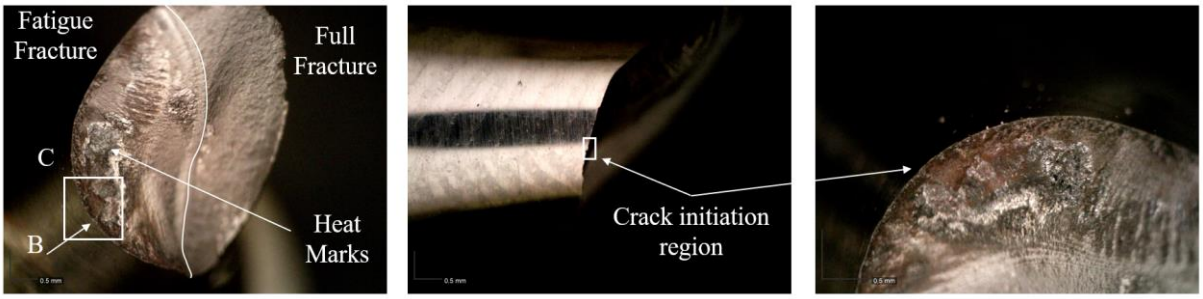

Figure 5-29. AISI P20 pure torsion specimen 3: (A) fatigue and full fracture surface: (B) Crack initiation angle; (C) fatigue fracture surface crack initiation region.

Xue et al. [115] observed similar surface crack initiation in ultrasonic pure torsional fatigue to perlitic D38MSV5S steel. With a pure torsion ultrasonic machine following the same LH pin TH specimen concept, they observed a crack initiation at the maximum shear plane (normal to the axisymmetric axis of the specimen) followed by an increasing crack angle towards 45º degrees, the maximum principal stress plane.

SEM analysis of the fracture surface allowed for more detailed crack initiation and propagation analysis. The crack initiation region has a smooth surface. After some propagation, the radial marks of the induced shear stress start to appear with increasing shape.

Figure 5-30 shows the crack initiation location, smooth area propagation region, and radial marks of pure torsion specimen 4. Specimen 4 fatigue crack bifurcated after the smooth area region of propagation. Both bifurcated fatigue crack paths showed a 45º degree angle of propagation.

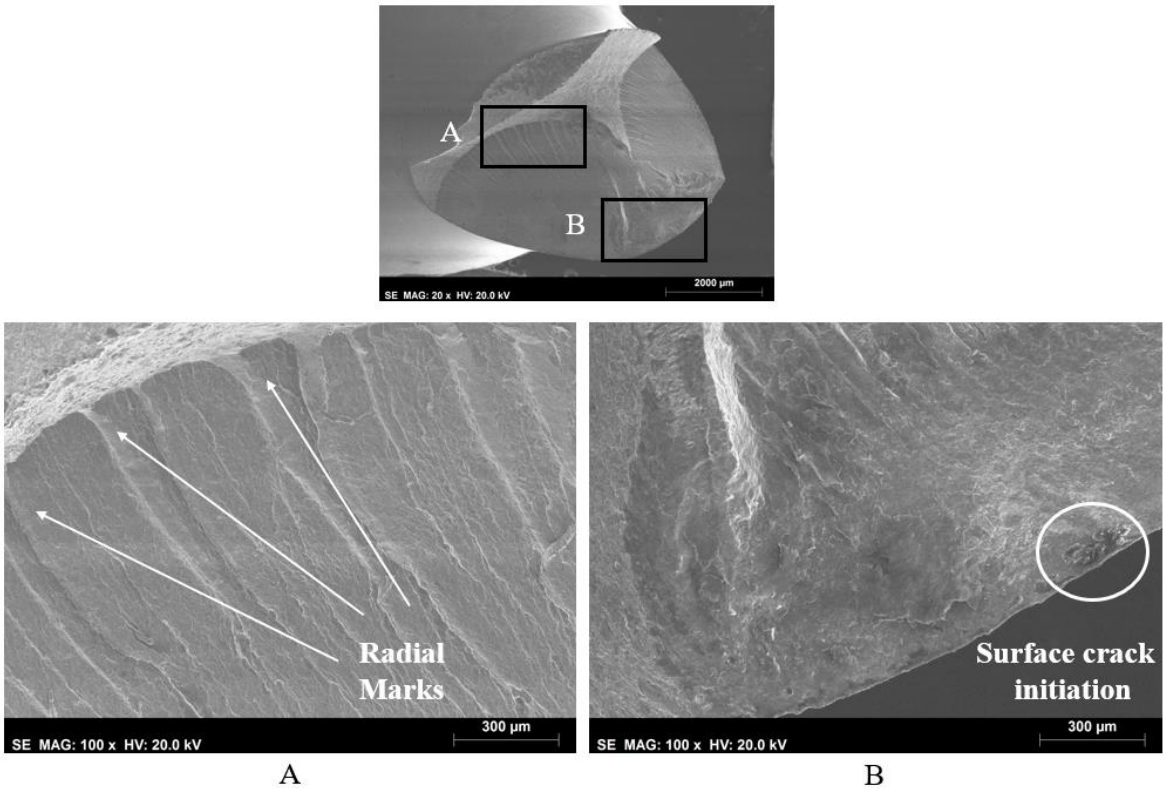

Figure 5-30. Pure torsion specimen 4 fatigue crack surface: (A) radial marks; (B) surface crack initiation.

5.5 Multiaxial Ultrasonic Fatigue Testing Results

5.5.1 Tension-Torsion

As depicted by the FEA study, three different three throated specimens (Spc*x*) were machined and tested. All specimens were manufactured from the same cylindrical bar as the tension-compression and pure torsion ultrasonic fatigue specimens. Due to the somewhat complex shape, all specimens were machined by CNC lathe machine. Afterwards, the specimens were carefully polished on their main throat only.

Just as for the pure torsion specimens' small groves were made at the specimen's free base. The groves enabled the free base rotation measurement through the Polytec vibrometer laser. Strain gauges were also applied to the polished main throat of all tested tension-torsion three throated specimens.

All specimens were first carefully studied in their modal response and respective mode shape deformation. The modal response was also conducted to the specimens before the polishing treatment and subsequent strain gauge placement. The before and after polishing treatment modal change was also quantified.

All specimens were attached to the multi-horn and the two uniaxial tapered and hyperbolic axial horns. Since the specimens were designed with the first longitudinal mode, the specimens can fully function in an ultrasonic tension-compression setup.

The modal analysis of all specimens within the three setups, multi-horn and two uniaxial horns, is first presented. Afterwards, the displacement and strain measurements are presented. The experimental modal shape and transducer power to displacement and stress behaviour results were compared to all FEA results. Only after all required data was taken and verified a given stress combination amplitude was established for a given transducer power setting and UFT until fracture was finally conducted.

5.5.1.1 Modal FDD analysis

The followed measuring and control methodology was extensively presented in chapter 4.4 for all here presented modal analysis. Only one displacement laser aligned with the specimen's length was applied for the two axial booster horn setups. For the booster multi-horn setup a second laser was focused on the made groves at the specimen's free base.

All three throated specimens were able to be excited within the transducer frequency range of the two axial booster horn setups. A clear single axial resonant mode is achieved within the transducer range, 19450 to 20450 Hz. Figure 5-31 shows the axial laser measurement for a polished SPC2 specimen attached to the booster hyperbolic setup.

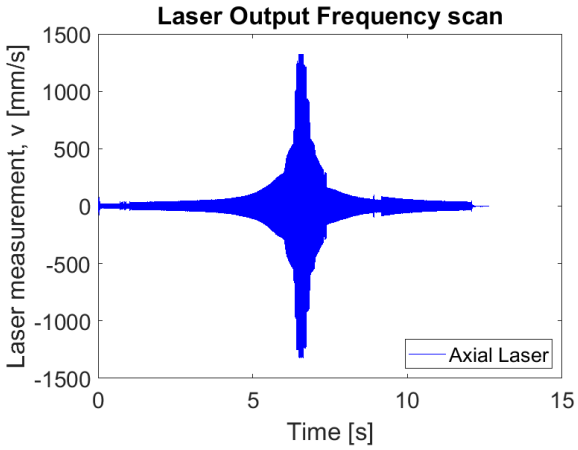

Figure 5-31. Laser measurement result across a transducer frequency scan of the booster axial hyperbolic horn setup with an Spc2.

Figure 5-31 laser output has one high amplitude peak. This axial displacement peak across the frequency stepwise scan is the setup achieving resonance. One peak, therefore, one only clear resonant mode present within the transducer frequency range, showing the booster axial horn setup ability to excite the three throat specimens in their longitudinal mode. All specimens presented a similar result for both hyperbolic and tapered horns.

When exciting the complete multiaxial setup, the MI and the PM1 are present in all three different SPC geometries. Both modes remained before and after the polishing sequence. After the polishing surface treatment, there is a change in frequency to both modes in all specimens. Figure 5-32 shows an Spc2 axial and rotation displacement laser measurements to a transducer frequency scan sequence before and after the polish surface treatment. As previously explained and showed in Figure 4-27, the rotation displacement was measured in machined groves at the specimen's free base.

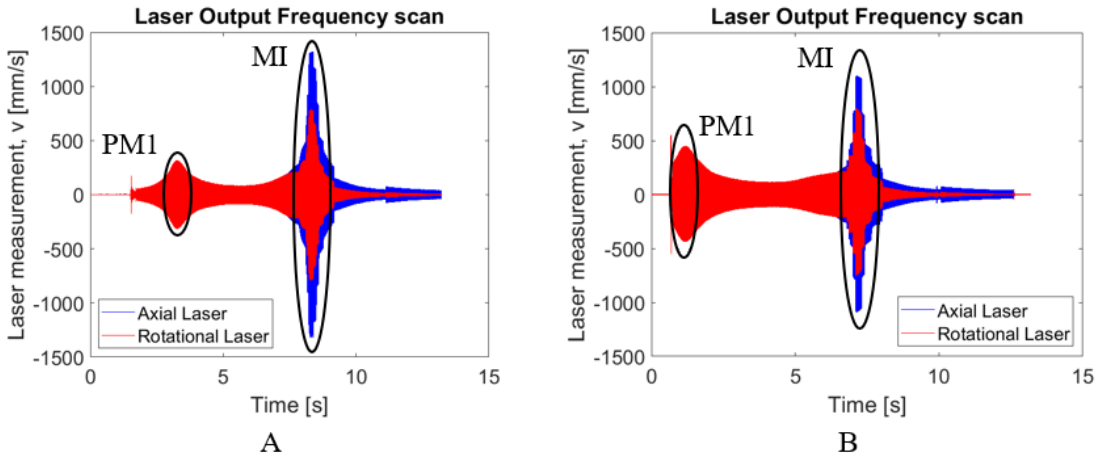

Figure 5-32. Axial and rotation displacement laser output from a frequency transducer scan for an Spc2 (A) unpolished; (B) polished.

As predicted by the FEA free vibration and steady-state modal results, more than one resonant mode was excited by the axial cyclic transducer displacement. PM1 and MI are within the transducer frequency range and are visually identifiable from the laser output. MI has a higher overall amplitude in both axial and rotational displacement, and the two measuring signals are in-phase.

From Figure 5-32 output laser signal, the FDD modal analysis was conducted. Both the FDD method and the provided data by the transducer controller indicated the presence of two MI and PM1 resonant modes. The indicated phase by FDD verifies and distinguishes the MI and PM1 excitation. Figure 5-33 presents the FDD determined result for Figure 3-32 Spc2 before and after the polishing treatment. Similar to the FEA steady-state modal presented results, the FDD analysis was focused on the same frequency range, 18.5 to 21.5 kHz.

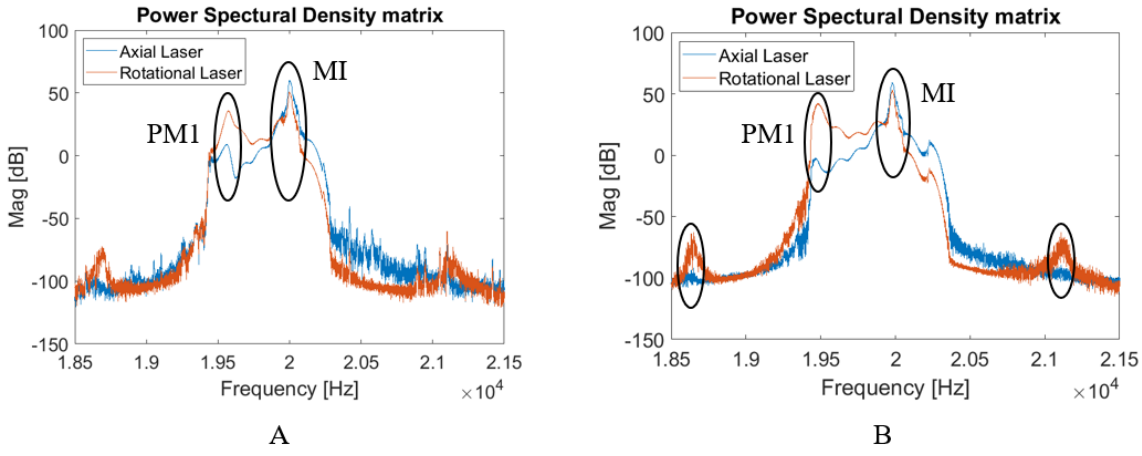

Figure 5-33. FDD modal analysis of an Spc2 (A) unpolished; (B) polished.

PM1 and MI magnitude peaks are clear and identified. The frequency, phase and rotational axial displacement ratio were taken from each peak. The polishing treatment removed thin-layer was enough to change the specimen resulting modal shape, thus showing Spc specimens high dimensional sensitivity.

Just as observed in the uniaxial specimens, the polishing treatment resulted in a frequency decrease. Spc2 FDD Figure 5-33 modal analysis determined a 20 Hz in MI and 66 Hz in PM1 decrease from the polishing treatment. The FEA sensitivity analysis predicted the obtained higher decrease in PM1 frequency from Tr reduction. PM1 higher frequency change occurs since it is intrinsically dependent on the specimen torsional frequency, which is more sensitive than the longitudinal to Tr dimensional changes derived by the polishing treatment.

A decrease in the rotational axial displacement ratio was also obtained. As predicted by FEA sensitivity analysis, a decrease in the smallest cross-section Tr dimension by the polishing treatment results in a frequency and displacement ratio decrease of the MI. In this case, the ratio went from 0.57 to 0.52 (rotational/axial).

Two other resonant modes with considerable rotation appear within the studied frequency range but outside the transducer working range. Due to their considerable rotation magnitude in relation to the axial displacement, both were considered torsional resonant modes. The highest frequency of the two was linked to PM2. PM2 FEA obtained 20496 Hz frequency (booster multi-horn Spc2) is considerably lower than the experimental 21150±100 Hz. The higher experimental frequency can be associated with the observed 98Hz frequency increase of the booster multi-horn result (Table 5-2) to the FEA obtained. Meaning the obtained increase from FEA to experimental could have increased PM2 considerably. Also, FDD analysis is not as accurate outside the transducer frequency range because the excited signal should be random and not stepwise.

The same FDD analysis was conducted on all tested specimens. PM1 and MI were inside the frequency transducer range in all tested specimens. The displacement rotation/axial ratio between the two laser locations was determined together with the signal phase, again for both modes. The polishing treatment always resulted in a frequency decrease in both modes and a displacement ratio decrease in the MI.

A direct comparison was made between the FEA sensitivity analysis to the FDD displacement ratio results. Since the specimens were modally analysed through the free base displacement ratio before and after the polish treatment, the same was numerically computed

to compare directly. Figure 5-34 plots for both FEA and experimental results the MI specimen free base rotational/axial displacement ratio relative to the PM1 frequency. The experimentally obtained booster multi-horn excitation 98 Hz frequency increase difference was taken to all PM1 experimental results to compare experimental to FEA results.

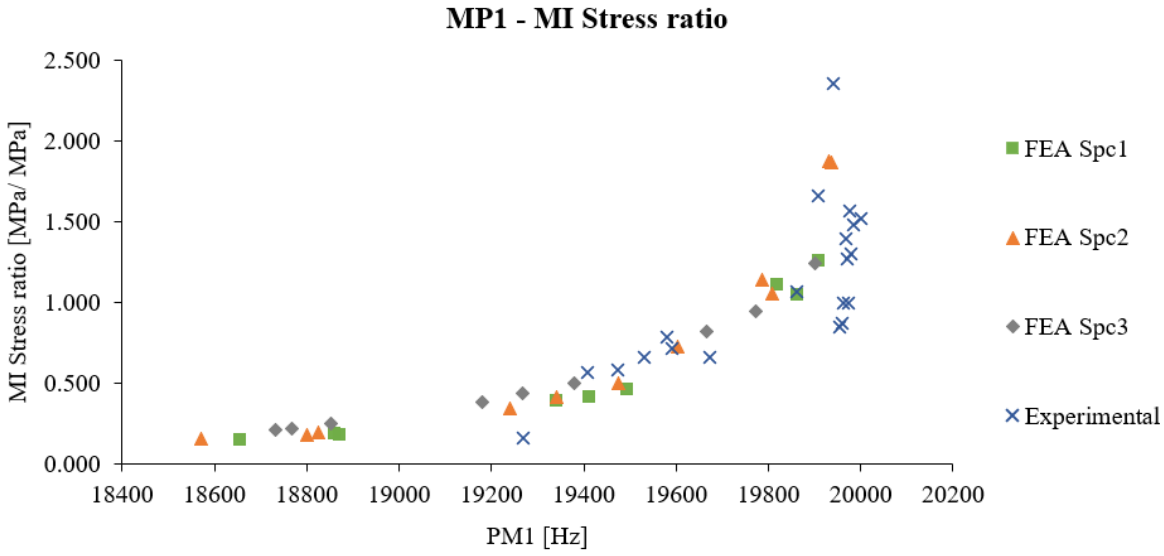

Figure 5-34. MI specimen free base rotational/axial displacement ratio relative to the PM1 frequency, FEA experimental comparison.

Just as predicted by the in-depth FEA, a direct link between PM1 frequency to the MI shear/ axial stress ratio induced is observed by all experimental results. Specimens with PM1 closer to the booster multi-horn setup excitation frequency presented a higher displacement ratio and, therefore, a higher main throat shear/axial stress ratio.

The before and after polishing treatment reinforced such behaviour. The higher PM1 frequency decrease from the polishing treatment resulted in decreased free base rotation/axial displacement ratio. Therefore, just as predicted by FEA, the decrease in the smallest cross-section radius results in a frequency and shear/axial stress ratio decrease.

5.5.1.2 Strain and displacement measurements

Just as the followed experimental methodology for the tension-compression ultrasonic specimens, displacement and strain measurements were conducted to a sequence of transducer power settings. Again, all specimens were subjected to the three available booster horn setups, two uniaxial and the multi-horn. The displacement and strain from the roseate strain gauge were recorded for each power setting. All presented results are separated by Spc geometry since each had its stress amplitude and displacement to stress ratio. The axial displacement at the free base amplitude is similar across all specimens, but the associated axial stress amplitude is geometry-dependent.

A linear and coherent behaviour was obtained between almost all setups and measured specimens. Figure 5-35 shows one Spc2 specimen axial displacement to axial stress results for all three tested setups.

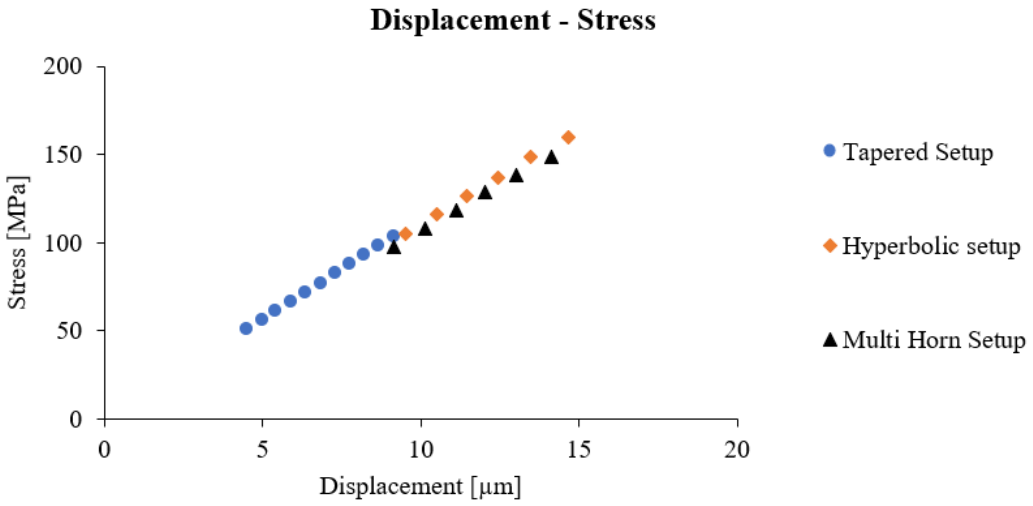

Figure 5-35. Axial displacement to stress comparison between the three tested booster horn setups with an Spc2 specimen.

With all conducted chosen transducer powers, the displacement and determined stress were associated and compared to the FEA computed steady-state modal.

Figure 5-36 presents all Spc2 three setup's axial displacement to axial stress relation determined experimentally with the FEA steady-state determined. A 10 % difference to the obtained experimental trendline is also included.

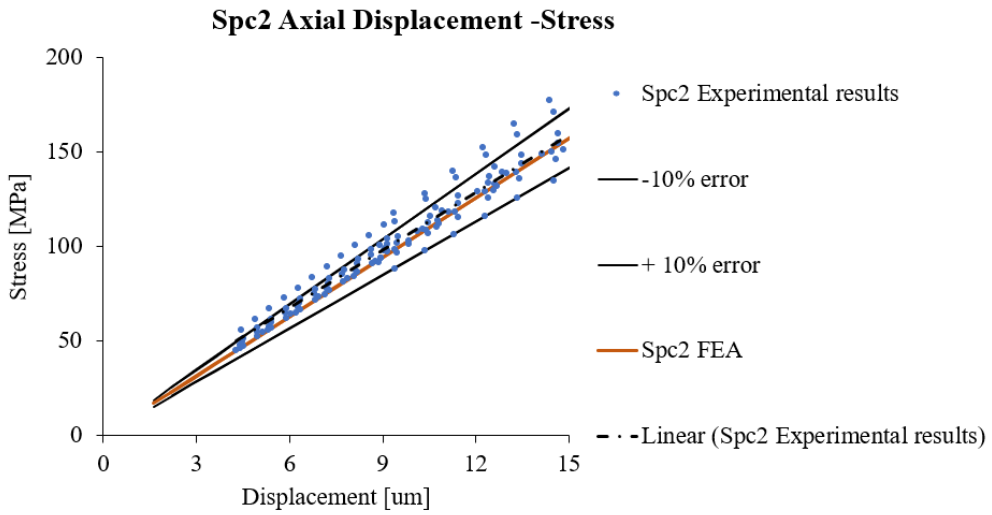

Figure 5-36. FEA and experimental comparison of the Spc2 axial displacement to stress relation.

Two Spc2 specimens exceeded the 10% error difference from the average displacement measurements. The axial modal shape proved stable and replicated between all specimens of a given geometry. The steady-state analysis presented a low difference from the obtained experimental trend across all strain gauges. Compared with the Spc3, an even lower difference between specimens and FEA results was obtained. Figure 5-37 shows Spc1 and Spc3 experimental and FEA axial displacement to axial stress results.

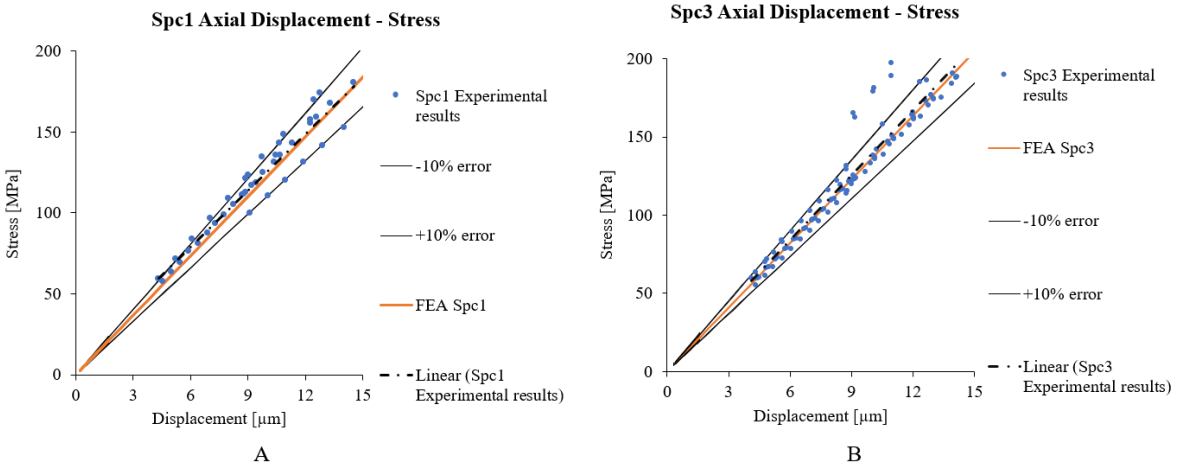

Figure 5-37. Spc1 and Spc3 FEA and experimental comparison of the axial displacement to stress relation.

Similar to Spc2, most axial experimental results follow the same displacement stress linear trend. Only a few exceptions have exceeded a 10% difference.

The negligible difference between the experimental mean and FE steady-state modal analysis has proven its ability as a tool to determine the three throated specimens axial stress through the measured free base axial displacement.

The same analysis was conducted on all three geometries regarding the rotation displacement to shear stress ratio. Since only the booster multi-horn setup induces shear stress, fewer measuring points were obtained. Figure 5-38 plots the rotation to shear stress of all three specimens.

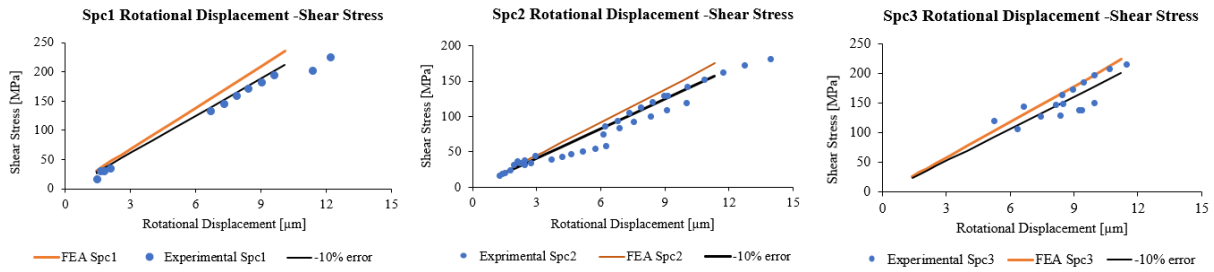

Figure 5-38. Spc1 to Spc3 FEA and experimental comparison of the rotational displacement to shear stress relation.

A considerable difference is present between FEA and experimental results in several specimens. Shear stress values tend to be lower than predicted by FEA. The resulting shear axial stress ratio variation between specimens is again associated with PM1 influence and the specimen high geometrical sensitivity. PM1 influence lead to a changing rotation displacement to shear stress relation. Still, some measured points presented a good linear agreement with FEA.

Axial displacement to axial stress has maintained a similar behaviour to tension-compression specimens across different excitation frequencies. Rotational displacement to shear stress, on the other hand, does not. From FDD and the modal shape analysis through displacement and strain measurements, the following conclusion was taken:

The specimen rotation is highly sensitive to dimensional changes, but its displacement to stress variable behaviour is only associated with PM1.

As FEA predicted, the rotational behaviour is derived by the axial excitation, meaning the complete setup will be excited in their axial resonance, only then rotational excitation is made by the slits of the multi-horn.

Looking at the steel bar experiment or the tension-compression Ti6Al4V polishing treatment frequency change, the complete setup changed frequency with each machined step. Ti6Al4V specimens with hyperbolic setup had similar frequency changes as the Spc MI to the polish treatment. Also, a small axial amplitude change to the same transducer amplitude settings was perceived across all Spc exciting frequencies.

The multiaxial MI frequency adjustment between specimens is mainly made to the axial resonance of the specimen and not the torsional. This means that the specimen torsional mode can have a higher frequency difference to the excited by the transducer resulting in lower rotational displacement/shear amplitude. If no PMs were present, the mode shape would remain relatively the same, and only the rotational amplitude would decrease.

PM1 influence may increment the influence of the specimen frequency difference to the transducer excited, but it will most likely change the mode shape and, therefore, the displacement to stress ratio. This means the ratio will not follow the same behaviour across different specimens with the same geometry. If no PM were present, the rotation to axial differences would be similar to the 2B+2H first specimen, where there is a much higher frequency difference between MI and PM1 that can be considered non-existing. In this case, the displacement/stress ratio is retained, and, therefore, both stresses could be determined by FEA and possibly by analytical means.

The two proposed improvements tackle this issue: the rotational sensitivity by separating the specimen into three sections and the PM1 influence with the 2B+2H setup, which increases its frequency difference.

5.5.1.3 Ultrasonic tension-torsion AISI P20 fatigue results

Similar to the uniaxial specimens, a thermal analysis was conducted before the final UFT. Since the first tested tension-torsion specimens before the present study showed higher stress combination outside the fatigue testing region, the used thermographic camera visualized the complete specimen and its connection to the horn. The thermal camera was applied to ensure the main throat fatigue testing region had the highest heat generation and no other unwanted heat generated locations were present. The thermal camera was also able to detect PM1 influence. Also, a temperature control across all conducted UFT was conducted through the pyrometer.

Has seen by the FEA results, PM1 increases the shear stress in the lower secondary throat. Therefore, in specimens with considerable PM1 influence, the secondary lower throat will have a higher than the upper throat stress combination resulting in a higher heat generation.

All new specimens presented the highest heat generation from the thermal camera at the main throat with one single exception. An Spc2 presented higher heat generated at the multi-

horn specimen connection. This specimen had the closest PM1 frequency and was also excited in PM1 by the transducer and not in the MI.

Figure 5-39 presents thermal images of the three mentioned heat generation cases: The correctly working specimen, MI with considerable PM1 influence, and the referenced Spc2 PM1 excited specimen.

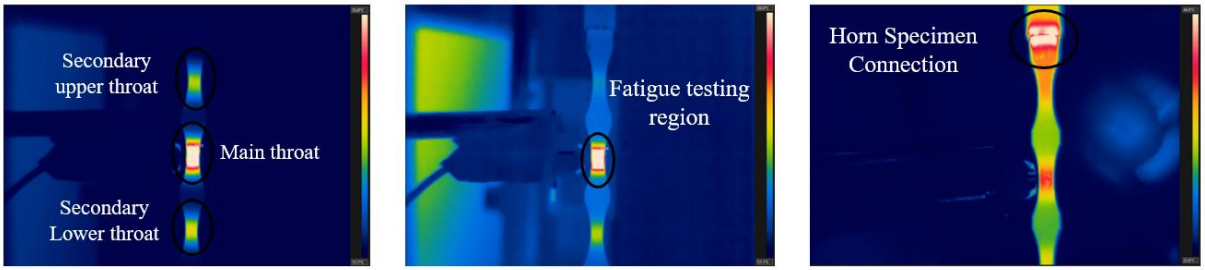

Figure 5-39. Thermal imaging of different tension-torsion specimens: (A) working as intended; (B) with a considerable PM influence; (C) PM transducer excited specimen.

The von Mises equivalent stress criterium was calculated. The respective obtained life was associated with the axial stress, shear stress and calculated von Mises stress amplitude and plotted in Figure 5-40. Figure 5-40 also distinguishes the specimens with a higher and lower shear/axial stress ratio than the von Mises 0.577 ratio.

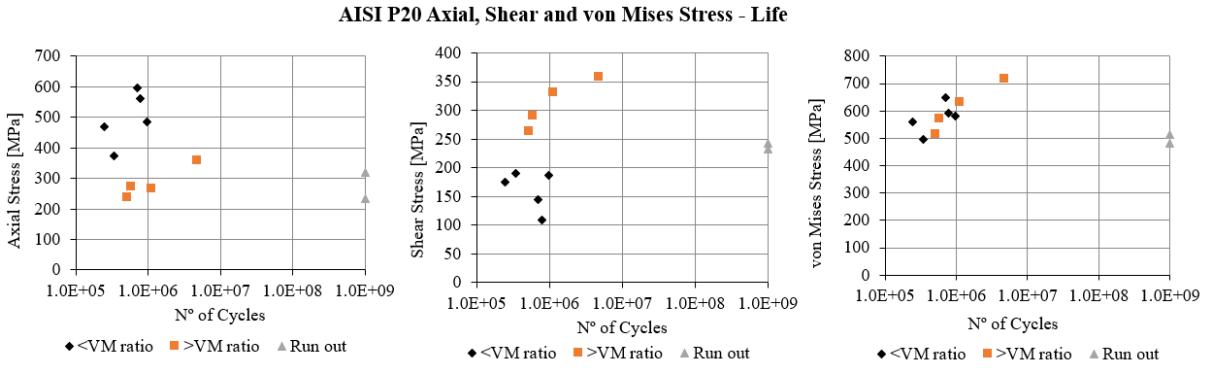

Figure 5-40. AISI P20 tension-torsion R=-1 Axial, Shear and von Mises S-N fatigue results.

The different stress combinations made difficult the experimental UFT to reach higher fatigue life cycle results. An unclear HCF and VHCF stress life tendency was obtained. A clear difference between higher and lower shear/axial stress ratio than the von Mises 0.577 ratio can be observed with the individual axial and shear stress to life plots.

The specimens were fully fractured in servo-hydraulic machines after reaching resonance loss due to the nucleated fatigue crack. The obtained fracture surface was first

analysed in the crack initiation angle. Since all specimens presented a surface crack initiation, a simple microscope view was used with image analysing software. Figure 5-41 shows three multiaxial specimens with different stress ratios under a microscope for crack initiation angle determination.

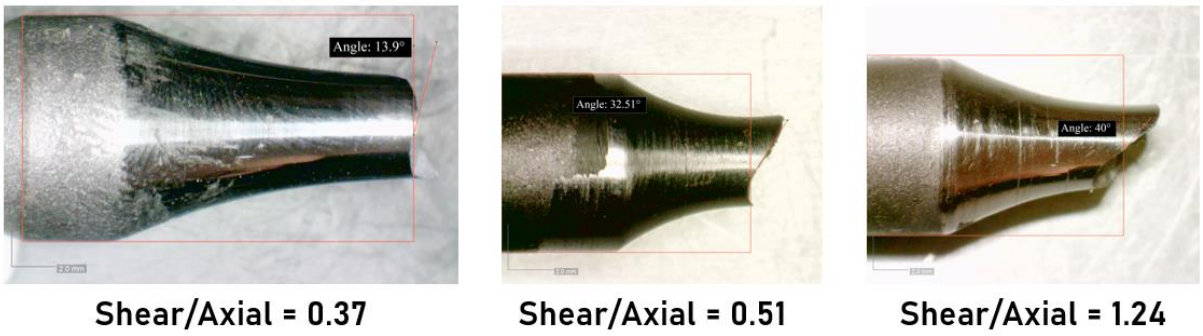

Figure 5-41. Crack initiation angle for three different specimens with different UFT shear/axial stress ratio.

The crack initiation angle showed an increasing tendency as the shear/axial ratio increased. Figure 5-42 associates the tested stress ratios with the induced crack initiation angle showing the increasing tendency. The obtained 0º angle in AISI tension-compression tests was also added.

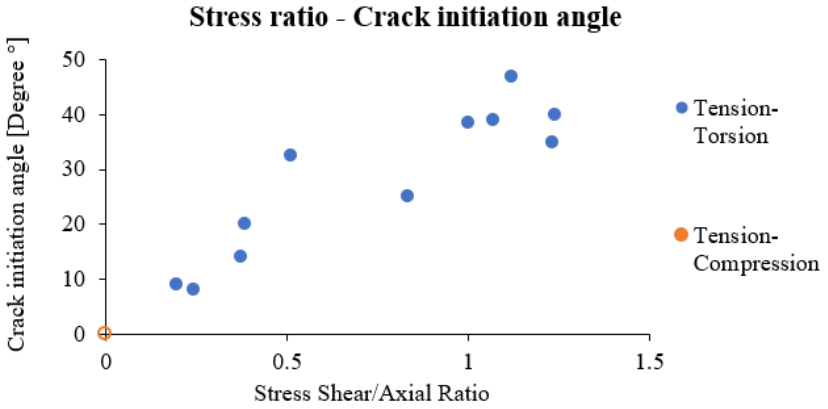

Figure 5-42. Crack initiation surface angle change across different stress shear/axial ratios.

SEM analysis of the fatigue fracture surfaces was again followed. Just as tension-compression and pure torsion, all specimens showed an explicit surface crack initiation.

A distinct and predicted mixed-mode crack propagation is present for all stress shear/axial ratios. The fatigue crack presented a mixed-mode I and II crack propagation. With the increase of shear/axial ratio, more predominant shear damage marks were present. Figure 5-43 compares the fatigue crack surface of three specimens with considerable different shear/axial ratios.

Figure 5-43. Fatigue crack surface comparison between different stress ratio specimens.

The crack initiation region in both low and high-stress ratios has a similar morphology to the obtained in tension-compression fatigue specimens. A small dark region surrounds the pinpointed crack initiation location, as is shown in Figure 5-44.

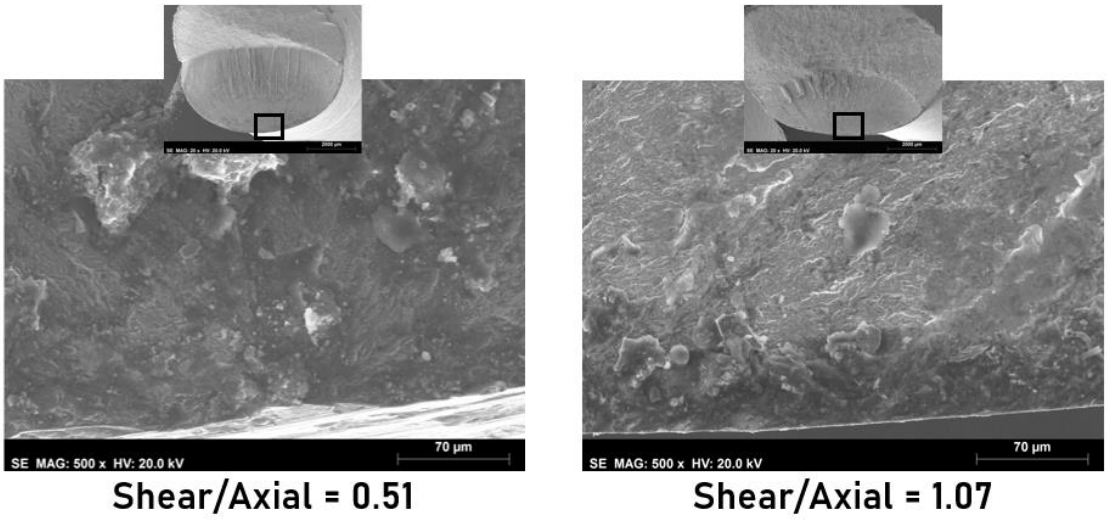

Figure 5-44. Fatigue crack initiation morphology in two different shear /axial stress ratio specimens.

Concerning mean and high stress ratios, the crack propagation has an initial stage with a ‘smother’ surface, followed by increasingly more prominent radial marks close to the final fracture. Pure torsional specimens have similar propagation zones.

The radial marks are associated with high shear deformation. They appear more pronounced with higher shear fatigue amplitude specimens. The radial marks increased size from crack initiation to final fracture indicates an increasingly more dominant shear stress across the fatigue crack propagation. Radial marks also showed in certain instances secondary cracks. Therefore, the fatigue crack propagates as a mixed-mode I and II with the increasing dominance of mode II. Figure 5-45 shows the two described regions in detail for the 0.51 stress ratio specimens presented in Figure 5-44.

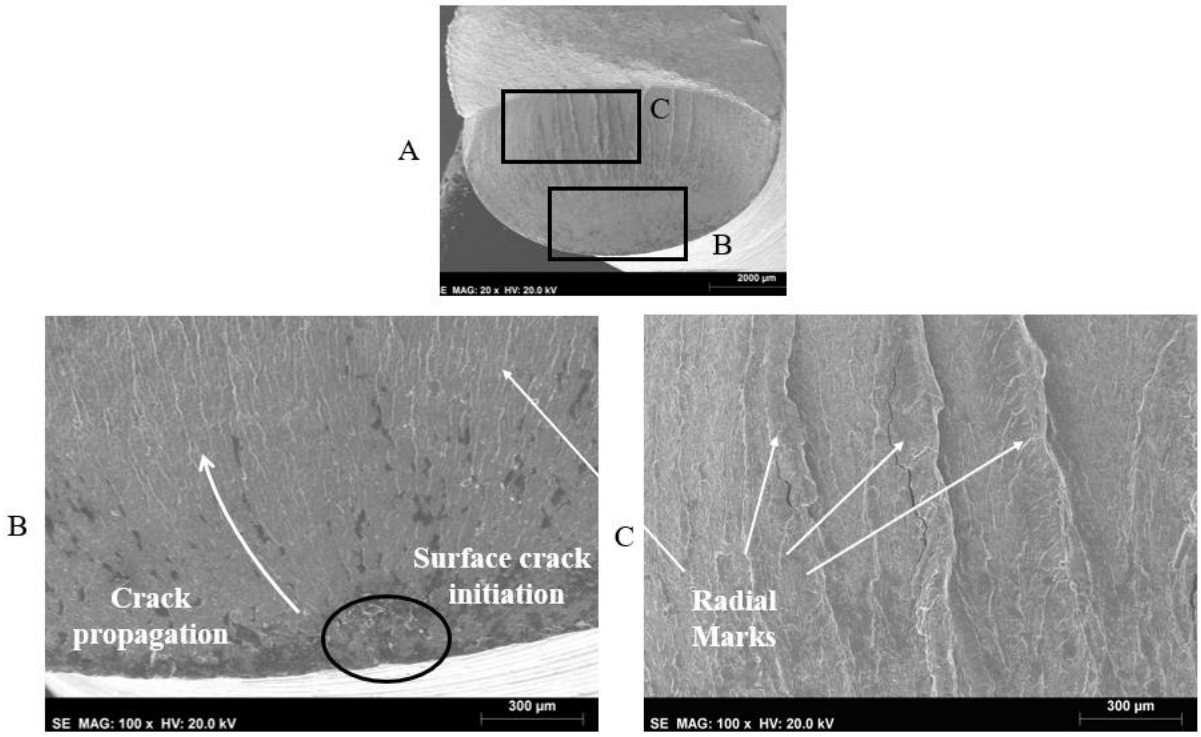

Figure 5-45. 0.51 shear/axial ratio Spc fatigue fracture surface (A), crack initiation and propagation with 'smooth' region (B) and radial marks with and without secondary cracks (C).

A comparison between the 0.37 stress ratio tension-torsion and a tension-compression specimen is made in Figure 5-46.The lowest 0.37 stress ratio specimen (Figure 5-46.A) does not have the two shown propagation regions. A dominant crack mode I propagation resulted in a crack surface similar to tension-compression specimens with minor shear radial marks very close to the final fracture.

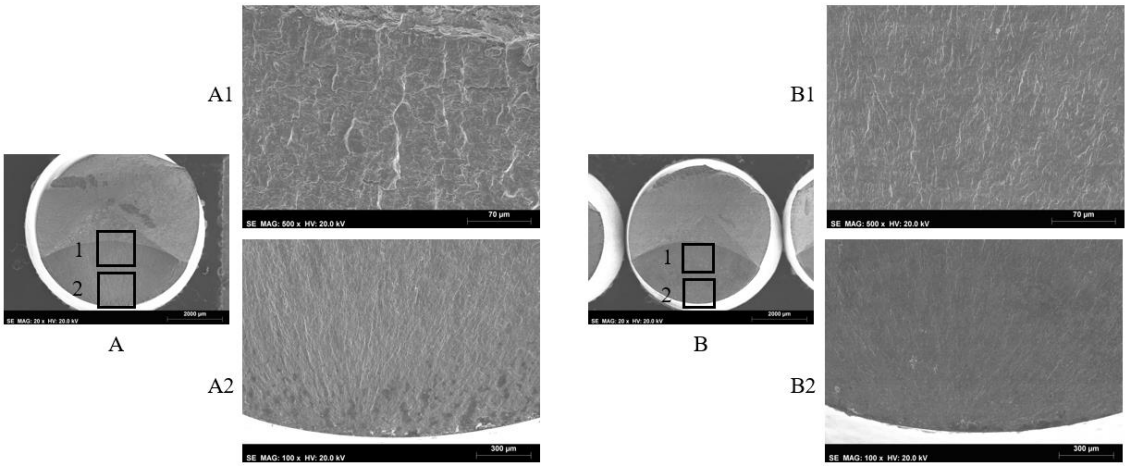

Figure 5-46. Fatigue crack final propagation (1) and initiation (2) comparison between: (A) tension-torsion 0.37 shear/axial ratio (B) tension-compression specimen 6.

The SEM fracture surface analysis proves the induced tension-torsion stress field and the determined ratios from the experimental measurements. The added torsion contributed to the fatigue damage specimen since the axial amplitude of all specimens was lower than the conducted tension-compression UFT, even in the lowest shear/axial ratio 0.37 Spc specimen.

5.5.2 In-plane Biaxial Cruciform

As already mentioned, three different cruciform unitary ratio specimens were tested: the original and first in-phase T-T specimen (F*x* T-T); a new in-phase T-T specimen (N*x* T-T), where the found problems in the original T-T were considered in the FEA designing process; and out-of-phase C-T specimens (C-T *x*). Table 5-4 shows the cruciform specimens under discussion in this study and their respective designations.

Table 5-4. Unitary ratio tested cruciform specimen designations.

Original in-phase F*x* T-T	Newly designed in-phase N*x* T-T	Out-of-phase C-T *x*
F1 T-T	N1 T-T	C-T 1
F2 T-T	N2 T-T	C-T 2
F3 T-T		C-T 3

Table 5-4 specimens underwent FDD modal analysis, power to displacement and strain experimental procedures. Both the presented laser measurement setup A and B (Figure 4-28) were conducted.

The second group of T-T specimens (Nx T-T) were created and tested since only one original F T-T proved to be working as intended. F T-T cruciform specimens showed an undesirable resonant deformed shape associated with a PM in the transducer frequency. Initially, some specimens could not even be under higher power excitation transducer settings. Due to their non-working as intended resonance, deformation occurred in the specimen-horn connection.

The present specimen-horn connection was achieved by a M2-M6 screw connection that did not allow for a strong applied attachment. This consequently led to the specimen disconnection or even fracturing the connection with clear heat marks. Figure 5-47 shows a broken and burned specimen-horn screw connection made by one of the presented first specimens.

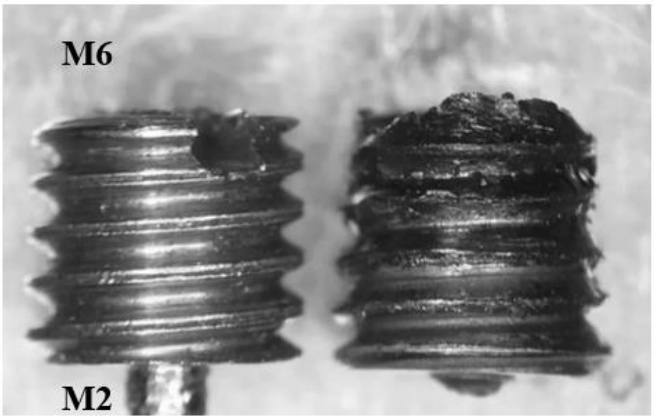

Figure 5-47. M2- M6 specimen-horn screw connection with a broken and burned example from ultrasonic fatigue testing.

For all non-working original F*x* T-T specimens, a new, more resistant M3 thread was machined. With the M3 connection, the specimens were attached with higher torque, ensuring the specimen-horn connection throughout all required measuring experiments. Not only does the new, improved connection allow for frequency scan and sequential power to displacement experiments, but it also allows for UFT even with a PM excitation. A failed cruciform from PM fatigue failure is not a reliable fatigue result. Their fracture test only served as an experiment to observe the maximum stress-inducing location of the PM excited resonance.

5.5.2.1 Modal FDD analysis

From a first observation output stepwise frequency signal's, the MI or/and the PM are observable in all tested Table 5-4 specimens. Figure 5-48 shows Laser setup B (Figure 4-28) stepwise frequency scan output for the F1 T-T and N1 T-T. The F1 and N1 T-T Figure 5-48 results show the MI and PM within the transducer frequency range. The PM has to the MI a lower frequency for F1 T-T and higher for N1 T-T specimen.

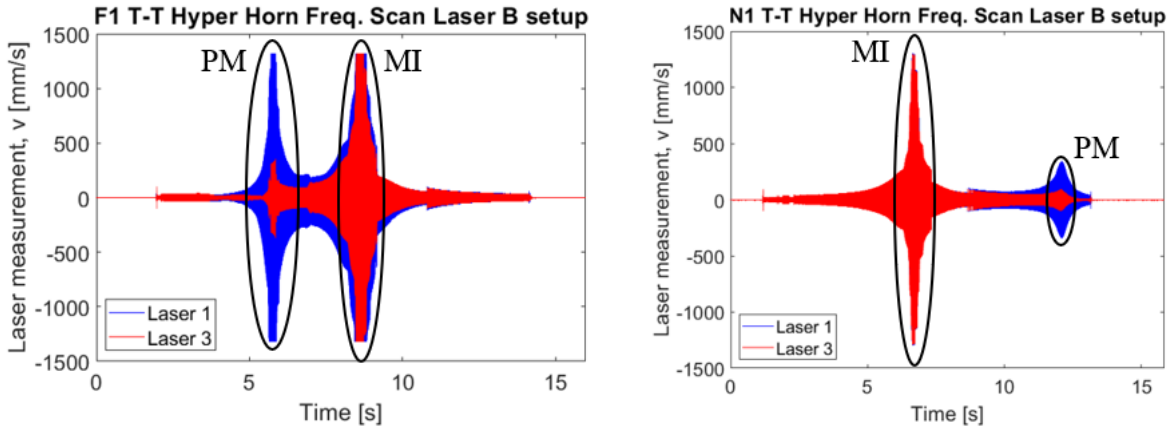

Figure 5-48. Frequency scan laser setup B results for F1 T-T and N1 T-T specimens.

A clear PM amplitude difference of both L1 and L3 is perceived between the original F1 and new N1 T-T specimen. Following the FDD method, the power spectral density (PSD) is first calculated from the measured output. The resonance modes frequency is determined from the observable PSD peaks. The calculated PSD magnitude to frequency results of the shown Figure 5-48 frequency scans is presented in Figure 5-49.

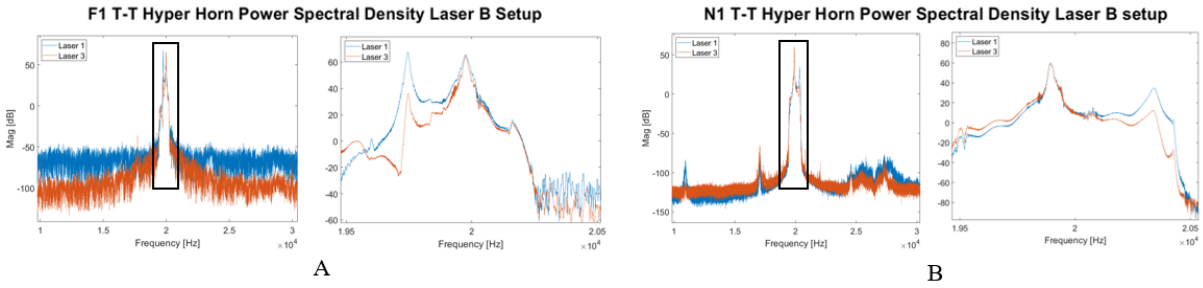

Figure 5-49. PSD Mag/frequency F1 T-T and N1 T-T result in laser B setup with a respective enlarged view in the transducer frequency range.

Singular value decomposition (SVD) is afterwards calculated from the presented Figure 5-49 PSD results. FDD has shown a higher and more consistent MI to PM difference in the new T-T specimens than the original T-T specimens. While in the F1 T-T the frequency difference between modes is ~-1% (180 Hz), the new specimens have a higher ~+2% (330 Hz) difference. The small improvement proved quite significant in terms of the PM impact on the MI deformed shape. The closer frequency proximity of the PM translates into displacement amplitude amplification as measured from L2 in the MI and higher variability between axial-axial ratio

displacements (L1/L3). Comparing the N1 T-T and the F1 T-T, the vertical displacement at the horizontal arms (L2) proved to be less than half to the vertical arms (L1) in MI. A clear improvement was achieved.

The C-T specimens showed the PM outside the frequency transducer range with a ~+11% (2200 Hz) in respect to the MI, as expected by FE analysis. It was only possible to determine PM frequency experimentally by the FDD method.

For C-T and new T-T geometries, resonance frequencies and associated mode shapes (displacement ratios) are consistent for both MI and PM from one specimen to another. In contrast, the original T-T specimens presented a greater frequency variability of both modes. One single first F3 T-T specimen showed a high ~-4% (700 Hz) MI to PM frequency difference. Its mode shape proved a similar behaviour to new T-T and C-T specimens. A rosette strain gauge was applied to this specimen.

The original T-T specimens proved variable frequency results having both MI and PM, only MI and only PM mode within the operating range of the transducer. The frequency scan laser output and the FDD magnitude to frequency result for the first F2 T-T specimen with just the PM within the transducer frequency range is shown in Figure 5-50. MI is not perceived in the recorded output signal, but FDD methods reveal it. MI and PM are identified in the PSD respective peaks shown in Figure 5-50.

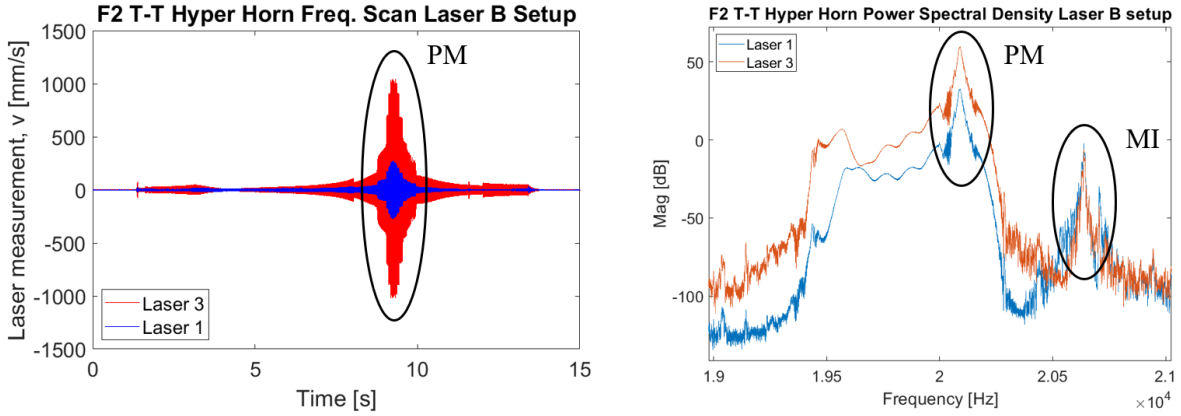

Figure 5-50. Frequency scan and respective PSD calculation of the F2 T-T specimen with only PM within the piezoelectric frequency range.

The specimens with only PM within the transducer frequency range show the FDD method interest and the negative impact on the specimen-horn connection. PM mode has

deformation in the specimen-horn connection, which has led to unscrewing or even connection fracture.

The amplitude-phase between each measured point was also determined by the FDD method. Both the setup B and Setup A signals phase was determined. Setup B proved the T-T in-phase and C-T out-of-phase. Setup A phase will influence the L3 amplitude. The manner in which it affects the L3 amplitude magnitude was predicted by the FEA results and is in line with the experimentally obtained. The mode shape displacement resulting measurements will help perceive better the L3 amplitude difference concerning the obtained phase

5.5.2.2 Strain and displacement measurements

Power/displacement experiments in A and B laser setups were conducted along with the conducted FDD analysis. Afterwards, strain gauges were applied. Five and ten power transducer settings for each laser setup were performed to the hyperbolic and Tapered horn set, respectively. Differently from FDD frequency scans, the excitation occurs at a constant frequency. The excitation frequency is the respective MI frequency for MI only or MI and PM specimens (within the transducer working frequency). Contrarily, PM only specimens were excited in resonance in their respective PM frequency. From each power setting, the displacement amplitudes were taken and from the roseate strain gauges the strain values.

Figure 5-51 shows the power displacement for F1 T-T, N1 T-T, and a C-T1 specimen. Figure 5-51 Laser B experimental setup (Figure 4-28) results were obtained with both tapered and hyperbolic horn sets.

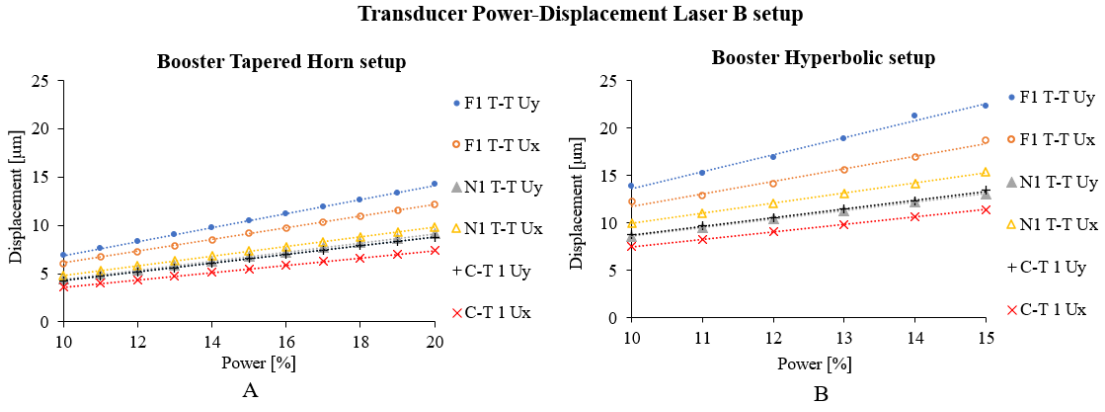

Figure 5-51. Both tapered (A) and hyperbolic (B) horn booster cruciform setups Laser B displacement amplitude measurements for different transducer power settings.

F1 T-T specimen shows a considerably higher displacement amplitude in both *x* and *y* directions. Such behaviour is due to the existing to close PM. The increased displacement amplitude is parallel to the measured amplitude in F T-T specimens with only the PM within the transducer frequency range, as the F2 T-T showed in Figure 5-50.

F1 T-T average difference between x and y displacement amplitude is also higher. It has a 14% and 20% average difference for the tapered and hyperbolic set, respectively, while the N1 T-T specimen has 7% and 14%, and the C-T 1 14% and 16% difference. Only the F3 T-T specimen with a high MI to PM frequency difference was similar to new T-T and C-T specimens. It showed an even lower x y amplitude difference of 3% for both hyper and tapered horns.

Between UFT specimens, especially under multiaxial loadings, minor dimensional variations result in variations in power/displacement relation. But the significant amplitude increase and higher difference present in the F1 T-T specimen is too high to be neglected without considering outside interference.

An amplitude difference between *x* and *y* is present in all specimens. The difference is to be expected, even with a negligible PM mode. As discussed in the FEA subchapter 3.5.2, the induced 'flapping motion' of the specimen's horizontal arms is associated with its frequency difference to the working ultrasonic set. The frequency difference leads to a displacement node adjustment creating the 'flapping' motion. From Figure 5-51 close observation, the *x* displacement is lower than *y* in the F1 T-T and C-T 1 specimen, while N1 T-T specimen has higher *x* displacement. The 'flapping' motion phase to L1 will result in a lower *x* to *y* amplitude when in-phase, as for F1 and C-T 1, and vice-versa in out-of-phase, as in N1.

Transducer power settings to displacement amplitude measurements made with Laser A setup reinforce the PM interference beyond the 'flapping mentioned motion. F1 T-T has considerably higher L2 amplitudes than those measured by new T-T and C-T specimens. Figure 5-52 presents transducer power to displacement results in laser A setup (Figure 4-28) for the same specimens compared in Figure 5-51.

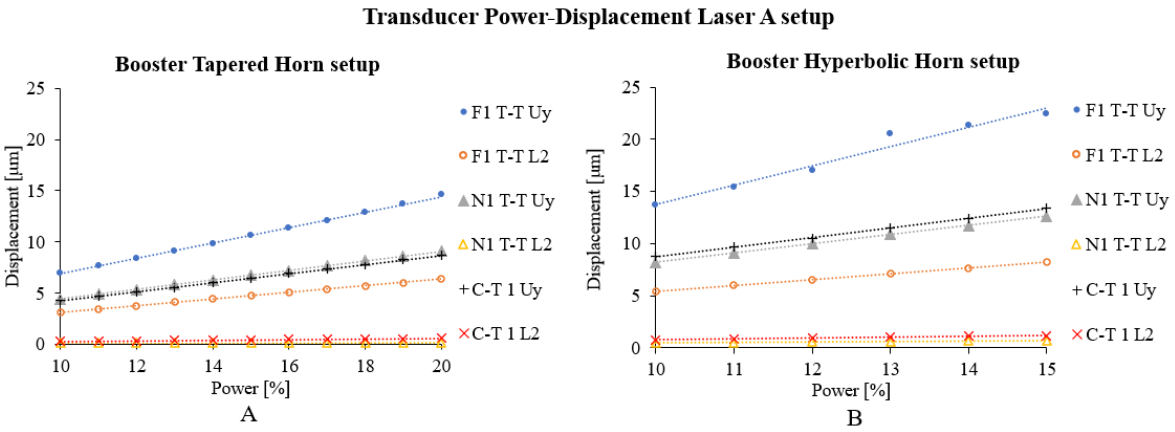

Figure 5-52. Both tapered (A) and hyperbolic (B) horn booster cruciform setups Laser A displacement amplitude measurements for different transducer power settings.

In summary, for the F1 T-T specimen, the detrimental influence of the PM is noticeable on (i) the interference with the MI shown on FDD results; (ii) the *x* and *y* higher displacement amplitudes and disproportion, and (iii) considerable L2 displacement amplitude. On the contrary, following the same three criteria for the New T-T and C-T specimens, a negligible influence of the PM is demonstrated.

From the laser power-displacement measurements and FDD modal results, rosette strain gauges were attached to the cruciform's midpoint. Strain gauges were only used in specimens proving a negligible PM influence and closer behaviour to FE analysis. The strain gauges were aligned with the induced x/y stress tension-tension and tension-compression. The same transducer power settings were again applied, and the strain values were recorded. Again, both mentioned horns sets were used. Strain results were subsequently transformed to stress values through Hooke's law. Figure 5-53 shows stress results for the same N1 and C-T 1 tested in Figure 5-51 and Figure 5-52 with the only original working F3 T-T specimen.

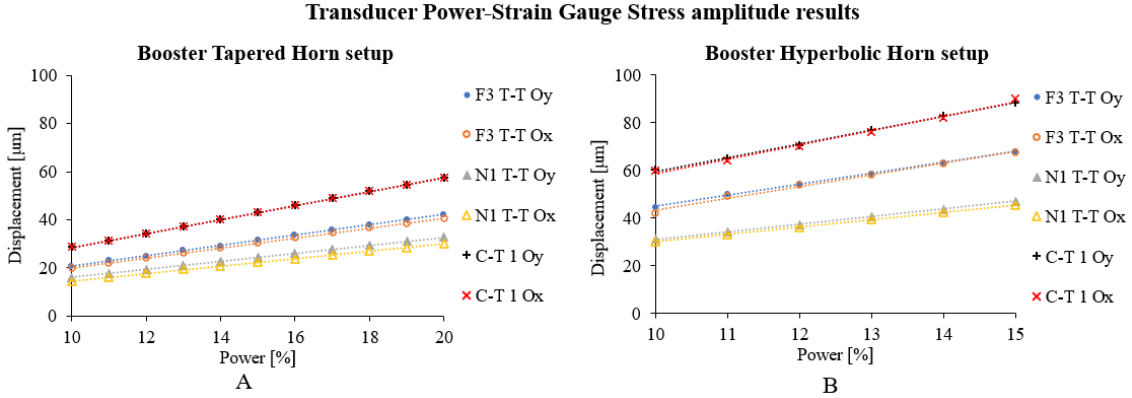

Figure 5-53. Stress axial-axial (x-y) amplitude for several transducer power settings on tapered and hyperbolic horns sets.

The *x* stress values are lower in all tested specimens. This is to be expected since the flapping motion of the cruciform will take part in the imposed deformation shape involved along the horizontal arms. Still, the average difference is acceptable: 3% and 0.5% in the First T-T nº3 with the Tapered and Hyperbolic set, respectively; 8% and 4% for the N1 T-T; 1% and 0.5% for the C-T specimens.

The frequency scan FDD method used in the method was also conducted while measuring strain. The results show the predicted negligible PM influence in the final midpoint induced stress amplitude. Again, the negligible influence of the under-consideration PM in new and C-T specimens was reinforced, and the final fatigue experiments began.

5.5.2.3 Analytical and FEA solution results for stress determination

An analytical method was proposed for stress induce determination. The main objective is to reach a deterministic method that predicts the induced fatigue stress from displacement measurements. Tension-compression specimens follow the same methodology. Through displacement measurement, a deterministic stress method will eliminate the need for strain gauge application and standardize the ultrasonic fatigue method.

Two different methods are here proposed for ultrasonic cruciform. Both require FEA analysis of the specimens.

One method brings the tension-compression analytical method to the cruciform geometries. The cruciform is first considered as two uniaxial specimens with one shared fatigue testing region, as previously described in subchapter 3.5.2.3. The stress distribution differences between the FE free vibration analysis of the cruciform and analytically calculated uniaxial specimen are compensated by the denoted area difference compensation factor (δ). The presented equation (3.9) is here repeated for convenience.

$$\begin{cases} \sigma(x) = EA_0(1+\delta)\varphi(L_1,L_2)[\beta\cosh(\beta x) - \alpha\sinh(\beta x)]\exp(-\alpha x), for\ x \le L_2 \\ \sigma(x) = E\cdot k\cdot A_0(1+\delta)\sin\big(k(L-x)\big) \qquad\qquad , for\ L_2 < x \le L \end{cases} \quad (5.1)$$

A second method requires a steady-state FE modal analysis of the booster horn cruciform. From it, the displacement to stress relation is taken.

The always present flapping motion effect on the measured horizontal displacement must be corrected in both methods. The proposed 'flapping motion' factor (γ) is the horizontal arms displacement amplitude correction. Again, the γ factor equation (3.10) is here repeated for convenience.

$$\begin{cases} \gamma = \delta_{x,corrected} = \left(\delta - 1.75\frac{A_{0x}-A_{0y}}{A_{0y}}\right), & for\ A_{0x} \geq A_{0y} \\ \gamma = \delta_{x,corrected} = \ (\delta - 0.75\frac{A_{0x}-A_{0y}}{A_{0y}}), & for\ A_{0x} \leq A_{0y} \end{cases} \tag{5.2}$$

The two results are here now shown for the two followed methods. Figure 5-54 compares the displacement stress relation obtained experimentally by strain gauges and the first proposed analytical method. Only the booster hyperbolic horn ultrasonic setup results for a single specimen is shown for better results observation. The stress was associated with the measured displacement without being corrected by the applied δ and γ factors.

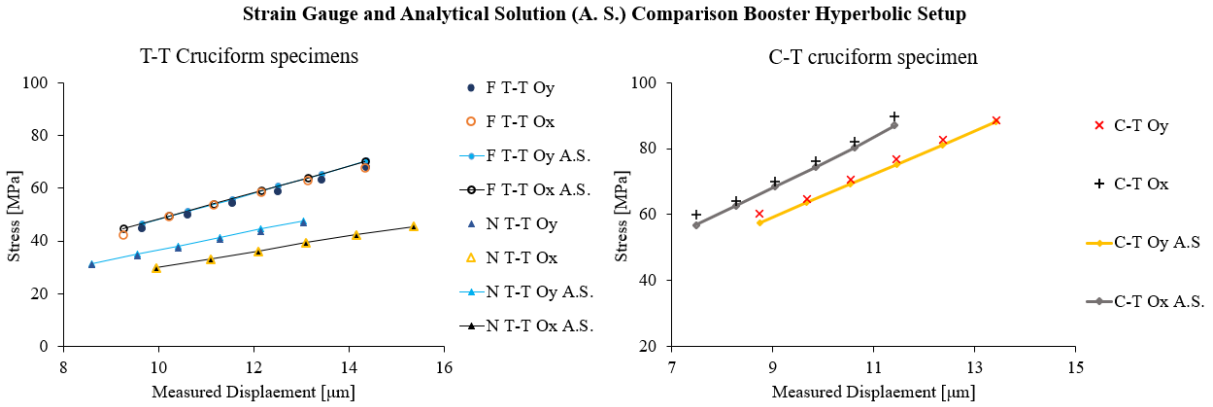

Figure 5-54. Comparison between the experimental strain gauge to the proposed analytical method for stress calculation booster hyperbolic ultrasonic cruciforms setup.

Again, the horizontal and vertical arms difference is observed as first concluded in the constant frequency displacement amplitude modal analysis. The proposed analytical solution showed a low correlation error with the strain measurements. For every tested cruciform in two different horn setups, a maximum average difference of 5% was obtained. There was only one exception where an N T-T *x* stress presented close to a 9% stress difference.

The same comparison of the experimental strain gauge to stress values is made to the second FEA method in Figure 5-55. The plotted experimental results horizontal *x* displacements are with and without the 'flapping motion' γ correction factor.

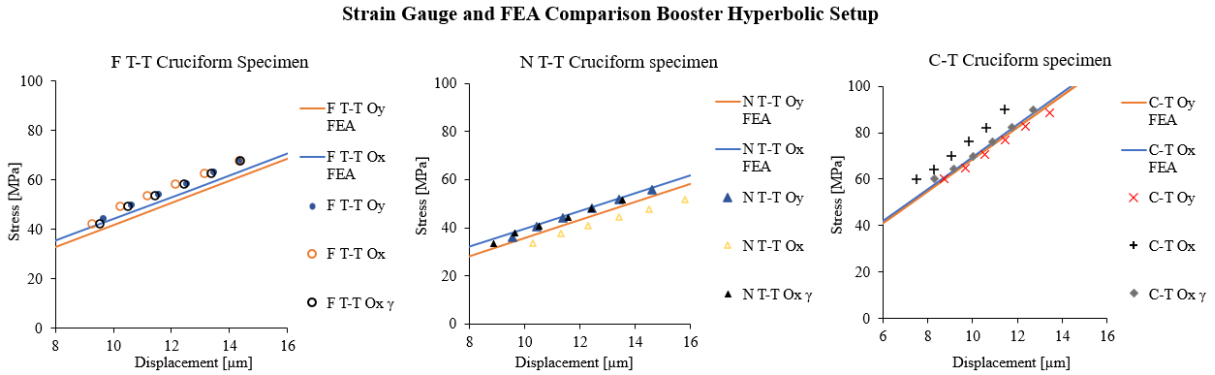

Figure 5-55. Comparison between the experimental strain gauge to the FEA predicted for booster hyperbolic ultrasonic cruciforms setup.

Experimental to the FEA method presented a good linear agreement across all tested specimens. Looking first at the vertical stress F3 T-T presented the worst result with a 9 and 9.5% difference to the tapered and hyperbolic horn setup, respectively. The correction γ improved the FEA to experimental results in almost all specimens across all booster horn setups. Only the F3 T-T horizontal stress *x* in the tapered setup presented a 10% average difference and N2 T-T in booster hyperbolic 8%. The remaining results had a below 5% difference.

Both analytical methods have proved a good agreement with the experimentally obtained values. The present errors could be associated with the strain gauge's alignment and centre point placement. The strain gauge small size or/and the cruciform's small and curved gauge strain measurement area make this experiment very difficult to execute.

Future fatigue tests on different ultrasonic cruciform specimens are needed to improve further the two applied factors, δ and γ, and to reach a complete analytical method that may not require FE computation.

5.5.2.4 Ultrasonic fatigue cruciform results

UFT was conducted on all specimens: cruciform with only the PM or the MI within the frequency range. A thermal camera was used to observe the highest strain locations of all specimens. Figure 5-56 shows thermal images of parasite only (PM) and working as intended (MI) specimens together with the highlighted region predicted by FE analysis. The scale was reduced and turned grey to perceive better the heat generation locations since aluminium did not present a significant heat generation.

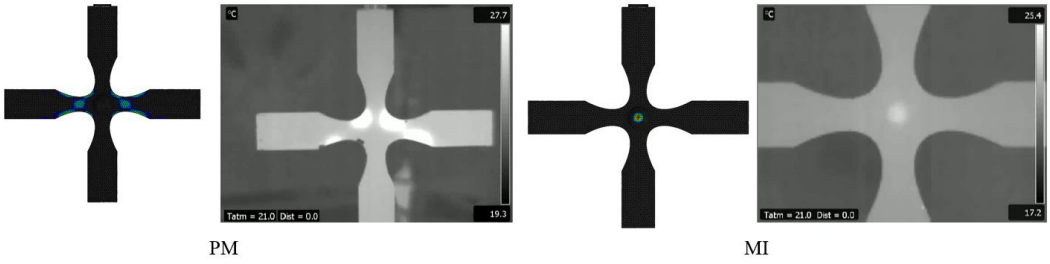

Figure 5-56. FEA highest strain locations and resulting thermal imaging of PM and MI only specimens.

In PM only specimens, the highest cycling strains occur at the arms' elliptical corners and horizontal arms, while MI only specimens showed a higher heat generation on the midpoint. Correlation between thermal imaging and FE results proves the predicted behaviour of the PM.

UFT to F2 T-T (PM only within the transducer frequency range) induced fatigue cracks in all four corners of the specimen. Figure 5-57 shows F2 T-T fatigue fracture locations, size, and mention transformation. Some fatigue fractures propagated and reached the cruciform central circle. Halfway crack propagation, a behaviour change was perceived, having a more linear and faster propagation behaviour (Figure 5-57 C and D).

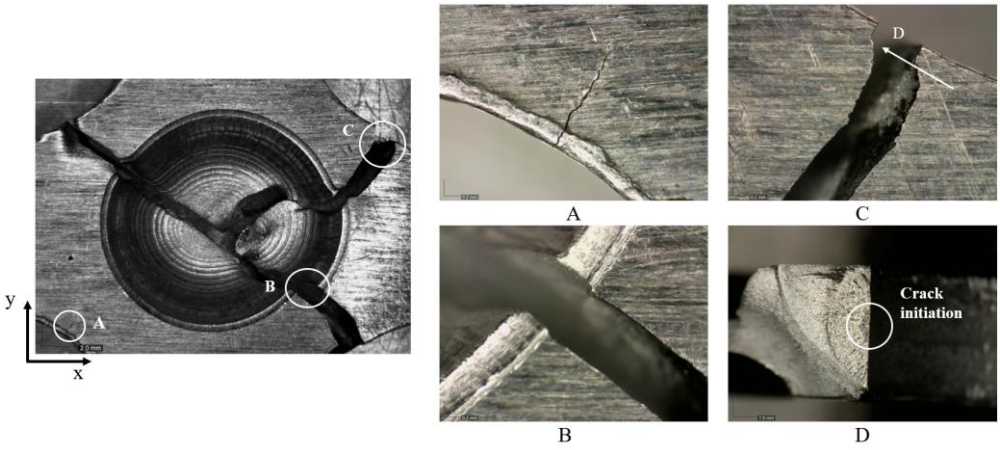

Figure 5-57. PM only F2 T-T Fatigue fractured F2 T-T: (A) fractures locations; (B) corner fracture; (C) and (D) fracture at the front surface.

Three C-T specimens, the only correctly working F3 T-T specimens, and two new T-T specimens were subjected to UFT until failure. These are the cruciform specimens that prove a stress combination and modal shape of interest. All tested C-T and F3 T-T presented crack initiation at the midpoint.

Table 5-5 shows all fatigue lives to applied stresses at the midpoint for all the tested specimens. Stresses were determined in both the x and y directions and the initial crack path

direction is also shown. Fatigue life testing results tend to yield higher lives for lower stress combinations in all tested specimens.

Table 5-5. Fatigue testing life, stress, and angle results.

Specimen	σ_y [MPa]	σ_x [MPa]	θ(º)	N (nº of cycles)
C-T 1	144.30	137.00	40.9	2.67E6
C-T 2	133.10	124.00	23.8	1.36E7
C-T 3	137.20	131.70	48.1	9.25E6
N1 T-T	112.47	107.07	-	1.21E7
N2 T-T	128.23	125.51	-	6E6
F3 T-T	176.48	174.96	51.2	763000

Tested C-T specimens with 40º-50º degree crack initiation at the specimen's centre showed bifurcation on both ends, Figure 5-58.A and Figure 5-58.B, while 24º degree crack initiation presented single crack growth, Figure 5-58.C. The fracture result is consistent with previous studies on aluminium cruciform specimens. Through FE analysis, Garcia et al. have determined the bifurcation effect when a 45º crack initiates in out-of-phase loadings [217]. Considering the applied unitary biaxiality ratio, Lee et al. [218] showed that the initial crack path occurs at 45º. Wolf et al. [219] observed similar crack behaviour in aluminium cruciform specimens with a 45º degree initial path leading to a similar bifurcation.

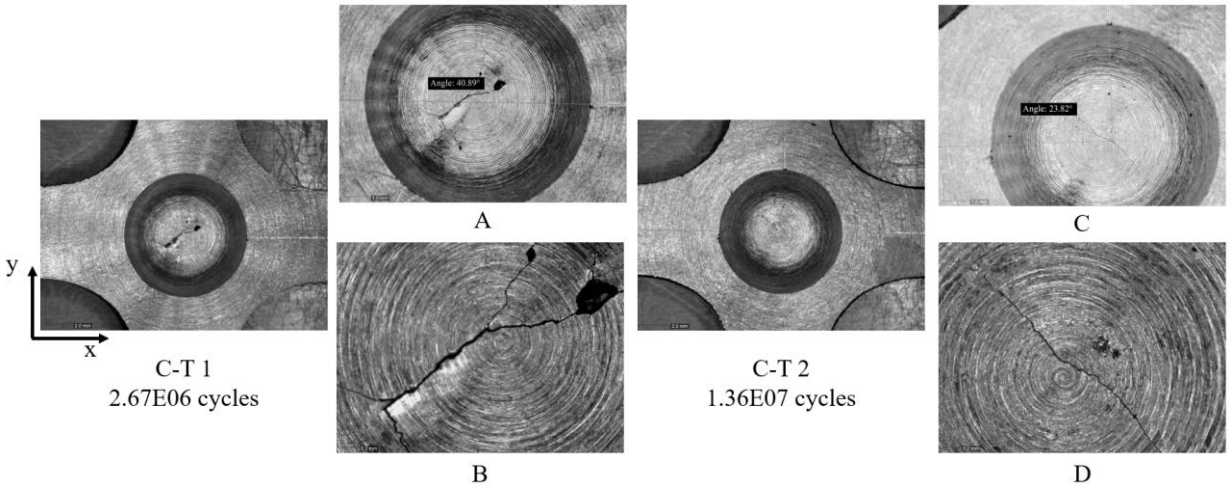

Figure 5-58. C-T 1 (σy=144.3MPa; σx=137MPa; Cycles to failure = 2.67E6) and C-T 2 (σy=133.1MPa; σx=124MPa; Cycles to failure = 13.6E6) fatigue fracture: angle, (A) and (C) respectively; Shape (B) and (D), respectively.

The new N T-T specimens presented crack initiation at the arms' corners. This result was not predicted. Thermal imaging first observation indicated a higher heat generation at the midpoint. However, a careful observation showed a heat generation at the arms corners was also present.

The corner failure was associated with MI and PM, both present within the transducer frequency range. MI and PM mode shapes have a high-stress combination at the corners in T-T specimens. PM increased the lower corner stress combination in the excited MI enough to have crack initiation. Damage at the corners was also observed caused by poor machining. The surface damage may have contributed to stress concentration and crack initiation. PM influence, together with geometrical stress concentration, has thus resulted in fatigue failure on a non-desired region. Figure 5-59 shows the two present crack locations, size, the damaged surface, and thermal imaging where slight heat generation can be seen at the failed corner.

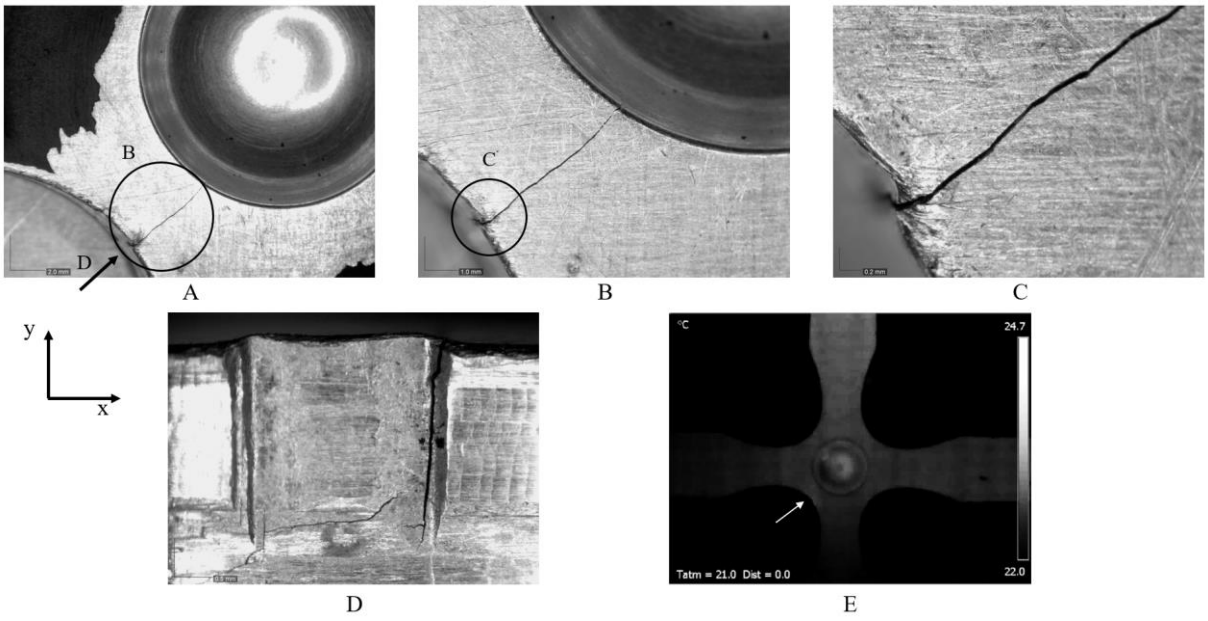

Figure 5-59. N1 T-T (σy=112.5MPa; σx=107.1MPa; Cycles to failure = 12.1E6) fatigue fractures location (A); shape (B-D); Thermal image of midpoint and corner heat generation (E).

N T-T fatigue results highlight the importance of surface quality at the corners and the need to further optimise the T-T geometry. Nevertheless, experimental analysis has shown that the PM effect at the midpoint is negligible in terms of induced stresses.

F3 T-T specimen presented a better surface quality with no visible damage at the arms corners. When conducting UFT, no heat generation at the corners was perceived, and a clear

and single 53.9º crack initiation at the midpoint was obtained. Figure 5-60 presents microscope images of the resulting crack path, initiation angle and location.

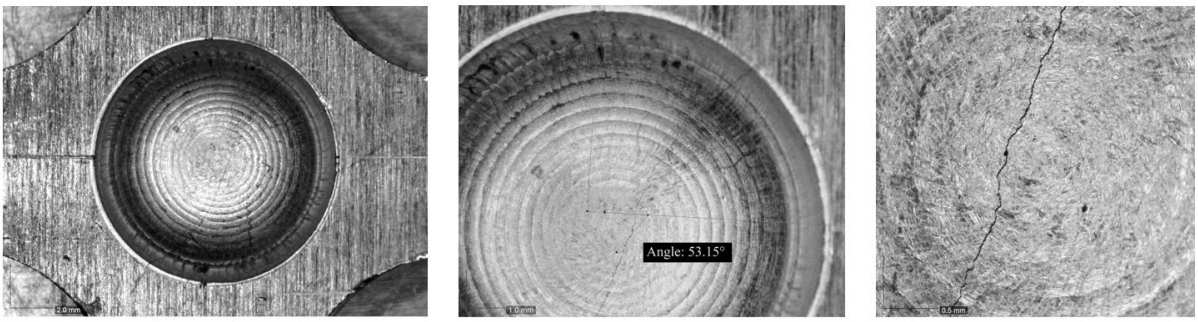

Figure 5-60. F3 T-T (σy=176.5MPa; σx=175MPa; Cycles to failure = 0.76E6) fatigue fracture (A) location; (B) angle; (C) shape.

Initial crack growth under ultrasonic loading conditions displays similar patterns to conventional methods when correctly designed and manufactured specimens fail. Other authors have described both analytically and experimentally the branching found in out-of-phase and one singular crack in in-phase specimens. Once the initial crack size becomes significant, further propagation in ultrasonic testing is no longer symmetric between the two growing crack edges. The branching found in 40-50º crack C-T is close to symmetrical as found by Garcia et al. [217] but with different angles between branches on each crack edge. After considerable crack propagation, the behaviour no longer presents complete symmetry. The non-symmetrical, and in some specimens, chaotic behaviour is associated with the specimen resonance change with crack propagation. As the crack size increases, the specimen rigidity changes, thus changing its resonance frequency and mode shape. Numerical analyses with different initial cracks are required to understand crack propagation and the occasional final chaotic behaviour.

After crack propagation analysis, all cruciform with midpoint crack initiation were fractured in a servo-hydraulic machine. Samples of the fatigue fracture surfaces were cut and put under SEM.

From an overview observation of the fatigue crack surface, there are three separate propagation stages before the final fracture: stage I at the smallest-cross section region and two in the thickness growing region. Each propagation stage presents different crack propagation characteristics. The two last propagations do not follow the stress fatigue field of interest. When the crack propagation stage I reaches a certain size, the stress field at the crack tip no longer is

intended. This was predicted by the observed crack chaotic and non-symmetrical behaviour at a certain length. Also, the specimen rigidity loss can change its resonance mode shape and, therefore, the induced stress combination. Figure 5-61 shows C-T 1 and F3 T-T fatigue crack surface overview with the three mentioned propagation stages identified.

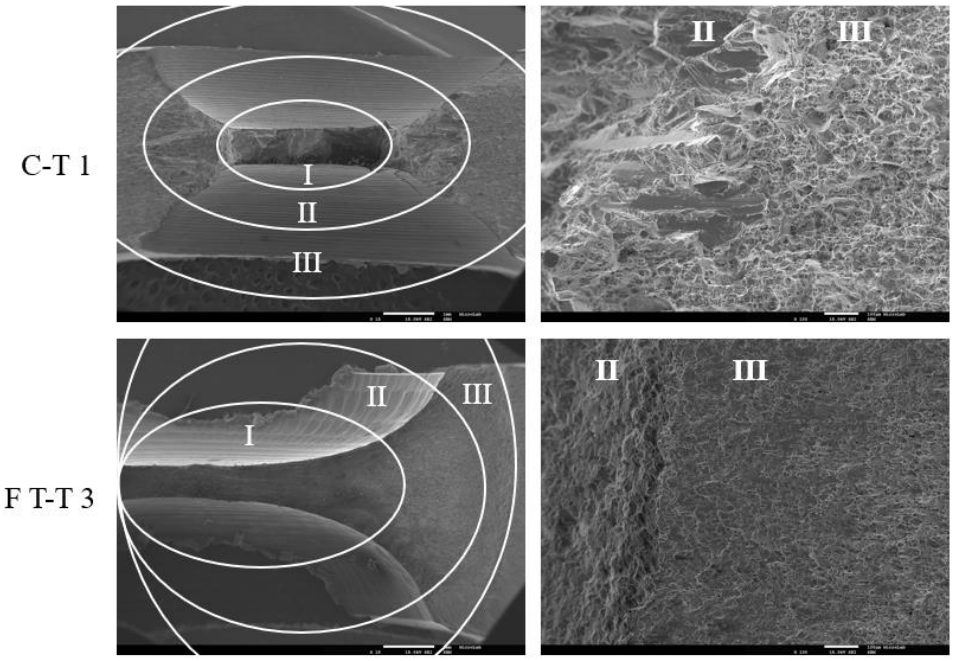

Figure 5-61. C-T 1 and F3 T-T fatigue crack surface with the three crack propagation stages identified.

In F3 T-T, the surface crack initiation location was determined. Crack mode I propagation striations are observed across the stage I propagation. Microcracks are also perceived across the stage one crack surface. Figure 5-62 identifies the crack initiation location, the mode I striations and highlights the present microcracks.

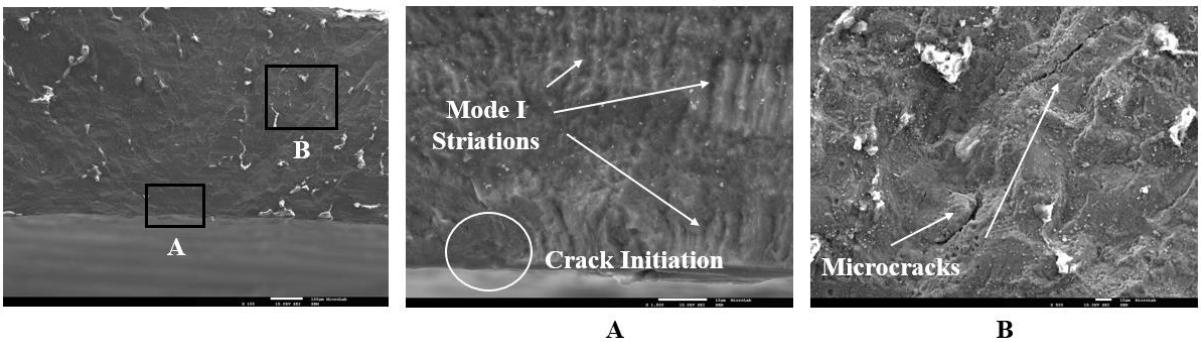

Figure 5-62. F3 T-T fatigue stage I surface: (A) surface crack initiation and mode I striations; (B) micro secondary cracks.

C-T specimens crack initiation pinpoint location is not fully clear. The stage I crack surface has a mixed-mode I+II crack propagation. The associated mixed-mode I+II crack propagation characteristics are similar to pure torsion and tension-torsion high shear/axial ratio radial marks. Figure 5-63 C-T1 SEM analysis identifies the crack initiation region and shear marks similar to the radial marks of pure torsion and tension-torsion specimens.

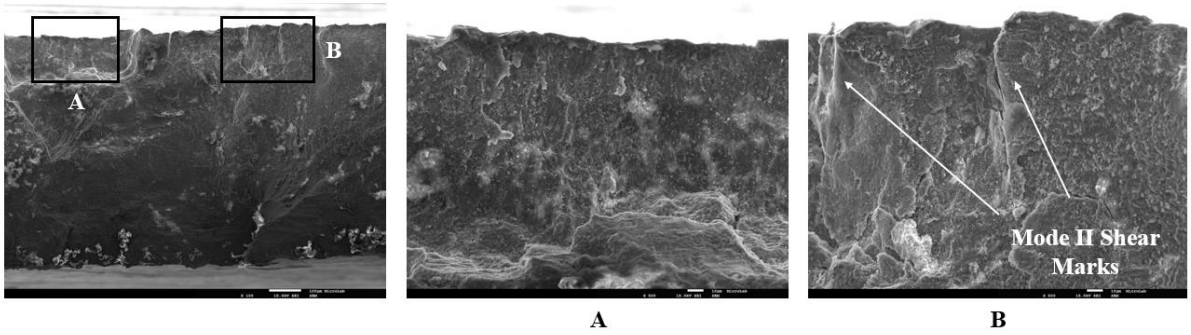

Figure 5-63. C-T1 fatigue stage I surface: (A) surface crack initiation region; (B) mode II shear marks.

The C-T fatigue crack surface also has mode II propagation with crack rubbing morphology, as perceived in Figure 5-64.

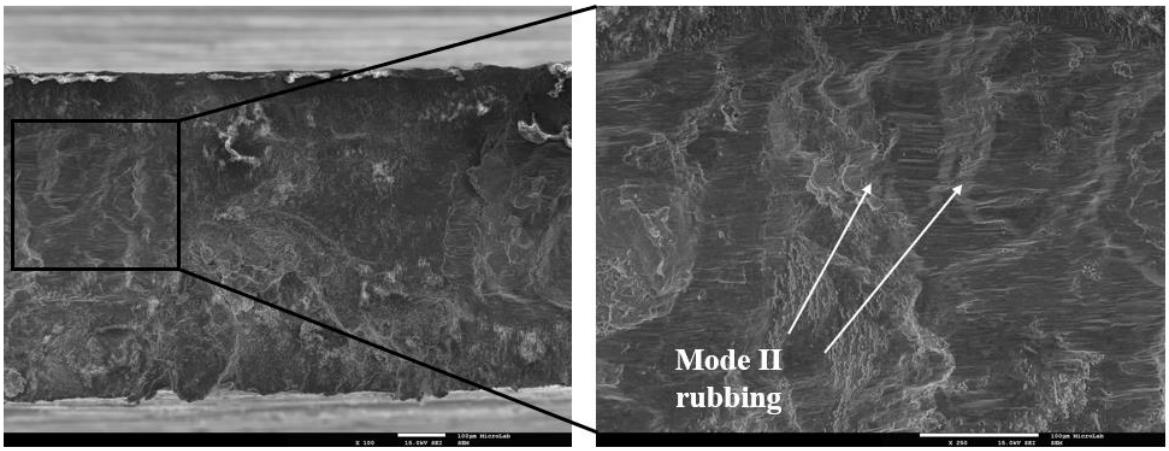

Figure 5-64. C-T2 fatigue crack surface and mode II shear rubbing marks.

Neerukatti et al. [220] conducted conventional cruciform fatigue testing both in-phase and out-of-phase loading conditions to Al7075-T651 aluminium. Similar fatigue crack surface characteristics were found. Three different propagation crack stages were also present. However, stages II and III are not similar to Figure 5-61 ultrasonic specimens stages II and III. In-phase specimens presented mode I striations across the crack propagation, and out-of-phase showed mode II shear marks denoted as slip steps by the authors. Neerukatii et al. out-of-phase cruciforms also presented a crack bifurcation similar to ultrasonic C-T1 Figure 5-58.

6

Conclusions and Future Works

The following chapter closes the present dissertation. All reached conclusions for each designed, assembled and operated ultrasonic fatigue machines and respective methodologies are discussed, followed by an overall perspective on the design and development of new ultrasonic fatigue methods.

From all conclusions and acquired knowledge, future prospect works and research paths are here proposed. All given proposals intend to improve or rectify observed problems, conduct innovative research on this high-interest scientific field, and reach fully functional and standardised uniaxial and multiaxial ultrasonic fatigue methods.

6.1 Conclusions

This thesis studied and developed four different ultrasonic fatigue methods: tension-compression; pure torsion; cruciform axial-axial; and cylindrical tension-torsion. For all four methods, the core of the study was dedicated to three main objectives:

- Design and develop consistent, stable and reliable ultrasonic fatigue machines and methodologies
- Adapt ultrasonic concepts and methods towards more complex fatigue stress combination experiments
- Establish the requirements for the ultrasonic machine methods and respective methodologies to be standardised

A deep study of all published analytical, numerical and experimental applied methods and machines created the basis for the research. It utilised the known concepts, knowledge and experience around ultrasonic machines to design and develop two novel multiaxial ultrasonic fatigue methods. A pure torsional ultrasonic machine was also built following Claude Bathias design expanding the research team knowledge and fatigue testing capabilities.

Prior to the developments of the novel multiaxial ultrasonic methods and pure torsion machine, the study focused on the already existing tension-compression machine, accessible components and measuring equipment. The existing machine underwent a modal behaviour response analysis together with an evaluation of all available capabilities. The analysis of the machine state, existing components and equipment capabilities lead to new vital improvements for the execution of the present thesis experiments. The DAQ system, machine structure, electric connections, cooling system, user accessibility to machine built software, and the complete working environment were improved and made adaptable to all conducted and future experiments.

All changes to the workstation allowed to modify experimental setups, adjust testing software configurations, and optimize the use of available equipment. The new built environment was fundamental to the success of the three new added ultrasonic methods.

Every ultrasonic fatigue test was first analysed through FEA from a created numerical method in ABAQUS software. The free vibration frequency analysis was used as customary for specimen design. The further addition of steady-state modal analysis and its translation towards the experimental executed method and final comparison, created the ability to study in detail any ultrasonic fatigue machine setup.

From FEA steady-state, an exceptional correlation with low error to the experimental displacement and strain measurements showed that it can be a vital tool for machine calibration and UFT execution.

The FEA results were first compared with the analytical solutions already proposed by Claude Bathias and the Japanese Welding Engineering Standard WES 1112 [71; 187] for tension-compression and pure torsion loading cases. FEA showed a negligible difference to the analytical displacement and stress distribution, displacement to stress ratio and improved the design of the specimen towards a final geometry closer to 20 kHz frequency. The steady-state analysis also showed the ability to predict the induced stress by the experimentally measured displacement. Strain gauge and displacement measurements in the two tested materials in

ultrasonic tension-compression presented a ratio with lower than 1% and 9% error, respectively, to FEA estimations. The higher difference for Ti6Al4V was related to ultrasonic specimen design without first conducting mechanical tests to determine static material properties. This higher difference proved the importance of sequenced experimental methodology execution.

With a proven correlation between analytical, experimental and the FEA results, the same method was applied towards the pure torsional machine and the two novel multiaxial methods. Regarding the two multiaxial studied methods, an increased complexity was undoubtedly present. FEA proved to be a vital tool for studying and quantifying all present modal behaviours and induced stresses. FEA results showed a correlation to the experimental results; it predicted and explained all obtained issues and was fundamental for achieving the proposed analytical methods to tension-torsion and cruciform axial-axial.

An experimental modal analysis method was required to compare FEA results with the resulting ultrasonic machine setup frequency behaviour. To the author's knowledge, the applied cyclic excitation force needed to describe the system through a frequency response function is not yet possible to be measured. An adaptation of a frequency analysis method used in big structures with an unknown force of excitation was applied, the Frequency Domain Decomposition (FDD) method. Its application was a significant step towards quantifying any ultrasonic setup overall frequency response. FDD allows for frequency quantification of all present resonant modes, even outside the piezoelectric transducer frequency range of operation. It also provided a phase and magnitude ratio between measured locations in each detected resonant mode. The resonant modes could then be identified and correlated to the FEA frequency and steady-state results through the phase and magnitude ratio.

With the numerical and FDD method, a working pure torsional ultrasonic fatigue machine was achieved. The first machine iteration did not work as intended. It was only through FDD that a lower than required frequency of the torsional horn was detected. A calibration methodology was created, and together with the FDD modal analysis, a correct 20 kHz working setup was achieved. The engineered methodology surrounding the pure torsional setup will always guarantee a working set of ultrasonic components. The final setup showed an unpredicted too high displacement amplification that did not allow for specimen displacement measurement required to correctly execute UFT. The succeeding built setup must have a lower projected amplification and will follow the same approach to ensure a 20 kHz pure torsional resonance.

At the beginning of the thesis, the tension-torsion method was proven possible but not fully operational. The specimens presented variable behaviour; the multi-horn had stress-induced issues that required a change in geometry; the test specimens modal behaviour was not fully described with an uncomprehended response, no measuring proven fatigue methodology was yet achieved, and, therefore, no full UFT was ever conducted.

Following Pedro R. da Costa master thesis [194], a new multi-horn design was made focusing on induced stresses. The new multi-horn did not change modal shape and frequency over extensive experiments and UFT.

The three throat specimen was then studied extensively by FEA and experimental means. The first design specimen by Mario et al. [85] and three new specimens were under numerical analysis, modally analysed within the ultrasonic setup on their deformed shape and frequency response, and put finally under UFT. The study numerically quantified all present behaviours associated with the three throat specimen concept. From the in-depth FEA, the following specimens modal behaviours were characterised:

- The dimensional effect on the excited frequency of the specimens alone and within the setup;
- The ability to manipulate the shear distribution was comprehended and, therefore, the capability of achieving different shear/axial stress ratios;
- Origin of all the current shear/axial ratio variation problems in-between specimens and means to rectify in the future.

Several strain gauges were applied to the fatigue testing region following FEA results. Mario et al. [85] machined groves concept for rotational measurement were applied and correlated to the measured shear strains. The extensive experimental measurements were correlated between induced shear and axial stresses to the measured rotational and axial displacements. FEA axial displacement to axial stress ratio presented a good correlation. However, the measured rotation at the specimens groves and shear stress by strain gauge had considerable differences to FEA predicted. The results were associated with the comprehended Parasite Mode (PM) influence over the torsional mode shape of the specimen. It was concluded that the PM influence and the specimens high dimensional sensitivity were responsible for varying shear amplitude between similar specimens.

An analytical method was proposed from all taken conclusions surrounding the tension-torsion specimen. Up to this moment, all three throat specimens required a time consuming iterative FEA frequency analysis to reach one geometry with the desired modes at 20 kHz. The proposed method provides a direct calculation that can be scripted in software for a first 20±1 kHz range resonance. The presented sensitive dimensional analysis for different geometries allows for a quick geometric adjustment solution to reach the final 20 kHz. The proposed analytical method also predicts the shear and axial stress amplitudes for the final determined geometry, showing a lower than 4% and 10% error to FEA predicted shear and axial stress amplitudes, respectively.

The improvements to the multi-horn, the numerical and measurements methodology and the conducted study of all results enabled full testing of well-defined specimens in multiaxial UFT. Never before was it possible to conduct a tension-torsion multiaxial ultrasonic fatigue. The path towards a reliable and standardizable method was drawn.

The second novel multiaxial ultrasonic fatigue testing method applied equibiaxial and pure shear cruciform specimens. Three different geometries of cruciform specimens were analysed and tested in an ultrasonic fatigue machine: Two equibiaxial in-phase tension-tension (T-T) and one pure shear tension-compression (C-T).

Based on the FEA results, two different measuring setups were conducted to study the cruciforms modal shape and frequency response by FDD. From the modal analysis, and as predicted by steady-state FEA, two modes with similar frequency were able to be excited by the ultrasonic setup: the intended to be induced, the resonant Mode of Interest (MI), and an undesirable and influential resonant mode, denoted the Parasite mode (PM). FDD modal analysis method showed both MI and PM frequency for all analysed specimens, even when outside of the working transducer frequency range.

The proximity of the PM mode and its negative impact on the final MI shape was defined from both FEA and FDD. With the described cruciform modal behaviour, an analytical method was also proposed. The analytical method does not allow for specimen geometry determination. Nevertheless, and most importantly, it can predict the stress amplitude for a given measured displacement in each arm of the applied cruciforms. The method considers the cruciform specimen as two ultrasonic exponential tension-compression specimens sharing one fatigue testing region. Therefore, the associated tension-compression analytical solution was adapted considering the cruciform stress distribution and modal behaviour. The found

analytical solution can also bring the FEA steady-state displacement to stress ratio towards the experimental procedure with a good correlation.

A complete comparison between numerical results, conducted measurements, UFT with respective fatigue fracture results, and the ultrasonic scientific community published results consolidated all findings and conclusions. The methods proved to induce fatigue in the desired stress state cycle combined with an improved measuring methodology. The multiaxial methods still require numerical knowledge for their application and continuous improvement. Even so, the proposed analytical solutions and proven methodologies can adequately be used as guidance in future experiments. The thesis has proven their aptitude to further improve ultrasonic fatigue testing practice and results reliability towards the desired standardisation.

6.2 Future Works

There is still continuous work to be made from all reached conclusions surrounding ultrasonic testing methods. Future ultrasonic fatigue experiments concerning all four methods with a proven material in the VHCF regime, as the tested Selective Laser Melting Ti6Al4V, are recommended to be conducted. In addition, by having reached a working method with respective measuring and fatigue methodology, other possibilities for more complex fatigue studies are now accessible.

As previously discussed in subchapter 3.4.2.6, two proposed solutions were studied to improve the ultrasonic tension-torsion fatigue machine observed shear/axial ratio variability. Both solutions were only yet studied in FEA and, therefore, they only showed numerically proven improvements. Future experiments following the presented FEA study are here proposed to improve the tension-torsion ultrasonic fatigue machine. The undesirable variability is associated with the specimen torsional mode dimensional sensitivity, and the influence of a PM with mode shape similarities and a similar frequency to the MI. The first proposed solution tackles the dimensional specimen sensitivity on its resulting frequency. The created concept divides the specimen into three sections; Two sections composed of the secondary throats established Ts2 and Ts3; and the main throat section Ts1. A representation was made in Figure 3-42. This will mean that the specimen will now be composed only by the main throat section. The two outer sections would remain in-between UFT specimens. There will be minor dimensional variations between specimens by reducing ~2/3 of the dimensional specimen

variability. Also, the specimen requires less manufacturing time and less testing material, and the proposed analytical solution remains unchanged. The only issue is the proven axial stress in the new created screw connection. Even though the deformation was proven to be 74% lower than the fatigue testing region, it can cause similar problems to those witnessed by the PM excited cruciform specimens (Figure 5-47). Only experimentally tests can prove the reliability of the proposal.

The second proposed solution focuses on reducing the PM influence by following the same concept as tension-compression mean stress ultrasonic fatigue machines. A second set of booster and multi-horn are proposed to be machined and attached to the free base of the three throat specimen. The setup would then be composed of a piezoelectric transducer, two boosters, two multi-horns (2B+2H) and a three throat specimen. FEA free vibration and steady-state have proven a lower PM influence due to a mode shape change and the increased frequency difference to MI, which resulted in a considerably lower stress ratio variation. The built structure allows for a quick adaptation to include the second booster and horn.

With the build 2H+2B setup, the tension-torsion machine can then conduct ultrasonic fatigue testing with mean axial and shear stress. The rotational and axial load application can be made through the boosters support ring, similar to the described machines on the published research in [121–124], for mean axial load, and Mayer et al. [127], for a mean torsional load.

Regarding ultrasonic cruciform specimens, three proposed future research paths are here presented. Similar to the proposed 2B+2H set for mean tension and/or torsion load fatigue, a proposed work is to adapt the same concept to the ultrasonic cruciform method. The reliability of adding two other sets of a booster and horn at the horizontal arms of the cruciform geometries must be numerically studied. The study should begin with 2B+2H and therefore only one direction with mean stress. And afterwards the possibility of adding mean stress in the horizontal direction. If resonance is possible with four boosters and four horns, the ultrasonic cruciform method will be able to conduct fatigue tests with applied mean stresses in both axial-axial directions. No servo-hydraulic or electromechanical machine present at the hosting institution can apply two directional loads. Therefore, a two directional static load machine must be acquired or even built specifically to this end. Another possibility is a structure attached to an electromechanical machine that through one directional load can equally apply the required two to the ultrasonic setup. One example is Barroso et al. [221] built and tested device for biaxial cruciform testing in uniaxial machines.

Looking at the ultrasonic cruciform followed midpoint shape, a small risk volume fatigue testing was present in both equibiaxial T-T and pure shear C-T. The risk volume has been proven by referenced research (subchapter 2.3.5.1) to influence obtained VHCF stress-life results. A redesign of the cruciform geometry through an optimisation method similar to the Baptista et al. [54] methodology is proposed considering the resonance deformation mode shape distribution (i.e. not the conventional applied load deformation), and an increased fatigue risk volume of the specimen.

Together with the coworking team at Bournemouth University, an already study of ultrasonic cruciforms with non-unitary ratios was conducted [198]. The present work proposes the application of the same numerical and experimental analysis methodologies towards non-unitary ratio cruciform specimens.

References

[1] W. Schütz, A history of fatigue, Eng. Fract. Mech., **54**, 2, 263–300, (1996).

[2] M. Fonte, L. Reis, and M. Freitas, Failure analysis of a gear wheel of a marine azimuth thruster, Eng. Fail. Anal., **18**, 7, 1884–1888, (2011).

[3] M. Fonte, P. Duarte, V. Anes, M. Freitas, and L. Reis, On the assessment of fatigue life of marine diesel engine crankshafts, Eng. Fail. Anal., **56**, 51–57, (2015).

[4] M. de Freitas, Multiaxial fatigue: From materials testing to life prediction, Theor. Appl. Fract. Mech., **92**, 360–372, (2017).

[5] C. Bathias and P. C. Paris, Gigacycle fatigue of metallic aircraft components, Int. J. Fatigue, **32**, 6, 894–897, (2010).

[6] I. Marines, X. Bin, and C. Bathias, An understanding of very high cycle fatigue of metals, Int. J. Fatigue, **25**, 9–11, 1101–1107, (2003).

[7] M. Schläfli and E. Brühwiler, Fatigue of existing reinforced concrete bridge deck slabs, Eng. Struct., **20**, 11, 991–998, (1998).

[8] M. K. Lee and B. I. G. Barr, An overview of the fatigue behaviour of plain and fibre reinforced concrete, Cem. Concr. Compos., **26**, 4, 299–305, (2004).

[9] R. Harte and G. P. A. G. Van Zijl, Structural stability of concrete wind turbines and solar chimney towers exposed to dynamic wind action, J. Wind Eng. Ind. Aerodyn., **95**, 9–11, 1079–1096, (2007).

[10] F. A. Canut *et al.*, Monitoring of corrosion-fatigue degradation of grade R4 steel using an electrochemical-mechanical combined approach, Fatigue Fract. Eng. Mater. Struct., **42**, 11, 2509–2519, (2019).

[11] C. M. Sonsino, Course of SN-curves especially in the high-cycle fatigue regime with regard to component design and safety, Int. J. Fatigue, **29**, 2246–2258, (2007).

[12] J. Y. Huang, J. J. Yen, S. L. Jeng, C. Y. Chen, and R. C. Kuo, High-cycle fatigue behavior of type 316L stainless steel, Mater. Trans., **47**, 2, 409–417, (2006).

[13] M. Benedetti, V. Fontanari, M. Bandini, F. Zanini, and S. Carmignato, Low- and high-

cycle fatigue resistance of Ti-6Al-4V ELI additively manufactured via selective laser melting: Mean stress and defect sensitivity, Int. J. Fatigue, **107**, August 2017, 96–109, (2018).

[14] H. Soares, P. Costa, M. Freitas, and L. Reis, Fatigue life assessment of a railway wheel material under HCF and VHCF conditions, MATEC Web Conf., **165**, 09003, (2018).

[15] T. Zhao and Y. Jiang, Fatigue of 7075-T651 aluminum alloy, Int. J. Fatigue, **30**, 5, 834–849, (2008).

[16] I. De Baere, W. Van Paepegem, and J. Degrieck, Comparison of different setups for fatigue testing of thin composite laminates in bending, Int. J. Fatigue, **31**, 6, 1095–1101, (2009).

[17] A. M. Harte, N. A. Fleck, and M. F. Ashby, The fatigue strength of sandwich beams with an aluminium alloy foam core, Int. J. Fatigue, **23**, 6, 499–507, (2001).

[18] G. Palomba, V. Crupi, and G. Epasto, Collapse modes of aluminium honeycomb sandwich structures under fatigue bending loading, Thin-Walled Struct., **145**, April, 106363, (2019).

[19] L. Nascimento, S. Yi, J. Bohlen, L. Fuskova, D. Letzig, and K. U. Kainer, High cycle fatigue behaviour of magnesium alloys, in *Procedia Engineering*, (2010).

[20] Y. Wang, D. Culbertson, and Y. Jiang, An experimental study of anisotropic fatigue behavior of rolled AZ31B magnesium alloy, Mater. Des., (2020).

[21] Smartech Analysis, Additive Manufacturing Applications Market Analysis: Metal Additive Manufactured Parts Produced, (2019).

[22] W. E. Frazier, Metal additive manufacturing: A review, J. Mater. Eng. Perform., **23**, 6, 1917–1928, (2014).

[23] J. Alcisto *et al.*, Tensile properties and microstructures of laser-formed Ti-6Al-4V, J. Mater. Eng. Perform., **20**, 2, 203–212, (2011).

[24] O. Abdulhameed, A. Al-Ahmari, W. Ameen, and S. H. Mian, Additive manufacturing: Challenges, trends, and applications, Adv. Mech. Eng., **11**, 2, 1–27, (2019).

[25] A. Sterling, N. Shamsaei, B. Torries, and S. M. Thompson, Fatigue Behaviour of Additively Manufactured Ti-6Al-4 v, Procedia Eng., **133**, 576–589, (2015).

[26] P. Edwards and M. Ramulu, Fatigue performance evaluation of selective laser melted Ti-6Al-4V, Mater. Sci. Eng. A, **598**, 327–337, (2014).

[27] W. Liu *et al.*, Study of pore defect and mechanical properties in selective laser melted Ti6Al4V alloy based on X-ray computed tomography, Mater. Sci. Eng. A, **797**, February, 139981, (2020).

[28] H. K. Rafi, N. V. Karthik, H. Gong, T. L. Starr, and B. E. Stucker, Microstructures and mechanical properties of Ti6Al4V parts fabricated by selective laser melting and electron beam melting, J. Mater. Eng. Perform., **22**, 12, 3872–3883, (2013).

[29] J. Gockel, L. Sheridan, B. Koerper, and B. Whip, The influence of additive manufacturing processing parameters on surface roughness and fatigue life, Int. J. Fatigue, **124**, October 2018, 380–388, (2019).

[30] G. Kasperovich and J. Hausmann, Improvement of fatigue resistance and ductility of TiAl6V4 processed by selective laser melting, J. Mater. Process. Technol., **220**, 202–214, (2015).

[31] C. de Formanoir, S. Michotte, O. Rigo, L. Germain, and S. Godet, Electron beam melted Ti-6Al-4V: Microstructure, texture and mechanical behavior of the as-built and heat-treated material, Mater. Sci. Eng. A, **652**, 105–119, (2016).

[32] L. Denti, E. Bassoli, A. Gatto, E. Santecchia, and P. Mengucci, Fatigue life and microstructure of additive manufactured Ti6Al4V after different finishing processes, Mater. Sci. Eng. A, **755**, April, 1–9, (2019).

[33] L. Reis, B. Li, and M. De Freitas, A multiaxial fatigue approach to Rolling Contact Fatigue in railways, Int. J. Fatigue, **67**, 191–202, (2014).

[34] V. Bonnand, J. L. Chaboche, P. Gomez, P. Kanouté, and D. Pacou, Investigation of multiaxial fatigue in the context of turboengine disc applications, Int. J. Fatigue, **33**, 8, 1006–1016, (2011).

[35] P. Costa *et al.*, Review of multiaxial testing for very high cycle fatigue: From "Conventional" to ultrasonic machines, Machines, **8**, 2, (2020).

[36] H. J. Gough and H. V. Pollard, The strength of metals under combined alternating stresses, Proc. Inst. Mech. Enginners, **131**, 1, (1935).

[37] M. DE Freitas and D. François, Analysis of Fatigue Crack Growth in Rotary Bend

Specimens and Railway Axles, Fatigue Fract. Eng. Mater. Struct., **18**, 2, 171–178, (1995).

[38] R. A. Cláudio, L. Reis, and M. Freitas, Biaxial high-cycle fatigue life assessment of ductile aluminium cruciform specimens, Theor. Appl. Fract. Mech., **73**, 82–90, (2014).

[39] D. Lefebvre, C. Chebl, L. Thibodeau, and E. Khazzari, A high-strain biaxial-testing rig for thin-walled tubes under axial load and pressure, Exp. Mech., **23**, 4, 384–392, (1983).

[40] T. Morishita, T. Itoh, M. Sakane, H. Nakamura, and M. Takanashi, Multiaxial fatigue property of Ti-6Al-4V using hollow cylinder specimen under push-pull and cyclic inner pressure loading, Int. J. Fatigue, **87**, 370–380, (2016).

[41] D. Zhao, H. Gao, H. Liu, P. Jia, and J. Yang, Fatigue properties of plain concrete under triaxial tension-compresion-compression cyclic loading, Shock Vib., **2017**, (2017).

[42] D. L. Mcdiarmid, A new analysis of fatigue under combined bending and twisting, Aeronaut. J., **78**, 763, 325–329, (1974).

[43] M. Raghu, On the collapse of long thick-walled circular tubes under biaxial loading, California Institute of Technology, (1988).

[44] H. Soares, V. Anes, M. Freitas, and L. Reis, A railway wheel evaluation under multiaxial loading conditions, MATEC Web Conf., **300**, December, 09002, (2019).

[45] P. Heuler and H. Klätschke, Generation and use of standardised load spectra and load-time histories, Int. J. Fatigue, **27**, 8, 974–990, (2005).

[46] L. Reis, J. Caxias, H. Soares, P. R. Costa, V. Anes, and M. Freitas, Damage evaluation under complex fatigue loading conditions, Frat. ed Integrita Strutt., **13**, 48, 318–331, (2019).

[47] R. Sunder and B. V. Ilchenko, Fatigue crack growth under flight spectrum loading with superposed biaxial loading due to fuselage cabin pressure, Int. J. Fatigue, **33**, 8, 1101–1110, (2011).

[48] R. F. Young, J. E. Bird, and J. L. Duncan, An automated hydraulic bulge tester, J. Appl. Metalwork., **2**, 1, 11–18, (1981).

[49] C. Brugger, T. Palin-Luc, P. Osmond, and M. Blanc, Gigacycle fatigue behavior of a cast aluminum alloy under biaxial bending: experiments with a new piezoelectric fatigue testing device, Procedia Struct. Integr., **2**, 1179–1180, (2016).

[50] J. M. H. Andrews and E. G. Ellison, A testing rig for cycling at high biaxial strains, J. Strain Anal. Eng. Des., **8**, 3, 168–175, (1973).

[51] M. Freitas *et al.*, In-Plane Biaxial Fatigue Testing Machine Powered by Linear Iron-Core Motors, in *Application of Automation Technology in Fatigue and Fracture Testing and Analysis*, 100 Barr Harbor Drive, PO Box C700, West Conshohocken, PA 19428-2959: ASTM International, (2014), 63–79.

[52] A. Makinde, L. Thibodeau, and K. W. Neale, Development of an apparatus for biaxial testing using cruciform specimens, Exp. Mech., **32**, 2, 138–144, (1992).

[53] H. Fessler and J. K. Musson, A 30 ton biaxial tensile testing machine, J. Strain Anal. Eng. Des., **4**, 1, 22–26, (1969).

[54] R. Baptista, R. A. Claudio, L. Reis, J. F. A. Madeira, I. Guelho, and M. Freitas, Optimization of cruciform specimens for biaxial fatigue loading with direct multi search, Theor. Appl. Fract. Mech., **80**, 65–72, (2015).

[55] A. Makris, T. Vandenbergh, C. Ramault, D. Van Hemelrijck, E. Lamkanfi, and W. Van Paepegem, Shape optimisation of a biaxially loaded cruciform specimen, Polym. Test., **29**, 2, 216–223, (2010).

[56] A. Smits, D. Van Hemelrijck, T. P. Philippidis, and A. Cardon, Design of a cruciform specimen for biaxial testing of fibre reinforced composite laminates, Compos. Sci. Technol., **66**, 7–8, 964–975, (2006).

[57] D. S. Dawicke and W. D. Pollock, Biaxial Testing of 2219-T87 Aluminum Alloy Using Cruciform Specimens. Analytical Services @ Materials, Inc, Hampton, Virginia.

[58] A. A. Lebedev and N. R. Muzyka, Design of cruciform specimens for fracture toughness tests in biaxial tension (review), Strength Mater., **30**, 3, (1998).

[59] S. Demmerle and J. P. Boehler, Optimal design of biaxial tensile cruciform specimens, J. Mech. Phys. Solids, **41**, 1, 143–181, (1993).

[60] K. A. Laydova, V. V Shadrin, L. V Kovtanyuk, and A. S. Ustinova, Shape optimization of a biaxially loaded specimen, Proc. XLI Int. Summer Sch. APM 2013, 360–367, (2013).

[61] I. Guelho, L. Reis, M. Freitas, B. Li, J. F. A. Madeira, and R. A. Cláudio, Optimization of Cruciform Specimen for Low Capacity Biaxial Testing Machine, 10th Int. Conf.

Multiaxial Fatigue Fract., (2013).

[62] R. Baptista, L. Reis, I. Guelho, M. Freitas, and J. F. A. Madeira, Design optimization of cruciform specimens for biaxial fatigue loading, Frat. ed Integrita Struct., **30**, 118–126, (2014).

[63] T. Kuwabara, S. Ikeda, and K. Kuroda, Measurement and analysis of differential work hardening in cold-rolled steel sheet under biaxial tension, J. Mater. Process. Technol., **80–81**, 517–523, (1998).

[64] W. Müller and K. Pöhlandt, New experiments for determining yield loci of sheet metal, J. Mater. Process. Technol., **60**, 1–4, 643–648, (1996).

[65] J. Gozzi, A. Olsson, and O. Lagerqvist, Experimental investigation of the behavior of extra high strength steel, Exp. Mech., **45**, 6, 533–540, (2005).

[66] Y. Murakami, Metal Fatigue: Effects of Small Defects and Nonmetallic Inclusions. (2002).

[67] R. O. Ritchie, Near-threshold fatigue-crack propagation in steels, Int. Met. Rev., **24**, 1, 205–228, (1979).

[68] C. Bathias, There is no infinite fatigue life in metallic materials, Fatigue Fract. Eng. Mater. Struct., **22**, 559–565, (1999).

[69] B. Pyttel, D. Schwerdt, and C. Berger, Very high cycle fatigue - Is there a fatigue limit?, Int. J. Fatigue, **33**, 1, 49–58, (2011).

[70] Y. Zhang, Z. Duan, and H. Shi, Comparison of the very high cycle fatigue behaviors of INCONEL 718 with different loading frequencies, Sci. China Physics, Mech. Astron., **56**, 3, 617–623, (2013).

[71] C. Bathias and P. C. Paris, Gigacycle fatigue in mechanical practice. (2005). Taylor & Francis INC

[72] B. Hopkinson, A high-speed fatigue-tester, and the endurance of metals under alternating stresses of high frequency, R. Soc., **86**, 584, (1911).

[73] H. Mughrabi and S. D. Antolovich, A tribute to Claude Bathias – Highlights of his pioneering work in Gigacycle Fatigue, Int. J. Fatigue, **93**, 217–223, (2016).

[74] C. Bathias, Piezoelectric fatigue testing machines and devices, Int. J. Fatigue, **28**, 11,

1438–1445, (2006).

[75] S. Stanzl-Tschegg, Very high cycle fatigue measuring techniques, Int. J. Fatigue, **60**, 2–17, (2014).

[76] N. M. M. Maia and J. M. M. Silva, Theoretical and Experimental Modal Analysis. Research Studies Press LTD.

[77] I. Marines *et al.*, Ultrasonic fatigue tests on bearing steel AISI-SAE 52100 at frequency of 20 and 30 kHz, Int. J. Fatigue, **25**, 9–11, 1037–1046, (2003).

[78] G. J. Yun, A. B. M. Abdullah, and W. Binienda, Development of a Closed-Loop High-Cycle Resonant Fatigue Testing System, Exp. Mech., **52**, 3, 275–288, (2012).

[79] T. J. George, J. Seidt, M. H. Herman Shen, T. Nicholas, and C. J. Cross, Development of a novel vibration-based fatigue testing methodology, Int. J. Fatigue, **26**, 5, 477–486, (2004).

[80] I. Milošević, P. Renhart, G. Winter, F. Grün, and M. Kober, A new high frequency testing method for steels under tension/compression loading in the VHCF regime, Int. J. Fatigue, **104**, 150–157, (2017).

[81] M. Freitas, V. Anes, and D. Montalvao, Design and assembly of an ultrasonic fatigue testing machine, An. Mecânica la Fract., **1**, 28, 335–340, (2011).

[82] N. Ranc, D. Wagner, and P. C. Paris, Study of thermal effects associated with crack propagation during very high cycle fatigue tests, Acta Mater., (2008).

[83] Y. Lage, A. M. R. Ribeiro, D. Montalvão, L. Reis, and M. Freitas, Automation in Strain and Temperature Control on VHCF with an Ultrasonic Testing Facility, Appl. Autom. Technol. Fatigue Fract. Test. Anal., 80–100, (2014).

[84] K. Takahashi and T. Ogawa, Evaluation of giga-cycle fatigue properties of austenitic stainless steels using ultrasonic fatigue test, Nihon Kikai Gakkai Ronbunshu, A Hen/Transactions Japan Soc. Mech. Eng. Part A, **72**, 11, 1731–1736, (2006).

[85] M. Vieira, L. Reis, M. de Freitas, and A. Ribeiro, Preliminary evaluation of the loading characteristics of biaxial tests at low and very high frequencies, Procedia Struct. Integr., **1**, April, 205–211, (2016).

[86] S. Heinz, F. Balle, G. Wagner, and D. Eifler, Analysis of fatigue properties and failure mechanisms of Ti6Al4V in the very high cycle fatigue regime using ultrasonic

technology and 3D laser scanning vibrometry, Ultrasonics, **53**, 8, 1433–1440, (2013).

[87] P. R. da Costa, M. Sardinha, L. Reis, M. Freitas, and M. Fonte, Ultrasonic fatigue testing in as-built and polished Ti6Al4V alloy manufactured by SLM, Forces Mech., **4**, May, 100024, (2021).

[88] J. Petit, Z. Jiang, O. Polit, and T. Palin-Luc, Optimisation of an ultrasonic torsion fatigue system for high strength materials, Int. J. Fatigue, **151**, July, 106395, (2021).

[89] W. Cui, X. Chen, C. Chen, L. Cheng, J. Ding, and H. Zhang, Very high cycle fatigue (VHCF) characteristics of carbon fiber reinforced plastics(CFRP) under ultrasonic loading, Materials (Basel)., **13**, 4, (2020).

[90] H. Mayer, Recent developments in ultrasonic fatigue, *Fatigue and Fracture of Engineering Materials and Structures*, **39**, 1. Blackwell Publishing Ltd, 3–29, (2016).

[91] M. Vieira, M. De Freitas, L. Reis, A. M. R. Ribeiro, and M. Da Fonte, Development of a very high cycle fatigue (VHCF) multiaxial testing device, Frat. ed Integrita Strutt., **10**, 37, 131–137, (2016).

[92] P. R. da Costa, D. Montalvão, M. Freitas, R. Baxter, and L. Reis, Cruciform specimens' experimental analysis in ultrasonic fatigue testing, Fatigue Fract. Eng. Mater. Struct., **42**, 11, 2496–2508, (2019).

[93] M. Vieira, L. Reis, M. Freitas, and A. Ribeiro, Strain measurements on specimens subjected to biaxial ultrasonic fatigue testing, Theor. Appl. Fract. Mech., **85**, 2–8, (2016).

[94] S. E. Stanzl-Tschegg, Influence of material properties and testing frequency on VHCF and HCF lives of polycrystalline copper, Int. J. Fatigue, **105**, September, 86–96, (2017).

[95] D. Backe, F. Balle, and D. Eifler, Fatigue testing of CFRP in the very high cycle fatigue (VHCF) regime at ultrasonic frequencies, Compos. Sci. Technol., **106**, 93–99, (2015).

[96] M. Baaske, A. Illgen, A. Weidner, H. Biermann, and F. Ballani, Influence of ceramic particles and fibre reinforcement in metal matrix composites on the VHCF behaviour. Part II: Stochastic modelling and statistical inference, Fatigue Mater. Very High Numbers Load. Cycles, 319–342, (2018).

[97] A. Illgen, M. Baaske, F. Ballani, A. Weidner, and H. Biermann, Influence of ceramic particles and fibre reinforcement in metal matrix composites on the VHCF behaviour. Part I: Stochastic modelling and statistical inference, Fatigue Mater. Very High Numbers

Load. Cycles, 296–318, (2018).

[98] G. Just, I. Koch, and M. Gude, Characterisation and modelling of the inter-fibre cracking behaviour of CFRP up to very high cycles, Fatigue Mater. Very High Numbers Load. Cycles, 607–628, (2018).

[99] A. Tridello, VHCF response of two AISI H13 steels : effect of manufacturing process and size-effect, Metals (Basel)., **9**, 133, (2019).

[100] H. Mayer, M. Fitzka, and R. Schuller, Constant and variable amplitude ultrasonic fatigue of 2024-T351 aluminium alloy at different load ratios, Ultrasonics, (2013).

[101] M. Cremer, M. Zimmermann, and H. J. Christ, High-frequency cyclic testing of welded aluminium alloy joints in the region of very high cycle fatigue (VHCF), Int. J. Fatigue, **57**, 120–130, (2013).

[102] Q. Y. Wang, T. Lib, and X. G. Zenga, Gigacycle fatigue behavior of high strength aluminum alloys, Procedia Eng., **2**, 1, 65–70, (2010).

[103] S. Stanzl-Tschegg, H. Mughrabi, and B. Schoenbauer, Life time and cyclic slip of copper in the VHCF regime, Int. J. Fatigue, **29**, 9–11, 2050–2059, (2007).

[104] V. Favier *et al.*, Very high cycle fatigue for single phase ductile materials: Comparison between α-iron, copper and α-brass polycrystals, Int. J. Fatigue, **93**, 326–338, (2016).

[105] A. Weidner, D. Amberger, F. Pyczak, B. Schönbauer, S. Stanzl-Tschegg, and H. Mughrabi, Fatigue damage in copper polycrystals subjected to ultrahigh-cycle fatigue below the PSB threshold, Int. J. Fatigue, **32**, 6, 872–878, (2010).

[106] M. Fitzka *et al.*, Ultrasonic fatigue testing of concrete, Ultrasonics, **116**, October 2020, 0–9, (2021).

[107] H. Q. Xue, H. Tao, F. Montembault, Q. Y. Wang, and C. Bathias, Development of a three-point bending fatigue testing methodology at 20 kHz frequency, Int. J. Fatigue, **29**, 2085–2093, (2007).

[108] S. E. Stanzl-Tschegg, H. R. Mayer, and E. K. Tschegg, High frequency method for torsion fatigue testing, Ultrasonics, **31**, 4, 275–280, (1993).

[109] W. Hoffelner, Fatigue crack growth at 20 kHz - A new technique, J. Phys. E., **13**, 6, 617–619, (1980).

[110] W. Reß, G. Khatibi, B. Weiss, and V. Gröger, An ultrafast mechanical test system for bending fatigue studies of multilayered electronic components, 2012 4th Electron. Syst. Technol. Conf. ESTC 2012, October 2016, (2012).

[111] T. J. Adam and P. Horst, Experimental investigation of the very high cycle fatigue of GFRP [90/0]s cross-ply specimens subjected to high-frequency four-point bending, Compos. Sci. Technol., **101**, 62–70, (2014).

[112] I. Marines-Garcia, J. P. Doucet, and C. Bathias, Development of a new device to perform torsional ultrasonic fatigue testing, Int. J. Fatigue, **29**, 9–11, 2094–2101, (2007).

[113] E. Bayraktar and H. Xue, Torsional fatigue behaviour and damage mechanisms in the very high cycle regime, Arch. Mater. …, **43**, 2, 77–86, (2010).

[114] H. Q. Xue and C. Bathias, Crack path in torsion loading in very high cycle fatigue regime, Eng. Fract. Mech., **77**, 11, 1866–1873, (2010).

[115] H. Q. Xue, E. Bayraktar, I. Marines-garcia, and C. Bathias, Torsional fatigue behaviour in gigacycle regime and damage mechanism of the perlitic steel, Manuf. Eng., **31**, 2, 391–397, (2008).

[116] A. Nikitin, C. Bathias, and T. Palin-Luc, A new piezoelectric fatigue testing machine in pure torsion for ultrasonic gigacycle fatigue tests: Application to forged and extruded titanium alloys, Fatigue Fract. Eng. Mater. Struct., **38**, 11, 1294–1304, (2015).

[117] Y. Shimamura *et al.*, Fatigue properties of carburized alloy steel in very high cycle regime under torsional loading, Int. J. Fatigue, **60**, 57–62, (2014).

[118] H. Mayer, Ultrasonic torsion and tension-compression fatigue testing: Measuring principles and investigations on 2024-T351 aluminium alloy, Int. J. Fatigue, **28**, 11, 1446–1455, (2006).

[119] R. Schuller, H. Mayer, A. Fayard, M. Hahn, and M. Bacher-Höchst, Very high cycle fatigue of VDSiCr spring steel under torsional and axial loading, Materwiss. Werksttech., **44**, 4, 282–289, (2013).

[120] Y. Akiniwa, S. Stanzl-Tschegg, H. Mayer, M. Wakita, and K. Tanaka, Fatigue strength of spring steel under axial and torsional loading in the very high cycle regime, Int. J. Fatigue, **30**, 12, 2057–2063, (2008).

[121] T. Sakai, Y. Sato, Y. Nagano, M. Takeda, and N. Oguma, Effect of stress ratio on long

life fatigue behavior of high carbon chromium bearing steel under axial loading, Int. J. Fatigue, **28**, 11, 1547–1554, (2006).

[122] Z. Y. Huang, H. Q. Liu, H. M. Wang, D. Wagner, M. K. Khan, and Q. Y. Wang, Effect of stress ratio on VHCF behavior for a compressor blade titanium alloy, Int. J. Fatigue, **93**, 232–237, (2016).

[123] F. Ritz and T. Beck, Influence of mean stress and notches on the very high cycle fatigue behaviour and crack initiation of a low-pressure steam turbine steel, Fatigue Fract. Eng. Mater. Struct., **40**, 11, 1762–1771, (2017).

[124] S. Kovacs, T. Beck, and L. Singheiser, Influence of mean stresses on fatigue life and damage of a turbine blade steel in the VHCF-regime, Int. J. Fatigue, (2013).

[125] H. Mayer, M. Fitzka, and R. Schuller, Constant and variable amplitude ultrasonic fatigue of 2024-T351 aluminium alloy at different load ratios, Ultrasonics, **53**, 8, 1425–1432, (2013).

[126] M. Sander, T. Müller, and C. Stäcker, Very high cycle fatigue behavior under constant and variable amplitude loading, Procedia Struct. Integr., **2**, 34–41, (2016).

[127] H. Mayer *et al.*, Cyclic torsion very high cycle fatigue of VDSiCr spring steel at different load ratios, Int. J. Fatigue, **70**, 322–327, (2015).

[128] Y. Furuya, K. Kobayashi, M. Hayakawa, M. Sakamoto, Y. Koizumi, and H. Harada, High-temperature ultrasonic fatigue testing of single-crystal superalloys, Mater. Lett., (2012).

[129] D. Wagner, F. J. Cavalieri, C. Bathias, and N. Ranc, Ultrasonic fatigue tests at high temperature on an austenitic steel, Propuls. Power Res., (2012).

[130] X. Zhu, A. Shyam, J. W. Jones, H. Mayer, J. V. Lasecki, and J. E. Allison, Effects of microstructure and temperature on fatigue behavior of E319-T7 cast aluminum alloy in very long life cycles, Int. J. Fatigue, **28**, 11, 1566–1571, (2006).

[131] T. Y. Wu, G. Jago, J. Bechet, C. Bathias, and D. Guichard, Accelerated vibratory fatigue test by ultrasonic frequency at cryogenic temperature, Eng. Fract. Mech., (1996).

[132] R. Pérez-Mora, T. Palin-Luc, C. Bathias, and P. C. Paris, Very high cycle fatigue of a high strength steel under sea water corrosion: A strong corrosion and mechanical damage coupling, Int. J. Fatigue, **74**, 156–165, (2015).

[133] R. Ebara, Corrosion fatigue crack initiation in 12% chromium stainless steel, Mater. Sci. Eng. A, **468–470**, SPEC. ISS., 109–113, (2007).

[134] T. Palin-Luc, R. Pérez-Mora, C. Bathias, G. Domínguez, P. C. Paris, and J. L. Arana, Fatigue crack initiation and growth on a steel in the very high cycle regime with sea water corrosion, Eng. Fract. Mech., **77**, 11, 1953–1962, (2010).

[135] S. Stanzl-Tschegg and B. Schönbauer, Near-threshold fatigue crack propagation and internal cracks in steel, in *Procedia Engineering*, (2010).

[136] U. Karr, A. Stich, and H. Mayer, Very high cycle fatigue of wrought magnesium alloy AZ61, in *Procedia Structural Integrity*, (2016).

[137] Y. Murakami, T. Nomoto, and T. Ueda, Factors influencing the mechanism of superlong fatigue failure in steels, Fatigue Fract. Eng. Mater. Struct., **22**, 7, 581–590, (1999).

[138] R. W. Neu, Progress in standardization of fretting fatigue terminology and testing, Tribol. Int., **44**, 11, 1371–1377, (2011).

[139] Z. D. Sun, C. Bathias, and G. Baudry, Fretting fatigue of 42CrMo4 steel at ultrasonic frequency, Int. J. Fatigue, **23**, 5, 449–453, (2001).

[140] P. F. Filgueiras, C. Bathias, E. S. Palma, and C. Wang, Inducing very high cycle fretting-fatigue in the ultrasonic regime, Tribol. Int., (2014).

[141] A. Amanov, I. S. Cho, D. E. Kim, and Y. S. Pyun, Fretting wear and friction reduction of CP titanium and Ti-6Al-4V alloy by ultrasonic nanocrystalline surface modification, Surf. Coatings Technol., **207**, 135–142, (2012).

[142] C. E. Philips and R. B. Heywood, The size effect in fatigue of plain and notched steel specimens loaded under reversed direct stress, Proc. Inst. Mech. Eng., **165**, 113, (1951).

[143] Y. Lee, J. Pan, R. Hathaway, and M. Barkey, Fatigue testing and analysis - theory and practice. Elsevier, (2005).

[144] M. Shirani and G. Härkegård, Fatigue life distribution and size effect in ductile cast iron for wind turbine components, Eng. Fail. Anal., **18**, 1, 12–24, (2011).

[145] J. Pegues, M. Roach, R. Scott Williamson, and N. Shamsaei, Volume effects on the fatigue behavior of additively manufactured Ti-6Al4V parts, Solid Free. Fabr. 2018 Proc. 29th Annu. Int. Solid Free. Fabr. Symp. - An Addit. Manuf. Conf. SFF 2018, 1373–1381, (2020).

[146] Y. Furuya, Specimen size effects on gigacycle fatigue properties of high-strength steel under ultrasonic fatigue testing, Scr. Mater., **58**, 11, 1014–1017, (2008).

[147] D. S. Paolino, A. Tridello, G. Chiandussi, and M. Rossetto, On specimen design for size effect evaluation in ultrasonic gigacycle fatigue testing, Fatigue Fract. Eng. Mater. Struct., **37**, 5, 570–579, (2014).

[148] Y. Furuya, Notable size effects on very high cycle fatigue properties of high-strength steel, Mater. Sci. Eng. A, **528**, 15, 5234–5240, (2011).

[149] A. Tridello *et al.*, VHCF response of heat-treated SLM Ti6Al4V Gaussian specimens with large loaded volume, Procedia Struct. Integr., **18**, 314–321, (2019).

[150] H. Xue, Z. Sun, X. Zhang, T. Gao, and Z. Li, Very High Cycle Fatigue of a Cast Aluminum Alloy : Size Effect and Crack Initiation, J. Mater. Eng. Perform., **27**, 10, 5406–5416, (2018).

[151] R. G. Davies and C. L. Magee, The effect of strain-rate upon the tensile deformation of materials, J. Eng. Mater. Technol. Trans. ASME, **97**, 2, 151–155, (1975).

[152] L. Krüger, S. Wolf, U. Martin, P. Scheller, A. Jahn, and A. Weiß, Strain rate and temperature effects on stress-strain behaviour of cast high alloyed CrMnNi-steel, May, 1069–1074, (2009).

[153] C. F. Jenkin, High-Frequency Fatigue Tests., Proc. R. Soc., **109**, 119–143, (1925).

[154] C. F. Jenkin and G. D. Lehmann, High Frequency Fatigue, R. Soc., **125**, 796, (1929).

[155] M. Kikukawa, K. Ohji, and K. Ogura, Push-pull fatigue strength of mild steel at very high frequencies of stress up to 100 kc/s, J. Basic Eng., **87**, 4, 857–864, (1965).

[156] N. J. Myung and N. S. Choi, Dynamic stress analysis of the specimen gauge portion with a circular profile for the ultrasonic fatigue test, Int. J. Fatigue, **92**, 71–77, (2016).

[157] D. F. Pessoa, G. Kirchhoff, and M. Zimmermann, Influence of loading frequency and role of surface micro-defects on fatigue behavior of metastable austenitic stainless steel AISI 304, Int. J. Fatigue, **103**, 48–59, (2017).

[158] J. Bach, M. Göken, and H.-W. Höppel, Fatigue of low alloyed carbon steels in the HCF/VHCF-regimes, Fatigue Mater. Very High Numbers Load. Cycles, 1–23, (2018).

[159] N. Tsutsumi, Y. Murakami, and V. Doquet, Effect of test frequency on fatigue strength

of low carbon steel, Fatigue Fract. Eng. Mater. Struct., **32**, 6, 473–483, (2009).

[160] I. Nonaka, S. Setowaki, and Y. Ichikawa, Effect of load frequency on high cycle fatigue strength of bullet train axle steel, Int. J. Fatigue, **60**, 43–47, (2014).

[161] B. Zettl, H. Mayer, C. Ede, and S. Stanzl-Tschegg, Very high cycle fatigue of normalized carbon steels, Int. J. Fatigue, **28**, 11, 1583–1589, (2006).

[162] B. Guennec, A. Ueno, T. Sakai, M. Takanashi, and Y. Itabashi, Effect of the loading frequency on fatigue properties of JIS S15C low carbon steel and some discussions based on micro-plasticity behavior, Int. J. Fatigue, (2014).

[163] Y. Furuya, S. Matsuoka, T. Abe, and K. Yamaguchi, Gigacycle fatigue properties for high-strength low-alloy steel at 100 Hz, 600 Hz, and 20 kHz, Scr. Mater., **46**, 2, 157–162, (2002).

[164] N. Schneider, J. Bödecker, C. Berger, and M. Oechsner, Frequency effect and influence of testing technique on the fatigue behaviour of quenched and tempered steel and aluminium alloy, Int. J. Fatigue, **93**, 224–231, (2016).

[165] A. Zhao, J. Xie, C. Sun, Z. Lei, and Y. Hong, Effects of strength level and loading frequency on very-high-cycle fatigue behavior for a bearing steel, Int. J. Fatigue, (2012).

[166] J. Bach, H. W. Höppel, E. Bitzek, and M. Göken, Influence of specimen geometry on temperature increase during ultrasonic fatigue testing, Ultrasonics, **53**, 8, 1412–1416, (2013).

[167] Y. B. Liu *et al.*, Thermal effect of bainite/martensite duplex-phase steel under ultrasonic fatigue testing, J. Mater. Sci., **45**, 10, 2553–2557, (2010).

[168] P. Starke, F. Walther, and D. Eifler, PHYBAL-A new method for lifetime prediction based on strain, temperature and electrical measurements, Int. J. Fatigue, (2006).

[169] V. Wagner, P. Starke, E. Kerscher, and D. Eifler, Cyclic deformation behaviour of railway wheel steels in the very high cycle fatigue (VHCF) regime, Int. J. Fatigue, (2011).

[170] S. Suresh and R. O. Ritchie, Near-Threshold Fatigue Crack Propagation: a Perspective on the Role of Crack Closure, Fatigue Crack Growth Threshold Concepts, 227–261, (1984).

[171] Y. Akiniwa, K. Tanaka, and H. Kimura, Microstructural effects on crack closure and

propagation thresholds of small fatigue cracks, Fatigue Fract. Eng. Mater. Struct., **24**, 12, 817–829, (2001).

[172] Y. Murakami, M. Takada, and T. Toriyama, Super-long life tension-compression fatigue properties of quenched and tempered 0.46% carbon steel, Int. J. Fatigue, **20**, 9, 661–667, (1998).

[173] Y. Furuya, T. Abe, and S. Matsuoka, 1010-cycle fatigue properties of 1800 MPa-class JIS-SUP7 spring steel, Fatigue Fract. Eng. Mater. Struct., **26**, 7, 641–645, (2003).

[174] L. T. Lu, J. W. Zhang, and K. Shiozawa, Influence of inclusion size on S-N curve characteristics of high strength steels in the gigacycle fatigue regime, Int. J. Fatigue, **29**, 8, 765–771, (2007).

[175] T. Makino, The effect of inclusion geometry according to forging ratio and metal flow direction on very high-cycle fatigue properties of steel bars, Int. J. Fatigue, (2008).

[176] Y. Murakami and M. Endo, Effects of defects, inclusions and inhomogeneities on fatigue strength, Int. J. Fatigue, **16**, 3, 163–182, (1994).

[177] Y. Murakami and M. Endo, Effects of hardness and Crack Geometries on ΔKth of Small Cracks Emanating from Small De, *The Behaviour of Short Cracks*, **1**. 275–293, (1986).

[178] Q. Jiang, C. Sun, X. Liu, and Y. Hong, Very-high-cycle fatigue behavior of a structural steel with and without induced surface defects, Int. J. Fatigue, **93**, 352–362, (2016).

[179] Y. Murakami, H. Matsunaga, A. Abyazi, and Y. Fukushima, Defect size dependence on threshold stress intensity for high-strength steel with internal hydrogen, Fatigue Fract. Eng. Mater. Struct., **36**, 9, 836–850, (2013).

[180] Z. Xu, W. Wen, and T. Zhai, Effects of pore position in depth on stress/strain concentration and fatigue crack initiation, Metall. Mater. Trans. A Phys. Metall. Mater. Sci., **43**, 8, 2763–2770, (2012).

[181] K. Shiozawa, Y. Morii, S. Nishino, and L. Lu, Subsurface crack initiation and propagation mechanism in high-strength steel in a very high cycle fatigue regime, Int. J. Fatigue, (2006).

[182] T. Sakai, Y. Sato, and N. Oguma, Characteristics S-N properties of high-carbon-chromium-bearing steel under axial loading in long-life fatigue, Fatigue Fract. Eng. Mater. Struct., **25**, 8–9, 765–773, (2002).

[183] Y. Murakami, N. N. Yokoyama, and J. Nagata, Mechanism of fatigue failure in ultralong life regime, Fatigue Fract. Eng. Mater. Struct., **25**, 8–9, 735–746, (2002).

[184] K. Shiozawa, L. Lu, and S. Ishihara, S-N curve characteristics and subsurface crack initiation behaviour in ultra-long life fatigue of a high carbon-chromium bearing steel, Fatigue Fract. Eng. Mater. Struct., **24**, 12, 781–790, (2001).

[185] K. Tanaka and Y. Akiniwa, Fatigue crack propagation behaviour derived from S-N data in very high cycle regime, Fatigue Fract. Eng. Mater. Struct., **25**, 8–9, 775–784, (2002).

[186] Y. Murakami, T. Nomoto, T. Ueda, and Y. Murakami, On the mechanism of fatigue failure in the superlong life regime (N>107 cycles). Part I: Influence of hydrogen trapped by inclusions, Fatigue Fract. Eng. Mater. Struct., **23**, 11, 893–902, (2000).

[187] J. W. E. Society, Standard method for ultrasonic fatigue test in metallic materials, WES 1112, (2017).

[188] Y. Furuya and E. Takeuchi, Gigacycle fatigue properties of Ti-6Al-4V alloy under tensile mean stress, Mater. Sci. Eng. A, **598**, 135–140, (2014).

[189] Y. Lage, A. M. R. Ribeiro, D. Montalvão, L. Reis, and M. Freitas, Automation in Strain and Temperature Control on VHCF with an Ultrasonic Testing Facility, Appl. Autom. Technol. Fatigue Fract. Test. Anal., 80–100, (2014).

[190] L. Du, G. Qian, L. Zheng, and Y. Hong, Influence of processing parameters of selective laser melting on high-cycle and very-high-cycle fatigue behaviour of Ti-6Al-4V, Fatigue Fract. Eng. Mater. Struct., **44**, 1, 240–256, (2021).

[191] A. Grigorescu, P.-M. Hilgendorff, M. Zimmermann, C.-P. Fritzen, and H.-J. Christ, Fatigue behaviour of austenitic stainless steels in the VHCF regime, Fatigue Mater. Very High Numbers Load. Cycles, 49–71, (2018).

[192] Y. Gu, C. Tao, Y. He, and C. Liu, The effect of frequency and sample shape on fatigue behaviors of DZ125 superalloy, Theor. Appl. Mech. Lett., **2**, 3, 031009, (2012).

[193] C. Brugger, T. Palin-Luc, P. Osmond, and M. Blanc, Gigacycle fatigue behavior of a cast aluminum alloy under biaxial bending: experiments with a new piezoelectric fatigue testing device, 21st Eur. Conf. Fract. ECF21, **2**, 96–100, (2016).

[194] P. R. da Costa, Estudo e desenvolvimento de novos componentes de uma máquina de VHCF em regime multiaxial, Universidade de Lisboa, Instituto Superior Técnico,

(2017).

[195] P. Costa, M. Vieira, L. Reis, A. Ribeiro, and M. de Freitas, New specimen and horn design for combined tension and torsion ultrasonic fatigue testing in the very high cycle fatigue regime, Int. J. Fatigue, **103**, 248–257, (2017).

[196] P. R. da Costa, H. Soares, L. Reis, and M. Freitas, Ultrasonic fatigue testing under multiaxial loading on a railway steel, Int. J. Fatigue, **136**, March, 105581, (2020).

[197] D. Montalvão and A. Wren, Redesigning axial-axial (biaxial) cruciform specimens for very high cycle fatigue ultrasonic testing machines, Heliyon, **3**, 11, e00466, (2017).

[198] D. Montalvão, A. Blaskovics, P. R. da Costa, L. Reis, and M. Freitas, Numerical Analysis of VHCF Cruciform Test Specimens with Non-Unitary Biaxiality Ratios, Int. J. Comput. Methods Exp. Meas., **7**, 4, 327–339, (2019).

[199] L. E. Murr *et al.*, Metal Fabrication by Additive Manufacturing Using Laser and Electron Beam Melting Technologies, J. Mater. Sci. Technol., **28**, 1, 1–14, (2012).

[200] L. Thijs, F. Verhaeghe, T. Craeghs, J. Van Humbeeck, and J. P. Kruth, A study of the microstructural evolution during selective laser melting of Ti-6Al-4V, Acta Mater., **58**, 9, 3303–3312, (2010).

[201] K. Hoffmann, An Introduction to Measurements using Strain Gages. Hottinger Baldwin Messtechnik GmbH, Darmstadt, (1989).

[202] S. S. Rao, Mechanical Vibrations, 6th Global. Pearson, (2018).

[203] R. Brincker and L. Zhang, Frequency Domain Decomposition Revisited, Proc. 3rd Int. Oper. Modal Anal. Conf., (2009).

[204] R. Brincker, C. E. Ventura, and P. Andersen, Damping estimation by frequency domain decomposition, Conf. IMAC2001 A Conf. Struct. Dyn., **1**, 698–703, (2001).

[205] L. Zhang, T. Wang, and Y. Tamura, A frequency-spatial domain decomposition (FSDD) method for operational modal analysis, Mech. Syst. Signal Process., **24**, 5, 1227–1239, (2010).

[206] T. Müller and M. Sander, On the use of ultrasonic fatigue testing technique - Variable amplitude loadings and crack growth monitoring, Ultrasonics, **53**, 8, 1417–1424, (2013).

[207] A. Tridello, D. S. Paolino, G. Chiandussi, and M. Rossetto, Effect of electroslag

remelting on the VHCF response of an AISI H13 steel, Fatigue Fract. Eng. Mater. Struct., **40**, 11, 1783–1794, (2017).

[208] Y. Yu, J. L. Gu, L. Xu, F. L. Shou, B. Z. Bai, and Y. B. Liu, Very high cycle fatigue behaviors of Mn-Si-Cr series Bainite/Martensite dual phase steels, Mater. Des., (2010).

[209] J. Günther *et al.*, Fatigue life of additively manufactured Ti–6Al–4V in the very high cycle fatigue regime, Int. J. Fatigue, **94**, 236–245, (2017).

[210] E. Wycisk, S. Siddique, D. Herzog, F. Walther, and C. Emmelmann, Fatigue performance of laser additive manufactured Ti–6Al–4V in very high cycle fatigue regime up to 10 9 cycles, Front. Mater., **2**, December, 2–9, (2015).

[211] H. Yu, F. Li, Z. Wang, and X. Zeng, Fatigue performances of selective laser melted Ti-6Al-4V alloy: Influence of surface finishing, hot isostatic pressing and heat treatments, Int. J. Fatigue, **120**, July 2018, 175–183, (2019).

[212] G. Qian, Y. Li, D. S. Paolino, A. Tridello, F. Berto, and Y. Hong, Very-high-cycle fatigue behavior of Ti-6Al-4V manufactured by selective laser melting: Effect of build orientation, Int. J. Fatigue, **136**, March, 105628, (2020).

[213] Z. Xiao *et al.*, Study of residual stress in selective laser melting of Ti6Al4V, Mater. Des., **193**, 108846, (2020).

[214] C. Casavola, S. L. Campanelli, and C. Pappalettere, Preliminary investigation on distribution of residual stress generated by the selective laser melting process, J. Strain Anal. Eng. Des., **44**, 1, 93–104, (2009).

[215] M. Shiomi, K. Osakada, K. Nakamura, T. Yamashita, and F. Abe, Residual stress within metallic model made by selective laser melting process, CIRP Ann. - Manuf. Technol., **53**, 1, 195–198, (2004).

[216] A. K. Syed *et al.*, An experimental study of residual stress and direction-dependence of fatigue crack growth behaviour in as-built and stress-relieved selective-laser-melted Ti6Al4V, Mater. Sci. Eng. A, **755**, April, 246–257, (2019).

[217] D. Infante-García, G. Qian, H. Miguélez, and E. Giner, Analysis of the effect of out-of-phase biaxial fatigue loads on crack paths in cruciform specimens using XFEM, Int. J. Fatigue, **123**, January, 87–95, (2019).

[218] E. U. Lee and R. E. Taylor, Fatigue behavior of aluminum alloys under biaxial loading,

Eng. Fract. Mech., **78**, 8, 1555–1564, (2011).

[219] C. H. Wolf, S. Henkel, A. Burgold, Y. Qiu, M. Kuna, and H. Biermann, Investigation of fatigue crack growth under in-phase loading as well as phase-shifted loading using cruciform specimens, Int. J. Fatigue, **124**, February, 595–617, (2019).

[220] R. K. Neerukatti, S. Datta, A. Chattopadhyay, N. Iyyer, and N. Phan, Fatigue crack propagation under in-phase and out-of-phase biaxial loading, Fatigue Fract. Eng. Mater. Struct., **41**, 2, 387–399, (2018).

[221] A. Barroso, E. Correa, J. Freire, and F. París, A Device for Biaxial Testing in Uniaxial Machines. Design, Manufacturing and Experimental Results Using Cruciform Specimens of Composite Materials, Exp. Mech., **58**, 1, 49–53, (2018).

Annex

A.1 Ultrasonic Analytical Solutions

All analytical calculations in their respective sequence are shown for the ultrasonic uniaxial fatigue testing in tension-compression and pure torsion.

Tension – Compression

From the material under testing static properties, the wave propagation c is first determined.

$$c = \sqrt{\frac{E}{\rho}} \tag{A.1}$$

From c:

$$k = \frac{w}{c} = \frac{2\pi f}{c} \tag{A.2}$$

The pretended specimen geometry must be established and then determined. Two different curvature geometries are possible: (A) Hyperbolic Curvature; (B) Exponential Curvature.

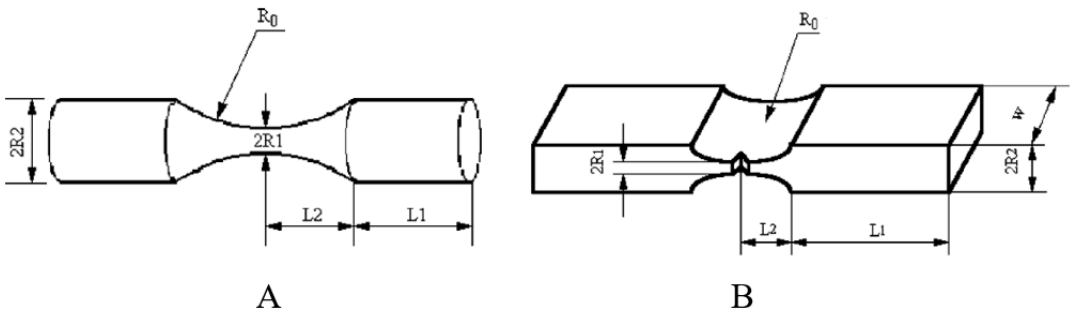

Figure A-8-1. Uniaxial tensile ultrasonic fatigue curved specimens and respective dimensional variables: (A) hyperbolic curvature; (B) exponential curvature [71].

The user first establishes L2, R1 and R2. L1 is analytically determined. Each curvature has its analytical solution.

Hyperbolic Curvature

L1 dimension determination:

$$\alpha = \frac{1}{L_2} arccosh(\frac{R_2}{R_1}) \tag{A.3}$$

$$\beta = \sqrt{\alpha^2 - k^2} \tag{A.4}$$

$$\varphi(L_1, L_2) = \frac{\cos(kL_1)\cosh(\alpha L_2)}{\sinh(\beta L_2)} \tag{A.5}$$

$$L_1 = \frac{1}{k}\arctan\left\{\frac{1}{k}[\beta \coth(\beta L_2) - \alpha\tanh(\alpha L_2)]\right\} \tag{A.6}$$

Displacement distribution:

$$\begin{cases} U(x) = A_0 \cdot \varphi(L_1, L_2)\frac{\sinh(\beta x)}{cosh(\alpha x)}, for\ x < L_2 \\ U(x) = A_0 \sin\big(k(L-x)\big), for\ L_2 < x < L \end{cases} \tag{A.7}$$

Strain distribution:

$$\begin{cases} \varepsilon(x) = A_0 \cdot \varphi(L_1, L_2)\left[\frac{\beta\cosh(\beta x)\cdot\cosh(\alpha x) - \alpha\sinh(\beta x)\cdot\sinh(\alpha x)}{cosh^2(x\alpha)}\right], for\ x < L_2 \\ \varepsilon(x) = k \cdot A_0 \sin\big(k(L-x)\big), \qquad for\ L_2 < x < L \end{cases} \tag{A.8}$$

Stress distribution:

$$\sigma(x) = E\ \varepsilon(x) \tag{A.9}$$

$$\begin{cases} \sigma(x) = E \cdot A_0 \cdot \varphi(L_1, L_2)\left[\frac{\beta\cosh(\beta x)\cdot\cosh(\alpha x) - \alpha\sinh(\beta x)\cdot\sinh(\alpha x)}{cosh^2(\alpha x)}\right]\ for\ x \le L_2 \\ \sigma(x) = E \cdot k \cdot A_0 \sin\big(k(L-x)\big), \qquad for\ L_2 < x \le L \end{cases} \tag{A.10}$$

Exponential Curvature

L1 dimension determination:

$$\alpha = \frac{1}{2L_2}\ln(\frac{R_2}{R_1}) \tag{A.11}$$

$$\beta = \sqrt{\alpha^2 - k^2} \tag{A.12}$$

$$\varphi(L_1, L_2) = \frac{\cos(kL_1)\exp(\alpha L_2)}{\sinh(\beta L_2)} \tag{A.13}$$

$$L_1 = \frac{1}{k}\arctan\left\{\frac{1}{k}[\beta\coth(\beta L_2) - \alpha]\right\} \tag{A.14}$$

Displacement distribution:

$$\begin{cases} \mathrm{U(x)} = \mathrm{A_0}\cdot\varphi(\mathrm{L_1},\mathrm{L_2})\cdot sinh(\beta x)\cdot exp\ (-\alpha x), \text{for } \mathrm{x} < \mathrm{L_2} \\ \mathrm{U(x)} = \mathrm{A_0}\cdot\cos\big(\mathrm{k(L-x)}\big) \quad , \text{for } \mathrm{L_2} < \mathrm{x} < \mathrm{L} \end{cases} \tag{A.15}$$

Strain distribution:

$$\begin{cases} \varepsilon(x) = A_0\cdot\varphi(L_1,L_2)[\beta\cosh(\beta x) - \alpha\sinh(\beta x)]\exp(-\alpha x)\,, \ for\ x \le L_2 \\ \varepsilon(x) = k\cdot A_0\sin\big(k(L-x)\big)\,, \quad for\ L_2 < x \le L \end{cases} \tag{A.16}$$

Stress distribution:

$$\begin{cases} \sigma(x) = E\cdot A_0\cdot\varphi(L_1,L_2)[\beta\cosh(\beta x) - \alpha\sinh(\beta x)]\exp(-\alpha x)\,, \ for\ x \le L_2 \\ \sigma(x) = E\cdot k\cdot A_0\sin\big(k(L-x)\big)\,, \quad for\ L_2 < x \le L \end{cases} \tag{A.17}$$

Pure Torsion

A similar sequence is followed for pure torsion specimens. The rotational wave propagation c is first determined from the material under testing static properties.

$$c = \sqrt{\frac{G}{\rho}} \tag{A.18}$$

From c:

$$k = \frac{w}{c} = \frac{2\pi f}{c} \tag{A.19}$$

For pure torsional specimens, only the hyperbolic curvature specimen has an analytical solution. The same dimension designations of tension-compression specimens are followed.

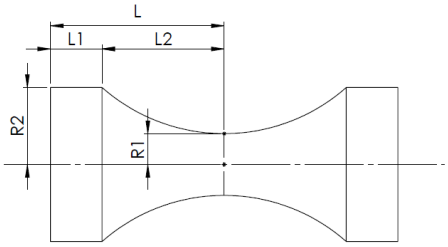

Figure A-8-2. Uniaxial pure torsion ultrasonic fatigue dimensional variable designations.

L1 dimension determination:

$$\alpha = \frac{1}{L_2} arccosh(\frac{{R_2}^2}{{R_1}^2}) \tag{A.20}$$

$$\beta = \sqrt{\alpha^2 - k^2} \tag{A.21}$$

$$\varphi(L_1, L_2) = \frac{\cos(kL_1)\cosh(\alpha L_2)}{\sinh(\beta L_2)} \tag{A.22}$$

$$L_1 = \frac{1}{K} arctan\left\{\frac{1}{K}\left[\frac{\beta}{\tanh(\beta L_2)} - \alpha\tanh(\alpha L_2)\right]\right\} \tag{A.23}$$

Displacement distribution:

$$\begin{cases} U(x) = A_{0r} \cdot R_1 \cdot \varphi(L_1, L_2)\left[\frac{\sqrt{\cosh(\alpha x)}\sinh(\beta x)}{\cosh(\alpha x)}\right], for\ x < L_2 \\ U(x) = A_{0r} \cdot R_2 \cos\big(k(L-x)\big) \quad , for\ L_2 < x < L \end{cases} \tag{A.24}$$

Stress distribution:

$$\begin{cases} \sigma(x) = GA_{0r}R_1\varphi(L_1, L_2)\left[\frac{\sqrt{\cosh(\alpha x)}[\beta\cosh(\beta x)\cosh(\alpha x) - \alpha\sinh(\beta x)\sinh(\alpha x)]}{cosh^2(\alpha x)}\right], for\ x \le L_2 \\ \sigma(x) = \mathrm{G}A_{0r}R_2\sin\big(k(L-x)\big), \quad , for\ L_2 < x \le L \end{cases} \tag{A.25}$$

Tension-Torsion

The analytical solution for tension-torsion specimen is now described in sequence. First is established the method for a 20kHz 1ºlongitudinal and 3º torsional resonance mode geometry. The specimen geometry and respective dimensional designations are shown in Figure A-8-3.

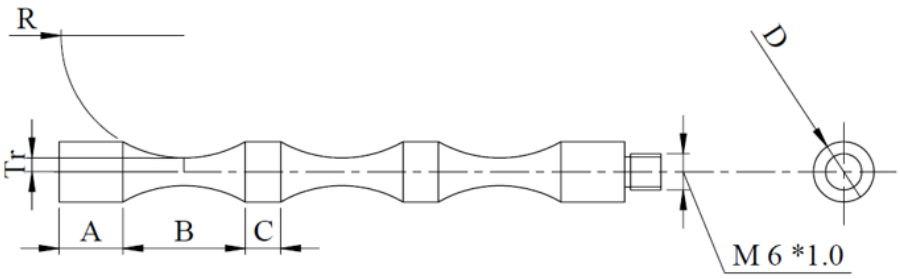

Figure A-8-3. Tension-torsion specimen dimension variables acronyms.

The method first divides the specimen into three sections, Ts1, Ts2 and Ts3. Each section represents a pure torsion specimen. The divided sections presented in chapter 3.4.2.4 Figure 3-34 are again shown in Figure A-8-4. Figure A-8-4 also represents the dimensional acronyms and the displacement (Dn) and stress (Sn) nodes.

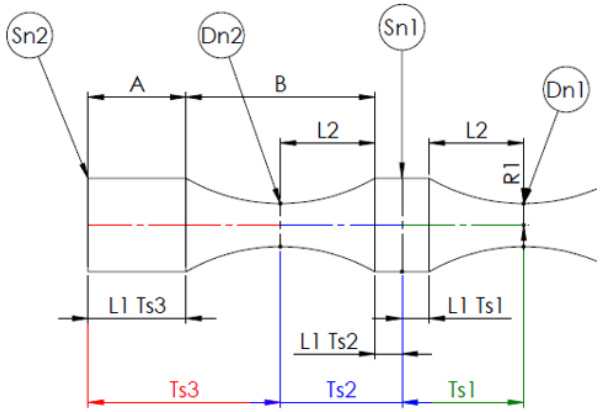

Figure A-8-4. Half a three throated new specimen rotational displacement distribution with stress and displacement nodes identification, key dimension designations, and three pure torsion section Ts.

The Ts-sliced half specimen sections were attributed to pure torsion specimens. The main throat section (Ts1) was proven to be a 20 kHz specimen. Meanwhile, the two secondary throat sections (Ts2 and Ts3) were associated with two pure torsion specimens with a combining 20 kHz mean frequency. Different combinations of Ts2 and Ts3 frequencies are possible. One example is to combine f=24000 Hz for Ts2 and f=16000 Hz for Ts3.

For $L_{1\ Ts1}$ determination the pure torsion analytical calculations are followed with a 20 kHz f frequency.

$$c = \sqrt{\frac{G}{\rho}} \tag{A.26}$$

$$k = \frac{w}{c} = \frac{2\pi f}{c} \tag{A.27}$$

$$\alpha = \frac{1}{(\frac{B}{2})} arccosh(\frac{(D/2)^2}{{T_r}^2}) \quad \text{(A.28)}$$

$$\beta = \sqrt{\alpha^2 - k^2} \quad \text{(A.29)}$$

$$L_{1\,Ts1} = \frac{1}{K} arctan\left\{\frac{1}{K}\left[\frac{\beta}{\tanh\,(\beta(\frac{B}{2}))} - \alpha\tanh\,(\alpha(\frac{B}{2}))\right]\right\} \quad \text{(A.30)}$$

$L_{1\,Ts2}$ and $L_{1\,Ts3}$ can be analytically determined from the following equation (A.26) to equation (A.30). The difference is in equation (A.27) applied frequency, *f*.

Only one Ts2 and Ts3 combination has a 20kHz longitudinal frequency. The hyperbolic curvature tension-compression L_1 determination sequence of equations are applied with B and Tr throat dimensions for an equivalent L_{axail} of a one throat specimen. Due to the secondary throats reduced stiffness, L_{axial} must be rectified. The first prediction for Ts2-Ts3 combination length is to consider 80% of the determined L_{axial}. The frequency combination of Ts2-Ts3 with the analytically determined 80% L_{axial} must be iteratively determined.

For the L_{axial} determination

$$c = \sqrt{\frac{E}{\rho}} \quad \text{(A.31)}$$

$$k = \frac{w}{c} = \frac{2\pi f}{c} \quad \text{(A.32)}$$

$$\alpha = \frac{1}{(\frac{B}{2})} arccosh(\frac{(\frac{D}{2})}{T_r}) \quad \text{(A.33)}$$

$$\beta = \sqrt{\alpha^2 - k^2} \quad \text{(A.34)}$$

$$L_{axial} = \frac{1}{k}\arctan\left\{\frac{1}{k}\left[\beta\coth\left(\beta(\frac{B}{2})\right) - \alpha\tanh\,(\alpha(\frac{B}{2}))\right]\right\} \quad \text{(A.35)}$$

Then $L_{1\,Ts2}$ and $L_{1\,Ts3}$ must be iteratively determined for different frequency combinations until the followin equation is meet

$$0.8L_{axial} = L_{1\,Ts1} + B + L_{1\,Ts2} + L_{1\,Ts3} \quad \text{(A.36)}$$

To determine the stress ratio of a tension-torsion specimen we first must consider a unitary axial A_0 and rotational A_{0r} displacement at the stress node Sn2 and Sn1, respectively.

The shear stress at the main throat Ts1 smallest cross section area (x=0) is determined following

$$\varphi\left(L_{1\,Ts1},\left(\frac{B}{2}\right)\right)=\frac{\cos(kL_{1\,Ts1})\cosh\left(\alpha\left(\frac{B}{2}\right)\right)}{\sinh\left(\beta\left(\frac{B}{2}\right)\right)} \tag{A.37}$$

$$\sigma_{shear}(x,A_{0r})=$$
$$GA_{0r}T_r\varphi\left(L_{1\,Ts1},\left(\frac{B}{2}\right)\right)\left[\frac{\sqrt{\cosh(\alpha x)}[\beta\cosh(\beta x)\cosh(\alpha x)-\alpha\sinh(\beta x)\sinh(\alpha x)]}{cosh^2(\alpha x)}\right]\ ,for\ x<\frac{B}{2} \tag{A.38}$$

Again, the tension-compression method cannot correctly describe the displacement and stress distribution behaviour due to the specimen geometry complexity. From a complete set of specimens, an equivalent constant section L_{eq} was determined to the analytically determined one throat specimen L_{axial}. The equivalent L_{eq} is attained by equation (3.5), solely dependent on L_{axial}.

$$L_{eq}=-0.0227L_{axial}^2+0.7112L_{axial} \tag{A.39}$$

L_{eq} is then used to determine the axial stress

$$\varphi\left(L_{eq},\frac{B}{2}\right)=\frac{\cos(kL_{eq})\cosh\left(\alpha\left(\frac{B}{2}\right)\right)}{\sinh\left(\beta\left(\frac{B}{2}\right)\right)} \tag{A.42}$$

$$\sigma_{axial}(x,A_0)=E\cdot A_0\cdot\varphi(L_1,L_2)\left[\frac{\beta\cosh(\beta x)\cdot\cosh(\alpha x)-\alpha\sinh(\beta x)\cdot\sinh(\alpha x)}{cosh^2(\alpha x)}\right]\ for\ x\le\frac{B}{2} \tag{A.41}$$

The specimen stress ratio considering A_0 and A_{0r} unitary displacement is then

$$\sigma_{specimen\ ratio}=\frac{\sigma_{shear}(0,1)}{\sigma_{axial}(0,1)} \tag{A.42}$$

The final induced stress ratio result is dependent on the rotational Sn1/Sn2 specimen ratio and multi-horn displacement ratio in the region where the components meet.

The rotational displacement ratio of the specimen depends on the determined Ts3 frequency (f_{Ts3}) follows the determined equation

$$U_{Sn1/Sn2\ ratio}=0.0276e^{1.79E-04\cdot f_{Ts3}} \tag{A.43}$$

The multi-horn rotational/axial displacement ratio ($U_{SnH\ ratio}$) must by numerically determined. The present study multi-horn has a 0.41 rotational/axial displacement ratio.

The setup stress ratio is determined through equation (A.44) with the specimen unitary stress ratio equation (A.42), the displacement ratio between its stress nodes Sn1 and Sn2 ($U_{Sn1/Sn2\ ratio}$) (A.43), and the complete setup displacement ratio at the SnH region ($U_{SnH\ ratio}$).

$$\sigma_{setup\ ratio}=\frac{U_{SnH\ ratio}}{U_{Sn1/Sn2\ ratio}}\sigma_{specimen\ ratio} \tag{A.44}$$

In-plane Biaxial Cruciform

The present analytical solution regarding cruciform specimen does not determine a 20kHz geometry. The applied cruciform follows the referenced Baptista et al. [54] optimised goemtry and require iterative FE free vibration frequency analysis to reach a 20 kHz geometry.

The proposed analytical method determines the induced stress through the measured displacements at the cruciform arms (Laser B measuring setup, Figure 4-28) and the normalised stress distribution across the cruciform arm's length (taken from FE free vibration frequency analysis at 20kHz).

The analytical concept considered the cruciform geometry as two figurative perpendicular plane specimens with one shared fatigue testing region. Two different combinations of axial specimens' are possible from the cruciform geometry. Each combination was considered as 'Slices' (S*x*) made to the cruciform arms. Plane S specimen defining dimensions were then associated with the cruciform dimensional variables. Figure A-8-5 shows the two possible 'slices' (S1 and S2) in a cruciform specimen with the associated tension-compression specimen variable designations. Both S1 and S2 follow an exponential curvature.

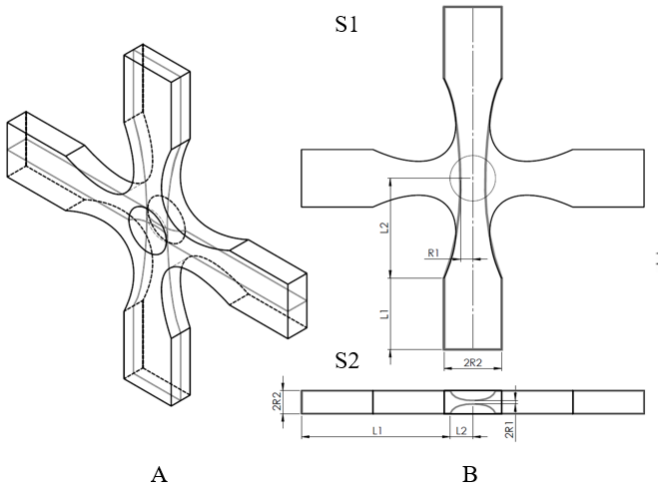

Figure A-8-5. Cruciform equivalent uniaxial plane S specimen representation: (A) 3D cut representation; (B) S1 and S2 dimensional variables;

For S1 and S2 slices, one equivalent dimension needs to be determined: R1 for S1; and L_1 for S2.

For S1, R_1 is iteratively determined by changing its value until the cruciform equivalent L_1 is equal to the determined by the tension-compression analytical method. The L_1 for S2 is

determined following base tension-compression exponential curvature methodology, equation (A.11) to equation (A.14).

Figure A-8-6 compares S ‘slices’ with the New T-T (N T-T) and C-T specimens FEA obtained stress gradient results. An Approximation is also plotted for both presented specimens’ results. The made Approximation follows the initial and final tendency of the stress distribution. It does not consider the stress distribution changes associated with arm-to-arm link.

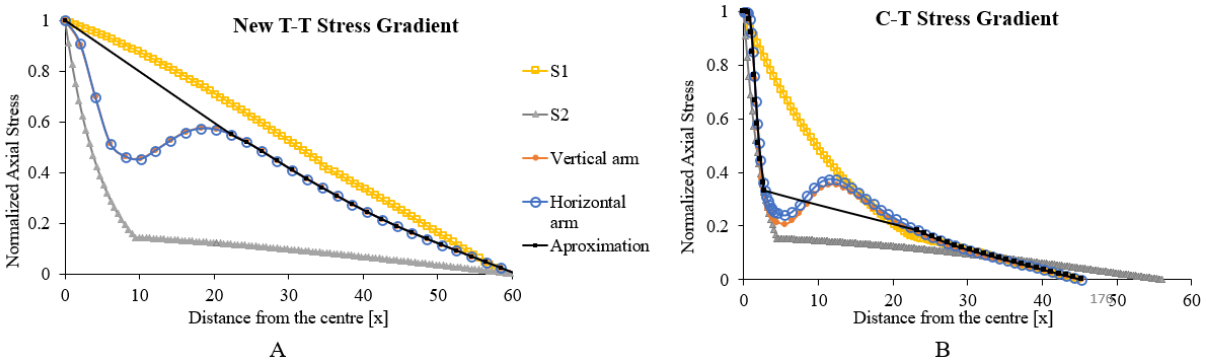

Figure A-8-6. Normalised stress distribution of N T-T (A) and C-T (B) vertical and horizontal arms, corresponding S1 and S2 ‘slices’; made Approximation.

The S stress distribution that better represents the cruciform arm’s made Approximation is chosen.

The differences between the made Approximation and the determined S stress distribution are made through strain energy correction. The strain energy correction is conducted through the stress distribution area. The strain energy is added or removed if the S stress area is higher or lower. The strain energy difference was denoted the area difference compensation factor (δ). Figure A-8-7 shows the area difference method and the area difference compensation factor (δ) determination.

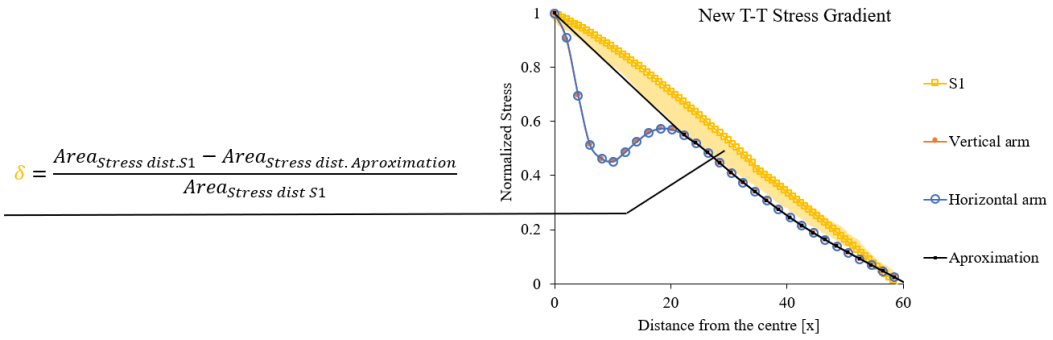

Figure A-8-7. Area difference compensation factor (δ) determination method for N T-T cruciform specimen.

The quantified 'flapping motion' must be corrected to the measured axial displacement at the horizontal arms. To corrected it the 'flapping motion' factor (γ) must be calculated

$$\begin{cases} \gamma = \delta_{x,corrected} = \left(\delta - 1.75\frac{A_{0x}-A_{0y}}{A_{0y}}\right), & for\ A_{0x} \geq A_{0y} \\ \gamma = \delta_{x,corrected} = \ (\delta - 0.75\frac{A_{0x}-A_{0y}}{A_{0y}}), & for\ A_{0x} \leq A_{0y} \end{cases} \quad (A.45)$$

The area difference compensation factor (δ) with the applied 'flapping motion' factor (γ) is then introduced in tension-compression analytical solution for the horizontal arm. The resulted equations for the vertical arms axial strain (ε_y) and horizontal arms axial strain (ε_x) are:

$$\varepsilon_y(y, A_{0y}) = A_{0y}(1+\delta)\varphi(L_1, L_2)[\beta\cosh(\beta y) - \alpha\sinh(\beta y)]\exp(-\alpha y) \quad (A.46)$$

$$\varepsilon_x(x, A_{0x}) = A_{0x}(1+\gamma)\varphi(L_1, L_2)[\beta\cosh(\beta x) - \alpha\sinh(\beta x)]\exp(-\alpha x) \quad (A.47)$$

Being the cruciform mid-point (x=0, y=0) the region of interest:

$$\varepsilon_y(0, A_{0y}) = \ A_{0y}(1+\delta)\varphi(L_1, L_2) \quad (A.48)$$

$$\varepsilon_x(0, A_{0x}) = A_{0x}(1+\gamma)\varphi(L_1, L_2) \quad (A.49)$$

The Hooke's law is afterwards calculated with null shear strain for the determination of the midpoint (x=0; y=0) biaxial stress state.

$$\begin{bmatrix} \sigma_x \\ \sigma_y \\ \sigma_{xy} \end{bmatrix} = \frac{E}{1-\nu^2}\begin{bmatrix} 1 & -\nu & 0 \\ \nu & 1 & 0 \\ 0 & 0 & 1-\nu \end{bmatrix} \cdot \begin{bmatrix} \varepsilon_x \\ \varepsilon_y \\ 0 \end{bmatrix} \quad (A.50)$$

FE steady-state analysis can determine a displacement to stress ratio. For FEA, γ equation (A.51) is calculated directly to the horizontal arm A_{0x} followed by the numerical determined ratio for stress determination.

$$\begin{cases} A_{0x,corrected} = A_{0x}\left(1 - 1.75\frac{A_{0x}-A_{0y}}{A_{0y}}\right), & for\ A_{0x} \geq A_{0y} \\ A_{0x,corrected} = A_{0x}\ (1 - 0.75\frac{A_{0x}-A_{0y}}{A_{0y}}), & for\ A_{0x} \leq A_{0y} \end{cases} \quad (A.51)$$

A.2 FEA sensitivity dimensional analysis

FEA Tension-Torsion specimens only

Dimensional changes to the specimen were made to all key dimensions (A, B, C, and Tr). Each dimension was altered in equal and symmetrical values alone to quantify their overall impact on the frequency (A ±1 mm; B ±1mm; C ±1mm; Tr ±0.05 mm). The resulting frequency changes for the torsional and longitudinal modes are presented from Table A-1 to Table A-4. Blue marks indicate non-altered key dimension. R constant section radius of 5 mm was not altered.

Table A-1. First tension-torsion specimen alone dimension to frequency sensitivity analysis results.

First Specimen Dimensions [mm]					Resonance Frequency [Hz]	
A	**C**	**B**	**$Tr_{Main\ Throat}$**	**$Tr_{Secundary\ throat}$**	**3º Torsional**	**1º Longitudinal**
12.15	24.3	12.15	1.64	1.8	20092	20121
12.15	24.3	12.15	1.7	1.85	20966	20368
12.15	24.3	12.15	1.6	1.75	19316	19939
13.15	24.3	12.15	1.64	1.8	19790	19690
11.15	24.3	12.15	1.64	1.8	20440	20574
12.15	25.3	12.15	1.64	1.8	19849	19841
12.15	23.3	12.15	1.64	1.8	20351	20408
12.15	24.3	13.15	1.64	1.8	19536	19539
12.15	24.3	11.15	1.64	1.8	20902	20740
Frequency Range (Max-Min)					1650	1201

Table A-2. Spc1 tension-torsion specimen alone dimension to frequency sensitivity analysis results.

Spc 1 key Dimensions [mm]				Resonance Frequency [Hz]	
A	**C**	**B**	**Tr**	**3º Torsional**	**1º Longitudinal**
10.5	5.83	20.23	2.3	20017	20000
10.5	5.83	20.23	2.35	20646	20235
10.5	5.83	20.23	2.25	19379	19756
11.5	5.83	20.23	2.3	19916	19409
9.5	5.83	20.23	2.3	20637	20124
10.5	6.83	20.23	2.3	19181	19781
10.5	4.83	20.23	2.3	20983	20216
10.5	5.83	21.23	2.3	19381	19445
10.5	5.83	19.23	2.3	20686	20585
Frequency Range (Max-Min)				1802	1176

Table A-3. Spc2 tension-torsion specimen alone dimension to frequency sensitivity analysis results.

Spc 2 key Dimensions [mm]				Resonance Frequency [Hz]	
A	**C**	**B**	**Tr**	**3º Torsional**	**1º Longitudinal**
7.3	4.1	25.43	2.4	19992	20002
7.3	4.1	25.43	2.45	20588	20212
7.3	4.1	25.43	2.3	19371	19777
8.3	4.1	25.43	2.4	19847	19365
6.3	4.1	25.43	2.4	20170	20696
7.3	5.1	25.43	2.4	19164	19772
7.3	3.1	25.43	2.4	20968	20233
7.3	4.1	26.43	2.4	19414	19472
7.3	4.1	24.43	2.4	20585	20554
Frequency Range (Max-Min)				1804	1331

Table A-4. Spc3 tension-torsion specimen alone dimension to frequency sensitivity analysis results.

Spc 3 key Dimensions [mm]				Resonance Frequency [Hz]	
A	**C**	**B**	**Tr**	**3º Torsional**	**1º Longitudinal**
14	14	15.07	2.5	20048	20039
14	14	15.07	2.55	20629	20228
14	14	15.07	2.45	19440	19836
15	14	15.07	2.5	19929	19555
13	14	15.07	2.5	20180	20554
14	15	15.07	2.5	19565	19801
14	13	15.07	2.5	20575	20279
14	14	16.07	2.5	19406	19482
14	14	14.07	2.5	20769	20639
Frequency Range (Max-Min)				1363	1157

Complete multiaxial setup

Table A-5 to Table A-8Table A-6 presents for each tested dimensional combination of the complete setup (Booster multi-horn specimen): PMs and MI frequencies; MI shear/axial stress ratio at the specimen's main throat; and displacement ratio at its free base.

Table A-5. Booster multi-horn first tension-torsion specimen setup, dimension to frequency sensitivity analysis results.

First Specimen Dimensions [mm]					Resonance Frequency [Hz]			MI Stress ratio	MI Disp. Ratio
A	**C**	**B**	**Tr_{Main}**	**$Tr_{Sec.}$**	**MI**	**PM1**	**PM2**	**Shear/Axial**	**Free base**
12.15	24.3	12.15	1.64	1.8	20028	19267	20534	0.193	0.310
12.15	24.3	12.15	1.7	1.85	20127	19998	20548	2.164	5
12.15	24.3	12.15	1.6	1.75	20002	18543	20529	0.107	0.125
13.15	24.3	12.15	1.64	1.8	19971	18963	20528	0.159	0.209
11.15	24.3	12.15	1.64	1.8	20086	19620	20542	0.278	0.572
12.15	25.3	12.15	1.64	1.8	19991	19042	20530	0.147	0.223
12.15	23.3	12.15	1.64	1.8	20066	19505	20539	0.276	
12.15	24.3	13.15	1.64	1.8	19950	19173	20525	0.105	0.129
12.15	24.3	11.15	1.64	1.8	20138	19990	20550	1.207	2.717
Range (Max – Min)					188	1455	25	2.059	4.875

Table A-6. Booster multi-horn Spc1 tension-torsion specimen setup, dimension to frequency sensitivity analysis results.

Spc 1 Specimen Dimensions [mm]				Resonance Frequency (Hz)			Stress ratio	Disp. Ratio
A	**C**	**B**	**Tr**	**MI**	**PM1**	**PM2**	**Shear/Axial**	**Free base**
10.5	5.83	20.23	2.3	20011	19412	20489	0.782	0.413
10.5	5.83	20.23	2.35	20174	19818	20555	1.857	1.114
10.5	5.83	20.23	2.25	19939	18871	20463	0.402	0.183
11.5	5.83	20.23	2.3	19898	19341	20467	0.792	0.390
9.5	5.83	20.23	2.3	20124	19493	20515	0.813	0.464
10.5	6.83	20.23	2.3	19940	18655	20462	0.326	0.154
10.5	4.83	20.23	2.3	20308	19910	20673	2.216	1.263
10.5	5.83	21.23	2.3	19883	18860	20457	0.394	0.186
10.5	5.83	19.23	2.3	20237	19863	20567	1.819	1.048
Range (Max-Min)				1255	425	216		

Table A-7. Booster multi-horn Spc2 tension-torsion specimen setup, dimension to frequency sensitivity analysis results.

Spc 2 Specimen Dimensions [mm]				Resonance Frequency (Hz)			Stress ratio	Disp. Ratio
A	**C**	**B**	**Tr**	**MI**	**PM1**	**PM2**	**Shear/Axial**	**Free base**
7.3	4.1	25.43	2.4	19989	19342	20496	0.61	0.41
7.3	4.1	25.43	2.45	20125	19787	20543	1.47	1.14
7.3	4.1	25.43	2.35	19954	18801	20484	0.32	0.18
8.3	4.1	25.43	2.4	19893	19241	20482	0.57	0.35
6.3	4.1	25.43	2.4	20129	19476	20527	0.65	0.50
7.3	5.1	25.43	2.4	19950	18572	20482	0.26	0.15
7.3	3.1	25.43	2.4	20290	19931	20629	2.55	1.88
7.3	4.1	26.43	2.4	19902	18826	20479	0.32	0.20
7.3	4.1	24.43	2.4	20172	19808	20547	1.42	1.05
Range (Max-Min)				397	1359	150	2.29	1.72

Table A-8. Booster multi-horn Spc1 tension-torsion specimen setup, dimension to frequency sensitivity analysis results.

Spc 3 Specimen Dimensions [mm]				Resonance Frequency (Hz)			Stress ratio	Disp. Ratio
A	**C**	**B**	**Tr**	**MI**	**PM1**	**PM2**	**Shear/Axial**	**Free base**
14	14	15.07	2.5	20001	19268	20485	0.641	0.440
14	14	15.07	2.55	20143	19696	20553	1.177	0.924
14	14	15.07	2.45	19954	18769	20462	0.379	0.222
15	14	15.07	2.5	19910	19180	20470	0.604	0.385
13	14	15.07	2.5	20132	19379	20517	0.681	0.502
14	15	15.07	2.5	19948	18853	20497	0.395	0.254
14	13	15.07	2.5	20138	19666	20542	1.145	0.824
14	14	16.07	2.5	19874	18731	20452	0.361	0.215
14	14	14.07	2.5	20241	19774	20577	1.228	0.946
Range (Max-Min)				367	1043	125	0.867	0.731

Two Boosters Two Horns (2B+2H) setup

Table A-9 to Table A-12 presents 2B+2H specimen setup sensitivity analysis: MI, PM1 and PM2 frequencies; stress ratio at the main throat; Displacement ratio at a horn-specimen connection; and the overall range between all computed results.

Table A-9. 2B+2H First specimen tension-torsion setup, dimension to frequency sensitivity analysis results.

First Specimen Dimensions [mm]					Resonance Frequency [Hz]			MI Stress ratio	MI Disp. Ratio
A	**C**	**B**	**Tr_{Main}**	**$Tr_{Sec.}$**	**MI**	**PM1**	**PM2**	**Shear/Axial**	**base**
12.15	24.3	12.15	1.64	1.8	20029	16442	20363	0.188	0.281
12.15	24.3	12.15	1.7	1.85	20049	17076	20416	0.253	0.281
12.15	24.3	12.15	1.6	1.75	20014	15981	20319	0.151	0.282
13.15	24.3	12.15	1.64	1.8	19998	16407	20484	0.185	0.273
11.15	24.3	12.15	1.64	1.8	20059	16476	20491	0.191	0.29
12.15	25.3	12.15	1.64	1.8	20009	16193	20486	0.166	0.279
12.15	23.3	12.15	1.64	1.8	20049	16716	20489	0.214	0.286
12.15	24.3	13.15	1.64	1.8	19986	15980	20484	0.146	0.272
12.15	24.3	11.15	1.64	1.8	20073	16985	20491	0.249	0.290
Range (Max – Min)					87	1096	172	0.24	0.02

Table A-10. 2B+2H Spc1 tension-torsion setup, dimension to frequency sensitivity analysis results.

Spc1 Specimen Dimensions [mm]				Resonance Frequency (Hz)			Stress ratio	Disp. Ratio
A	**C**	**B**	**Tr**	**MI**	**PM1**	**PM2**	**Shear/Axial**	**Base**
10.5	5.83	20.23	2.3	20016	18744	20382	0.782	0.412
10.5	5.83	20.23	2.35	20079	19177	20386	1.135	0.331
10.5	5.83	20.23	2.25	19965	18256	20375	0.555	0.447
11.5	5.83	20.23	2.3	19947	18720	20362	0.783	0.390
9.5	5.83	20.23	2.3	20077	18757	20397	0.790	0.440
10.5	6.83	20.23	2.3	19964	17992	20376	0.475	0.455
10.5	4.83	20.23	2.3	20129	19481	20385	1.611	0.204
10.5	5.83	21.23	2.3	19934	18229	20373	0.536	0.428
10.5	5.83	19.23	2.3	20118	19238	20388	1.215	0.336
Range (Max-Min)				63	1489	4	1.14	0.25

Table A-11. 2B+2H Spc2 tension-torsion setup, dimension to frequency sensitivity analysis results.

Spc2 Specimen Dimensions [mm]				Resonance Frequency (Hz)			Stress ratio	Disp. Ratio
A	**C**	**B**	**Tr**	**MI**	**PM1**	**PM2**	**Shear/Axial**	**Base**
7.3	4.1	25.43	2.4	20012	18508	20517	0.60	0.41
7.3	4.1	25.43	2.45	20061	18946	20420	0.84	0.37
7.3	4.1	25.43	2.35	19978	18063	20410	0.45	0.44
8.3	4.1	25.43	2.4	19945	18492	20398	0.60	0.39
6.3	4.1	25.43	2.4	20078	18524	20429	0.60	0.44
7.3	5.1	25.43	2.4	19972	17734	20411	0.37	0.44
7.3	3.1	25.43	2.4	20095	19340	20418	1.26	0.29
7.3	4.1	26.43	2.4	19948	18038	20408	0.43	0.41
7.3	4.1	24.43	2.4	20089	18988	20420	0.88	0.38
Range (Max-Min)				150	1606	31	0.89	0.15

Table A-12. 2B+2H Spc3 tension-torsion setup, dimension to frequency sensitivity analysis results.

Spc3 Specimen Dimensions [mm]				Resonance Frequency (Hz)			Stress ratio	Disp. Ratio
A	**C**	**B**	**Tr**	**MI**	**PM1**	**PM2**	**Shear/Axial**	**Base**
14	14	15.07	2.5	19994	18287	20504	0.620	0.408
14	14	15.07	2.55	20045	18660	20451	0.771	
14	14	15.07	2.45	19977	17877	20359	0.491	0.443
15	14	15.07	2.5	19955	18281	20348	0.613	0.390
13	14	15.07	2.5	20083	18329	20384	0.635	0.436
14	15	15.07	2.5	19975	17891	20363	0.488	0.431
14	13	15.07	2.5	20076	18738	20371	0.817	0.364
14	14	16.07	2.5	19930	17831	20355	0.464	0.421
14	14	14.07	2.5	20127	18784	20379	0.844	0.365
Range (Max-Min)				197	953	156	0.38	0.08